Seasonal Variability of Water Mass Properties in Bass Strait:

THREE-DIMENSIONAL OCEANOGRAPHIC MODELLING STUDIES

Paul Anthony Sandery, BSc (Hons)

A thesis submitted for the
Degree of Doctor of Philosophy
April 2007

Flinders University
Adelaide-Australia
School of Chemistry, Physics
and Earth Sciences

Table Of Contents

CHAPTER 1 Introduction & Background

CHAPTER 2 Literature Review

CHAPTER 3 Theory & Methods

CHAPTER 4 Results & Analysis

CHAPTER 5 Sensitivity to Variation in Forcing

CHAPTER 6 Summary & Conclusions

Abstract

The climatology of the seasonal cycle of water mass variation and transformation in Bass Strait, south-eastern Australia, is studied using a high resolution three-dimensional sigma-coordinate hydrodynamic model coupled with data from observations and previous studies.

Model forcing consists of the principal tidal constituents from the Australian National Tidal Centre and long-term monthly mean atmospheric forcing fields from NCEP reanalysis. The initial density field is established using temperature and salinity means and annual and semi-annual harmonics from the CARS2000 hydrographic atlas. This is also used to prescribe incoming water mass properties at model open-sea boundaries with seasonal variation. Far-field forcing is included with open-sea boundary parameterisation of residual sea-level representing both the South Australian Current and the East Australian Current. Lagrangian and Eulerian tracer methods are used to derive transport timescales, such as age, residence times and flushing times. These are used to examine and summarise model predictions and as a diagnostic tool in sensitivity studies.

Currents, sea-level and water mass properties in the model compare favourably with previous studies and observations, despite limitations in the model and in the data used for comparison. The seasonal cycle, in model results, is characterised by formation of a shallow (< 20 m) saltier surface-layer in late spring to summer and subsequent downward mixing and erosion of the salinity field in autumn to winter with water mass from the west. This leaves behind water mass with positive age and salinity anomalies in areas of low flushing. In late winter-early spring most parts of this water mass leave the Strait interior. These areas are thought to be related to the source water of the Bass Strait Cascade. The residual circulation in all model experiments is shown to be related to seasonal-mean sea-level anomalies, arising from both barotropic and baroclinic adjustment, both in and surrounding the Strait.

Acknowledgements

Firstly, I would like to thank Jochen Kämpf, my supervisor, for his enthusiasm, trust, encouragement and advice. I also wish to acknowledge Matthias Tomczak and Scott Condie for their co-supervision. Thank you for sharing your expertise and time.

This thesis would not have been possible without the support of an Australian Post-graduate Award, for which I am extremely grateful.

Data used in the study was provided by CSIRO Marine and Atmospheric Research, the Australian National Tidal Centre, the Australian Bureau of Meteorology, NOAA and Geoscience Australia. Simulations were carried out using computing facilities at SAPAC, the South Australian Partnership for Advanced Computing. I am thankful for the generosity extended by these organizations to facilitate this research project.

I would also like to acknowledge and thank my colleagues at Flinders University in the School of Chemistry, Physics and Earth Sciences for their interest, support and company during the time I was there. In particular, my gratitude is extended to John Bennett, Cäcillia Ewenz, Gail Jackson and Paul Gardner-Stephen. I also thank Patrick Luyten for providing the hydrodynamic model and advice. Lastly, I kindly thank Rudy Kloser and Alan Williams from CSIRO Marine and Atmospheric Research for giving me the opportunity to participate in Southern Surveyor Voyage SS0704.

I dedicate this work to Verity, Nicholas and Barbara.

Declaration of Authenticity

‘I certify that this thesis does not incorporate, without acknowledgment, any material previously submitted for a degree or diploma in any university; and that to the best of my knowledge and belief it does not contain any material previously published or written by another person except where due reference is made in the text’.

Paul Anthony Sandery

List Of Figures

List Of Tables

List Of Acronyms

AOMIP	Arctic Ocean Model Intercomparison Project
ASMD94	Atlas of Surface Marine Data 1994
BSC	Bass Strait Cascade
CARS	Climatological Atlas of Regional Seas
CC	Coastal Current
CFL	Courant-Friedrichs-Lewy stability condition
CGBAPS	Cape Grim Baseline Air Pollution Monitoring Station
COADS	Comprehensive Ocean Atmosphere Dataset
COHERENS	Coupled Hydrodynamical and Ecological Model for Regional and Shelf Seas
CSIRO	Commonwealth Scientific and Industrial Research Organisation
CTD	Conductivity-Temperature-Depth Sensor
CTW	Coastal-trapped Wave
EAC	East Australian Current
EACW	East Australian Current Water
FC	Flinders Current
GAB	Great Australian Bight
HR	Hellerman-Rosenstein
NCEP	National Centre for Environmental Prediction
NTC	National Tidal Centre
NOAA	National Oceanographic and Atmospheric Administration
SAC	South Australian Current
SACW	South Australian Current Water
SAPAC	South Australian Partnership for Advanced Computing
SASW	Sub-antarctic Surface Water
STC	Sub-tropical Convergence
TVD	Total Variation Diminishing
ZC	Zeehan Current

CHAPTER 1:
Introduction
& Background

1.1 Introduction

This study examines seasonal variation of water mass properties in Bass Strait, south-eastern Australia. This is facilitated with a three-dimensional hydrodynamic model, a range of observations and information provided by previous studies. The seasonal scale is focused on as this is important in the dynamics of regional climate and local marine ecosystems. A detailed knowledge of ocean properties, their characteristics and dynamics is a contemporary scientific research challenge. Direct observations of ocean currents and properties are relatively few, especially away from the surface. Numerical models can capture what might be missed by observations. They can be used to test hypotheses and theories. Their reliability depends on the reliability of the forcing data, the boundary conditions and the model itself. Interpretation of model results must therefore always be (re)considered with respect to the framework in which they originate.

In recent times there has been advances in techniques used to model ocean currents in shelf seas, for reviews see (Jones, 2002; Nihoul et al., 1989). A particular example is the COHERENS model which was specifically designed for shelf sea applications where sharp density fronts typically exist. COHERENS is a three-dimensional primitive equation sigma-coordinate hydrodynamic model which is coupled to biological, optical and sediment transport modules. It has the capability of simulating Eulerian or Lagrangian tracers. COHERENS has been documented in Luyten *et al.* (1999) and used in recent studies (Marinov et al., 2006; Sadrinasab and Kämpf, 2004). It is presently used in operational forecasting in the North Sea.

COHERENS is used in this study with relatively realistic forcing and boundary conditions. All boundary conditions and forcing data used in the model are derived from historical observations, except in the case of the parameterisation of open-boundary sea-level which is derived from sensitivity studies.

The forcing data consists of long-term monthly mean NCEP-reanalysis atmospheric variables (Kalnay et al., 1996), water properties from the CSIRO Climatological Atlas of Regional Seas (CARS2000) (Dunn and Ridgway, 2002) and tidal amplitudes and phases of the four principal constituents, the M_2, S_2, O_1 and K_1 tides, from the National Tidal Centre (NTC).

A simple approach is adopted for prescribing far-field oceanic forcing in the model. A seasonal signal is generated for residual sea-level amplitude at the coast. The amplitude is used to derive sea-level along the boundary which has decay scale, away from the coast, of the order of the Rossby radius. This is then applied to simulate background sea-level for the East Australian Current and the South Australian Current, both of which play a role in the region’s ocean circulation. The amplitudes of these signals are adjusted so that climate-averaged water mass properties of turbulent flow in the open-ocean part of the model domain have similar structure to climate-averaged values derived from observations.

Model currents in Bass Strait are tuned by refinement of bottom friction so that tidal harmonic co-variations are close to observations. CARS2000 atlas means and annual and semi-annual harmonics of temperature and salinity are found on the model grid and used for direct time-space comparison of atlas and model seasonal cycles. Comparisons are made with existing current meter mooring data and conductivity-temperature-depth (CTD) observations provided by CSIRO Marine and Atmospheric Research.

Tracer methods are developed to derive seasonally varying transport timescales such as flushing time, residence time and age distributions These are employed to identify and summarize features in the circulation which may be of importance to understanding pollution and contaminant pathways, advection of biota such as plankton and fish larvae and distributions of nutrients and water masses.

1.2 Aims and Objectives

The specific aim of the study is to develop a regional oceanographic model to study physical processes in Bass Strait, such as tidal, wind and density driven advection and mixing, at seasonal time scales from a climatological perspective. The objectives of the study are to use the model, observational data and previous scientific findings to

- study the character of the integrated tidal, wind and density driven flow.

- investigate seasonal variation of shelf water mass properties and the formation and export of dense water.

- develop transport timescale methods and use them as diagnostic tools for the advection-diffusion ‘climate’ in the model.

- investigate model sensitivity and response of circulation to variation in forcing.

1.3 Bathymetry and Physical Characteristics

Bass Strait is a broad, relatively shallow, shelf-sea connecting the southeast Indian Ocean in the west with the Tasman Sea in the east. It is located between Tasmania and Victoria in south-eastern Australia (Figure 1.3.1). The Strait’s mean depth is between 60-70 m and abyssal depths on either side are around 4-5 km. Oceanic margins are characterised by shelf break and continental slope incised by submarine canyons. Entrances to the Strait feature sills and island groups. The central basin has maximum depth of around 105 m.

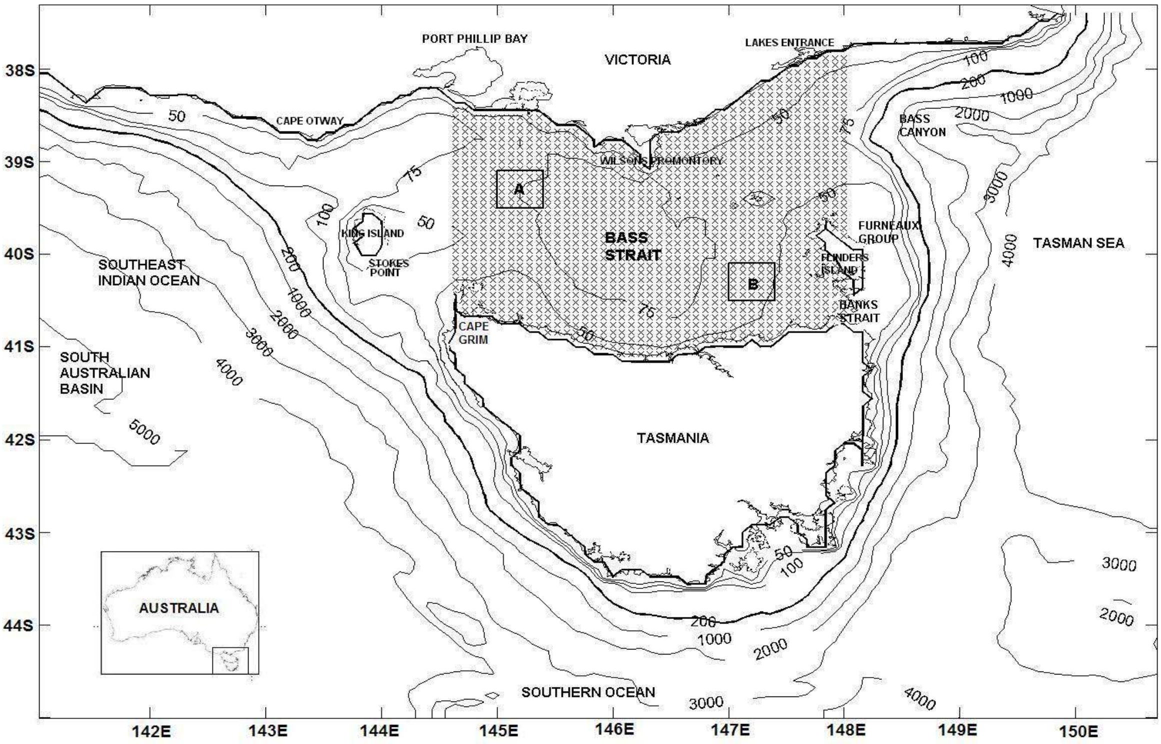

Figure 1.3.1. Model domain and bathymetry (model limited to maximum 1000 m depth). Model coastline (heavier line) shown to illustrate fitting of model to the region. Area within Bass Strait marked with crosses, at model horizontal grid resolution, is region of interest for transport timescales. Areas A and B are used to illustrate age distributions at different times of year. (Data source: Geoscience Australia, 2002)

Estimates of some important physical characteristics related to topography, seawater volume and surface area are given in Table 1.3.1. Statistics are based on gridded bathymetric data from *Geoscience Australia* (2002) which has spatial resolution 0.01^{o} or ~1.11 km. Calculations are based on a volume bounded by 37.8-41.2^{o}S and 143-149^{o}E with the condition that all depths > 200 m are excluded. Total volume and sea surface area assume a flat sea surface. Temperature ranges were calculated using the CARS atlas.

The semi-annual net heat flux cycle is an important parameter in the seasonal cycle of heating and cooling and in changes in salinity and buoyancy of water mass. In a volume representative of the Strait, the net heat flux required to warm the entire volume from winter to summer (inward directed net) and cool it down from summer to winter (outward directed net) by 4.5^{o}C over a 6 month period, assuming complete mixing, is of the order of ~73 Wm^{-2}.

Maximum interior depth	105 m
Mean depth	64 m
Total volume	1.11×10^7 km^3
Total sea surface area	1.72×10^5 km^2
Mean width	262 km
Minimum width	210 km
Mean length	452 km
Mean annual surface temperature range	5.5°C
Mean depth-averaged temperature range	4.5°C
Total heat flux required to change temperature of total volume by 4.5°C over 6 month period	1.26×10^{13} W
Heat flux per unit area required to change temperature of total volume by 4.5°C over 6 month period, assuming complete mixing	73 W m^{-2}

Table 1.3.1. Some estimates of physical characteristics for Bass Strait.

1.4 Background Climate

The seasons referred to in the text are in the context of the southern hemisphere, so for example, the austral Summer period is defined by the calendar months of December, January and February and the months of June, July and August define the austral Winter period. Salinity is given without units in the text, however, these are assumed to be either psu or g/kg. Wind and current directions are defined according to meteorological and oceanographic conventions. For example, an eastward current is directed towards the east and a westerly wind propagates from the west.

The climate is broadly defined as maritime temperate mesothermal *Cfb* in the Köppen climate classification (Kottek et al., 2006). Inspection of long-term monthly mean air temperatures show maxima in summer months around 17-18°C (Kalnay et al., 1996). Winter minimum air temperatures are around 10.5°C. Relative humidities show little variation from around 75% through the year. Mean precipitation in summer is around 1.3 mm/day, however this doubles to around 2.6 mm/day in winter. Bass Strait lies in the path of the westerly wind belt known as the Roaring Forties. Wind patterns are generally north-westerly in winter to south-westerly in summer, with stronger westerly mean winds usually found during winter and spring. The terrestrial air masses of mainland Australia, and to lesser extent Tasmania, are also involved in setting the climate of the Strait at certain times. In summer, a low pressure air mass typically forms over continental Australia and a high over the ocean south of the continent. This gives rise to southerly summer winds in Bass Strait.

A confluence of different water masses occurs in the region, which influences ecology and water mass in Bass Strait (Figure 1.4.1). The East Australian Current (EAC) is a western boundary current which transports between minimum of 7 Sv and maximum of 16 Sv in winter and summer, respectively, southwards between 23^{o}S and 43^{o}S off eastern Australia (Ridgway and Godfrey, 1997) (1 Sverdrup (Sv) = 10^6 m^3 s^{-1}). There may be periodic intrusions into north-eastern Bass Strait (Newell, 1960), however this is not well documented. For at least six months of the year, around the austral winter season, the South Australian Current (SAC) moves relatively saltier-warmer water eastward along the southern Australian shelf from the Great Australian Bight to western Bass Strait (Herzfeld and Tomczak, 1997; Tomczak, 1985). This current bifurcates near 39^{o}S, 143^{o}E with one extension moving into Bass Strait and one becoming the Zeehan Current (ZC) off western Tasmania. The ZC is about 40 km wide and 50 m deep and transports about 1 Sv (Baines *et al.*, 1983). The ZC is a part of the longest known coastal current system, a seasonal linkage of the Leeuwin Current (not shown), SAC and ZC, starting at the northwest shelf of Australia and continuing to eastern Tasmania (Ridgway and Condie, 2004).

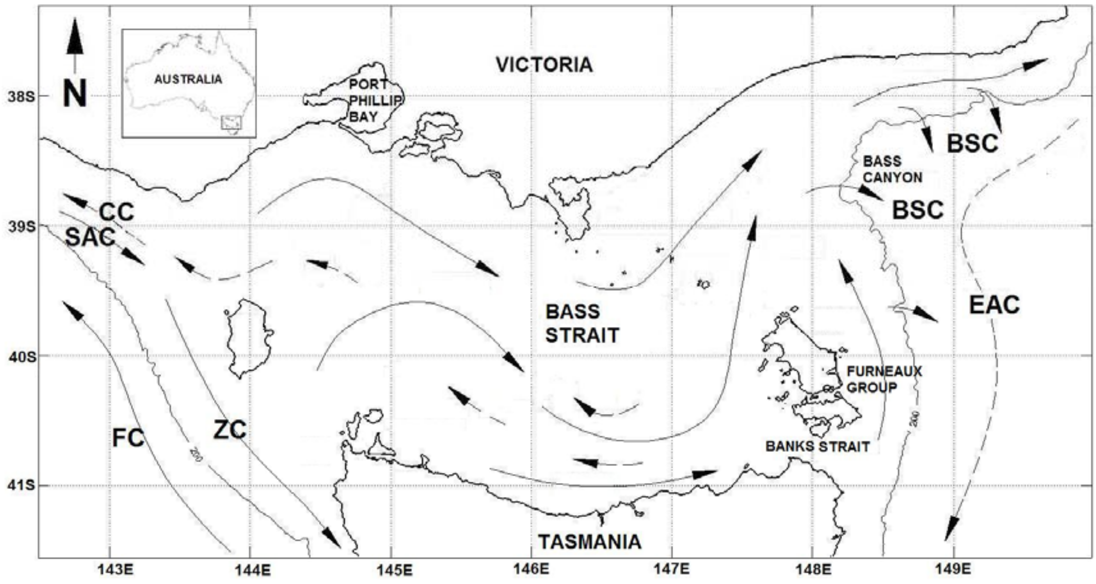

Figure 1.4.1. Schematic representation of currents in the Bass Strait region. Summer currents are denoted with dashed lines and the 200 m depth shelf break is shown. (Adapted and modified from the following: EAC - East Australian Current (Ridgway and Godfrey, 1997), SAC - South Australian Current (Ridgway and Condie, 2004), ZC - Zeehan Current (Baines *et al.*, 1983), FC - Flinders Current (Bye, 1983; Middleton and Cirano, 2002). CC – summer Coastal Current (Kämpf *et al.*, 2004).

The Flinders Current (FC), which has been observed from the surface to depths of ~ 800 m, depending on time of year, transports relatively fresher-cooler water along the continental slope in a northwest direction from western Tasmania as far west as Cape Leeuwin in Western Australia (Bye, 1983; Middleton and Cirano, 2002). The coastal current (CC) is part of a summer coastal upwelling system, resulting from regular south-easterly winds (Kämpf *et al.*, 2004), and is associated with low sea-level anomalies forming, at this time of year, along parts of the southern shelf of Australia.

The extent and influence of currents and water masses varies seasonally and inter-annually. Water mass properties in the Strait are influenced by local air-sea heat-salt/freshwater fluxes and properties carried by inflow mostly from the west (Herzfeld and Tomczak, 1997; Tomczak, 1985; Tomczak, 1987). The three primary water masses in the region are East Australian Current Water (EACW), South Australian Current Water (SACW) and sub-Antarctic Surface Water (SASW) (Newell, 1960; 1985; Tomczak, 1987). Bass Strait Water (BSW), is a modified combination these water masses, being the saltiest regional water mass (Gibbs et al., 1986; Godfrey et al., 1980). Transport of EACW into north-eastern Bass Strait is not well documented. The only evidence for this is found in the study by Newell (1960). Intrusions of SACW, through the western entrances, occur mainly during winter to spring, supported by local and remote winds (Gibbs et al., 1986; Middleton and Black, 1994; Newell, 1960; Tomczak, 1985; Tomczak, 1987). The SACW and EACW masses contain relatively warmer and saltier water, whereas SASW is significantly less saline and cooler (Newell, 1960).

The Strait has a reputation for large complex surface waves, high winds and strong tidal currents (Flinders, 1798; Jones, 1980). Shallow regions surrounding the island groups and in the Strait entrances are usually well mixed vertically throughout the year. Waters in the deeper interior are well mixed vertically for several months of the year (Gibbs et al., 1986). Stratification has seasonal variation over a large part of the interior (Baines and Fandry, 1983). In summer, a shallow warmer (by up to 4^oC) surface mixed layer up to ~30 m deep may be present. Wind stress controls levels of vertical mixing in the interior, where the tidal influence is small, and affects seasonal onsets and breakdowns of stratification (Sandery and Kämpf, 2007)

In winter, relatively dense BSW flows down the eastern continental slope to depths of between 300-500 m. This density or gravity current is known as the Bass Strait Cascade (BSC) (Boland, 1971; Gibbs et al., 1991; Godfrey et al., 1980; Luick et al., 1994; Tomczak, 1985; Tomczak, 1987).

1.5 Outline of the Thesis

The thesis follows the following outline. In chapter 2, a review of relevant literature is presented. This is a collection of field observations, theoretical interpretations and numerical simulations which provide a baseline to verify, refute or dispute model findings. Chapter 3 outlines the theory and details the methods used to apply the model and observational data to the study. Chapter 4 presents the atmospheric forcing climate and results of the reference simulation. These are compared with observations and analysed. Model sensitivity studies are presented and analysed in Chapter 5. In Chapter 6, a discussion of the overall results is followed by conclusions and recommendations for further work.

CHAPTER 2:
Literature Review

2.1 Introduction

Bass Strait is characterised by strong tidal flows and frequent storms (Jones, 1980). It is sometimes influenced by intrusions of East Australian Current Water (EACW), South Australian Current Water (SACW) and sub-Antarctic surface water (SASW) (Newell, 1960). These primary source water masses intrude via the surface-layer. SASW is found at depths below the shelf break and makes its way to the surface-layer by upward mixing, coastal and/or dynamic upwelling. The relative contributions of the primary water masses have an influence on local marine ecosystems owing to their different nutrient contents. Of the three primary water masses, SASW contains higher nutrient levels (Gibbs *et al*., 1986). The Strait is also a source region for water-mass modification due to air-sea interaction (Baines and Fandry, 1983; Gibbs et al., 1986; Godfrey et al., 1980; Luick et al., 1994; Tomczak, 1985; Tomczak, 1987). Studies also show that competing forces driving currents in Bass Strait operate on different time and space scales and create different appearances in the circulation (Baines and Fandry, 1983; Baines, 1991; Fandry, 1982; Fandry, 1983; Hannah, 1992; McIntosh and Bennett, 1984; Middleton and Black, 1994; Middleton and Viera, 1991; Sandery and Kämpf, 2006; Sandery and Kämpf, 2005).

This chapter presents a review of research carried out in the last 45 years to illustrate major processes driving currents and water mass modification in the Strait and their effects on circulation and water mass properties. In the next section a background overview of the literature is presented, followed by sections, for each major process, that detail relevant findings of the studies.

2.2 Overview

Early accounts of strong currents in the Bass Strait region are found in Matthew Flinders' *Narrative of the expedition of the Colonial Sloop Norfolk, 7 October 1798 - 12 January 1799 (Flinders, 1798)* which formed part of the later text '*Voyage to Terra Australis*' (Flinders, 1814). The existence of the Strait was unknown to British colonialists. Flinders, accompanied by George Bass, deduced that the Strait must be a broad area of shallow sea. On December 8, 1798, he wrote: "*the great strength of the tides setting westward, past the islands, could not be caused by some exceedingly deep inlet*". Later off the northwest of Tasmania, "*The tide had been running from the eastward all the afternoon, and contrary to expectation, we found it to be near low water by the shore; the flood therefore, came from the west, and not from the eastward, as at Furneaux's Isles.*" It will be shown in the next section of this chapter that Flinders' accounts of the tides in the region were correct.

Prior to 1980, few studies of the currents in Bass Strait had been carried out and were limited to the eastern side (Fandry, 1981). The first survey of water mass distribution was carried out by Newell (1960), who thought the source of high salinity northern-western Bass Strait Water was the South Australian Gulfs and Great Australian Bight and north-eastern Bass Strait Water was derived from East Australian Current Water (EACW). Newell (1960) also suggested expression of colder sub-Antarctic Surface Water (SASW) into the south-western entrance of Bass Strait in winter. Brodie and Radok (1970) investigated relationships between winds, tides and surface currents in eastern Bass Strait. They reported semidiurnal depth-independent tidal currents with small residuals and Ekman surface-layer currents and bottom-layer counter-currents, driven by persistent westerly winds. This work was confined to north-eastern Bass Strait and was motivated by petroleum industry interest in oil processing.

During the 1980's relatively greater attention was given to the Strait's circulation. Jones (1980) found currents were predominately tidal, however, residual currents were mainly wind-driven. Wind-driven currents tended to be aligned with isobaths implying topographic control. Fandry (1981) developed a numerical model to resolve wind and tidal driven flow and illustrated the basic circulation patterns resulting from each of these processes. Baines and Fandry (1983) showed from field observations that the annual cycle of density in the Strait was controlled by atmospheric forcing and the mixing induced by the M_2 tide. Tides were more important for mixing in localised areas such as in the passages. The principal tides affecting the circulation were observed and modelled by Fandry *et al.* (1985) who confirmed the M_2 as the dominant tide. The S_2, O_1 and K_1 were found to be the only other important tidal constituents and a shallow-water barotropic model was shown to be capable of resolving the tidal currents in Bass Strait.

Geostrophic and topographic control of sea-level set up in response to steady wind forcing was identified first by Fandry (1981; 1982) and then by Middleton and Viera (1991) and Hannah (1992). The effects of incident coastal-trapped waves (CTWs), emanating from the west, generated by non-local synoptic scale wind systems, was studied by Middleton and Viera (1991) and Middleton and Black (1994). Incident CTWs were suggested to influence the circulation in the Strait due to their effects on sea-level at the north-western corner. The Strait is also a possible source region for the generation of CTWs which propagate northwards along the eastern Australian coastline (Church *et al*., 1986).

Strait waters were suggested by Tomczak (1985; 1987) to be vertically well mixed for at least several months in the austral winter season. The general residual flow was thought to be eastward for most of the year, however brief periods of westward surface flow were thought to occur in summer. The volume leaving the eastern side of the Strait was estimated to range from 0.49 Sv to 3.05 Sv (Baines, 1991; Godfrey et al., 1980). Evidence was presented by Tomczak (1985) of an increase in depth-averaged density in winter from west to east. Eastward advecting Bass Strait Water eventually encountered the lighter surface waters of the Tasman Sea and some was forced downwards in density currents. The surface temperature front delimiting eastern Strait waters with Tasman Sea surface waters was defined, by Godfrey *et al*., (1980), as the location where the Bass Strait Water cascaded. The Bass Strait Cascade was shown to be most active in winter (Tomczak, 1985; 1987). Luick *et al*. (1994) found dense water export occurring at several locations along the eastern margin of the Strait. They also observed continuous horizontal bands of downwelled Bass Strait Water, leading oceanward underneath the surface-layer of the Tasman Sea.

The Tasman front, located at about 33^{o}S, is a formation zone for baroclinic EAC eddies which propagate southwards as a result of the mixing of warm EACW with cold SASW. These eddies are topographically steered by the shelf break and slope and guided past the eastern Strait margin. The EAC in summer is guided by the shelf break past the Strait to places further south (Ridgway and Godfrey, 1997). A secondary and relatively minor contribution to the density field in Bass Strait is made by Victorian and Tasmanian local riverine freshwater inputs. The input from Port Phillip Bay is thought to be minor because it is a semi-enclosed estuary with flushing times (with respect to Bass Strait waters) of over a year (Walker, 1999). The Tamar Estuary entrance channel maintains a salinity of around 34.5 with low seasonal variation (Lara and Neira, 2003).

The nutrient regime in Bass Strait reflects in some ways physical processes occurring in the region. Gibbs *et al.* (1986) found areas of enrichment at the margins, particularly on the eastern side, and relatively lower levels in the interior. The source of elevated nutrient concentrations was attributed to upward mixing of deeper water from below shelf break depth, and subsequent transport onto the shelf. A cold sub-surface water intrusion into western Bass Strait, accompanying a strong storm event was reported by Blackman *et al.* (1987). Evans and Middleton (1998) proposed an upwelling mechanism on the western slope with potential for enrichment of waters in western Bass Strait. This involved generation of a cyclonic eddy upon relaxation of westerly wind stress. This was an indication of another possible enrichment mechanism for Strait waters.

2.3 Tides

The coastal boundaries and horizontal distance and depth scales in the Strait combine to permit shallow-water waves, such as the tides, to be influenced by the Earth's rotation and propagate as Kelvin waves. This is due to the fact that the external Rossby deformation radius is around 200 km which is approximately equal to the Strait width (McIntosh and Bennett, 1984). The dominant tide is the M_2 which has its largest amplitude of around 1.2 m along the northern Tasmanian coastline (Fandry, 1981; Fandry et al., 1985; McIntosh and Bennett, 1984). The O_1, K_1 & S_2, are on average 5-

15% of the amplitude of the M_2 tide. A distinct tidal feature is found in central Bass Strait. It is a standing wave caused by the M_2 tide and is the superposition of two Kelvin waves travelling in opposite directions along opposite coasts, entering either ends with a phase difference of about 3 hrs (Fandry, 1981; Fandry, 1983; Fandry et al., 1985). Tidal currents are strong in the Strait passages yet weak in the interior. Tidal residual currents are in general small, except in narrow passages, such as the entrance to Port Phillip Bay and in Banks Strait (Middleton and Black, 1994; Sandery and Kämpf, 2005). Tidal currents are typically ignored in oceanographic studies of the general circulation (Ridgway and Condie, 2004). The purpose of including tides in the present study is to resolve tidal mixing processes at the Strait entrances as this has an influence on water mass modification, stratification and ultimately the density field (Baines and Fandry, 1983).

Tidal currents dominate short time-scale (hours to days) circulation at the edges of the Strait and tidal current speeds of 0.5 m s^{-1} are common with maximum flows of 3 m s^{-1} possible in some areas (Fandry *et al.*, 1985). The most distinctive feature of tidal flow in the Strait is that throughout the tidal cycle, flow at the eastern side is opposite to that at the western side. This results in generally small tidal currents in central Bass Strait. The first tidal model for Bass Strait was developed by Fandry (1981). This model was a two-dimensional depth-averaged barotropic shallow-water model. It was forced with M_2 tidal signals in open-sea boundaries. Figure 2.3.1 shows the relationship between M_2 tidal sea-level elevation and currents based on results of this model. At high tide in the central area currents flow inwards through the passages on both sides. The converse is true at low tide in the central area. In this situation currents flow outwards through the passages on both sides.

The M_2 wave entering the western side has amplitude of approximately 0.2 m and the wave entering the eastern side amplitude of approximately 0.4 m. The result is a superposition that produces tide with amplitudes ranging from 0.9 m near Wilsons Promontory to 1.2 m along the northern Tasmanian coastline (Fandry et al., 1985). There is simultaneous occurrence of high tide over the north-western and central region. Maximum tidal currents are usually found in the passage between Cape Grim and King Island, in Banks Strait and in the entrance to Port Phillip Bay. In the study by Fandry *et al.* (1985), tide records obtained at coastal stations near the ends of the open boundaries were used to generate linear interpolations of the signal along the boundaries. The predictive capacity of the model was limited by a number of factors creating errors which were noted by McIntosh and Bennett (1984). These included errors introduced by dynamical approximations, topographical errors, truncation errors in the finite difference approximations, interpolation errors in representing coastlines and islands on the grid, interpolation errors in locations of observation sites and the dependence of the model solution upon unreliable open-boundary data. Errors introduced by inadequate open boundary data were the most significant. An alternative solution for the M_2 tide was found by McIntosh and Bennett (1984) by treating the problem as an inverse one.

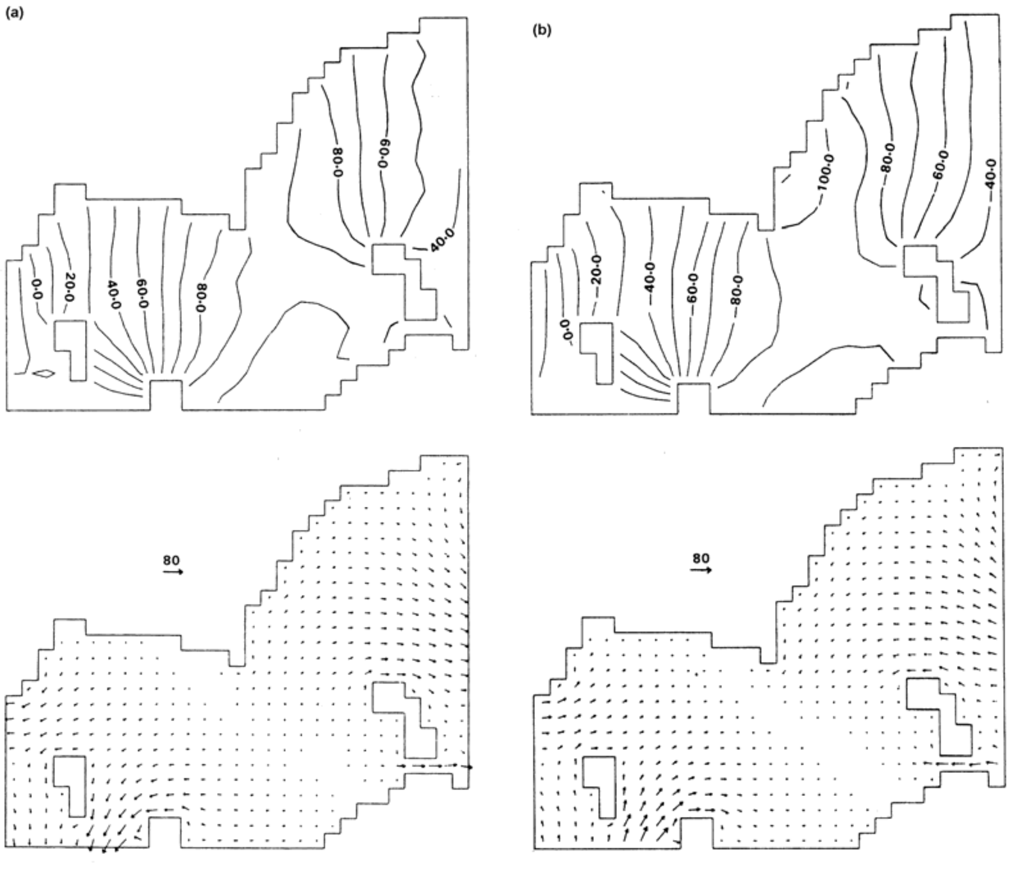

Figure 2.3.1. Instantaneous tidal sea-level elevations and associated current vector patterns from Fandry (1981). (a) High tide in central region. (b) Low tide in central region. Sea-level elevation is in cm, current scale vector in cm s^{-1}.

They verified that the tides are resolved well by the barotropic shallow-water equations and found a solution satisfying all the data for the region in a weighted least squares sense. This approach led to a full variational solution for the tidal ranges in the region (Figure 2.3.2). There is general agreement between these studies and others with the approximate 2.2 – 2.4 m M_2 tidal range adjacent northern Tasmania and the geographic distribution of M_2 co-amplitudes and co-phases. This is also supported by current National Tidal Centre tide gauge observations.

It is seen in Figure 2.3.3 by McIntosh and Bennett (1984) that dissipation of the M_2 tide is strongest in the passages and weakest in the central area, reflecting where the strongest currents are.

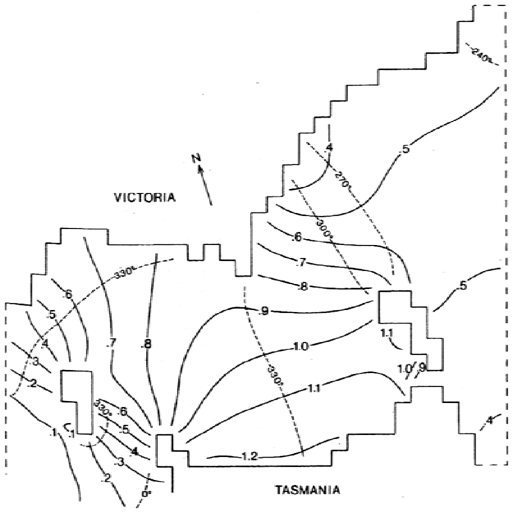

Figure 2.3.2. The full variational solution for the M_2 tidal co-range and co-phase for Bass Strait. Amplitudes in m. Phases in degrees relative to 10 h GMT. Taken from McIntosh and Bennett (1984).

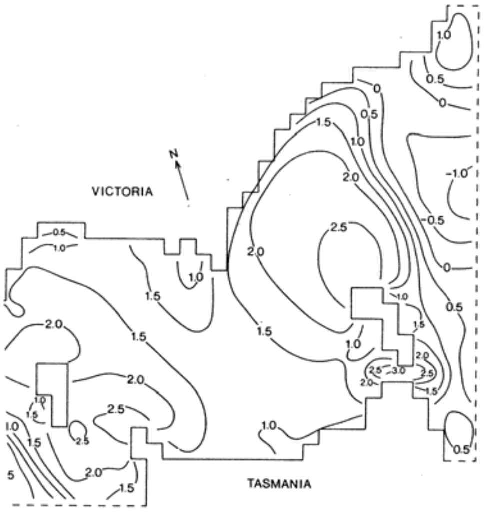

Figure 2.3.3. Contours of energy loss due to dissipation of the M_2 tide (10^3 W m^{-2}). Taken from McIntosh and Bennett (1984).

In a study by Fandry *et al.* (1985), predictions of the M_2, S_2, O_1 and K_1 tidal constituents were compared with observations from tide gauges at coastal and deep-ocean stations. Improvements to the earlier (1981) study, such as inclusion of open boundary data with greater accuracy, an extension of model domain to incorporate more of the region and better representation of the coastline led to closer agreement between model predictions and observations. Results of this study for the M_2, S_2, O_1 and K_1 tidal co-range and co-phase are given in Figure 2.3.4. The major factor influencing accuracy of results was unreliable open boundary data. A remaining limitation of the model was, however, relatively low resolution bathymetry (16.5 km grid spacing) which resulted in misrepresentation of topographic features such as islands, embayments and peninsulas. The important outcome of this study was improved co-tidal charts for the region and verification that the shallow-water model reproduced the regional tidal dynamics relatively accurately.

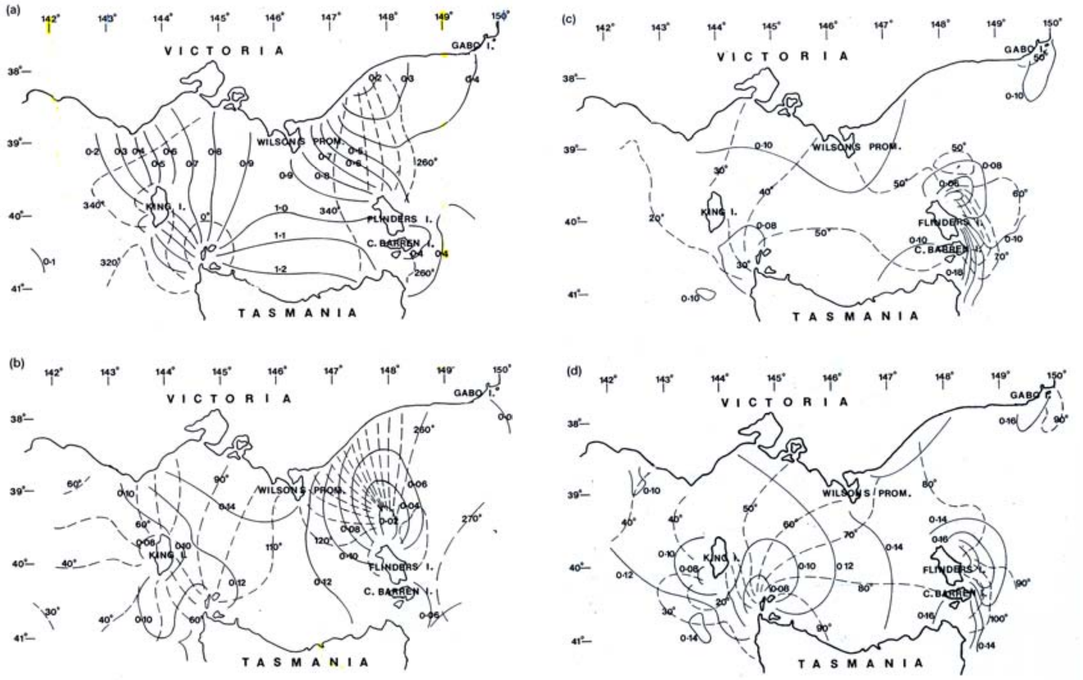

Figure 2.3.4 (a) M_2, (b) S_2, (c) O_1, (d) K_1 tidal co-range and co-phase for Bass Strait. Amplitudes in m. Phases in degrees relative to 10 h GMT. Adapted from Fandry *et al*. (1985).

2.4 Wind-Driven Flow

The general circulation of Bass Strait has been found to be influenced by local mean winds (Fandry, 1981; Fandry, 1982; Fandry, 1983; Hannah, 1992; Middleton and Black, 1994; Sandery and Kämpf, 2005). The general effect of winds is to create a current meander system like what is shown in Figure 1.4.1. This was first seen in the results of Fandry (1981). The first part of this section looks at observation-based studies and the second part examines modelling studies.

Observations

Profiles measured in summer indicate vertical variations in strength and direction resulting from wind forcing (Fandry, 1983). Wind-driven residual currents extracted from summer observations in north-eastern Bass Strait by Jones (1980) indicated the presence of a two layer system. An upper mixed layer above the thermocline was found to flow at 2% of the wind speed with a corresponding counter flow in the bottom-layer.

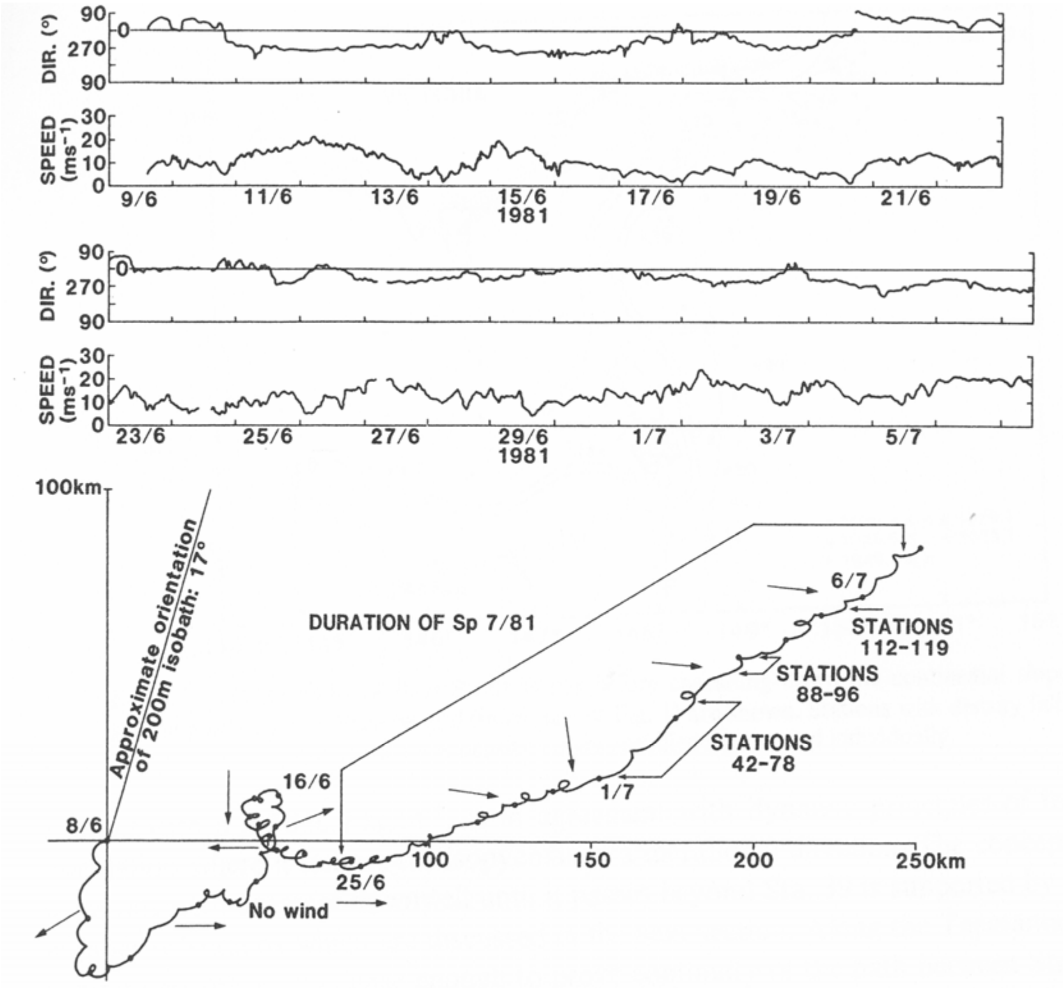

Figure 2.4.1. Time series of wind speed and direction and progressive vector current diagram during June and July 1981 at Kingfish B oil platform. Arrows on progressive vector diagram indicate approximate wind directions Adapted from Tomczak (1985).

Observations of surface-layer currents at 10 m depth at the Kingfish B platform (148.18E, 38.6S and 80 m water depth), reported by Tomczak (1985), show strong persistent westerly winds up to 20 m s^{-1} coinciding with north-westward drift (Figure 2.4.1). The period with no wind indicated illustrates how tidal oscillations produce very little residual flow.

A feature of wind-driven currents is depth dependence and prominent vertical structure. Fandry (1983) reported that in deep-water regions of the Strait, currents are dominated by surface Ekman layer flows whereas in the shallower parts, both Ekman layer and sea-surface gradient induced currents are important. In any case their relative contributions vary throughout the water column. In coastal areas of Bass Strait, sea-surface gradients as a result of wind forcing are relatively large. Due to the spatial scale of the Strait geostrophic currents occur when a steady wind is sustained over time larger than the inertial period.

Modelling

Various modelling studies show that sea-level set-up and geostrophic current patterns result from westerly winds (Fandry, 1981; Fandry, 1982; Fandry, 1983; Hannah, 1992; Middleton and Black, 1994; Middleton and Viera, 1991; Sandery and Kämpf, 2005).

Under the influence of westerly winds, sea-level response is characterised by a decrease in sea-level around the south-west of the Strait and an increase around the north-east. A nearly diagonal zero sea-level contour runs between the north-west and the south-east. Fig 2.4.2 shows results of wind-driven currents and sea-level anomalies from the study by Fandry (1981). The sea-level set-up for the southerly and westerly wind stress cases, after 36 hrs elapsed model time, are two scenarios depicting a response to maximum expected wind stress. The currents under both processes are affected by the interplay of geostrophy and friction at topographic boundaries (lateral and bottom friction). This is seen in the slight departure of the depth-averaged current direction from contours of sea surface elevation. The meandering pathway and eddies produced by the southerly wind stress are a type of reversal to the flow induced by westerly wind stress.

A study of the transient motion during the initial phase of wind-driven flow using a barotropic shallow-water model was carried out by Fandry (1982). It was found that at the onset of steady uniform wind, fluid near the surface is accelerated in the direction of the wind. The sea-surface elevation builds up at coastal boundaries. During intermediate stages towards steady state, the effects of the earth’s rotation, topography and bottom friction begin to interact. The topographic effect tends to dominate the

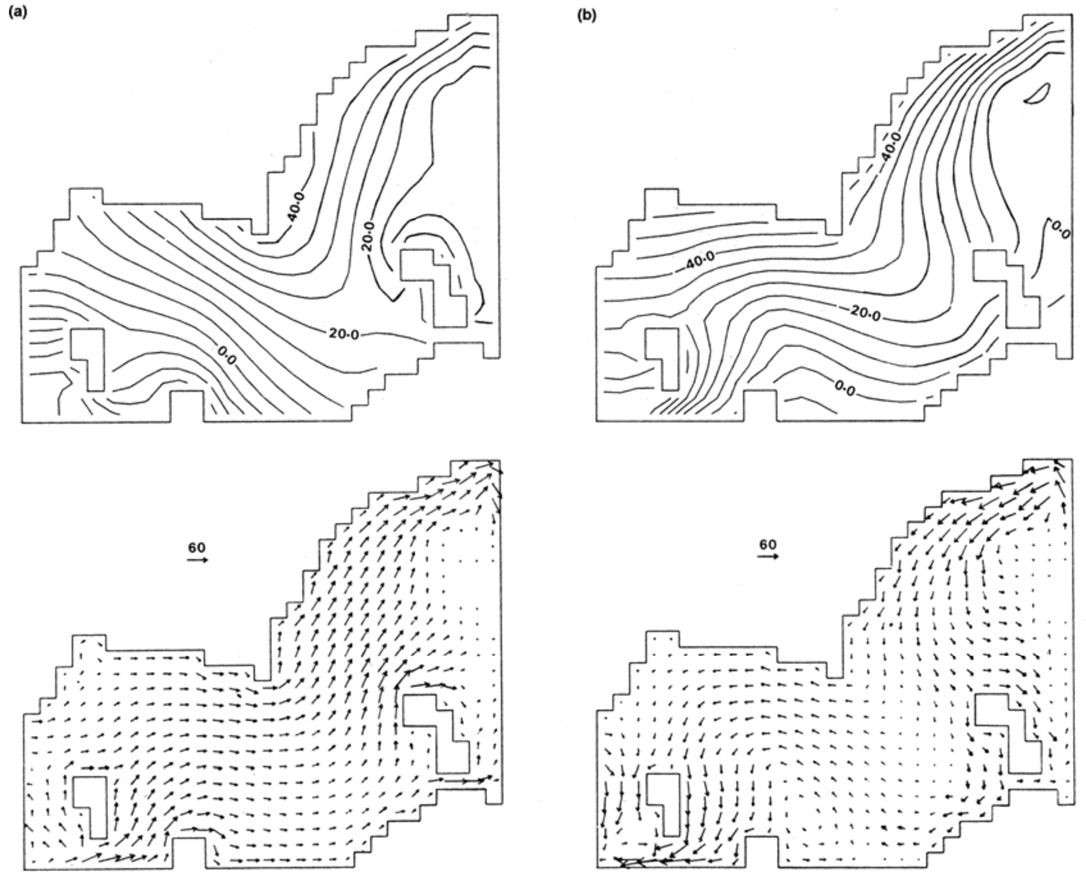

Figure 2.4.2 Steady state depth-averaged current fields and sea surface elevation produced by constant westerly (a) and southerly (b) wind stress of 1 N m^{-2} with variable bathymetry. Elevation contours (cm), current scale in cm s^{-1}. Source: Fandry (1981)

balance and acts to produce barotropic currents larger than those encountered with a flat bottom. These currents flow along depth contours and are balanced by bottom friction and the component of wind stress acting along isobaths.

Middleton and Viera (1991) and Hannah (1992) showed that local wind stress is important in driving currents in Bass Strait, and in any channel of similar spatial scale and geographical latitude. Both studies show that the steady-state numerical solution of an idealised sea-level set-up resulting from westerly wind stress, in a simplified channel resembling Bass Strait (Figure 2.4.3), is the tilting of sea-level across a diagonal axis. An important result of this finding is that that sea-level vanishes at the south-eastern and north-western corners of the Strait, resulting in geostrophic currents that are south-eastward parallel to sea-level contours.

By increasing the resolution of the shallow-water depth-averaged compared to Fandry (1981), Middleton and Black (1994) were able to resolve more details regarding the barotropic response of sea-level to zonal westerly wind stress (Figure 2.4.4).

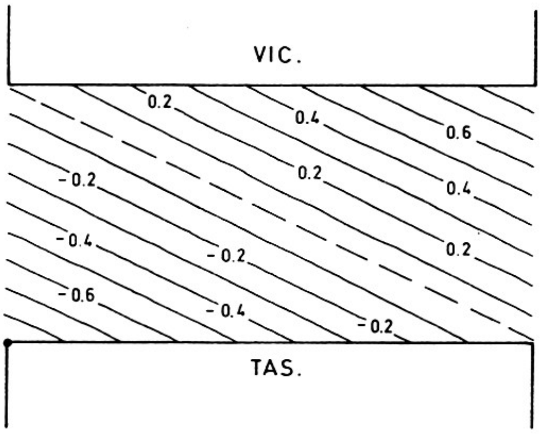

Figure 2.4.3 Westerly wind forced steady-state sea-level set-up in a simplified channel depicting Bass Strait Source Adapted from Middleton and Viera (1991).

This result contains eastward coastal jets along the zonally orientated coastlines and circulation in the interior characterised by weaker currents and eddies. A feature is also northward currents in western and eastern Bass Strait.

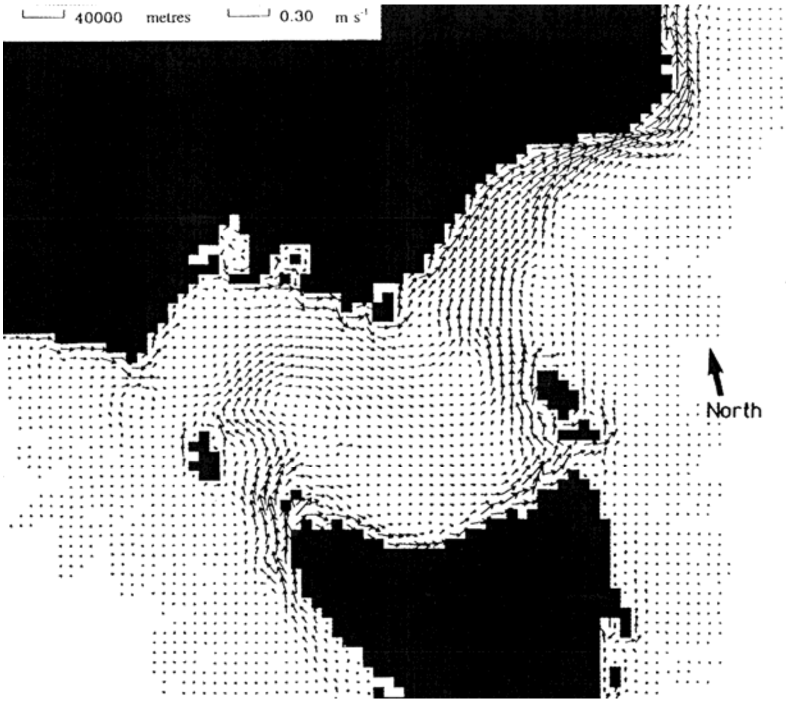

Figure 2.4.4. Current vectors induced by zonal wind stress with amplitude of 0.08 Pa at 21 days simulation time. Adapted from Middleton and Black (1994).

Later modelling studies using three-dimensional baroclinic models provided evidence of similar flow features developing in the Strait interior on the basis of realistic wind forcing. These models were able to represent features of regional currents such as the South Australian Current and Zeehan Current off south-western Victoria and western Tasmania respectively. An example is the study by Bruce *et al.* (2001) who used NCEP reanalysis winds for surface forcing. A distinct current pattern appears in Bass Strait in winter which appears to be related to both westerly winds and the SAC sea-level set-up in the model (Figure 2.4.5).

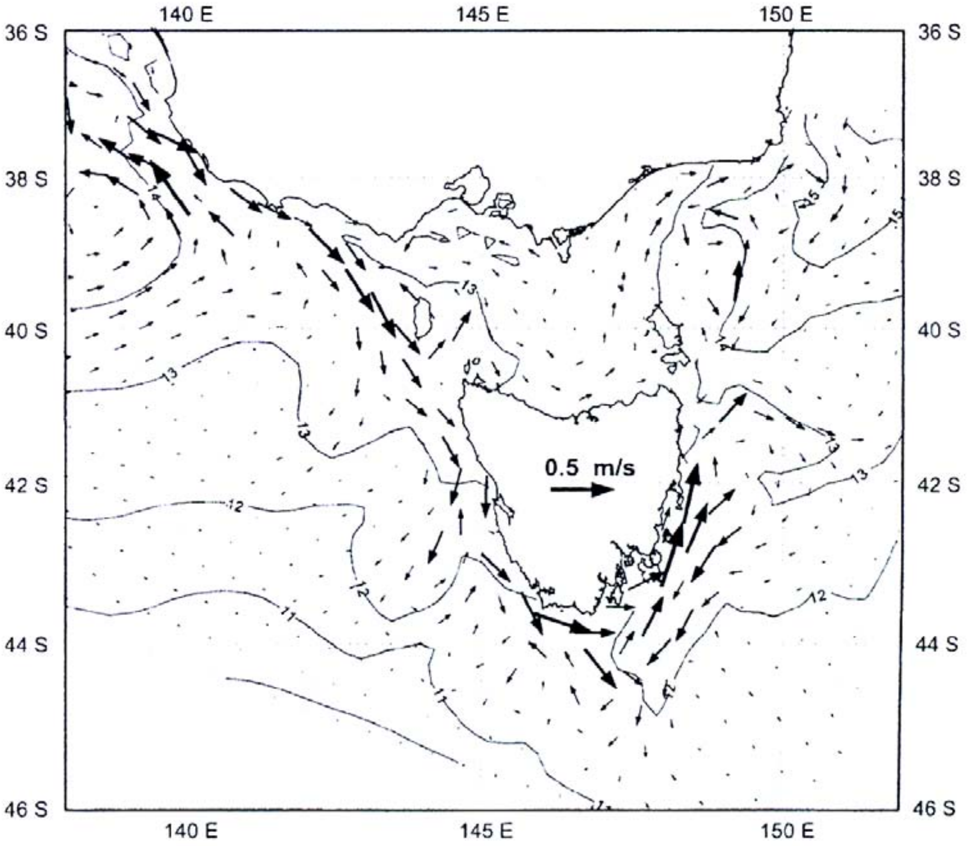

Figure 2.4.5. Current vectors and temperature (C) in winter at 20 m depth. Adapted from Bruce *et al.* (2001).

Further evidence of similar current patterns in Bass Strait in response to westerly winds and regional currents was found by Cirano and Middleton (2004) and is shown in Fig 2.4.6. The main difference between the results of the two-dimensional barotropic and three-dimensional baroclinic models is the appearance of the SAC and ZC in solutions.

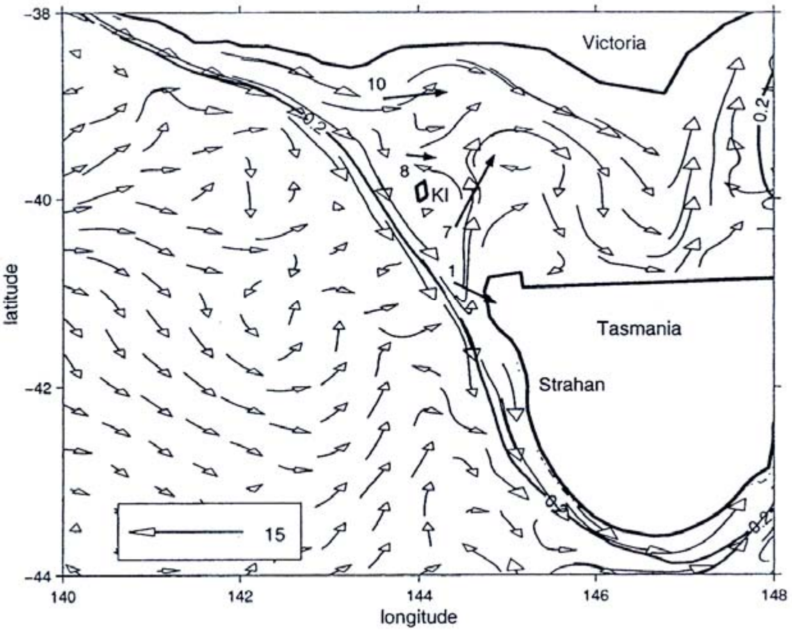

Figure 2.4.6. Predicted current pattern in winter at 30 m depth and model day 56 induced by Siefridt and Barnier (1993) wind stress. Vector length is 15 cm s^{-1}. Solid arrows indicate mean currents estimated from current-meter data. Solid line indicates 200 m isobath (Cirano, 2004).

Sandery and Kämpf (2005) used high frequency (hourly) winter to spring wind observations from Cape Grim Baseline Air Pollution Station to force a comparatively high resolution (~3.6 km) depth-averaged shallow-water model. The residual modelled current pattern resembled that of a mean westerly wind-driven pattern (Figure 2.4.7).

Except for the studies by Tomczak (1987) and Baines and Fandry (1983), description of the summer circulation in Bass Strait is largely absent in the literature. The result from Fandry (1981) in Figure 2.4.3(b), showing circulation resulting from a cross passage southerly wind may have some relevance for interpreting summer circulation, however, the magnitude of the wind stress used in this study (1 N m^{-2}) exceeds summer mean winds by at least an order of magnitude.

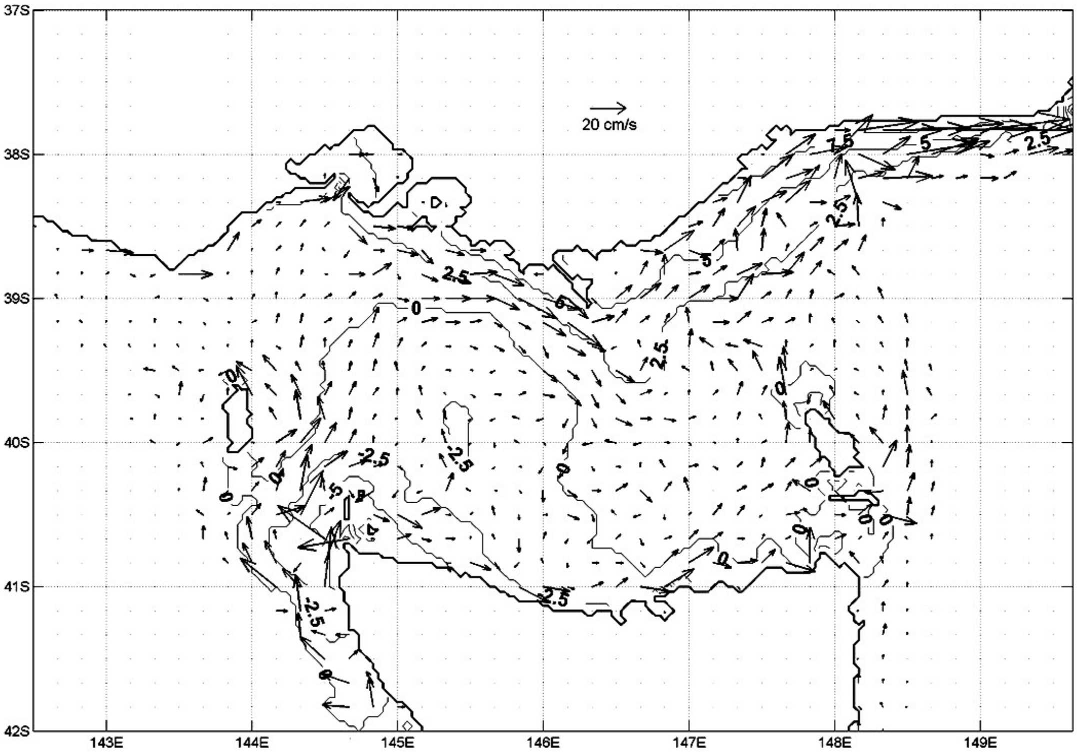

Figure 2.4.7. Wind-driven mean currents (cm/s) and sea-level (cm) prediction for the wind winter-spring of 1988. Adapted from Sandery and Kämpf (2005).

The uncertainty of modelled currents will be reflected in uncertainty in regional mean wind conditions. This is highlighted by the differences found between NCEP reanalysis data and other wind climatologies such as Hellerman-Rosenstein (Hellerman and Rosenstein, 1983), Trenberth (1989) and Siefridt and Barnier (1993), the latter being cited in Cirano (2000; 2004; 2002). See Chapter 4 for NCEP reanalysis and Hellerman-Rosenstein long-term monthly mean wind fields. Hellerman-Rosenstein mean wind stresses in the region are significantly larger in magnitude than NCEP reanalysis data with similar features regarding seasonal variation in wind direction. Trenberth (1989) wind stresses for the region show less seasonal variation in direction than NCEP reanalysis data. Trenberth (1989) and Siefridt and Barnier (1993), show almost no southerly component of wind stress throughout the year in the Bass Strait area.

2.5 Transport Timescales

Definitions of transport timescales and methods used to derive them can be found in section 3.5. These methods in general have not been widely applied or used in studies of the circulation in Bass Strait.

Bass Strait is suggested to flush on average 1% per day (Anon, 2005), implying mean flushing times of ~ 100 days. Baines and Fandry (1983) suggested that in winter water parcels transited the Strait in around 30 days, yet in summer residence times increased when parcels became confined in the stratified interior.

Conservative Eulerian tracer was used by Sandery and Kämpf (2005) to derive an e-folding flushing time distribution in Bass Strait from currents simulated under the influence of a winter-spring wind scenario (Jun-Nov, 1988). The model was a mesoscale barotropic shallow-water depth-averaged model with 3.6 km lateral resolution using realistic bathymetry. The results indicate the longer-term (seasonal) effect of high frequency (hourly) wind-driven currents.

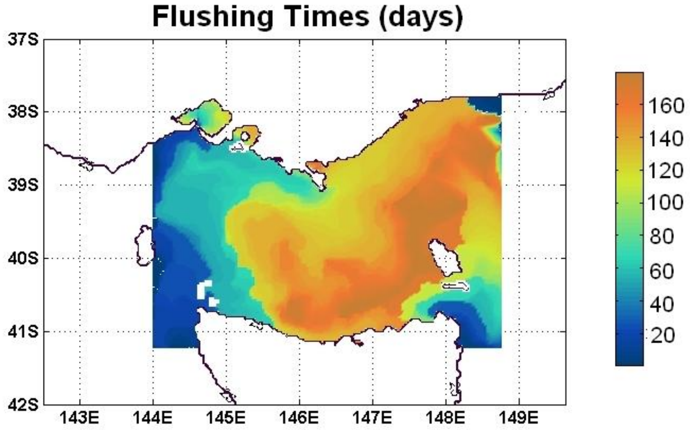

Figure 2.5.1 Bass Strait flushing time distribution in high mean westerly wind scenario. Adapted from Sandery and Kämpf (2005).

The flushing time distribution, shown in Figure 2.5.1, summarises mass transport over a 6 month period in the model. This is a signature of mean westerly wind-driven circulation. It gives an impression of the upper limits of flushing. The use of a two-dimensional model meant that the summer circulation, which involves density effects such as stratification, could not be resolved because of the model assumption of complete vertical mixing and constant density.

2.6 Regional Water Masses

Water mass properties in Bass Strait are determined by the properties of waters advected/mixed into the area and local modifications by air-sea fluxes. Air-sea fluxes in the Strait are significant and modify water properties enough to classify Bass Strait Water as an individual water mass formed locally (Tomczak, 1985). Northern Bass Strait Water of moderate temperature and high salinity, formed in summer in the South Australian Gulfs and the GAB, was found to be present along the southern Victorian coastline from October to April (Figure 2.6.1) (Newell, 1960). East Australian Current Water from the Coral Sea having high temperature and high salinity was identified on the north-eastern side of Bass Strait. Modified sub-Antarctic Surface Water of low temperature and low salinity was found to occupy parts of southern Bass Strait from May to September (Newell, 1960).

Newell's (1960) observations are summarised in T-S diagrams in Figure 2.6.2. Interestingly, these appear to be the only documented observations of relatively low salinity water (~ 35.05-35.22) in south-western Bass Strait.

Sub-Antarctic Surface Water has been observed at Bass Strait latitudes in the SEIO and Tasman Sea at depths greater than ~250 m. Within these waters there is a strong thermocline with a temperature gradient of 2.5-5.0 K from 250 to 500 m (Blackman *et al.*, 1987). Several possible ways are proposed for this water mass to enter Bass Strait. These include diffusive upward vertical mixing followed by lateral mixing across the shelf break (Gibbs *et al.*, 1986), coastal or dynamic upwelling (Condie, 1995; Evans and Middleton, 1998; Mirshak and Allen, 2005; Roughan and Middleton, 2002), and potentially cascade-driven upwelling (Kaempf, 2005).

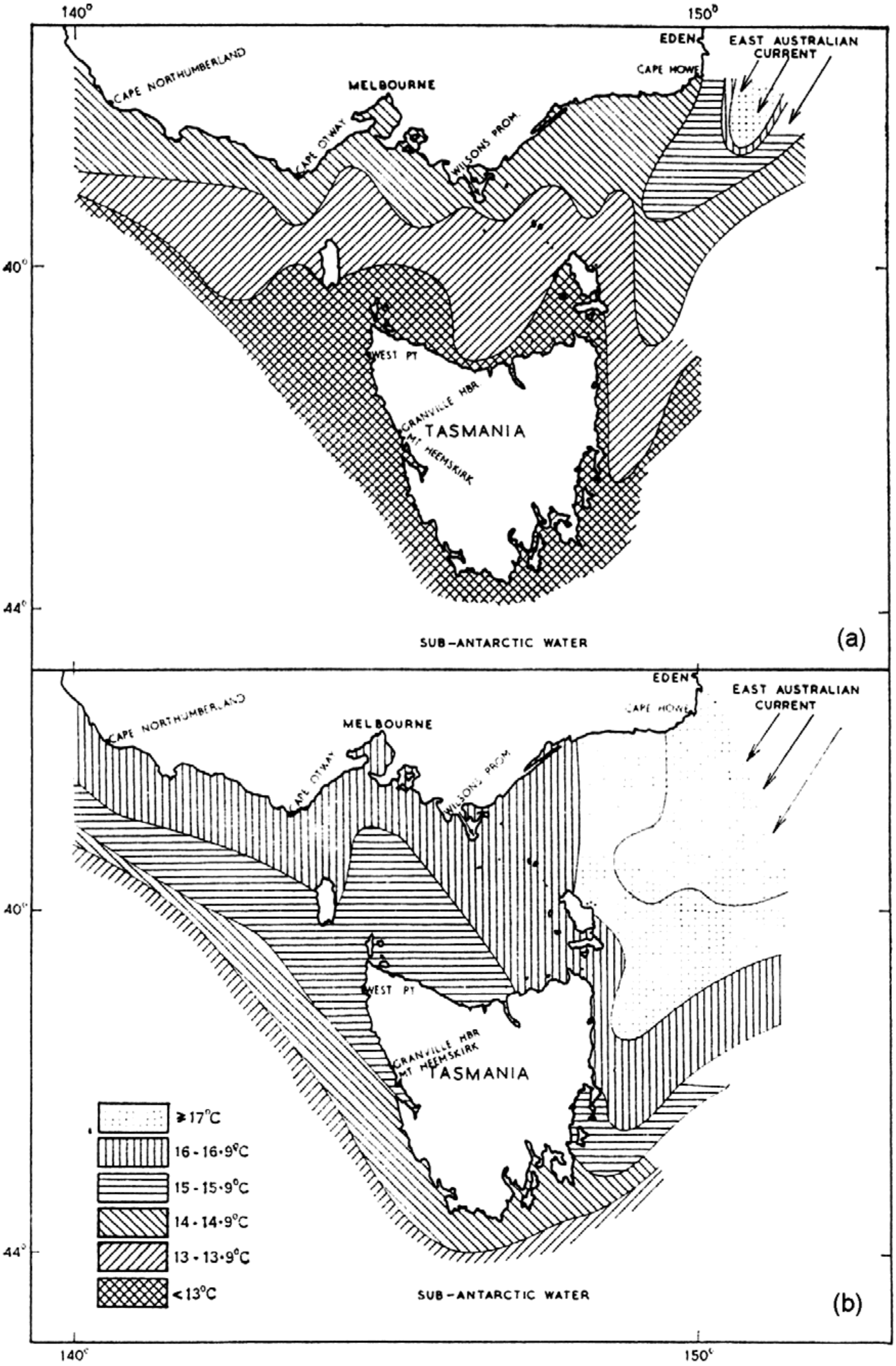

Figure 2.6.1a. Winter (above) and summer (below) temperature distributions. Adapted from Newell (1960).

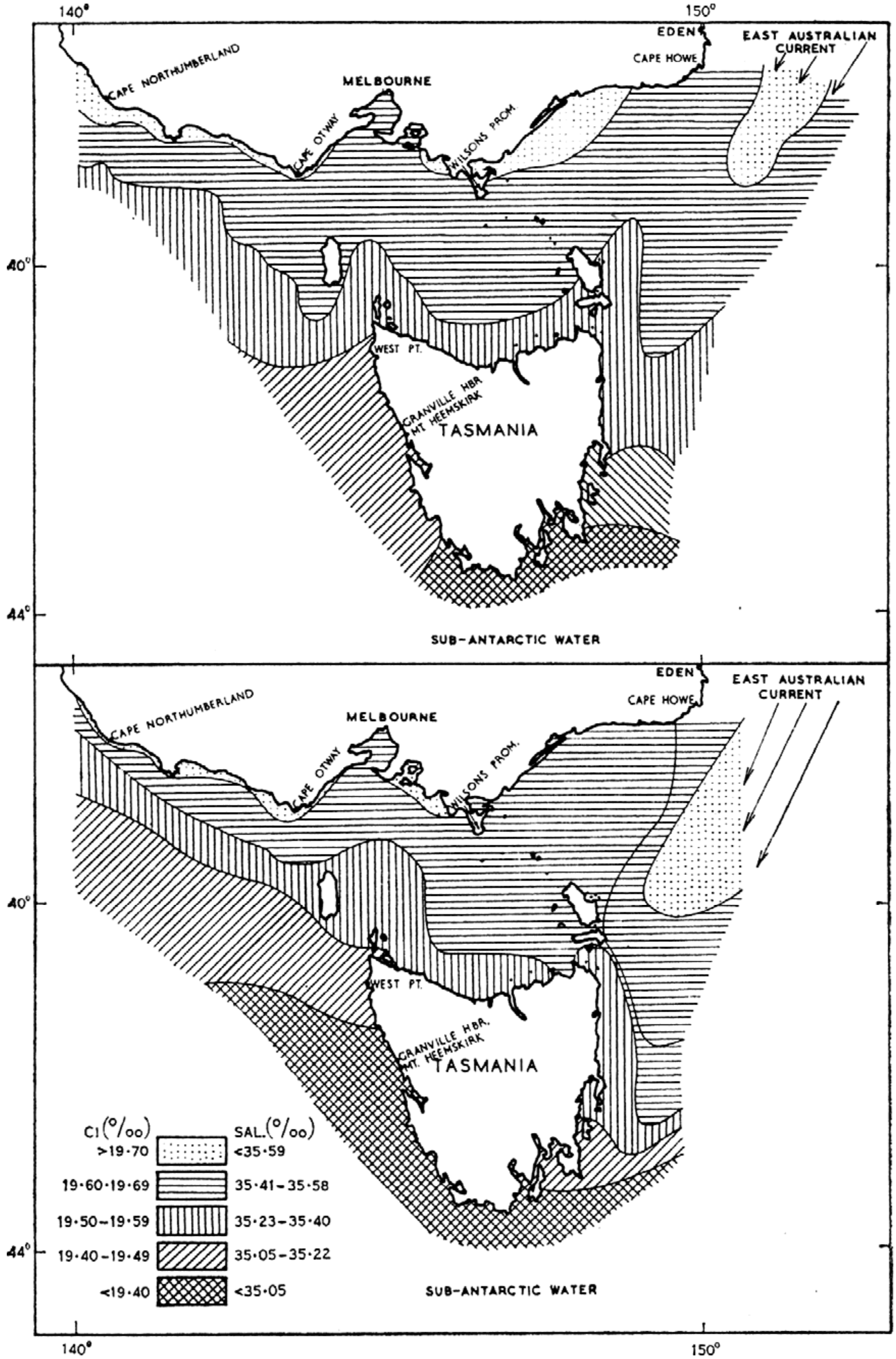

Figure 2.6.1b. Winter (above) and summer (below) salinity distributions. Adapted from Newell (1960).

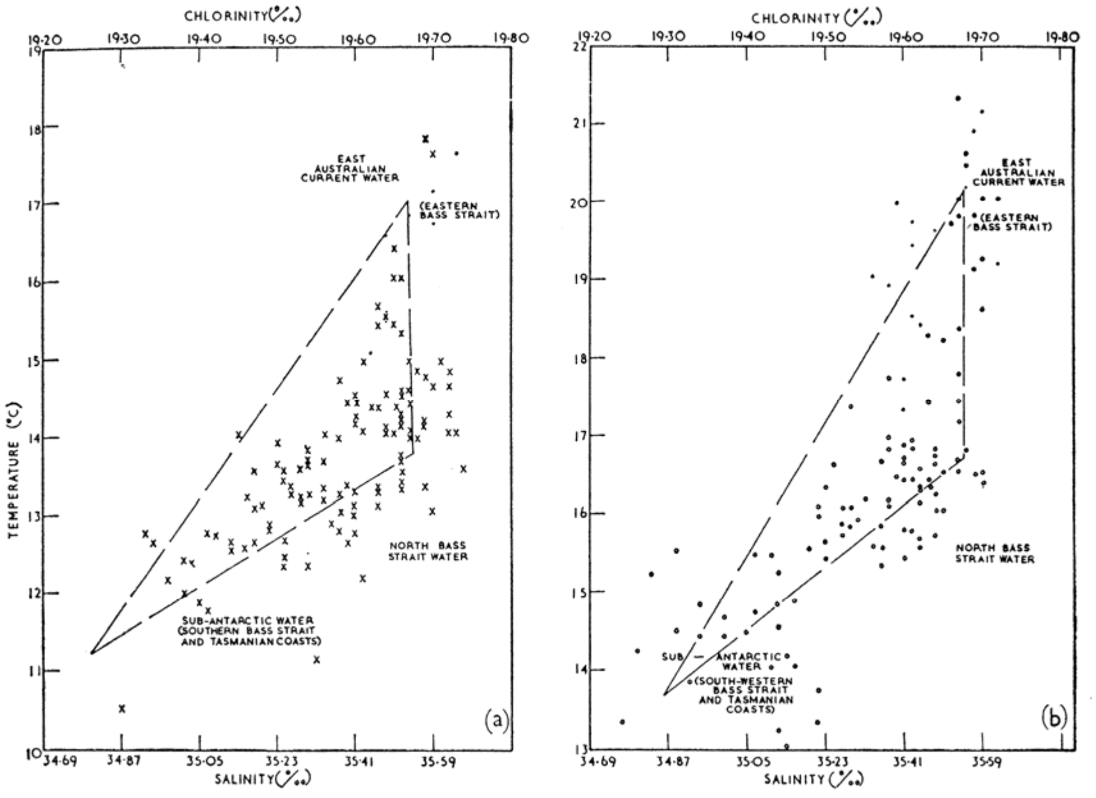

Figure 2.6.2. TS water mass properties for Bass Strait (a) winter, (b) summer. Solid circles are samples from EAC. Adapted from Newell (1960).

Surface water, formed in summer in the Great Australian Bight, was reported by Herzfeld (1997) to move eastwards and into Bass Strait in winter months. Tomczak (1985) stated that water which entered the Strait from summer to early autumn was modified to become warmer and more saline by air-sea buoyancy fluxes and tidal mixing.

Boland (1971) reported higher salinities (> 35.60) in northern Bass Strait, in September 1965, than encountered elsewhere in the study region (Fig 2.6.3). It was suggested Bass Strait was the source of positive salinity anomalies found in the Tasman Sea.

Tomczak (1985) showed that eastward moving water in the Strait eventually encounters the eastern side where a strong thermohaline front delimiting Strait waters and the Tasman Sea exists. This water was suggested by Gibbs *et al.* (1986) to be largely directed northward, with a suggestion of bifurcation south of Wilson’s Promontory as illustrated in the schematic of general current pathways in Fig 2.6.4.

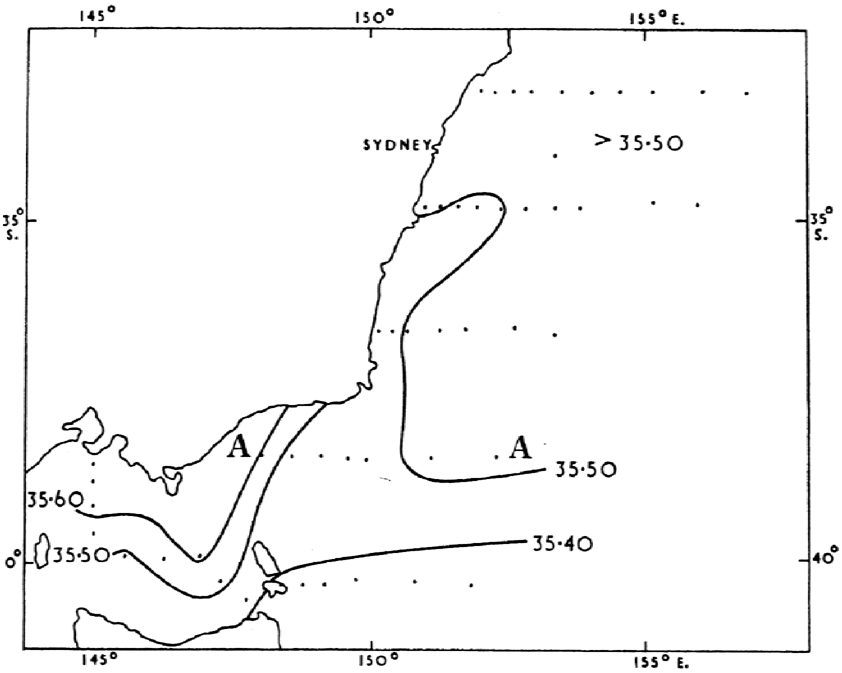

Figure 2.6.3. Surface salinity in Bass Strait and the Tasman Sea. Adapted from Boland (1971).

In relation to water masses of the Tasman Sea and the SEIO, Bass Strait Water is characterised as a positive anomaly on a mean TS-curve (Figure 2.6.5). Its distinct temperature-salinity signature makes it able to be traced in remote locations several hundred kilometres east in the Tasman Sea and as far north as the Coral Sea (Luick et al., 1994; Tomczak, 1985; 1987).

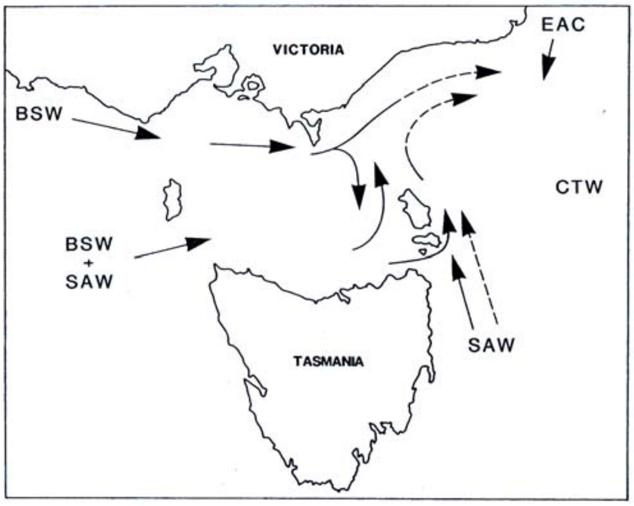

Figure 2.6.4. Water pathways in winter. BSW Bass Strait Water, EAC East Australian Current Water, CTW Central Tasman Water, SAW Sub-Antarctic Water. Adapted from Gibbs *et al.* (1986).

Water masses in region were characterised on a TS-diagram by Gibbs *et al.* (1986) (Figure 2.6.6). Again, Bass Strait Water exists as a positive density anomaly on a Tasman Sea TS-curve in the ~12-17^{o}C temperature range, owing to its greater salinity (~35.55-35.65). The source of the salinity anomaly in Bass Strait Water is either local air-sea interactions and/or inflow due to the South Australian Current. At present, the relative contributions of these processes have not been addressed in the literature.

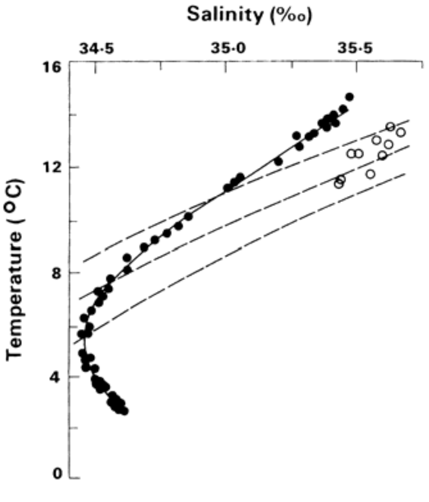

Figure 2.6.5. TS diagram illustrating relationship of Bass Strait Water to Tasman Sea Water. Mean temperature and salinity of water column in ten positions spread across Bass Strait (o) is compared to TS profile for seven locations in adjacent Tasman Sea in September 1963. Dashed lines are isopycnal surfaces. Adapted from Godfrey *et al.* (1980).

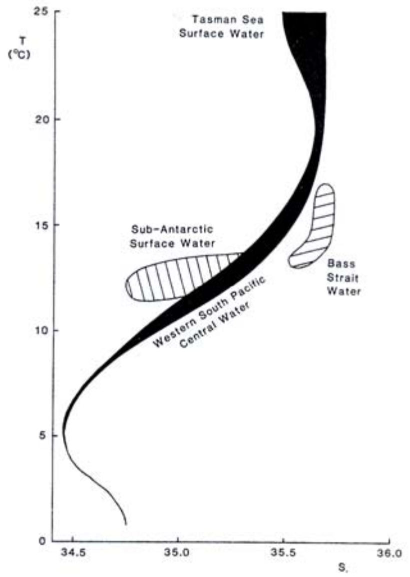

Figure 2.6.6. TS characteristics of regional water masses. Adapted from Gibbs *et al.* (1986).

2.7 Density Effects and Seasonal Variations

Density Fronts

Density fronts often exist at the western and eastern edges of Bass Strait during May-August. The most evident frontal region is between eastern Bass Strait and the

Tasman Sea where strong temperature gradients aligned with the shelf break are common (Boland, 1971; Godfrey et al., 1980; Tomczak, 1985). Direct evidence of this is given in Figure 2.7.1 in measures of thermal frontal frequency encountered by merchant ships, which has sampling bias towards eastern Bass Strait (Godfrey *et al.*, 1980).

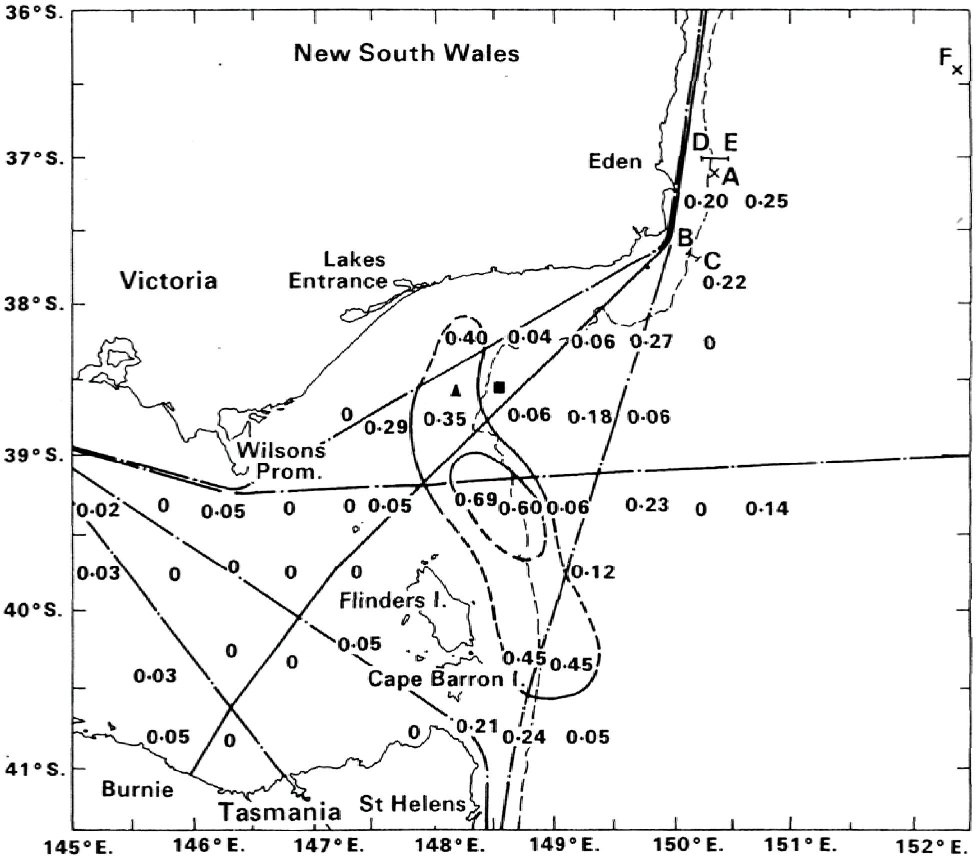

Figure 2.7.1. Fronts encountered by merchant ships. Numbers indicate fraction of merchant ship voyages that have a front in the given half-degree square. Contours show distribution of this fraction. Adapted from Godfrey *et al.* (1980).

Several studies (Gibbs et al., 1986; Godfrey et al., 1980; Luick et al., 1994; Tomczak, 1985; Tomczak, 1987) show that the location of the density front between eastern Bass Strait and the Tasman Sea coincides with the location of the shelf break.

Baines and Fandry (1983) show that in summer months fronts exist between the stratified interior and the well-mixed passages. The studies by Tomczak (1985:1987) show the density front between the eastern margin of Bass Strait and the Tasman Sea is more pronounced in winter.

Seasonal Variations

Bass Strait has characteristic seasonal variations in water mass properties and vertical density structure. An analysis of depth-averaged spatial temperature and salinity distributions from observations for the winter and early summer of 1981, by Tomczak (1985; 1987), is shown in Fig 2.7.2. This shows the densest water in the region in 1981 occurred in winter in eastern Bass Strait.

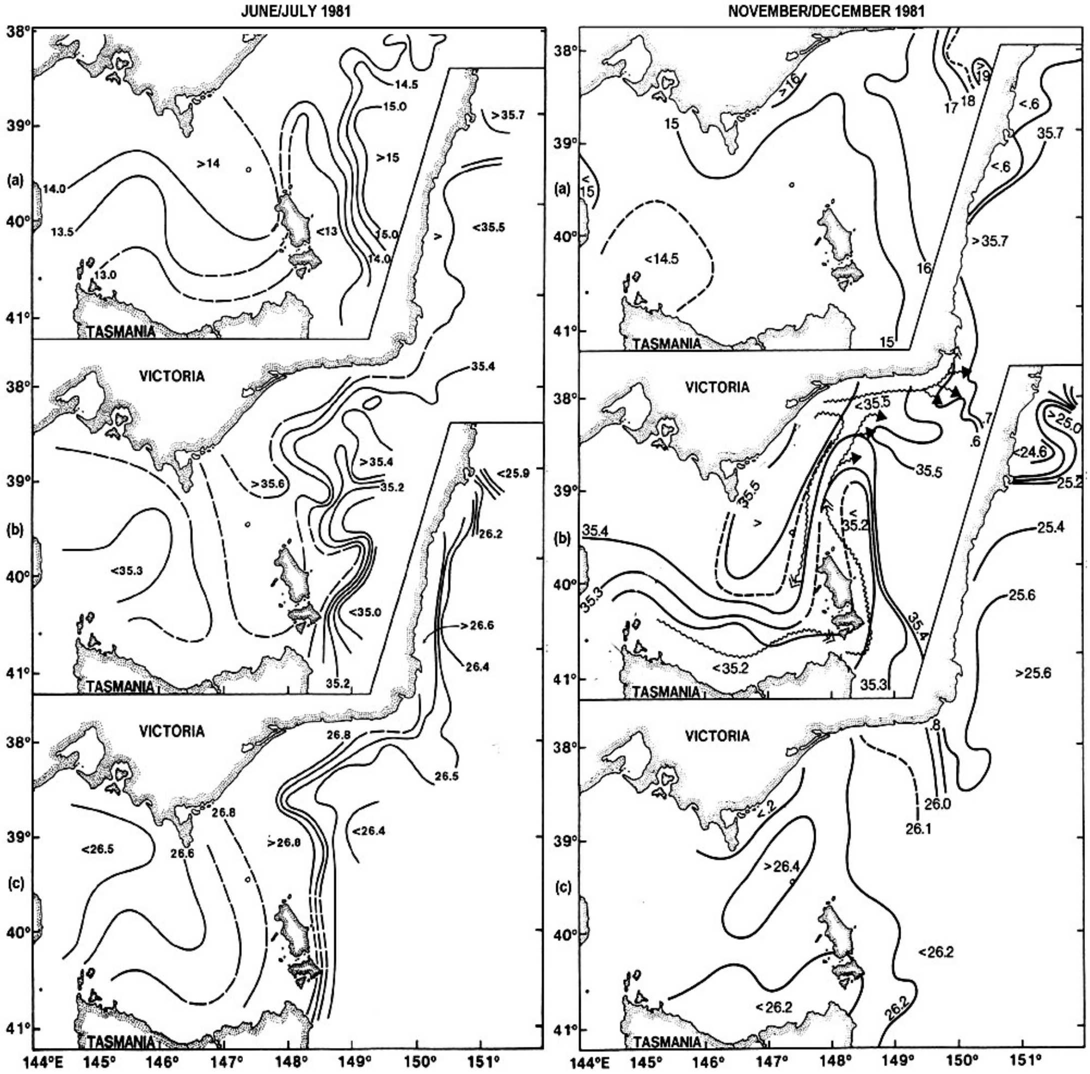

Figure 2.7.2. Winter and early summer 1981 T-S features in Bass Strait. (top) temperature (^{o}C), (middle) salinity, (bottom) σ_T (kg m^{-3}). Adapted from Tomczak (1985:1987).

The winter salinity is lowest in the south-west corner and appears to be derived from an intrusion through the passage between King Island and Cape Grim. The winter temperature field appears to have the signature of a westerly wind-driven flow field. The early summer situation has distinct differences, the eastern margin density front is weaker and the salinity field in the Strait interior is a signature of the meridional gradient in evaporation, being lower in the southern parts than in the northern parts. The summer salinities indicate presence of a weak but westerly wind-driven circulation evident in the shape of contours around the Furneaux group.

Godfrey *et al.* (1980) complied observations of minimum temperature in northern Bass Strait. Data indicated lowest minimum temperatures of ~11°C in August-September and highest minimum temperatures of ~ 17°C in February-March with a range of ~6°C (Figure 2.7.3).

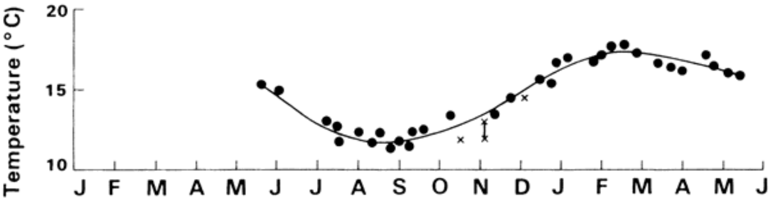

Figure 2.7.3. Seasonal variation in minimum temperature near 39°S in the period 1975-1976 recorded on voyages by M.V. Australian Trader between Burnie and Sydney. x denotes either internal mixed layer temperatures or inversion maximum temperatures from various XBT casts in 1978. Adapted from Godfrey *et al.* (1980).

Bass Strait Cascade

Tomczak (1985) shows that, in winter, Bass Strait Water is typically advected northward between the shelf break and the Furneaux Group (Fig 2.7.4). When this water reaches the bend in the continental shelf at the north eastern edge of the Strait near Bass Canyon (38.5°S, 149°E) it flows down the slope to depths of several hundred metres (Tomczak, 1985). Flow down the north-eastern continental slope into the Tasman Sea is known as the Bass Strait Cascade. Observations of the Cascade at the location where it is most pronounced are presented in Fig 2.7.5. Other locations along the eastern continental shelf are also probable pathways for cascading Bass Strait Water (Luick *et al.*, 1994).

Tomczak (1987) detected less cascade activity in summer than in winter. This led to the belief that the Cascade was mainly a winter process with outflow occurring mainly as a narrow undercurrent along the continental slope. Although the Cascade appeared to be inactive in summer, several patches, layers and intrusions of Bass Strait

Water south of the Cascade were suggested to be present along the shelf edge. These were thought to be remnants of winter activity which were advected in the general circulation.

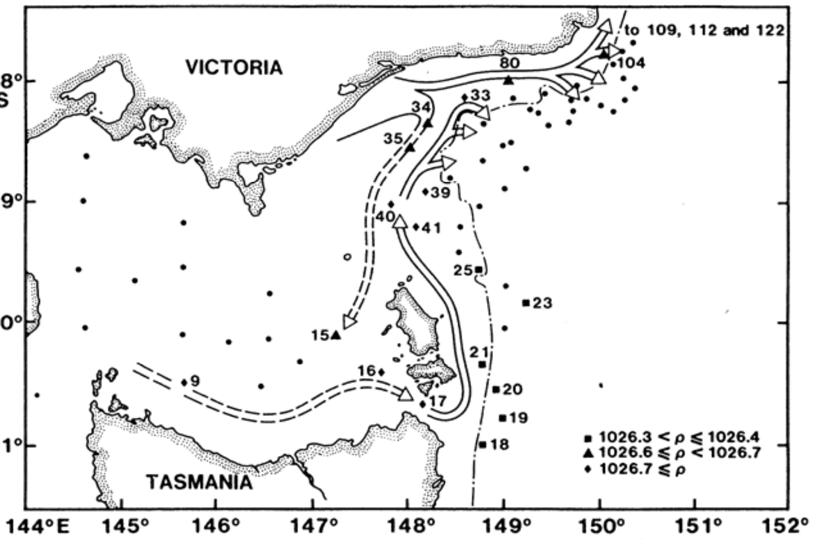

Figure 2.7.4. Possible pathways of water in Bass Strait before cascading down the continental slope. Adapted from Tomczak (1985).

On the north-eastern slope in the region of the Bass Strait Cascade observations of the eastward component of wind speed and the northward component of bottom currents by Godfrey *et al.* (1980) suggest enhancement in activity of deep bottom currents after the passage of storms (Figure 2.7.6).

The region where the Cascade flux was observed by Tomczak (1985) to be largest, off the Narrow shelf south of Lakes Entrance, is a surface convergence zone due to the topography, the typical westerly wind forced circulation and the barrier of the Tasman Sea thermohaline front. The level of surface convergence in this location appears connected to bottom currents, suggesting cascade activity may be strongly coupled to Strait-wide wind-forcing.

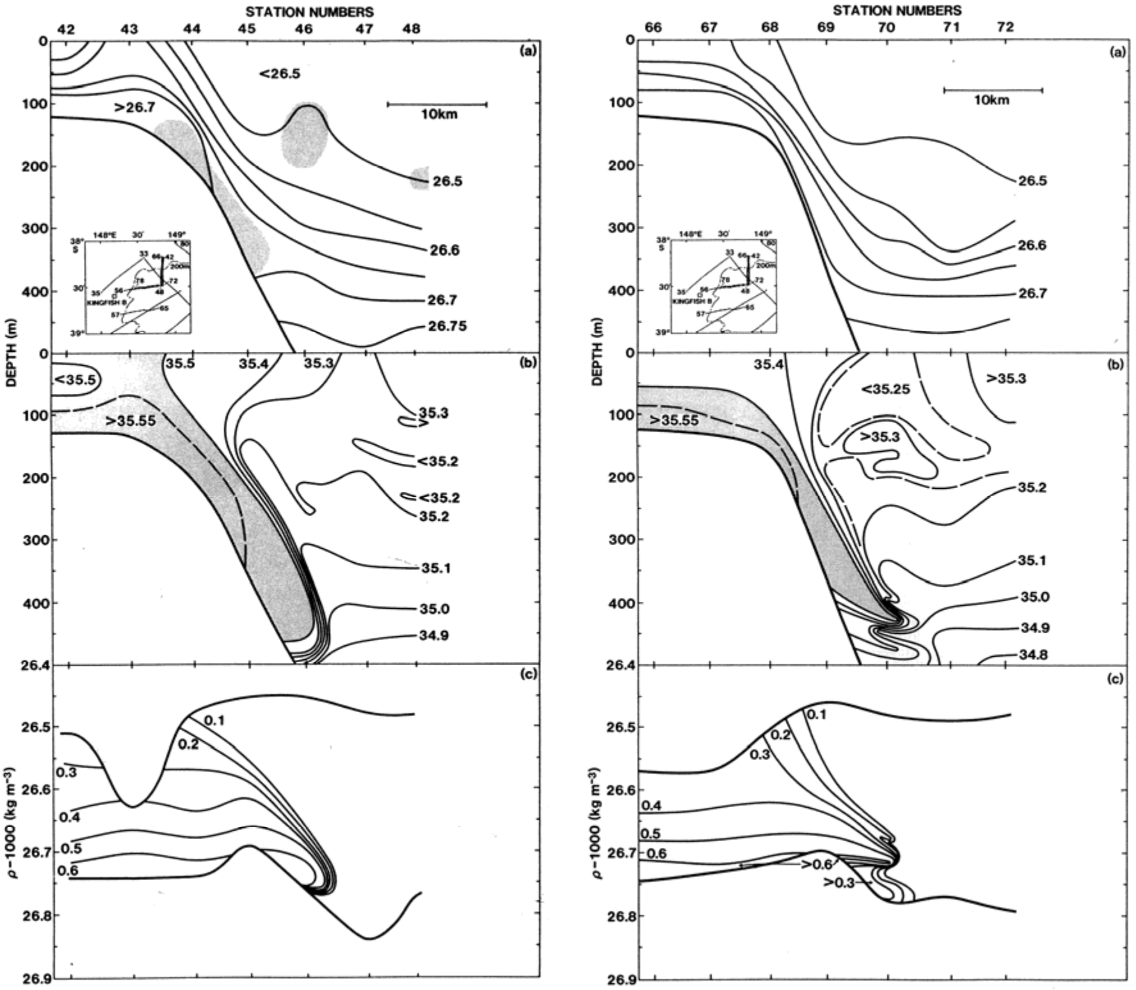

Figure 2.7.5. Depth profiles of (a) σ_T, (b) salinity and (c) salinity anomaly against σ_T for two transects. Section locations indicated in inner panel. Adapted from Tomczak (1985).

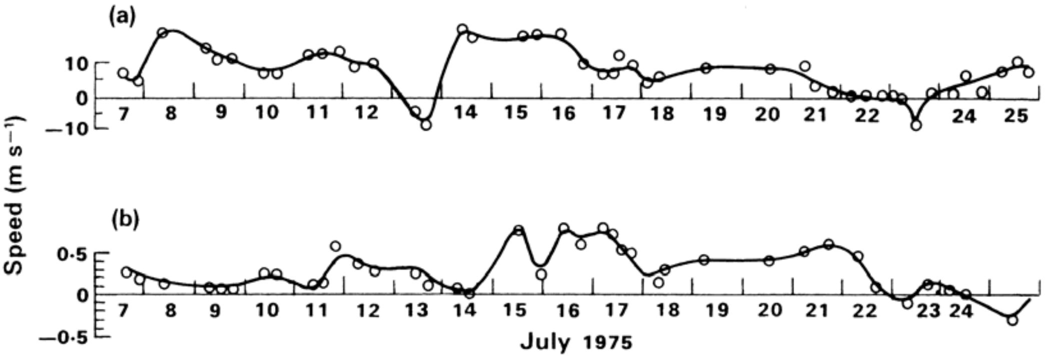

Figure 2.7.6. Three week time series comparing (a) eastward component of wind stress to (b) northward current component 20 m above 350 m bottom at 38°33'S, 148°33'E. Adapted from Godfrey *et al*. (1980).

Seasonal Cycle of Stratification

Jones (1980) observed a two layer system to be present during the summer. Here a thermocline is found separating a lower mixed layer from an upper mixed layer. The two layer nature of the water column in Bass Strait during summer months was suggested to lead to internal tides which oscillate the thermocline (Jones and Padman, 1983). Baines and Fandry (1983) conducted a study on the stratification in Bass Strait, using most of the available temperature and salinity data at the time. In late summer, the central area was found to be strongly stratified. There were regions near the southwest and southeast corners that were well mixed, owing to local tidal stirring. A sample of these findings is given in Figure 2.7.7 where contours represent $\log_{10} |\bar{A}|$, $\bar{A}$ being the potential energy of the observed stratification (Baines and Fandry, 1983).

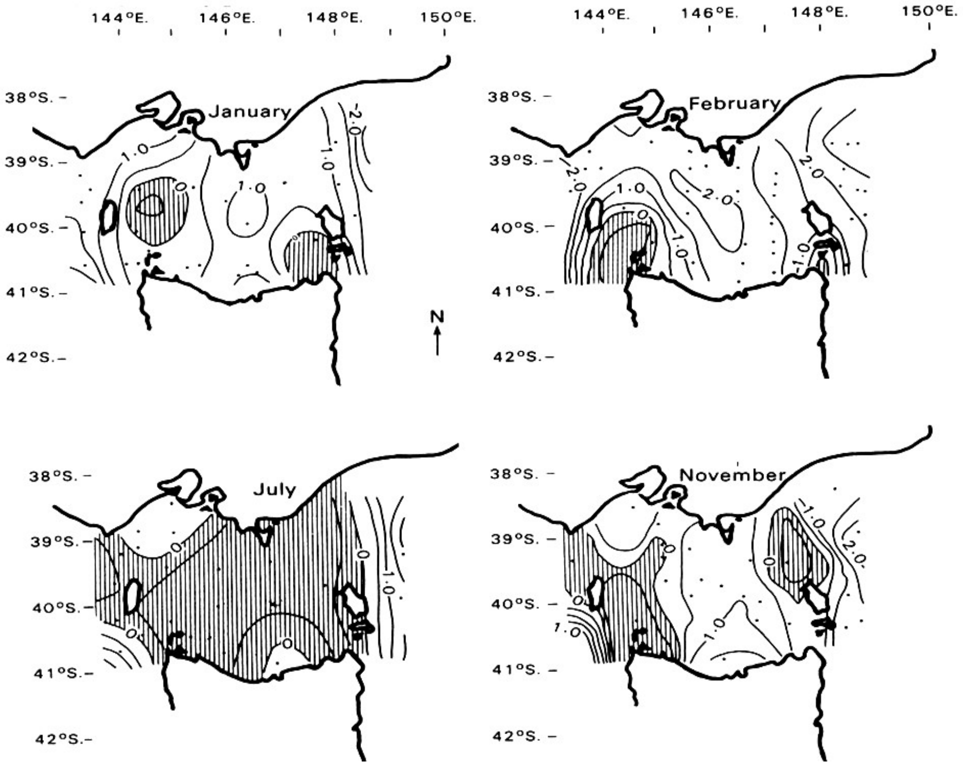

Figure 2.7.7. Seasonal characteristics of stratification in Bass Strait based on long term records of temperature and salinity. Shaded areas indicate vertically well mixed water column. Adapted from Baines and Fandry (1983).

The shaded areas in Figure 2.7.7 indicate vertically mixed water and increasing positive values correspond to an increasing degree of the potential energy of stratification. Widespread vertical mixing evident in July is representative of other winter months. The November pattern suggests weaker stratification than in February in the central region and widespread vertical mixing in the western region. Baines and

Fandry (1983) suggested stratification appeared to be primarily controlled by a competition between tidally forced mixing and surface heating, with wind forced mixing being of secondary importance.

Wind effects the stratification by its influence on the surface heat flux and by stirring of the surface and bottom mixed layers. Baines and Fandry (1983) reported that, in winter months, wind-driven vertical mixing is important throughout the Strait. According to Baines and Fandry (1982), under the influence of the prevailing winter westerlies, water parcels entering the western end of Bass Strait pass through a region where they are well mixed with depth. They continue to be mixed and are advected eastwards. A Strait traverse was thought to be possible in about 10-20 days. Baines and Fandry (1983) suggested that when tidal flows dominated motion in times of low mean wind stress, residence times were significantly longer. In summer, water parcels encountering the strongly stratified region in the centre of the Strait were thought to be restricted to particular depth levels for several months. Due to the residual motion they were thought to eventually exit on the eastern side after passing through the tidally mixed regions south and north of Flinders Island.

2.8 Influence of Coastal-Trapped Waves

Evidence of an approximate 10 day period variation in sea-level due to Coastal-trapped Waves at was found in the Australian Coastal Experiment (ACE) by Church *et al*. (1986).

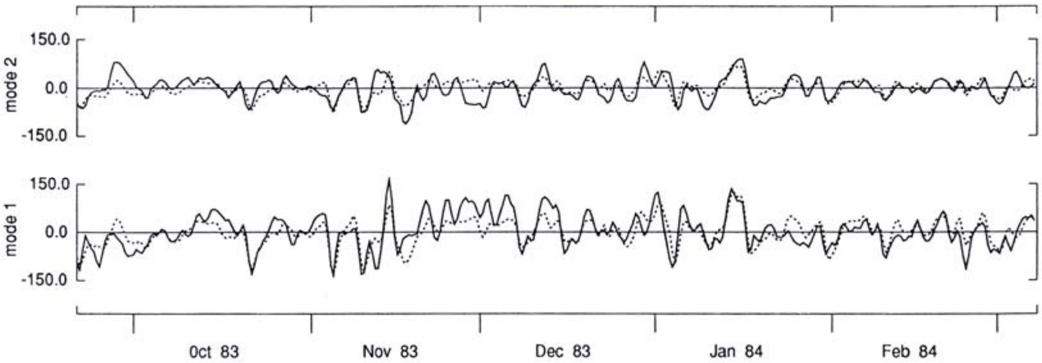

Figure 2.8.1. First and second CTW modes observed at line 1 in the ACE (arbitrary units). Solid line, observed; dashed line, derived from Lakes Entrance sea-level. Adapted from Church *et al.* (1986).

Strong correlation between CTW modes 1 and 2 at line 1, which is located off Cape Howe, in the ACE and sea-level at Lakes Entrance was found (Figure 2.8.1).

Middleton and Black (1994) modelled currents resulting from a 10 day period, 10 cm amplitude, CTW forcing signal which involved prescribing sea-level on the model western open-boundary. A wide spatial effect on currents in the Strait is found.

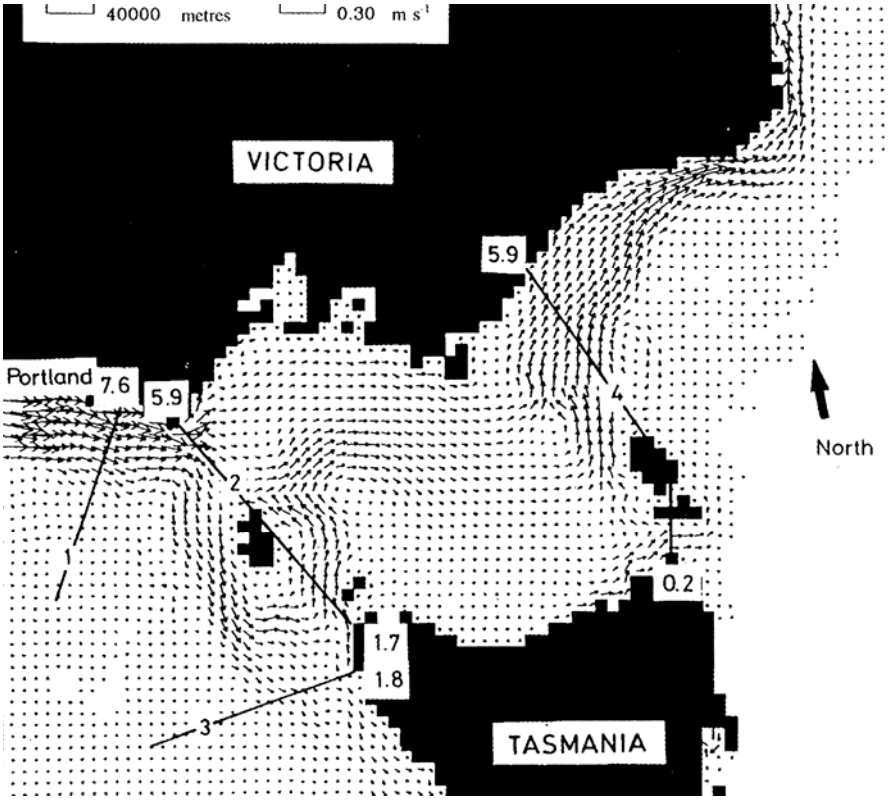

Figure 2.8.2. Instantaneous current velocity field at 312 h forced by mode 1 CTW at Portland. Coastal sea-level amplitude (cm) labelled for each of the sections. Adapted from Middleton and Black (1994).

It is not shown how currents resulting from this forcing change throughout the CTW forcing cycle. If sea-level at Portland oscillates with 10 cm amplitude around zero-mean sea-level then a flow pattern reversal should be expected when the CTW trough is in phase at Portland. According to Middleton and Black (1994), CTW energy is severely scattered at the western Strait entrance and the eastward flux is greater at the western entrance than at the eastern entrance.

2.9 Nutrient Distributions

On a seasonal basis, the highest nutrient concentrations in Bass Strait were observed by Gibbs *et al.* (1986) to be in winter and the lowest in summer. The distribution of nutrients appeared to be closely related to physical processes occurring on the eastern continental slope. Evidence was provided for relatively higher nitrate and phosphate levels in Banks Strait and along the eastern shelf break than in the interior.

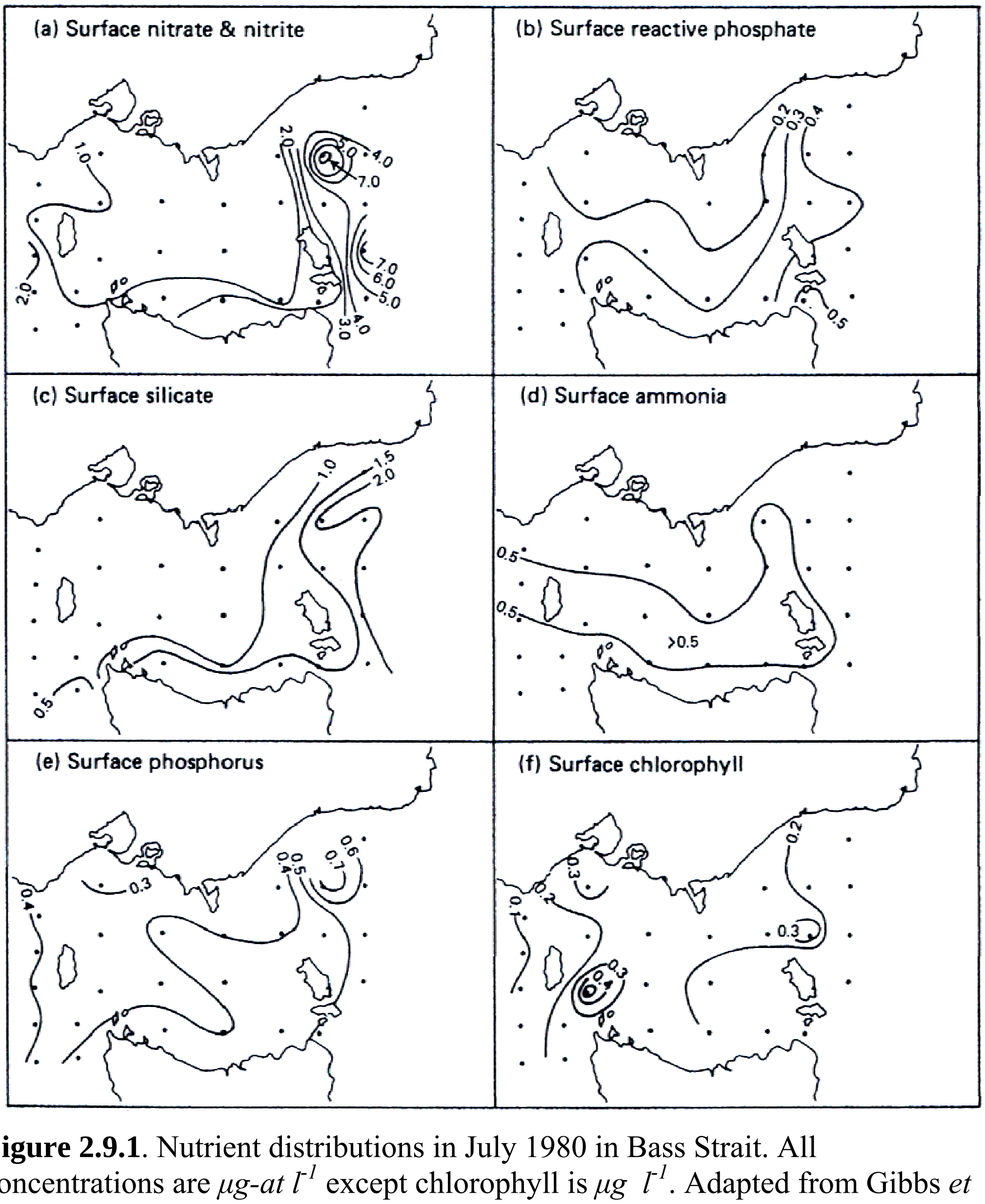

Figure 2.9.1. Nutrient distributions in July 1980 in Bass Strait. All concentrations are $\mu g\text{-}at\ l^{-1}$ except chlorophyll is $\mu g\ l^{-1}$. Adapted from Gibbs *et al*. (1986).

Temperature and salinity fields for the region were found to be compatible with strong tidal motions and weak residual flow of variable direction. It was thought that in winter eastward flow dominated. There was some uncertainty regarding the summer residual flow. Gibbs *et al.* (1986) suggested the major source of nutrients for Bass Strait was upward mixing of deeper water of sub-Antarctic origin occurring along the eastern shelf break. However, how this water dispersed in the Strait was not addressed. Figure 2.9.1 shows nutrient distributions in July 1980.

Smith and Longmore (1980) reported relatively low phosphate levels from a transect across the interior of Bass Strait and high levels approaching and inside Port Phillip Bay.

2.10 Air-Sea Heat Fluxes

Air-sea heat fluxes over Bass Strait involve coupling between ocean and atmosphere and modify the heat and salt content of Strait waters. Data has been published regarding latent, sensible and longwave heat fluxes in the region and is found in climatological heat flux atlases such as Oberhuber (1988), based on analysis on the Comprehensive Ocean Atmosphere Data Set (COADS), the Atlas of Surface Marine Data (ASMD94) by da Silva *et al.* (1994), based on analysis of UWM/COADS and NCEP (National Centre for Environmental Prediction) reanalysis data. This data has as yet not been utilised in studies of air-sea interaction in Bass Strait.

A large amount of uncertainty exists in quantifying air-sea fluxes over the ocean because they involve interactive coupled feedback cycles and largely depend on winds, currents and air and sea temperatures and humidity differences. Studies of air-sea fluxes in Bass Strait are limited to a few only. The only *in situ* measurements of momentum, sensible and latent fluxes in Bass Strait were made from the Kingfish B oil production platform, in slightly unstable conditions, at a height of approximately 5 m above the water over a one day period (Antonia *et al.*, 1977). Bulk transfer coefficients for momentum, sensible and latent fluxes were found to be in the range 0.001 – 0.004 and decreased slightly with decreasing wind speed. Transfer coefficients for moisture flux had strongest dependence on wind speed whilst the drag coefficient for momentum flux had least dependence. This study provided some guide to using transfer coefficients in regional modelling studies, despite the obvious limits of spatial and temporal resolution.

The study by Stephens *et al*. (1981), which is based on two years of observations, gives an indication of the annual net heat flux to be expected over the region and the annual and semiannual harmonic amplitudes of seasonal net heat flux variation. The expected annual net heat flux over Bass Strait, according to this study, is upward directed and attains values between 0 and -10 W m^{-2} (Figure 2.10.1). This is an indication that Bass Strait is located at a latitude where there may be a consistent annual net transfer of heat from the ocean to the atmosphere. Being close to zero suggests that a near seasonal equivalence in heating and cooling takes place in this region.

Stephens *et al*. (1981) estimates the annual amplitude in net heat flux over the Strait to be between ~110 and 120 W m^{-2} (Figure 2.10.2). The semi-annual amplitude is estimated to be ~5 W m^{-2} (not shown). This indicates the most important cycle in net heat flux variation is the annual cycle.

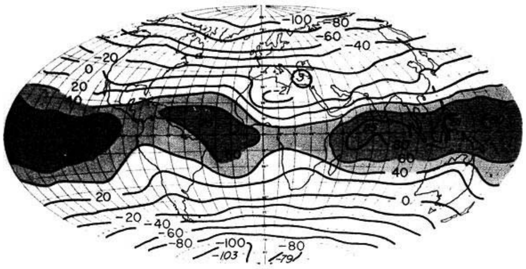

Figure 2.10.1. Estimated annual global net radiation (W m^{-2}). Adapted from Stephens *et al.* (1981).

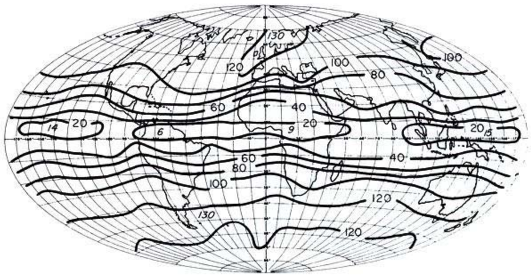

Figure 2.10.2. Estimated global annual amplitude in net heat flux (W m^{-2}). Adapted from Stephens *et al.* (1981).

Net heat flux for Bass Strait was estimated by Baines and Fandry (1983) based on records of long-term seasonal salinity trends. Some agreement between this study and the study by Stephens *et al.* (1981) is found in the annual amplitude of ~ 120 W m^{-2}. The annual net heat flux from Baines and Fandry (1983) is suggested to be close to zero, implying seasonal equivalence in the heating/cooling cycle (Figure 2.10.3).

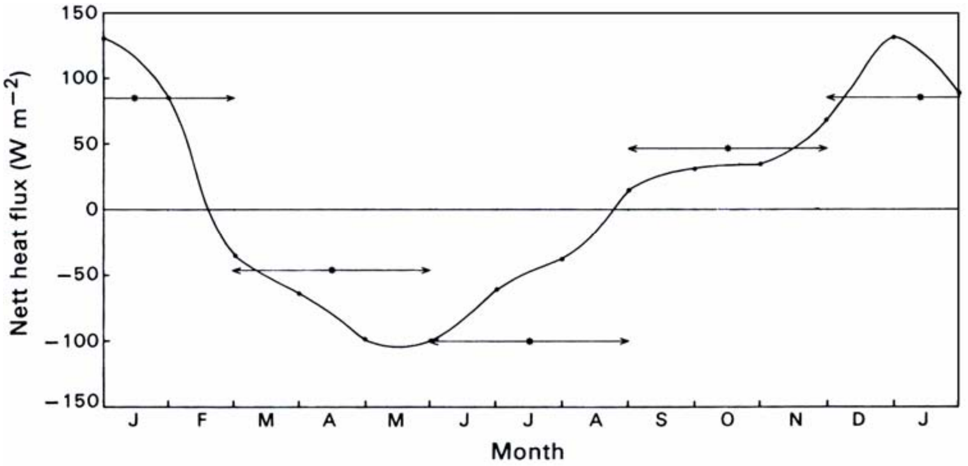

Figure 2.10.3. Estimates of the net heat flux based on long term seasonal salinity trends. Adapted from Baines and Fandry (1983). Asterisks indicate net downward seasonal averages of radiative flux at the top of the atmosphere from Stephens *et al*. (1981).

2.11 Summary and Relevant Knowledge Gaps

The M_2 tide creates strong currents in the passages of Bass Strait and plays an important role in local mixing of the water column. Transient storms frequent the region, particularly in winter and spring, bringing enhanced mixing and possible upwelling-driven intrusions of deeper water onto the shelf. Waters in the Strait can be well mixed during winter due to stronger thermohaline convection. Stratification occurs in the interior in summer and autumn and there is some evidence of establishment of a two-layer system. Mean winds in the region vary from being approximately southerly in summer to westerly in winter. On longer timescales winds and residual sea level at the entrances are thought to be the driving force of the circulation throughflow and flushing of Bass Strait waters.

The influential water masses in Bass Strait are EACW, SACW and SASW. Intrusions of EACW are periodic and mainly driven by local wind forcing or encroachment of the EAC onto the shelf. This however is not well documented. Intrusions of SACW are driven by local winds and the SAC system. SASW is an important water mass for marine ecosystems owing to its high nutrient content. This water-mass can be introduced into Bass Strait by various forms of upwelling and by diffusive vertical mixing at the shelf break. Water mass properties in the Strait are modified both by inflow of external water mass and by air-sea fluxes. In winter, Bass

Strait contains denser water than the surface-layer of the Tasman Sea. Bass Strait Water cascades downward on the continental slope to depths of ~300-400 m.

In taking account of the literature on the subject of Bass Strait oceanography, a number of relevant knowledge gaps and science questions are readily identified. Firstly, what is the effect of tides on water mass property variation? Also, how is the seasonal cycle of stratification characterised by an ocean model? Due to the fact that most salinity measurements have been made in either summer or winter at certain locations, the seasonal cycle of salinity in Bass Strait is not well resolved. So, what can a model tell us about the seasonal cycle of salinity which may not be measurable in practice? How reliable can the model results be? Far-field effects on Strait water mass properties are also not clearly understood, so what is the sensitivity of water mass properties in the Strait to these effects? On the subject of transport timescales, what is the seasonal variability of flushing times, residence times and water age in Bass Strait and what implications does this have for water mass properties? Another relevant question, and perhaps the most difficult to answer, is what is the physical response of Bass Strait to climate change. This question is beyond the scope of the present study.

The next section details the theory and methods which form the basis on which these scientific questions are addressed.

CHAPTER 3:
Theory & Methods

3.1 Introduction

The first section of this chapter provides an account of the ocean model physics and the methods used in deriving air-sea momentum, heat and salinity fluxes. The model description and its application to this study are then outlined. An outline of the theory and methods used to calculate flushing times, residence times and age distributions using Eulerian tracers and Lagrangian particle tracking follows. After this, details regarding model initial conditions and surface and open boundary forcing are presented. Finally, details of the observations used in the study are presented followed by methods used to derive remote forcing.

3.2 Theory

The COHERENS model is a primitive equation model based on the Navier-Stokes equations for an incompressible fluid on an *f*-plane. The hydrodynamic module of COHERENS is based on the Princeton Ocean Model (POM) by Blumberg and Mellor (1987) which has been widely used in the oceanographic modelling community. Some examples of the use of POM are found in Cirano and Middleton (2004) and Oke *et al*. (2002). The momentum equations and conservation equations for advection and diffusion of temperature and salinity form the basis of the model physics. The assumptions of vertical hydrostatic equilibrium and the Boussinesq approximation are made. The parameterisation of turbulence and the formulation of the surface fluxes are described in further detail later. The three-dimensional equations in Cartesian coordinates are:

$$\frac{\partial u}{\partial t}+u\frac{\partial u}{\partial x}+v\frac{\partial u}{\partial y}+w\frac{\partial u}{\partial z}-fv=-g\frac{\partial \eta}{\partial x}-\frac{1}{\rho_o}\frac{\partial q_d}{\partial x}+\nu_T\frac{\partial^2 u}{\partial z^2}+\frac{\partial \tau_{11}}{\partial x}+\frac{\partial \tau_{21}}{\partial y} \tag{1}$$

$$\frac{\partial v}{\partial t}+u\frac{\partial v}{\partial x}+v\frac{\partial v}{\partial y}+w\frac{\partial v}{\partial z}+fu=-g\frac{\partial \eta}{\partial y}-\frac{1}{\rho_o}\frac{\partial q_d}{\partial y}+\nu_T\frac{\partial^2 v}{\partial z^2}+\frac{\partial \tau_{12}}{\partial x}+\frac{\partial \tau_{22}}{\partial y} \tag{2}$$

$$\frac{\partial p}{\partial z}=-\rho g \tag{3}$$

$$\frac{\partial u}{\partial x}+\frac{\partial v}{\partial y}+\frac{\partial w}{\partial z}=0 \tag{4}$$

$$\frac{\partial T}{\partial t}+u\frac{\partial T}{\partial x}+v\frac{\partial T}{\partial y}+w\frac{\partial T}{\partial z}=\frac{1}{\rho_o c_p}\frac{\partial I}{\partial z}+\frac{\partial}{\partial x}\left(A_H\frac{\partial T}{\partial x}\right)+\frac{\partial}{\partial y}\left(A_H\frac{\partial T}{\partial y}\right)+\frac{\partial}{\partial z}\left(A_v\frac{\partial T}{\partial z}\right) \tag{5}$$

$$\frac{\partial S}{\partial t}+u\frac{\partial S}{\partial x}+v\frac{\partial S}{\partial y}+w\frac{\partial S}{\partial z}=\frac{\partial}{\partial x}\left(A_H\frac{\partial S}{\partial x}\right)+\frac{\partial}{\partial y}\left(A_H\frac{\partial S}{\partial y}\right)+\frac{\partial}{\partial z}\left(A_v\frac{\partial S}{\partial z}\right) \tag{6}$$

$$\tau_{11}=2\nu_H\frac{\partial u}{\partial x} \tag{7}$$

$$\tau_{12}=\tau_{21}=\nu_H\left(\frac{\partial u}{\partial y}+\frac{\partial v}{\partial x}\right) \tag{8}$$

$$\tau_{22}=2\nu_H\frac{\partial v}{\partial y} \tag{9}$$

where u, v and w are components of velocity in the x, y and z directions respectively and η is the free surface elevation. z is the depth coordinate positive downwards from the surface. The initial undisturbed sea-level is at $z = 0$. Horizontal and vertical turbulent eddy viscosity is parameterised with υ_H and υ_T respectively. Horizontal components of the stress tensor are denoted by τ_{11}, τ_{22}, τ_{12}, and τ_{21}. The Coriolis parameter f is approximated as a function of latitude φ using $f = 2\Omega \sin(\varphi)$ where $\Omega = 2\pi/86164$ radians s^{-1}. *In situ* sea water density is denoted by ρ and reference density by $\rho_o = 1026$ kg m^{-3}. p is pressure and $g = 9.81$ m s^{-2} represents gravitational acceleration. T and S are temperature and salinity. Horizontal and vertical turbulent eddy diffusivity of temperature and salinity is denoted by A_H and A_V respectively. The specific heat capacity of seawater is c_p = 3987.5 J kg^{-1} K^{-1}. The heating effect of incoming shortwave solar radiation is denoted by *I*.

The first two equations solve local current component accelerations based on forces acting on the fluid and advection and diffusion of momentum. The Boussinesq approximation is made in the evaluation of horizontal pressure gradients by the use of ρ_o and vertical hydrostatic equilibrium is implied in equation 3. Equation 4 is the continuity equation and equations 5 and 6 are for transport of heat and salt respectively.

Fluid transport is estimated using a hydrostatic equilibrium pressure field governed by both barotropic and baroclinic horizontal pressure gradients. The baroclinic pressure q_d is obtained by vertically integrating the buoyancy in the way described in Cushman-Roisin (1994).

The three-dimensional equations are solved numerically using the mode-splitting method which requires an additional set of two-dimensional depth-integrated continuity and momentum equations. The model runs both 2-D and 3-D modes simultaneously. The model solves equations (1) to (10) with numerical schemes designed for shelf-sea modelling applications. Details regarding the sigma-coordinate transformation and numerical techniques for implementation of the finite difference equations, are described in Luyten *et al.*, (1999).

Numerical computations involving equations (1)-(10), in finite difference form, are carried out on an Arakawa C grid with an implicit time scheme for diffusion and an explicit scheme for advection. Sub-grid scale horizontal turbulent diffusion of momentum, heat and salt is estimated using the Smagorinsky formulation. A total variation diminishing advection scheme (TVD) is used for momentum, heat, salt and Eulerian tracers (Luyten *et al.*, 1999). Vertical mixing is simulated using a κ-ε second-order turbulence closure scheme. The choice of advection and vertical turbulence closure schemes were informed by the sensitivity studies and tests of Luyten *et al.*, (1999). The general equation of state of seawater defined by the Joint Panel on Oceanographic Tables and Standards (UNESCO, 1981), simplified by assuming zero pressure effects, is used in the model. This approximation is valid for depths less than ~1 km.

Bottom friction is calculated using the quadratic law which parameterizes the dissipation of energy by tangential friction at the sea floor according to

$$\begin{aligned} \tau_{b,x} &= \rho_o r_b u_b^{\;2} \\ \tau_{b,y} &= \rho_o r_b v_b^{\;2} \end{aligned} \tag{10}$$

where and u_b and v_b represent bottom current components and r_b is an empirical bottom friction coefficient, calculated using a roughness length of 8 mm with the method given in Luyten *et al*., (1999). This corresponds to a bottom friction coefficient of 0.007.

3.3 Surface Fluxes

Transfer of momentum into the ocean due to the effect of wind acting on the sea surface, which induces horizontal currents and vertical mixing, is obtained by specifying surface stress as a function of wind speed components according to the quadratic law

$$\begin{aligned} \tau_{s,x} &= \rho_a c_d u_s \sqrt{u_s^{\;2} + v_s^{\;2}} \\ \tau_{s,y} &= \rho_a c_d v_s \sqrt{u_s^{\;2} + v_s^{\;2}} \end{aligned} \tag{11}$$

where (u_s, v_s) are the components of the wind vector at a reference height of 10 m, ρ_a = 1.2 kg m^{-3} is the mean air density and the surface drag coefficient c_d is evaluated with the empirical formulation of Geernaert *et al.* (1986).

The vertical flux of heat in the water column is given by

$$c_p \rho_o \lambda_T \frac{\partial T}{\partial z} = Q_{net} \tag{12}$$

where Q_{tot} is the downwards directed heat flux at the surface, c_p the specific heat of seawater at constant pressure, z represents vertical spacing and λ_T is an unknown parameter representing vertical turbulent diffusion of heat. The total heat flux Q_{net} is composed of a term $-Q_{nsol}$ of all non-solar contributions plus the shortwave radiative flux Q_{rad}. The non-solar heat flux has three components, i.e. $Q_{nsol} = Q_{la} + Q_{se} + Q_{lw}$ where Q_{la} is the latent heat flux released by evaporation, Q_{se} the sensible heat flux due to the turbulent transport of thermal energy across the air/sea interface and Q_{lw} the net longwave radiation emitted at the sea surface. The first two terms are related to turbulent fluxes of moisture and heat by

$$\begin{aligned} Q_{la} &= \rho_a L_v C_E |U_{10}| (q_s - q_a) \\ Q_{se} &= \rho_a c_{pa} C_H |U_{10}| (T_s - T_a) \end{aligned} \tag{13}$$

where U_{10} is the magnitude of the wind vector at a reference height of 10 m, T_s and T_a are sea surface and air temperature and q_s and q_a are sea-surface and air specific humidities. Latent and sensible heat fluxes involve two dimensionless parameters C_E & C_H, the Dalton and Stanton numbers. These are calculated as a function of air-sea temperature difference and wind speed using the Monin-Obukhov (1954) formulation. Specific heat of air c_{pa} at constant pressure is calculated using $c_{pa} = 1004.6(1 + 0.8375q_a)$ J kg^{-1} K^{-1}. Latent heat of vaporization L_v is taken as a function of sea surface temperature using $L_v = 2.5008 \times 10^6 - 2300T_s$ J kg^{-1} and q_s and q_a are calculated using

$$q = \frac{0.62e}{P_{ao} - 0.38e} \tag{14}$$

where P_{ao} = 1013.25 hPa is a reference atmospheric pressure. The vapour pressure e is obtained in *hPa* from the empirical relation given by

$$\log_{10} e = \log_{10} RH + \frac{0.7859 + 0.03477T}{1 + 0.00412T} \tag{15}$$

where RH is the relative humidity fraction (Gill, 1982). For q_s at the sea surface, a relative humidity of 100% is assumed. The specific humidity q, the vapour pressure e and the temperature T either represent sea surface or atmospheric values at the reference height. The long-wave radiation flux term is evaluated using

$$Q_{lw} = \varepsilon_s \sigma_{rad} (T_s + 273.15)^4 (0.39 - 0.05 e_a^{1/2})(1 - 0.6 f_c^2) \tag{16}$$

here $\varepsilon_s = 0.985$ is emissivity at the sea surface, $\sigma_{rad} = 5.67 \times 10^{-8}$ W m^{-2} K^{-4} is Stefan's constant, f_c is fractional cloud cover and e_a vapour pressure (Gill, 1982).

Surface salinity flux is determined by

$$\rho_o \lambda_T \frac{\partial S}{\partial z} = \frac{S_s (E_{vap} - R_{pr})}{1 - 0.001 S_s} \tag{17}$$

where E_{vap} and R_{pr} are the evaporation and precipitation rates in kg m^{-2} s^{-1} and S_s the surface salinity (Steinhorn, 1991). In the present study E_{vap} which is equal to Q_{la}/L_v is calculated and R_{pr} is supplied as input data.

The model includes an optical module for determining the way solar heat is absorbed and scattered (attenuated) in the upper part of the water column. Incident solar irradiance at the sea surface is expressed as the sum of an infrared and shortwave component (Paulson and Simpson, 1977). The infrared part decays exponentially and a constant attenuation length of 0.1 m is assumed. Shortwave radiation decays similarly but consists of two parts. The first part represents the standard diffuse attenuation coefficient for monochromatic light. The second part incorporates the 'yellow substance' effect due to very small neutrally buoyant particles of inorganic suspended particulate matter (iSPM). It is assumed that iSPM contributions are related to salinity (Luyten *et al.*, 1999). A constant surface albedo of 0.06 is used. Default optical module parameters are used. The meteorological time step is set to 1 hour. This ensures a sufficiently high resolution of the diurnal cycle of solar radiation. The daily and seasonally changing zenith angle of the sun, determined from the local hour angle, latitude and solar declination is included to resolve intra-annual variance of incident solar radiation. Details are given in Luyten *et al.* (1999).

3.4 Experimental Design

Bathymetric data were acquired from the 0.01-degree resolution *Geoscience Australia Bathymetry and Topography Grid* (2002). A larger region than Bass Strait is chosen to move open boundaries away from the region of interest and to include regional currents. This data were interpolated onto a 0.08 degree horizontal grid and subsequently smoothed by diffusion to have slopes less than or equal to 0.1 in order to satisfy the constraints of hydrostatic consistency (Mesinger and Janic, 1985).

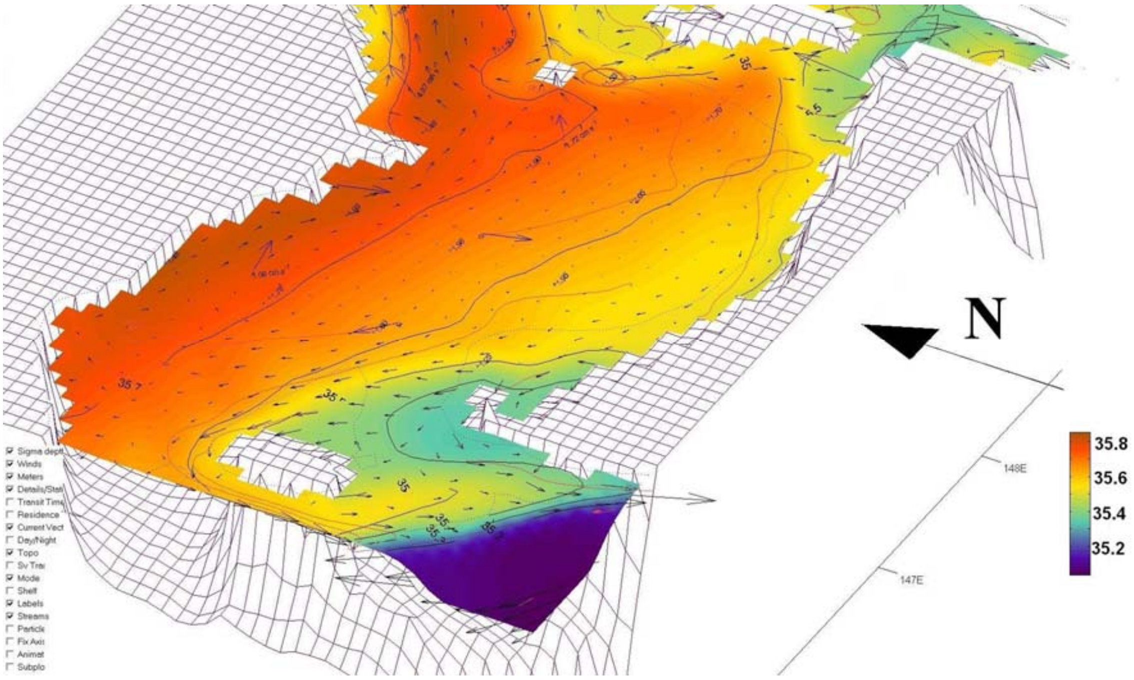

Figure 3.4.1. Example of surface σ-layer salinity in model on the 0.08^o spherical finite difference grid (each square is a grid cell). The σ-layer can be seen deepening over the continental slope south of King Island into fresher subsurface water.

The model grid is spherical and contains 128 x 96 x 20 grid points in the λ, φ, and σ directions respectively covering the region shown in Figure 1.4.1. The choice of a spherical rather than Cartesian grid is of no consequence for the dynamics at the space scale of the model, i.e. the f-plane approximation is valid, rather it assists with gridding geographically based input data. Results and comparisons between CARS and model data are presented on sigma-layer surfaces. These are three-dimensional and terrain following with scalar quantities approximated in the centre of grid cells. Figure 3.4.1 shows how surface σ-layer salinity becomes fresher as the layer deepens over the continental slope south of King Island in the model. The use of 20 vertical σ-levels means that in the shallower parts of Bass Strait in the model, surface σ-level depths are between 0.5-2 m and in the deepest part of the model domain (1000 m) they are 25 m (half way between surface and depth of first sigma layer). The difference between σ-layers and σ-levels is illustrated in a vertical section through 146^{o}E, which is shown in Figure 3.4.2. Crosses denote vertical positions of cell centres and are the points where scalar quantities are estimated in the model. Values at these points represent an average in the depth range of the cell between the sigma surfaces.

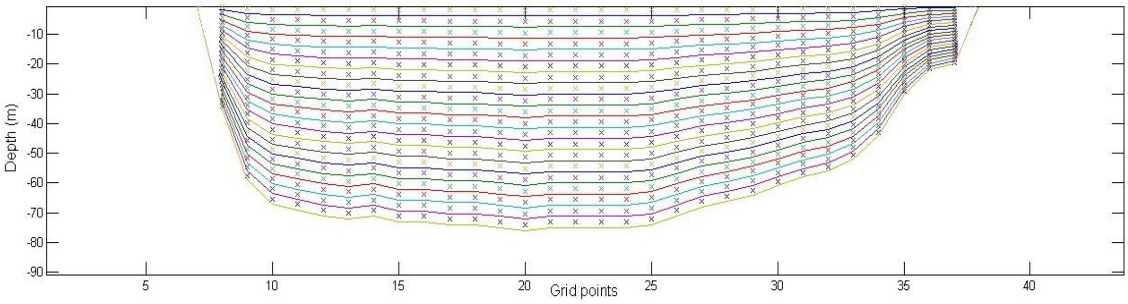

Figure 3.4.2. Section through 146^{o}E in model showing σ-levels (continuous lines) and vertical grid points where scalar quantities are estimated (crosses).

In the gridding and interpolation process, smaller scale features such as bays and islands are lost. The major omission is Port Phillip Bay with an entrance of ~ 2.8 km which is narrower than the model grid spacing (~ 6-9 km). It was necessary to set-up the model at this resolution to carry out multi-year simulations with sufficient vertical resolution in practical amounts of CPU time. The bathymetry used in the model in the Bass Strait region, after smoothing, is shown in Figure 3.4.3. A minimum depth of 20 m is used to avoid unrealistically large areas of shallow-water. A maximum depth of 1 km is prescribed for computational efficiency, and to maximize vertical resolution in the deeper sections of the domain. Also, CARS atlas temporal harmonics, which are used for boundary conditions, are only available to this depth. Additionally, water from depths greater than 1 km is considered to not play a significant role in water mass property variation in Bass Strait. All experiments are carried out with 20 σ-layers. This amount of vertical levels minimises pressure gradient errors, which is an issue with σ-coordinate models (Haney, 1990). Bottom friction was adjusted in the model based on tidal sensitivity studies. The model has a two-dimensional barotropic mode time step of 30 s, which satisfies the Courant-Friedrichs-Lewy (CFL) condition, and a three-dimensional baroclinic mode time step of 300 s.

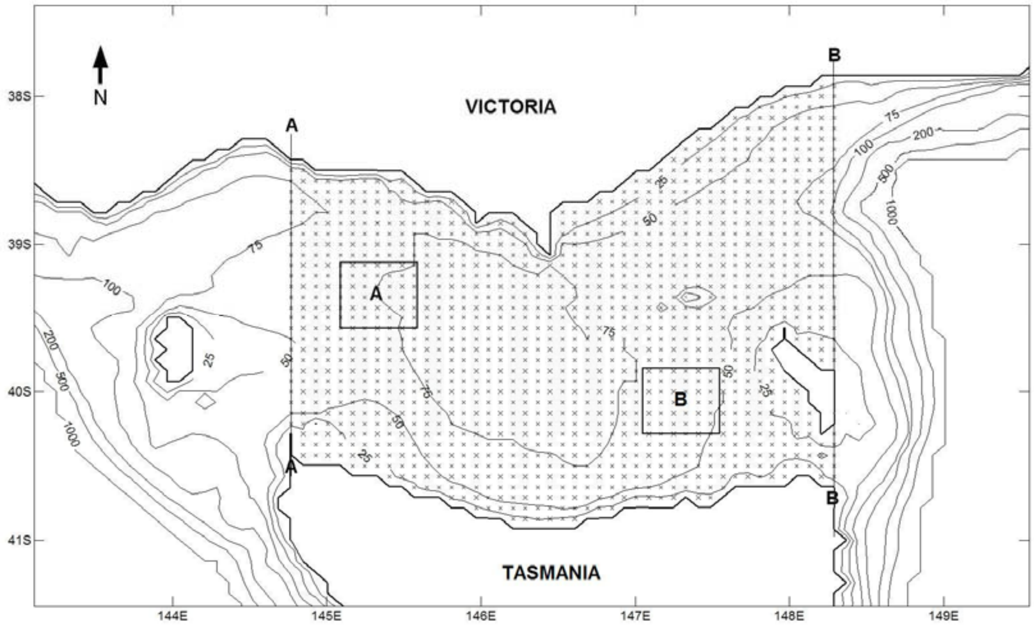

Figure 3.4.3. Area within Bass Strait delimited as control region (marked with crosses) and model bathymetry. Same area used for spatially averaging monthly mean model and observational summary data found in Table A1. Positions of vertical sections A-A and B-B are shown.

A reference simulation was developed by combining all the forcing. Model simulations up to 10 years in length with fewer vertical levels (5) were carried out to test the model's ability to reach a steady solution (not shown). It was found that the seasonal cycle in the second year of most simulations was close to steady state so results from the second year are focussed on. The methodology adopted for the spin-up was to first run the model for a year with the tides. A restart is then used to initialise the density field and the wind field is gradually increased to full strength over two days to minimise inertial oscillations in currents. All simulations are initialised at midnight on the 1st January.

Daily time-averaged solar and non-solar heat fluxes, spatially averaged over an arbitrary control region are also examined in conjunction with the results. The control region is the area marked by crosses shown in Figure 3.4.3. This region also delimits the area chosen to initialize tracer to derive flushing time, residence time and water age distributions. The positions of sections A-A and B-B, which are later used to examine the seasonal-mean vertical structure of water mass properties and currents, are indicated.

The simulations were carried out using Hydra, an IBM 1350 *e*Server at SAPAC (South Australian Partnership for Advanced Computing). The approximate CPU time on a single 2.4 GHz Xeon processor for a two year simulation was around 1200 hours. During the course of the project over 45,000 CPU hours were used.

A list of selected parameters and settings for COHERENS used in the reference simulation are given in Table 3.4.1.

Model Parameter	**Value**	**Description**
DLAREF	45S	Reference latitude (degrees)
DLOREF	141E	Reference longitude (degrees)
R0REF	1026.0	Reference density (kg m^{-3})
VISMOL	0.000001	Background vertical eddy viscosity (m^2/s)
DIFMOL	0.000001	Background vertical eddy diffusivity (m^2/s)
CM0	0.1	Coefficient in Smagorinsky diffusion formulation
CS0	0.1	Coefficient in Smagorinsky diffusion formulation
CDZ0UN	0.008	Constant bottom roughness length (mm)
CDB100	0.007	Constant bottom friction coefficient at 1 m above sea floor
DELT	30	2-D time step (s)
IC3D	300	3-D time step (s)
ICMET	3600	Meteorological time step (s)
Model Switch		
IADVC	3	TVD advection scheme for momentum
IADVS	3	TVD advection scheme for scalars
IADVWB	3	TVD vertical advection scheme for vertical sinking of suspended matter
IBSTR	1	Quadratic bottom friction
IDRAG	3	Surface drag coefficient evaluated with $C_D = 10^{-3}(0.43 + 0.097\|U_{10}\|)$
IGRDIM	3	Three dimensional model grid
IGTRH	1	Spherical coordinates
IODIF	2	Smagorinsky horizontal diffusion
IOPTC	2	Eulerian tracer with vertical advection/diffusion on
IOPTD	2	General UNESCO equation of state
IOPTHE	2	Temperature and optical modules on
IOPTK	2	Vertical turbulence one-equation model (k-ε)
IOPTM	3	Meteorological forcing both space and time dependent
IOPTP	1	Particle module on
IOPTSA	2	Salinity equation with surface freshwater flux using rainfall data
ITDIF	1	Surface exchange coefficients as function of air-sea temperature difference and wind speed using Monin-Obukov (1954)
IAHDHT	1	Transport of turbulence kinetic energy enabled

Table 3.4.1. Selected model parameters and settings.

3.5 Transport Timescales

3.5.1 Background

Hydrodynamic models are commonly used to predict flushing of water bodies or dispersion of toxic materials, such as those introduced by oil spills or outfalls, which may expose ecosystems to contamination. Methods include the use of transport timescales such as flushing times, residence times and more recently water age. To understand transport timescales we first consider that seawater is a discrete fluid made up of constituents such as pure water, suspended matter, dissolved gases and solids, pollutants, contaminants and biota. Each constituent has an age distribution associated with it.

Flushing time of a volume of seawater is usually defined as the time taken for most or all of the constituents to be overturned or replaced with water from outside the volume (Monsen et al., 2002; Sadrinasab and Kämpf, 2004; Takeoka, 1984; Zimmerman, 1988). The e-folding flushing time is typically used as an estimate of the mean flushing time (Delhez *et al.*, 2004). This is defined as the time taken for tracer concentration to drop to 1/e of its initial concentration. This definition is used in this study and in a number of previous studies (Monsen et al., 2002; Sandery and Kämpf, 2005; Walker, 1999).

Residence time is commonly defined as the time taken for a water parcel or introduced material to leave a region (Delhez, 2006; Delhez et al., 2004; Takeoka, 1984). Material can be introduced to the region by either point or diffuse sources.

Water age, on the other hand, is a property of each constituent and can be used to trace movements and variations of constituents within (or away from) a region of interest. The age of a constituent or water parcel is defined as the time since it entered the region or was last exposed to the region (Deleersnijder et al., 2001; Deleersnijder and Delhez, 2004; Deleersnijder et al., 2002; Delhez et al., 1999; Delhez and Deleersnijder, 2002; England, 1995; Hall and Haine, 2004; Hirst, 1999; Karstensen and Tomczak, 1998; Monsen et al., 2002). All constituents in a region age at the same rate but have different ages according to the time they enter the region (or were last exposed to the region) through some boundary to that region. Age is both a property of the constituent and a function of its pathway.

Transport timescales in general provide integral measures of advective and diffusive transport processes and can be used to highlight variability in the distribution of important properties critical to marine ecosystems and climate such as temperature, salinity, chlorophyll-*a,* macro and micro nutrients, dissolved O_2 and CO_2. Many case studies exist where transport timescales have been used to trace water mass and estimate ventilation rates in the deep ocean (Deleersnijder et al., 2002; England, 1995; Hirst, 1999; Karstensen and Tomczak, 1998) or to investigate circulation in semi-enclosed seas and estuaries (Delhez and Deleersnijder, 2002; Monsen et al., 2002; Oliviera and Baptista, 1997; Sadrinasab and Kämpf, 2004; Sandery and Kämpf, 2005; Walker, 1999).

Residence time and flushing time are the same in the integral sense, i.e. when distributions are summed and averaged over an entire volume. If tracer mass in a certain region decreases with time according to $m(t)=m(0)e^{-t/\tau f}$, where m is tracer mass, t is time and τ_f is flushing time, then mean flushing time is equal to mean residence time (Delhez *et al*., 2004).

While integral timescales are useful for comparing and classifying different systems, their relevance is limited to steady-state cases with strong mixing and they potentially misrepresent transport processes (Oliviera and Baptista, 1997). The distribution of a timescale, or its local variation, within a region of interest provides additional information, and can be used to determine the ‘advection-diffusion’ climate of the system (Monsen *et al*., 2002). This may be more important from an ecological point of view. In steady-state flow, local or integral transport timescales could be assessed by single release of a tracer concentration field with even distribution in the region of interest, at any time, provided a suitable period is allowed for the turnover of the mass or volume of the system.

To understand variation in a non-stationary system, such as one which exhibits seasonal variation, the use of release time dependent tracer concentration fields is required (Oliviera and Baptista, 1997). In this case, tracer should be released at appropriate time intervals. This is similar to prescribing a suitable sampling frequency. For example, seasonal variation in flushing can be captured by release of independent tracer fields in the region of interest at monthly to quarterly intervals. Timescale measurements can be made using either Lagrangian or Eulerian tracer in numerical models and found using arbitrary boundaries which delimit a control region of interest. There are advantages and disadvantages to both which are discussed later. The placement of the boundaries to define a region of interest is an arbitrary choice, and will influence absolute values of the timescales, however, to some extent, the differences in the system are of a relative nature and will be seen regardless of the location of the boundary.

Local flushing times for sub-volumes of a control region can only be defined with respect to the control region itself. The scale of smallest sub-volumes within the region of interest is also an arbitrary choice and influences the spatial resolution of the timescale distribution. This scale is best defined at model grid resolution. At the instance of a local e-folding flushing time in a sub-volume of a control region, the remaining 1/e proportion of matter in the sub-volume has tracer age equal to the local flushing time. When the control region has a local flushing time for each sub-volume, a snapshot of relative tracer age through time is obtained. The spatial age distribution in a control region can be used to identify age-fronts, which may delimit different water masses. By examining the time-varying spatial age distribution in a control region, the sources and sinks of the control region can be identified and the question of where the oldest water resides in the control region can be addressed.

In general, differences that occur between timescales stem from their definitions, which imply different initial and boundary conditions. Differences may be better understood by considering which statistics form part of the respective timescale distributions. Material entering, leaving or outside the control region is not part of the age distribution in the control region. Only material leaving a control region forms the residence time distribution, that entering or inside is not part of it (Takeoka, 1984). Flushing time distribution is similar to residence time distribution in this sense because it cannot be found until flushing times for all sub-volumes of a control region are obtained.

In the case of an oceanic strait, a number of flushing time, residence time and water age distributions are possible depending on the character of advective and diffusive flow regimes. Figure 3.5.1 diagrammatically illustrates how transport timescale distributions in a channel or strait may vary as a result of differing scenarios. Importantly, it shows how flushing time and residence time distributions differ within different scenarios, whereas flushing time and age distributions are similar across different scenarios. Scenario D is closest to representing the character of transport timescale distributions for Bass Strait.

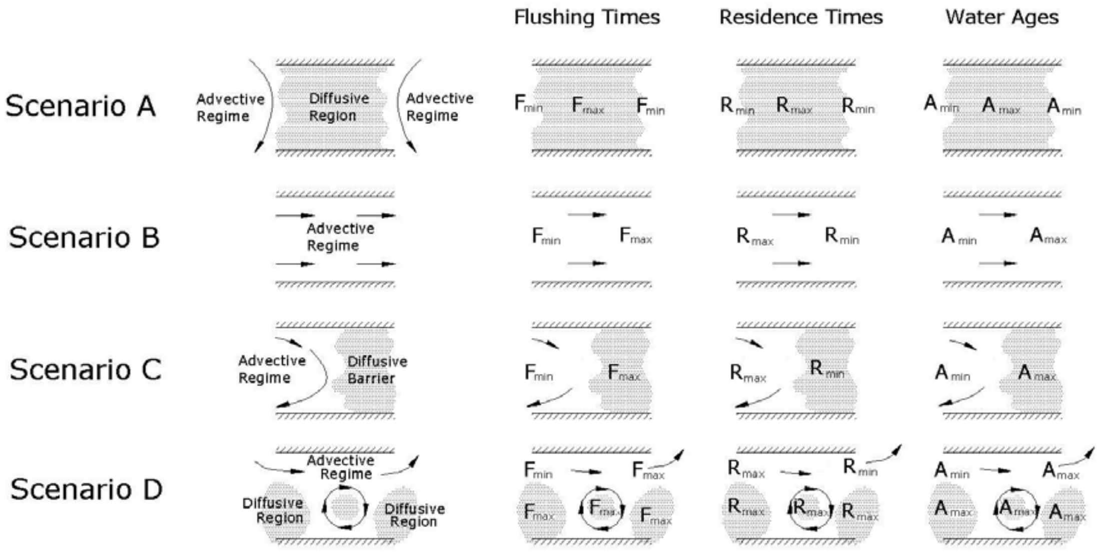

Figure 3.5.1 Variation in character of transport timescale distributions in an oceanic strait depending on advective and diffusive flow regime scenarios.

3.5.2 Methods

To find distributions of flushing times, residence times and water age, a control region is defined in the model (Figure 3.4.3). Eulerian tracer concentration fields are used for flushing time calculations and Lagrangian non-buoyant particles are used for age and residence time calculations. The number of particles used is 10000. The use of particles requires a significant source population to be continually available at the control region's open boundaries. Also, a sufficient number of particles need to be present in the control region at any point to find adequate representations of the age or residence time distributions with statistical significance. One important difference between the Eulerian and Lagrangian tracer methods is parameterisation of sub-grid scale mixing. Diffusion in the Lagrangian method is modelled using a Monte-Carlo or random walk method where particles are subjected to random motion with variance $\sigma^2 = 2K\Delta t$ where K is local diffusivity and Δt *is* model time step (Maier-Reimer and Sündermann, 1982). The Eulerian method models diffusion processes using the Smagorinsky scheme for sub-grid scale parameterization of horizontal turbulence. The Eulerian scheme contains finite-difference advection-diffusion conservation equations for transport of a conservative tracer. If tracer is initialised at unit concentration at all cells in the control region, then the tracer concentration field represents all mass in the volume of the control region. Change in concentration in a local cell represents change in mass with respect to the control region. Accompanying this change is an equal amount of mass leaving and new mass entering the control region. The Eulerian method offers advantages in terms of being a computationally efficient statistical representation of the mass distribution. Lagrangian tracers offer advantages over this approach if suitable amounts of particles are used. Computational effort is directed to areas where particles are concentrated, allowing sources and sinks to be represented and sharp fronts to be resolved (Luyten *et al.*, 1999). The Eulerian finite difference method uses the resolution defined by the grid and is usually a coarser resolution than that needed to resolve frontal structures. This approach introduces smoothing of frontal structures and numerical dispersion into the solution.

The Lagrangian particle tracking scheme uses a recycling method which keeps the same original number of particles (10000) in the model domain. Particles that leave the model domain are reinitialised at random locations at the sea surface inside and outside the control region on the shelf. This generates a steady introduction or rain of source particles in the model. This is useful because the circulation organises source particles from open boundaries to be concentrated in certain locations and we need to continually introduce source material in areas where low concentrations exist, otherwise these areas would not be sampled often enough. The particles that rain on the control region are only used for residence time calculations so that local cells in the control region have as many measurements as possible. Particles that rain on the control region are not used for age, even though they could be if we were considering age of constituents entering through the air-sea interface. Instead we are interested in age of external water mass coming into the control region through its open boundaries. Having suitable quantities of particles continually recycled through the system is important for attempting to obtain statistically significant residence time and age measurements.

Flushing time, residence time and age distributions are three-dimensional but have been depth-averaged in the analysis.

Flushing Time

To calculate e-folding flushing times we use 12 different three-dimensional Eulerian tracer concentration fields. Each tracer field has a different release time which is at the beginning of each month during the second year of the simulation. All tracer concentration fields are initialised at unit concentration, in the control region shown in

Figure 1. Flushing times are calculated for each model grid cell in the control region. The 12 different tracer concentration fields produce 12 different flushing time distributions. Annual-mean flushing time distribution is calculated as a time average of the 12 distributions. Seasonal-mean flushing time distributions are derived from tracers released during the season to determine the flushing characteristic of the season in which flushing takes place.

Residence Time

Residence times are derived from the time it takes for particles to leave the control region from sub-volumes within it. Sub-volumes are arbitrarily defined to be a volume bounded by model horizontal grid spacing and water column depth. Particles already in the system which enter sub-volumes are used as well as particles that are randomly introduced into the local cells. A distribution of residence times for each sub-volume is found by re-running the loop of particle trajectories for every sub-volume. Annual-mean residence times for each sub-volume are found by running through the full two year simulation of particle trajectories for each sub-volume. The average of each distribution is the residence time that is gridded to produce an Eulerian map. Residence times dependent on release time either in the summer months or winter months are found by using particles released in the respective seasons. Residence times are removed from the analysis if less than 25 samples per local cell are obtained.

Water Age

Particles entering the control region are assigned age as a property. Particles that leave the control region are not used for age. If particles re-enter they are considered new again. It is not possible to estimate initial ages of particles inside the control region, so it is necessary to 'spin-up' the age distribution over the first part of the simulation. Age distribution is mapped by gridding particle ages with respect to their locations. The age distribution takes about 6 months to spin up, so seasonal-mean age distributions for the final year of the simulation are presented.

3.6 Forcing and Initial Conditions

The initial sea-surface elevation is set to zero. A spin up period of two days was allowed for wind and tides. Wind was gradually increased to full strength from zero to minimise inertial oscillations. The simulations begin 1st January. The initial density field is established using CARS2000 atlas salinities and temperatures evaluated on the 1st January. Atlas fields are evaluated throughout the model run. This was achieved by regridding atlas means and annual and semi-annual harmonic coefficients onto the model grid to evaluate fields at every time step in sigma-coordinates in the model. This allows for assessment of the differences between model and atlas data, for relaxation towards climatological values to be included if desired and TS profile data for three-dimensional open boundary forcing to vary smoothly throughout the year at every time step. No data assimilation or relaxation towards atlas values is used in order to present dynamically adjusted/balanced results. A zero-gradient condition for current profiles is used throughout the simulations.

3.6.1 Tidal Forcing

Two dimensional open-sea boundary conditions employed in the model use the theory of Riemann characteristics to estimate the incoming and outgoing depth-integrated currents from the prescribed amplitudes and phases of sea-level signals. The open boundary condition effectively filters out waves introduced into the model domain at the same amplitudes and phases as the forcing and also acts as a radiation condition for long gravity waves.

Varying phases and amplitudes of the four main components of the tides for the region, obtained from the Australian National Tidal Centre, are used for tidal forcing in the open-sea boundaries. This data were extracted from a spatial 0.15° data set and non-linear regression was used to obtain varying phases and amplitudes of the four principal tidal constituents at the model open-boundary grid points. Open boundary tidal forcing is then expressed as a sum of a series of cosine waves with varying amplitude and phase such that for every open boundary point *i*,

$$\eta_i^T = A_i^{M2}\cos(\frac{2\pi t}{T_{M2}}+\phi_i^{M2}) + A_i^{S2}\cos(\frac{2\pi t}{T_{S2}}+\phi_i^{S2}) + A_i^{O1}\cos(\frac{2\pi t}{T_{O1}}+\phi_i^{O1}) + A_i^{K1}\cos(\frac{2\pi t}{T_{K1}}+\phi_i^{K1}) \qquad (18)$$

where η^T is tidal open-boundary sea-level, A indicates amplitude, T is tidal period and Φ is the phase of the four indicated constituents. The data used for T is T_{M2} = 12.42 h , T_{S2} = 12 h , T_{O1} = 25.82 h and T_{K1} = 23.93 h. The data used for Φ and A are shown in Figure 3.6.1. The model open-boundary grid positions from 1 to 327 begin at the western boundary adjacent the coast and progress anticlockwise around the domain ending adjacent the coast on the northern boundary.

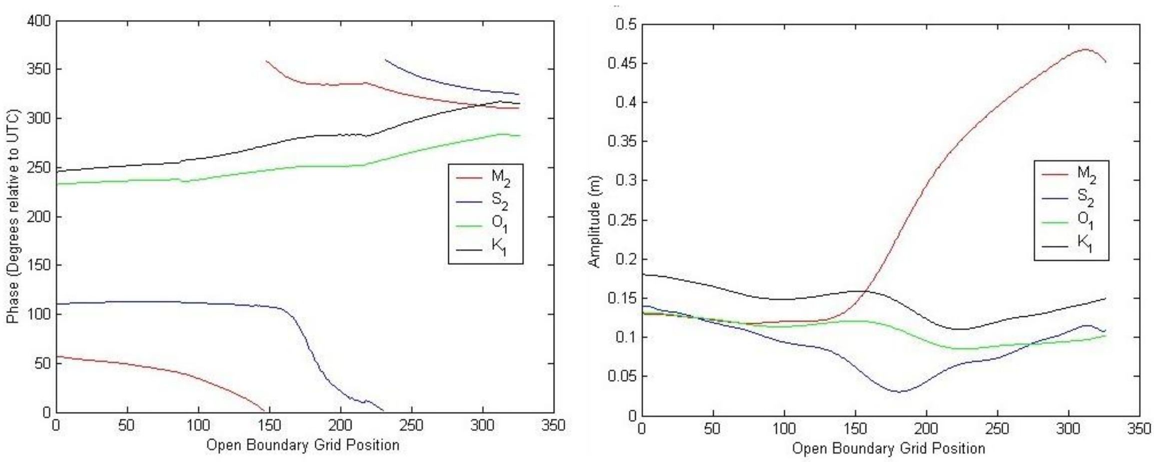

Figure 3.6.1. Tidal forcing phases *Φ* (degrees relative to UTC) and amplitudes *A* (m) at open-boundary grid positions (source: NTC, 2004).

Co-tidal charts from the Australian National Tidal Centre (NTC) illustrate the co-phases and co-amplitudes of the four main tidal constituents in Bass Strait (Figure 3.6.2).

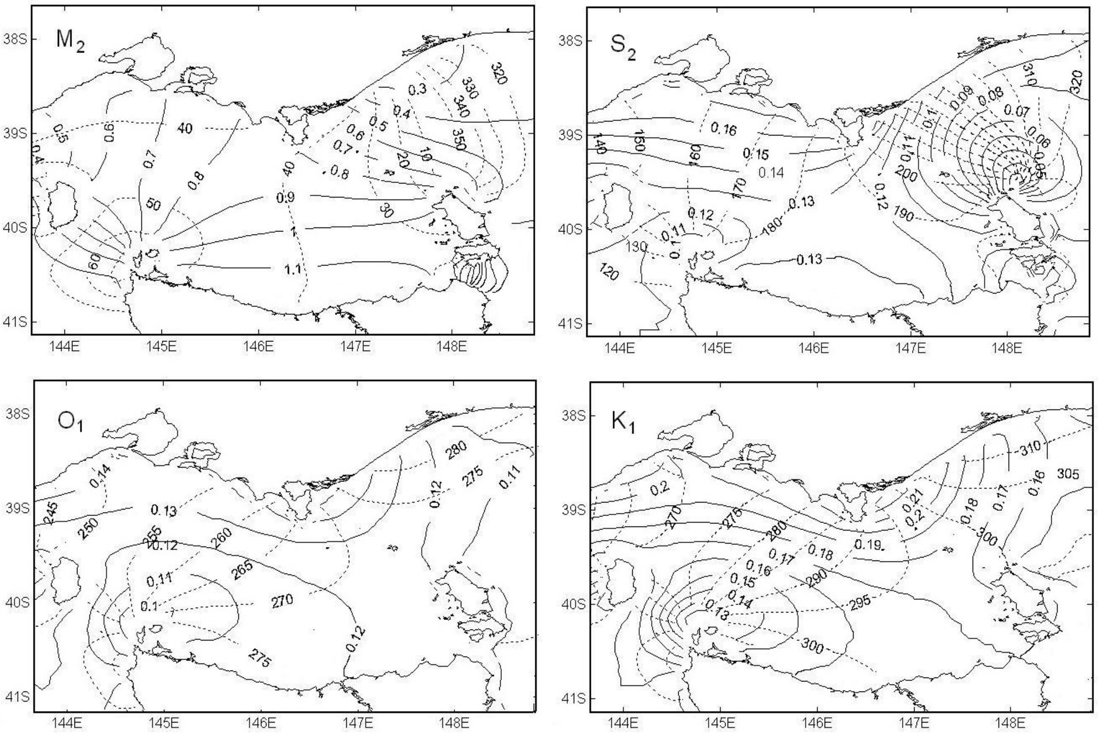

Figure 3.6.2. M_2, S_2, O_1, & K_1 co-tidal charts (source: NTC, 2004).

The amplitudes of the M_2 tide are evidently larger than the S_2, O_1 and K_1. The M_2 tide has nearly constant phase across central and north-western parts of the Strait and tidal range is largest along the northern Tasmanian coastline. Several virtual amphidromic points occur in the four constituents near Cape Grim, Lakes Entrance and Northern Flinders Island.

3.6.2 Atmospheric Surface Forcing

Monthly long-term means of spatially varying atmospheric forcing data are incorporated from various sources depending on availability and completeness. Two wind climatological data sets are investigated. In the reference simulation, NCEP reanalysis surface-level monthly long-term mean u and v wind speeds are used to drive momentum fluxes. In one of the sensitivity studies, Hellerman and Rosenstein long-term monthly-mean wind stresses are used (Hellerman and Rosenstein, 1983). Monthly long-term mean relative humidities, precipitation and air temperatures were accessed from NCEP reanalysis data. Long-term monthly fractional cloud cover was obtained from the Arctic Ocean Model Intercomparison Project (AOMIP). All atmospheric data were available online in different resolutions at NVODS, the National Virtual Ocean Data System. Due to the data being of coarser resolution than the model grid, interpolation and extrapolation was undertaken in order to create fields representing the original data. The monthly fields were temporally interpolated at each time step in the model from one month to another over the annual cycle. Analysis and discussion of this data is presented in section 4.1.1.

Wind data from Cape Grim Baseline Air Pollution Station (CGBAPS) for the period 1993 to 2003, based on hourly wind statistics, was analyzed to establish an additional guide to the climatological means and seasonal trends in the region, however, the model was not forced with this data. Even though local effects are important in measurements made at any particular location, the CGBAPS data are a reasonable indication of winds in the region.

3.6.3 CARS Atlas Temperature and Salinity Fields

The CARS atlas is derived from two datasets; the National Oceanographic Data Centre (NODC) World Ocean Atlas 1998 and the CSIRO archive of Australian hydrographic data (Dunn and Ridgway, 2002; Ridgway, 2001). Although the CARS atlas provides limited information in Bass Strait and is subject to biases related to spatial and temporal data density and resolution, it synthesizes observations and provides the only available guide to seasonal-mean variation in water mass properties in the region. As far as the author is aware, the two surveys made in November/December and June/July by Tomczak (1985; 1987) provide the only information regarding salinity for the southern half of the Strait which is documented in the literature.

The CARS atlas means and annual and semi-annual sines and cosines in netcdf format were read using the Matlab function *getmap* using the 'fill' option (Dunn, 2000). Only values for the upper 1000 m were extracted from the first 35 atlas 'standard levels' which are of non-uniform vertical spacing. The fields from the atlas for each level were extracted from the sub-domain (141E 151E 45S 37.5S). The data were horizontally interpolated onto the finer resolution model bathymetry. After this process, some coastal grid points still contained missing values. Extrapolation was carried out by replacing the missing values with an average of surrounding values. The fields were then interpolated onto the model sigma-coordinate grid. Temperature and salinity fields $\Re$ at any time of year were found using the following function as described by Ridgway and Dunn (2001).

$$\begin{aligned}\Re(\hat{\mathrm{X}},t) &= \overline{\Re}(\hat{\mathrm{X}}) + \cos_{ann}^{\Re}(\hat{\mathrm{X}})\cos(t) + \sin_{ann}^{\Re}(\hat{\mathrm{X}})\cos(t)\\ &+ \cos_{sa}^{\Re}(\hat{\mathrm{X}})\cos(2t) + \sin_{sa}^{\Re}(\hat{\mathrm{X}})\cos(2t)\end{aligned} \qquad (19)$$

where $\hat{\mathrm{X}}$ is a three dimensional position vector, $\overline{\Re}$ denotes means, $\cos_{ann}^{\Re}$ is annual cosine, $\sin_{ann}^{\Re}$ is annual sin, $\cos_{sa}^{\Re}$ is semi-annual cosine and $\sin_{sa}^{\Re}$ is semi-annual sine. Also, $t = 2\pi t_m/366$ and t_m is model decimal day of the year.

The data for $\overline{\Re}$, $\cos_{ann}^{\Re}$, $\sin_{ann}^{\Re}$, $\cos_{sa}^{\Re}$ and $\sin_{sa}^{\Re}$ are loaded into the model and equation 22 is used to evaluate the model density field at any time of year. Atlas fields are evaluated throughout the model run at every time step and output at the same intervals as model outputs, allowing direct comparison with values given by the atlas interpolated onto sigma-levels. Atlas fields are primarily used for initialization, boundary inflow properties and comparison. No nudging, sponges or data assimilation methods are used. Boundary inflows immediately mix atlas T-S values with model values in cells adjacent the boundaries. This can be seen in Chapter 4, where space and time averaged comparisons are made between atlas and model surface and bottom-layer temperatures, salinities and densities.

Atlas statistics for Bass Strait are presented for two different depth levels in Figures 3.6.3.1 and 3.6.3.2. The depth levels are surface-level (0 m) and 40 m. Both Figures show statistics of the data used to build $\overline{\Re}$.These are the number of data per 1^o cell, the weighted standard deviation (STD), the root mean squared of residuals (RMS) with respect to the spatial mean and the RMS of residuals with respect to the full temporal mapping.

Data for surface temperature in south-eastern Bass Strait has relatively high standard deviation of ~ 2.5^oC. Surface-level salinity has also has relatively high standard deviation of ~ 0.3 in the southern part of the Strait. Areas with high standard deviation arise from larger differences in individual values from mean values in a data set for a given area which is directly related to either variability in the data or insufficient data. Since the number of measurements is fairly uniform across the region, the data suggest variability in southern areas is higher relative to other areas. Slightly fewer observations were used at the depth of 40 m as seen in Figure 3.6.3. The standard deviation and the root mean squared of residuals are lower than encountered at the surface, reflecting less variability found at depth than at the surface.

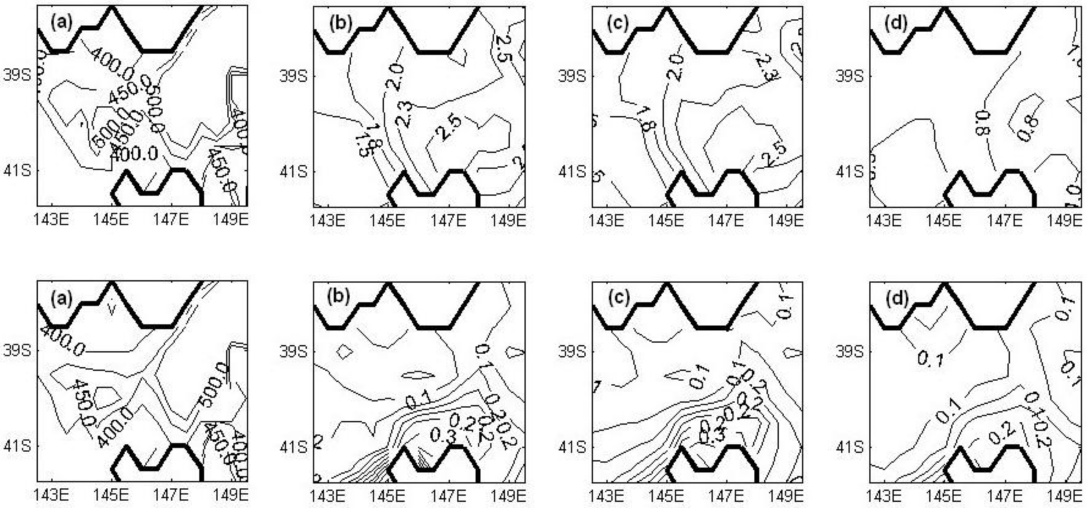

Figure 3.6.3 Atlas temperature (top row) and salinity (bottom row) data statistics at the surface. (a) number of data per 1^{o} cell. (b) weighted standard deviation. (c) root mean squared of residuals with respect to the spatial mean. (d) root mean squared of residuals with respect to full temporal mapping.

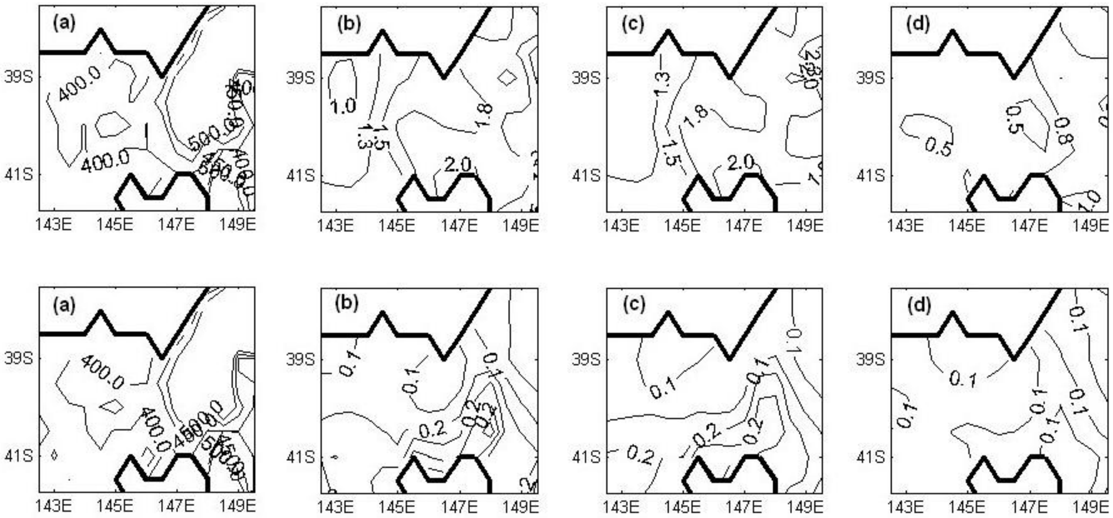

Figure 3.6.4. Same as for Figure 3.6.3 except for 40 m depth.

Figure 3.6.4 shows surface salinity in southern Bass Strait with standard deviation of ~ 0.3. This means that if the salinity data were distributed normally, 95.45% of data would fit within 2 standard deviations. This implies extreme values may vary ±0.6 about the mean. Similarly with surface temperature, extreme values may be expected to vary ±5 ^{o}C about the mean.

The spatial and temporal coverage of salinity data in the CARS2000 atlas is illustrated in Figure 3.6.5, where it can be seen around 100 observations per year occurred between 1950 and 1960, and a little more between 1980 and 2000.

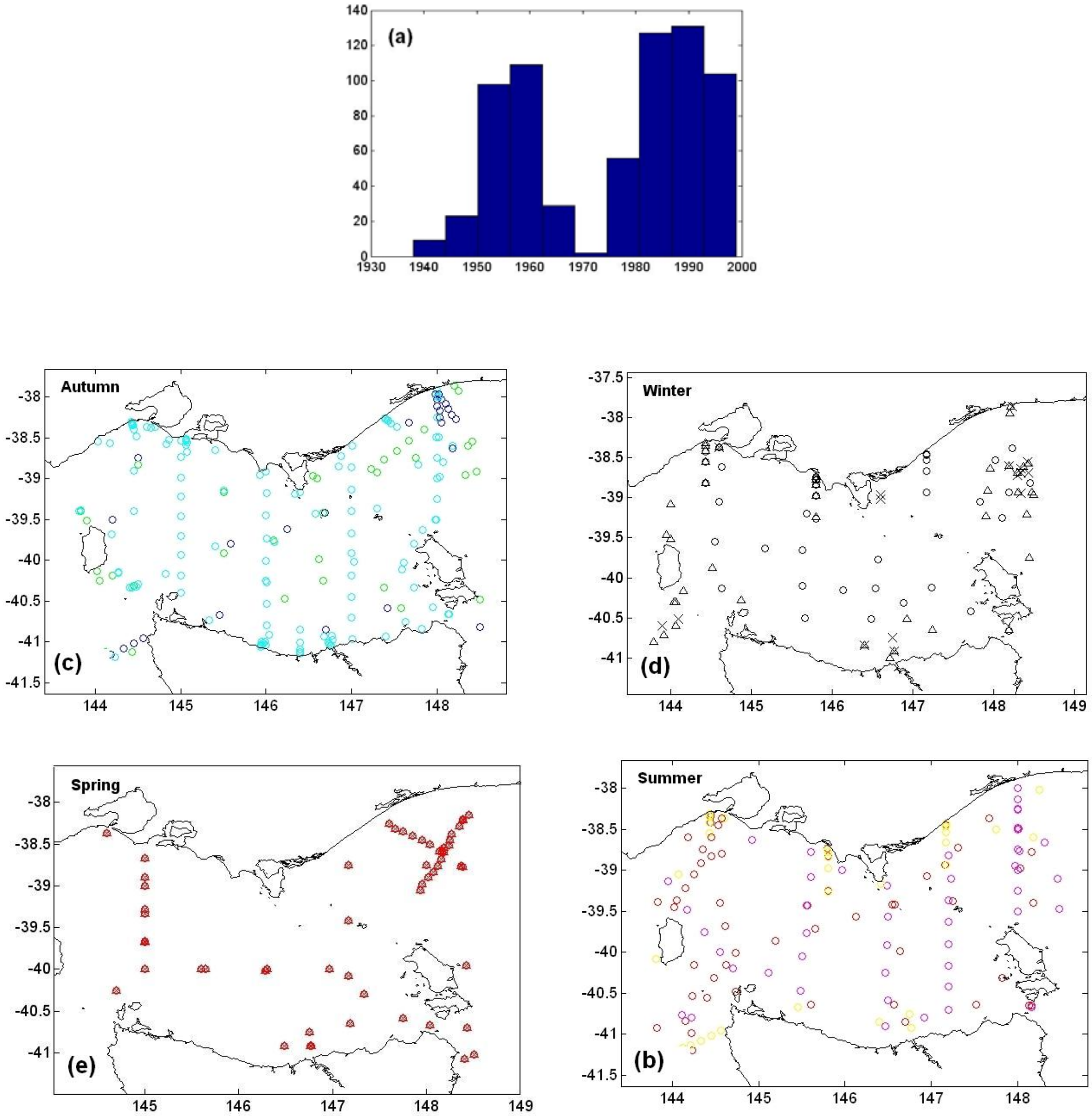

Figure 3.6.5. Number of salinity observations per year and spatial distribution of salinity observations, (b) Summer, (c) Autumn, (d) Winter (e) Spring.

Spatial coverage is lower in winter and spring, than in summer and autumn. This is illustrated in Figure 3.6.3.4(b)-(e). The total number of salinity observations in the CARS2000 atlas is 688.

3.7 CTD Observations

A collection of CTD based field observations of temperature and salinity in Bass Strait, taken on *RV Franklin* voyages FR198901, FR198908, FR198913, FR199101, FR199702, FR199711, FR199807 and FR199809, were provided by CSIRO Marine and Atmospheric Research in Hobart. These voyages took place between 1989 and 1998 in the months of May, June July, December and January. The data set contains 4150 observations from 98 CTD casts. 93 of these casts were in the Strait up to 120 m water depth. 5 casts were taken outside the Strait over the continental slope. Of these 5, 1 deep cast to 1302 m and 2 casts to 500 m were made on the western continental slope and 2 casts to 312 m and 268 m on the eastern slope. Observations from depths greater than 200 m are excluded from the analysis, except when shown on certain TS diagrams.

The analysis of this data is presented in section 4.7. Here, the spatial and temporal density of these observations is illustrated. Data are also presented on a TS diagram. This data is used to calculate a mean TS curve. The observations are then separated into either winter or summer groupings and depth-averaged spatial distributions of these groupings are found.

3.8 Underway Salinity Data

Underway salinity data from *RV Franklin* voyage FR199104 was obtained from CSIRO Marine and Atmospheric Research. This voyage took place between the 2nd and 23rd of May 1991 as part of the Trace Elements and Organic Pollutants 1989-1993 project. Data were collected continuously along the ship track with the underway Thermosalinograph which are recorded at or averaged over 5 minute intervals. A spatial distribution is derived using this data and presented later in the thesis.

3.9 Current Meter Mooring Data

Whilst this project was underway, observations from current meter moorings within in the interior confines of the Strait were not available, however, two surveys were made in between January 1991 and the late autumn/early winter months of 1991 which provide observations made in various locations at the Strait entrances. The surveys were M-BASS-CS91 from the Bass Strait Interdisciplinary Study (CSIRO) and M-BASS-UN91 from the Bass Strait Low Frequency Circulation Study (UNSW) 1991. All measurements were made with Aanderaa RCM 4/5 current meters. Data were acquired from CSIRO Marine and Atmospheric Research via the MARLIN website and compiled into a single database containing all records. A toolbox in Matlab was designed to interactively analyse, visualize and query this database. Not all mooring locations provided continuous recordings for the period of deployment. Comparison of model currents with all mooring observations is beyond this project, so comparison is made between current observations at selected locations and depths. The locations chosen for comparison are off Cape Otway, off Stokes Point, in Banks Strait and off Lakes Entrance. These locations are chosen because they occur in the vicinity of the Strait entrances. At these locations, frequency distributions of current magnitudes and directions are compared with model predictions. The observations at these locations are made at particular depths. For comparison, model data is interpolated to the depth at which the observation is made. Analyses of the results are found in section 4.3.

3.10 Coastal-Trapped Wave Forcing

Residual sea-level at the entrances and in adjacent shelf areas is important for low frequency variation in currents in Bass Strait (Cirano, 2004; Middleton and Black, 1994). Along the southern Australian shelves, mode 1 CTWs with amplitude around 10 cm and period around 10 days have been shown to account for a significant amount of the variance in the observed shelf circulation off south-eastern Australia (Church et al., 1986). Modelling studies suggest incident CTWs are scattered at the western entrance of the Strait (Middleton, 1994). The long-term residual effect of incident CTWs on circulation in Bass Strait is still unclear. A preliminary investigation is carried out to test the importance of CTW forcing on residual water mass transport using tracer in relatively long-term model simulations. A barotropic frictionless Kelvin wave propagating along the coast (Ruddick, 1995) was prescribed along the western open-sea boundary with a decay scale given by the external Rossby radius. This can be written as

$$\eta_{CTW}(y,t) = A_{CTW} e^{-fy/\sqrt{gh}} \cos(2\pi t/T_{CTW}) \qquad (20)$$

where η = sea-level, A is amplitude at the coast, g is gravitational acceleration, h is undisturbed water depth, T is wave period, t is time, f is the Coriolis parameter and y is a distance measure. The signal amplitudes A_{CTW} and period T_{CTW} were chosen to be 10 cm and 10 days respectively. This function is used to generate boundary forcing similar amplitude and frequency to observed coastal-trapped waves. A 1 year experiment was carried out using this forcing as a sensitivity study.

In a second CTW experiment, observed hourly adjusted residual sea-level from an NTC station at Portland in Victoria for the year 2004 is used to generate the open-boundary forcing. This signal contains coastal-trapped waves and local wind forced variation, however, the tides and inverse barometer effect have been filtered out. This is filtered further with a 5-day low-pass filter (see Figure 4.2.1). The data from this signal is used for A^{CTW}. In this case, eqn. 22 is modified by dropping the cosine term, since time variation is implicit in the data.

3.11 Regional Current Forcing

During the course of the project it was found that if a signal representing the seasonal South Australian Current inflow was not included on the western open boundary, the salinity in Bass Strait would stabilize at lower levels (~0.2-0.5) compared with observations. A simple parameterization for seasonal variation in regional current inflows is adopted in particular experiments. The shape of residual boundary sea-level representing regional current inflow is estimated using an equation similar to eqn. 20. For the SAC, an annual rise and fall of residual sea-level from zero in summer to maximum A^{SAC} in winter is prescribed in the northern part of the model western open boundary. The following equation is the function used to create the time varying exponentially shaped surface.

$$\eta(y,t) = Ae^{-fy/\sqrt{gh}} \sin(\pi t/T_{YE}) \qquad (21)$$

Apart from other previously described quantities, T_{YE} is 365 days. The residual sea-level along the open-sea boundary is set to increase in height towards the shelf break and become constant over the shelf.

As with the SAC, the EAC was not a seasonal feature of the model solutions unless treatment of a boundary condition for it was prescribed in the model. To test the seasonal effect of the EAC in the model, residual sea-level was set to rise, in the summer season, towards the north-eastern model boundary along both open boundaries, with the last 6 grid points being constant. The residual sea-level attains maximum values in summer and is zero in winter. Experiments were carried out with different weightings of both SAC and EAC signals to see how water mass is affected in the model domain. The final maximum amplitudes for the parameters A^{SAC} and A^{EAC}, used in the reference simulation, were 0.12 cm and 0.3 cm respectively. These were largely determined based on adjustments aimed at achieving annual-mean water properties of open-ocean waters in the model domain closer to those given by the CARS2000 atlas, rather than from a complete analysis of historical sea-level data.

The use of this method in a non-nested regional model was necessary to drive the far-field effects, which are generated outside the model domain. These play a role at in the region at the seasonal scale. The method is also useful in testing the sensitivity of water mass properties in the region to the far-field effects, which is done in Chapter 5.

CHAPTER 4:
Results & Analysis

4.1 Atmospheric Climatology

This section begins with a brief analysis of high frequency wind data (hourly observations) from Cape Grim Baseline Air Pollution Station to establish a guide to seasonal trends and long-term means from a ground based observation station. After this, the atmospheric surface forcing climatology used in the model is presented and discussed.

The analysis of CGBAPS wind magnitude and direction data from a time series spanning 1993-2003 is shown in Figure 4.1.1. Direction is given in degrees azimuth (the angle the wind vector makes with respect to north in a clockwise sense). The filtered signal has mean magnitude 4.1 m/s and direction 49.8^o (Az). Monthly means shown in (Fig 4.1.1(e) and 4.1.1(f)) illustrate that in this decade strongest mean winds have occurred in late spring and weakest in early summer/late autumn. Mean direction has shifted from predominately south-westerly in late summer to slightly north-westerly in winter. Winds have been mainly south-westerly through spring and shifted back to mainly southerly in late spring/early summer.

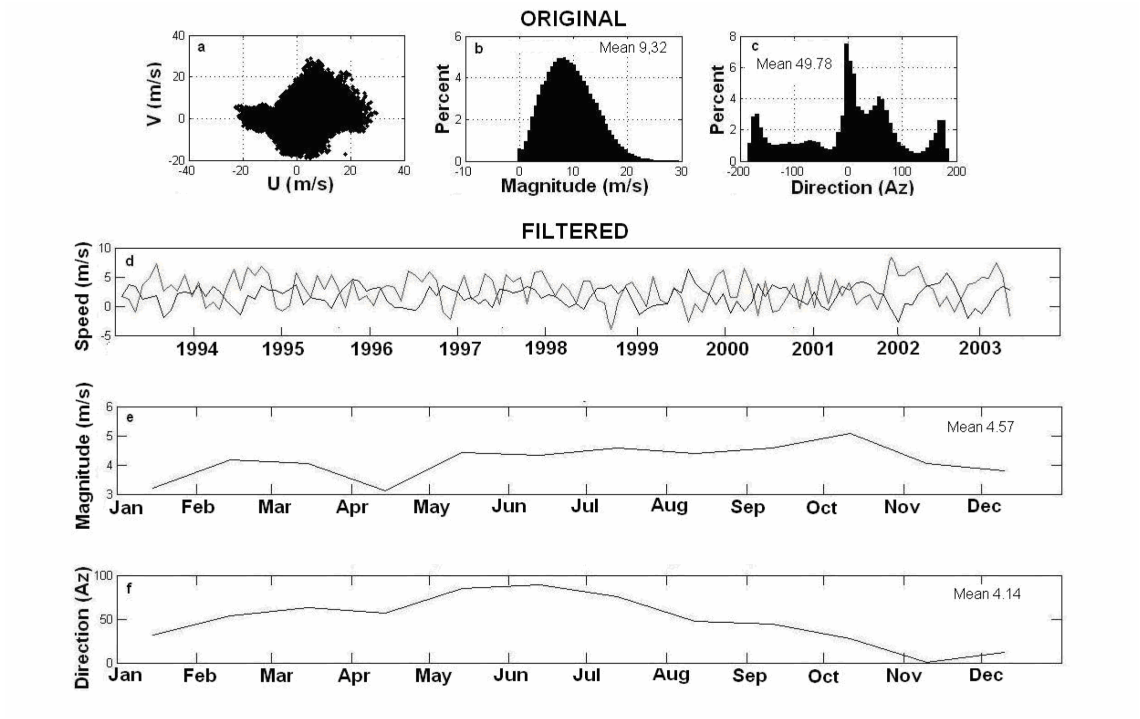

Figure 4.1.1. Analysis of wind data, for the period 1993 to 2003, from Cape Grim Baseline Air Pollution Station, Tasmania. (a) scattergram of u and v components of original data, (b) magnitude frequency distribution of original data, (c) direction frequency distribution of original data, (d) filtered time series of components u (red) v (black), (e) monthly-mean magnitude (m/s), (f) monthly-mean direction (Az).

A progressive vector diagram, also using the hourly wind statistic, from an earlier wind data set from CGBAPS illustrates seasonal variation in wind strength and direction (Figure 4.1.1). The labels are marked on the 1st of January for each successive year. The diagram illustrates the trend from southerly winds in the first half of the year to westerly for the remainder. Longer distances indicate stronger mean winds. For example, the stronger mean wind years occurred between 1990 and 1992. The year 1991, however, had less seasonal variation in direction of the mean winds. The winter-spring period of 1988 has the strongest mean westerly winds.

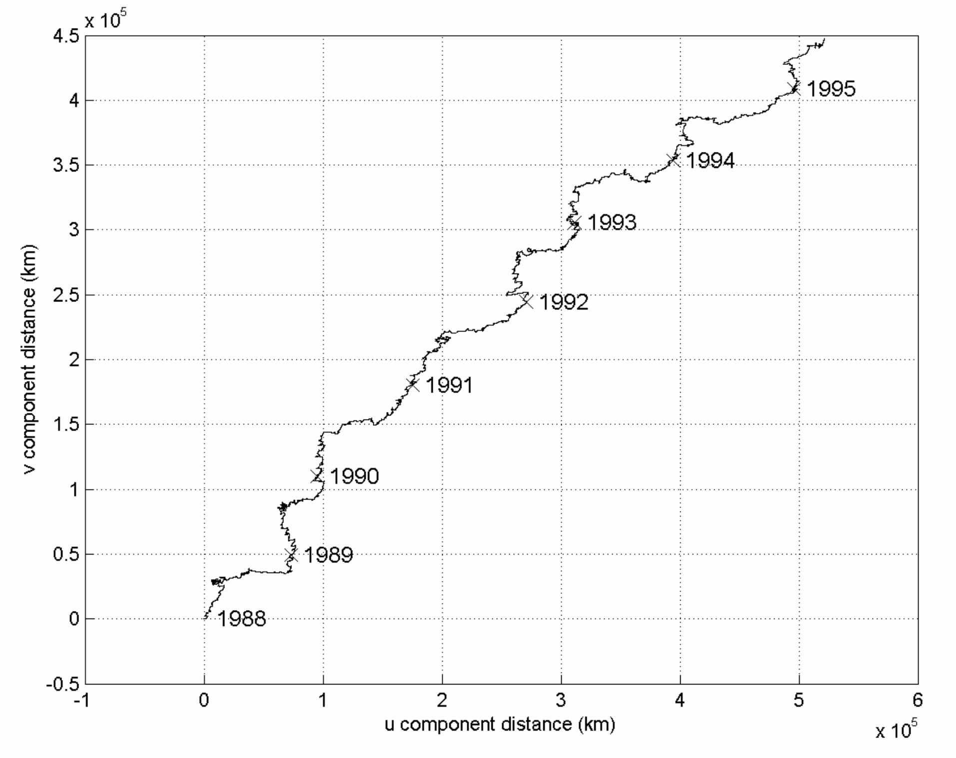

Figure 4.1.2. Progressive vector diagram of hourly wind data, for the period 1988 to 1995, from Cape Grim Baseline Air Pollution Station, Tasmania.

The Hellerman-Rosenstein (HR) monthly long-term wind vectors and speeds are shown in Figure 4.1.3. The components λ and φ of this data were converted from wind stress to speed with the following

$$u_{\lambda,\phi} = \sqrt{\frac{\tau_{\lambda,\phi}}{\rho_a c_d}} \tag{22}$$

with standard values of $\rho_a = 1.2$ kg m^{-3} and $c_d = 0.0013$.

This data presents a pattern of southerly to south-westerly winds from October to March and predominately westerly winds from April to September with a range of variation in wind speed of about 2.5 m s^{-1}. There is generally an increasing equatorward meridional gradient in summer and an increasing poleward meridional gradient in winter. HR winds are considered to overestimate the wind stress (M. Tomczak. personal comm.). They are used in a sensitivity study as a guide to an (unrealistic) upper limit for mean transport in the model.

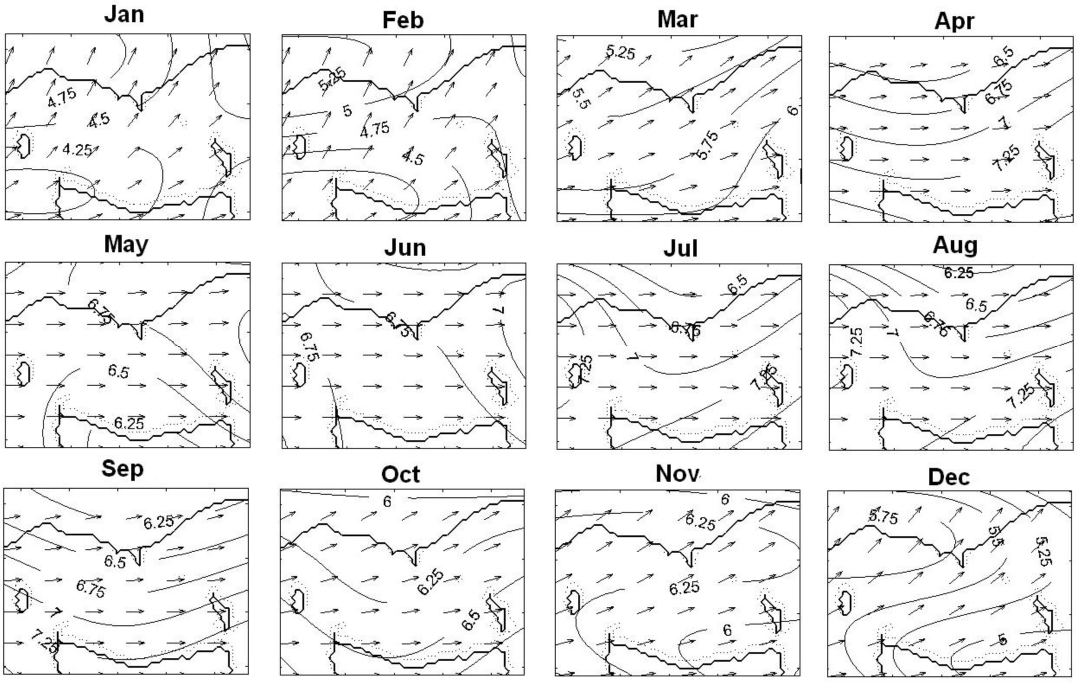

Figure 4.1.3. Monthly averaged surface winds (m s^{-1}) from Hellerman-Rosenstein.

Long-term monthly mean NCEP-reanalysis wind fields, derived from u and v components, are shown in Figure 4.1.4. These are based on a record from 1968-1998. Seasonal differences are immediately evident. The summer climate-averaged winds show a dominant southerly component. Autumn winds show a swing from south-west in March to north-west in April. May, June and July are dominated by north-westerlies with increasing strength in July and August. September to October winds show diminishing strength with a dominant westerly pattern. Continual weakening occurs from November through December with the dominant southerly component returning. According to this data the weakest winds in Bass Strait occur in March and the Strongest in July.

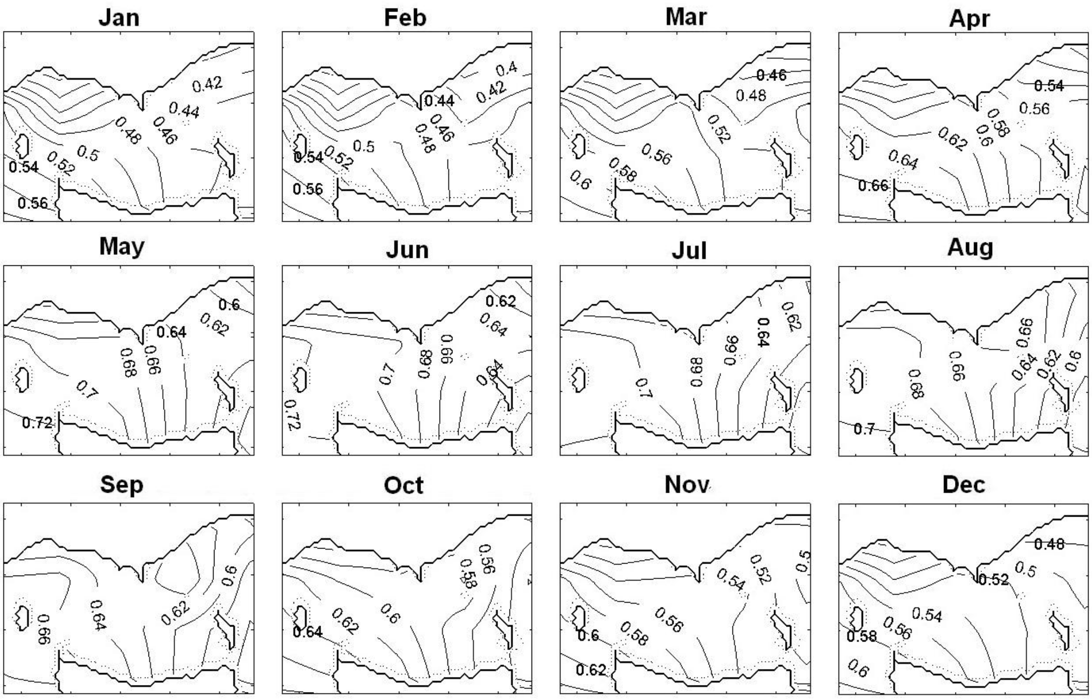

Figure 4.1.4. Monthly averaged surface winds (m s^{-1}) from NCEP reanalysis monthly long-term means.

NCEP reanalysis monthly long-term wind speeds for the region are shown in Figure 4.1.5. The long term monthly mean wind speeds are not calculated from the square root of the sum of the squares of the monthly long term u and v wind components. It can be seen that values of the former are about half of the latter. The wind component means are calculated from daily u and v means whereas the wind speeds are calculated from daily wind speed means which are summed and averaged for each month. After this both data sets average the months over the period of the long term record. Naturally, the different averaging methods yield different results. NCEP wind components are not suitable to drive the heat fluxes because averaging has smoothed out variation which influences them. Using this data to force the heat fluxes in the model leads to excessive overheating. It was found that if NCEP wind speeds were used to drive the heat fluxes and NCEP wind components the momentum fluxes a reasonable result for seasonal thermal variation was obtained.

Climate-averaged surface air temperatures from the NCEP reanalysis data set show a dominant meridional gradient for most months (Figure 4.1.6). In summer, this gradient is strongest and temperatures decrease poleward across the Strait from around 18°C to 15°C. January and February temperatures are similar. March through to August sees a decrease in temperatures to ~ 11°C with a lessening of spatial gradients. Gradual warming of about a degree per month in the central region from September through to January occurs. Maximum air temperatures occur in January and minimums occur in July. The annual range of variation is around 5°C.

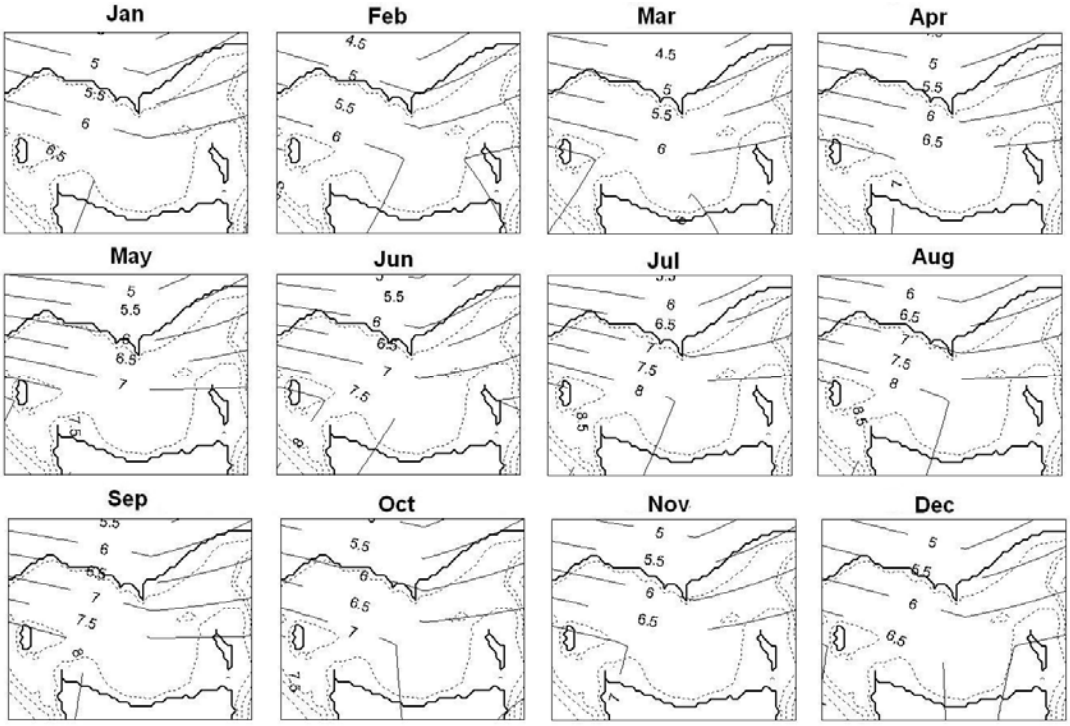

Figure 4.1.5. Monthly averaged surface wind speeds (m s^{-1}) from NCEP reanalysis monthly long-term means.

Monthly averaged cloudiness data from AOMIP suggests cloudiness in the Strait interior increases from lowest values in January and February of about 48% to maximum values in May, June and July of around 68% (Figure 4.1.7).

Long term monthly mean relative humidities have the least seasonal variation of the atmospheric variables presented (Figure 4.1.8). There is a slight increase of up to ~5% over the winter months and a lessening of the meridional spatial gradient seen in other seasons. The annual average relative humidity in the Strait interior is around 77% and the annual range is ~2%.

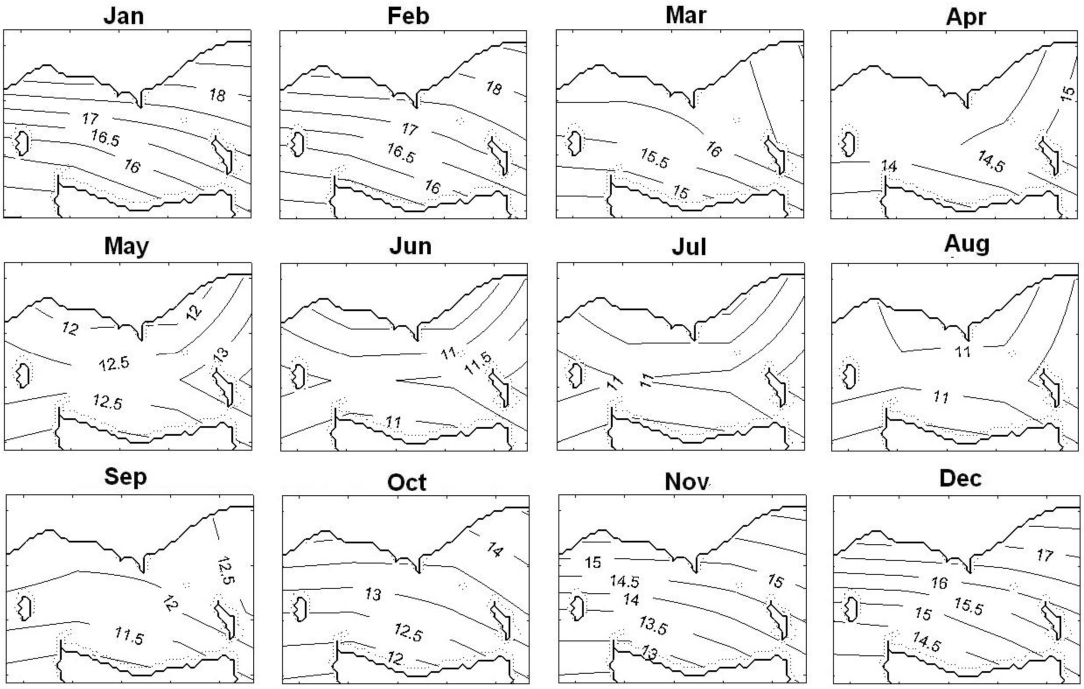

Figure 4.1.6. Monthly averaged surface air temperatures (^{o}C) from NCEP reanalysis monthly long-term means.

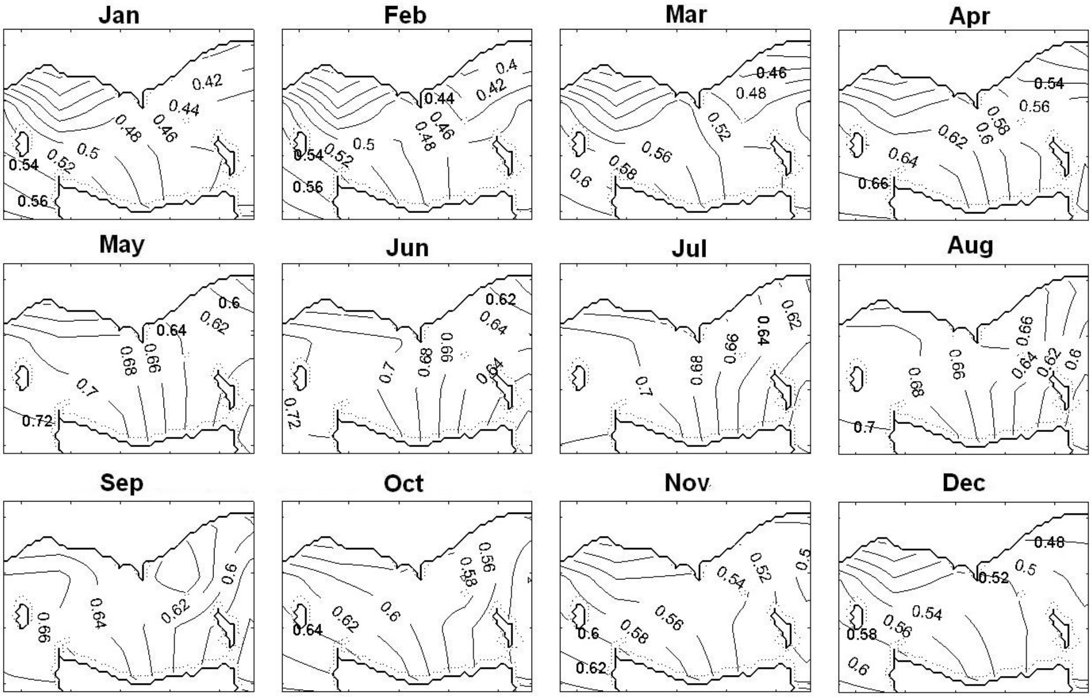

Figure 4.1.7. Monthly averaged cloudiness (fraction) from AOMIP.

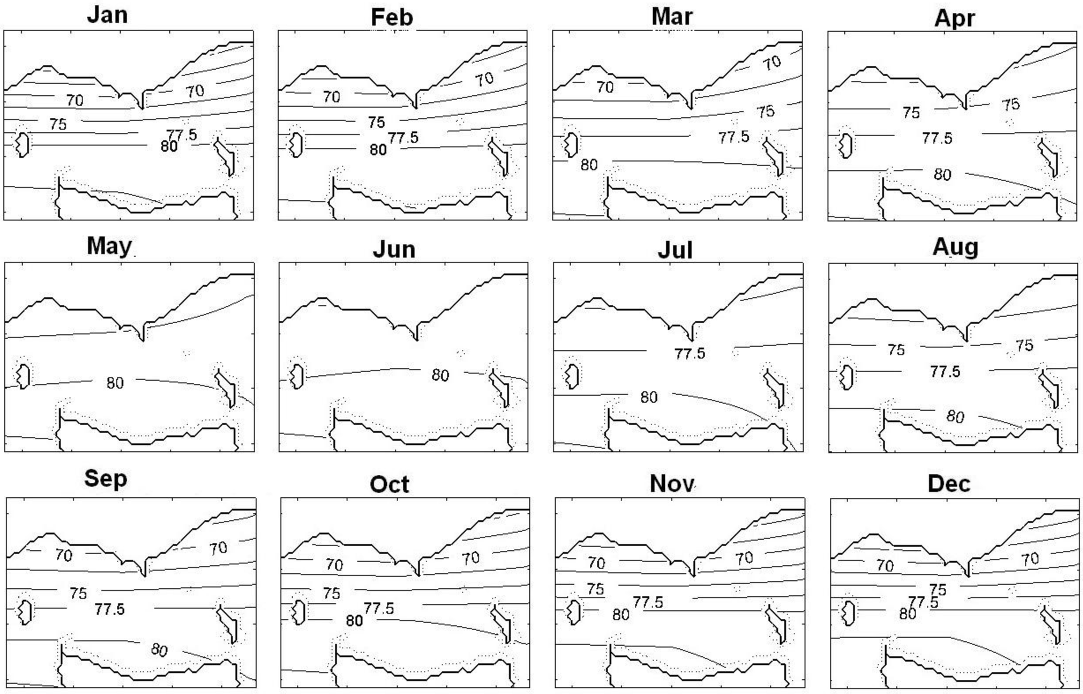

Figure 4.1.8. Monthly averaged relative humidity (%) from NCEP reanalysis monthly long-term means.

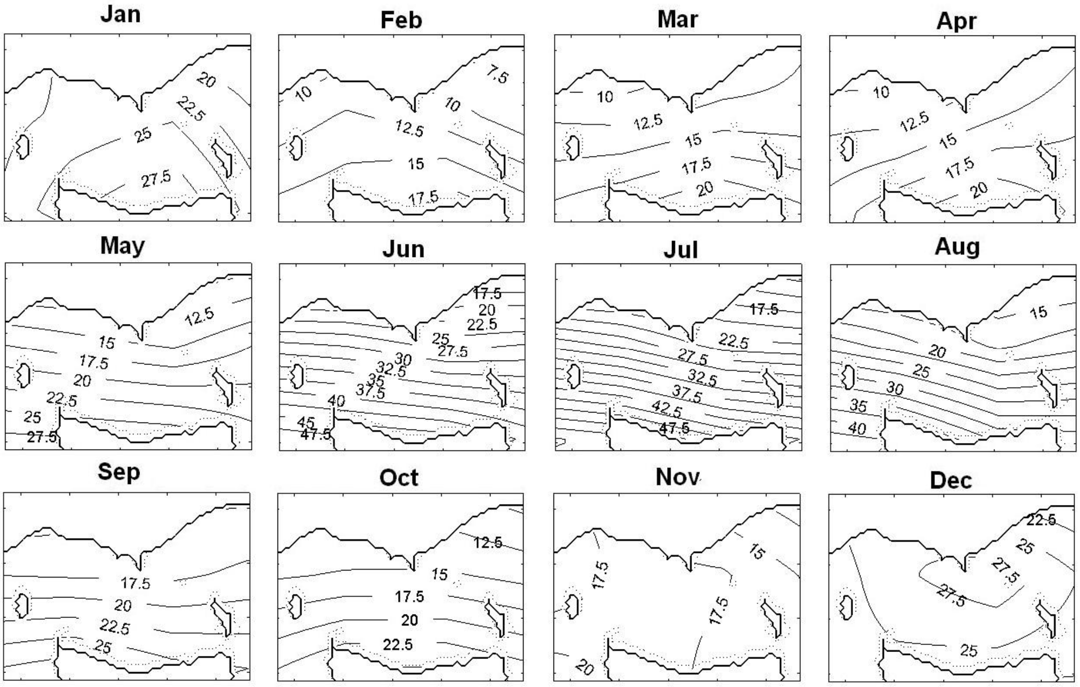

Figure 4.1.9. Monthly averaged precipitation (10^{-6} kg m^{-2} s^{-1}) from NCEP reanalysis monthly long term means.

Precipitation data is presented in Figure 4.1.9 in units of 10^{-6} kg m^{-2} s^{-1}. The inter-annual cycle of variation follows the southern hemisphere subtropical climate wet winter – dry summer cycle. Precipitation rates over the sea are smallest in February and largest in July. During most months of the year, except for November, December and January, a pronounced meridional gradient exists with increasing poleward values.

4.2 Model Tides

Harmonic analysis was carried out to find model co-amplitudes and co-phases for the four main tidal constituents (Figure 4.2.1). These can be compared with co-tidal charts presented in Fig 2.3.1.

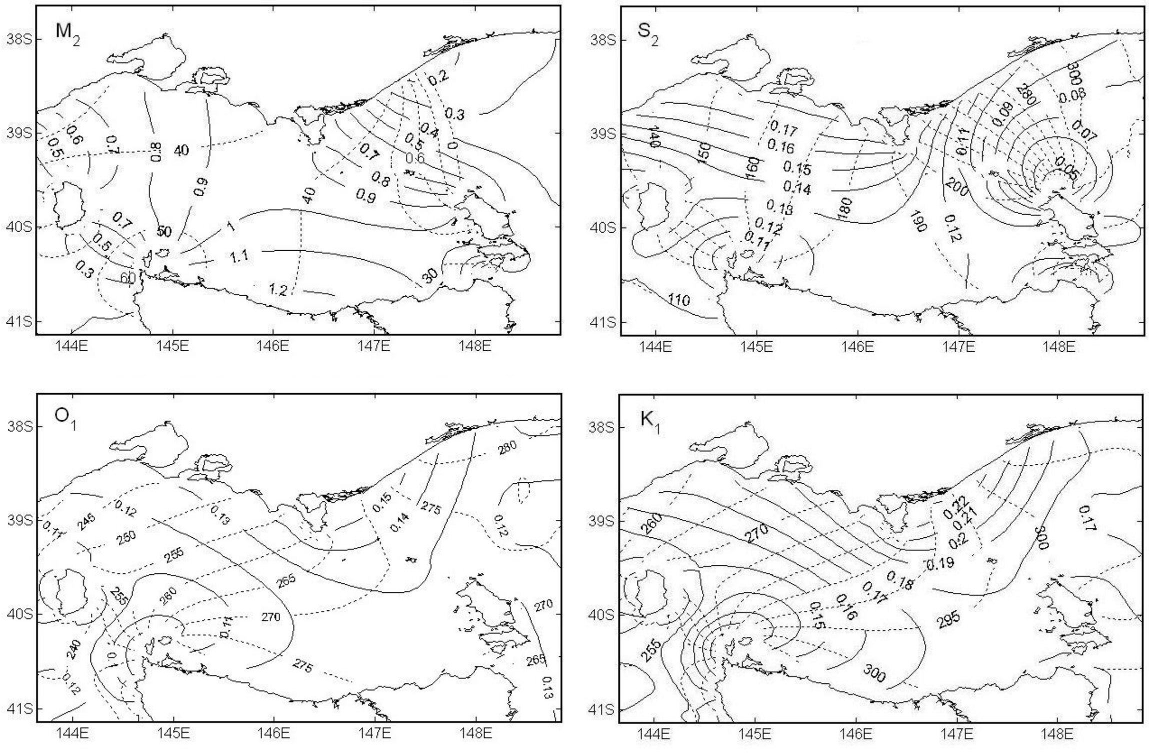

Figure 4.2.1. Model co-amplitudes (m) and co-phases (degrees relative to UTC) for the **(a)** M_2, **(b)** S_2, **(c)** O_1 and **(d)** K_1 tidal constituents.

The co-amplitudes and co-phases for the dominant M_2 semidiurnal tide and the O_1 and K_1 diurnal constituents are in agreement with NTC predictions and previous studies (Fandry et al., 1985; McIntosh and Bennett, 1984), with relative errors between ~ 3-8%. Model M_2 and S_2 amplitudes are approximately between 5-8% larger than NTC data. Model O_1 amplitudes are up to 10% different in the area east of Wilsons

Promontory, but they show less difference in other areas. Model K_1 amplitudes exhibit a difference of less than 5% from NTC data. Phases of the tidal constituents are also in agreement with only 5-8^o difference occurring between model and NTC data. The model resolves the locations of virtual amphidromic points, which are a feature of the tides in the region, in agreement with NTC predictions and previous studies. All main constituents exhibit a virtual amphidromic point near Cape Grim in north-western Tasmania. The M_2 tide has a virtual amphidromic point at about 147.5^{o}E, 38^{o}S near Lakes Entrance in south-eastern Victoria. The S_2 tide has a virtual amphidromic point at the northern end of Flinders Island.

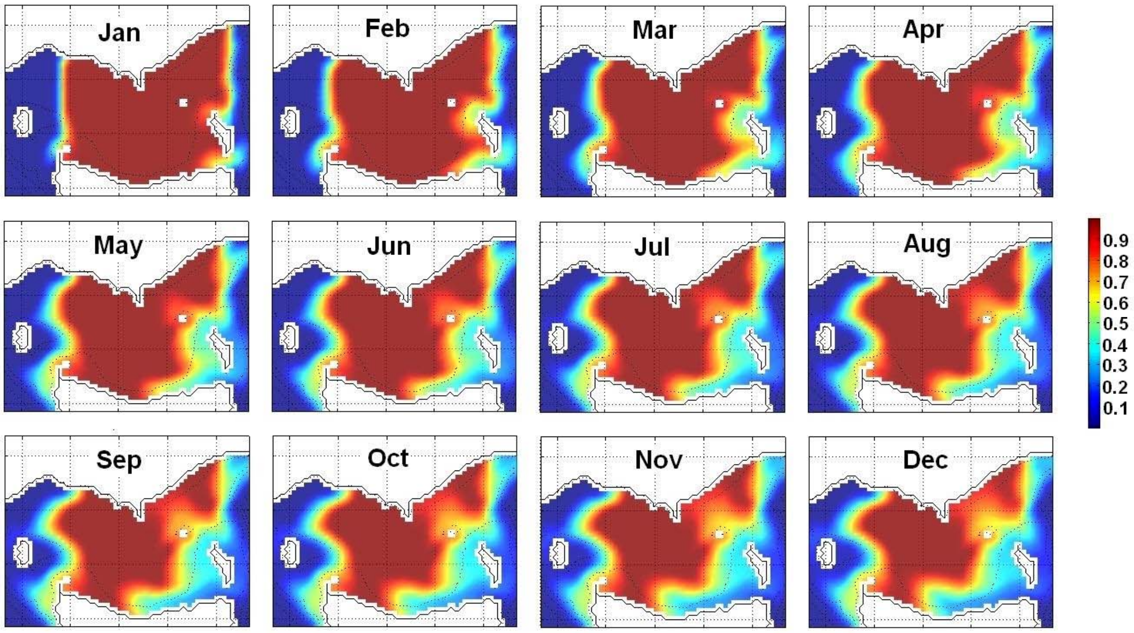

Figure 4.2.2. Monthly mean surface-layer tracer concentration resulting from tidal residual motion.

An example of the effect of tidal residual currents, mapped out with monthly mean surface-layer tracer concentration, is given in Figure 4.2.2. The initial conditions involved filling the control region, shown in Figure 1.3.1, with conservative tracer at unit concentration. After one year, the model predicts little residual flow resulting from the tides. Over 2/3 of the original tracer mass is still present in the Strait interior. Over long periods of time tidal mixing erodes the edges of the initial tracer concentration field. The effect is more pronounced in eastern Bass Strait, in particular in Banks Strait. Westward residual motion due to tidal forcing is most apparent in this area. This could possibly be explained by the fact that the dominant M_2 tidal wave at the eastern Strait entrance has about twice the amplitude than that at the western Strait entrance and in Banks Strait a topographic convergence produces the strongest tidal currents in the domain.

4.3 Current Comparisons at Selected Locations and Depths

Current meter mooring data, as described in section 3.8, and model currents are analysed and compared in the following diagrams. The geographic locations and corresponding depths where the comparisons are made are indicated in Figure 4.3.1. The locations were selected due to their proximity to the ends of the Strait entrances so that an estimate of the long-term (seasonal scale) mean current could be made. Agreement at depth was generally better than close to the surface.

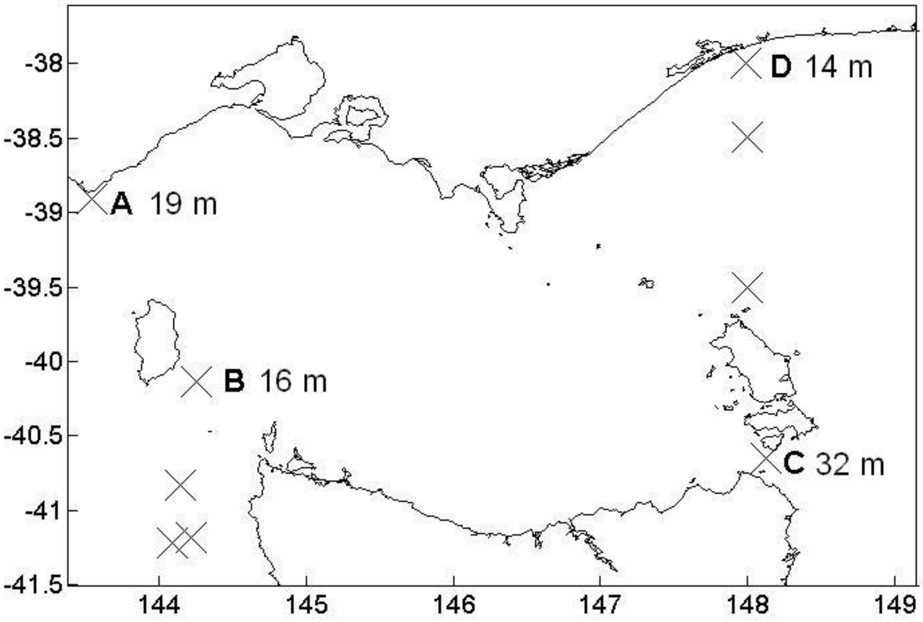

Figure 4.3.1. Locations A, B, C and D denote where current meter mooring data is used for comparison with the model.

The model is not expected to reproduce the observations, but rather to be in agreement with basic characteristics. The model has specific variation induced by tidal forcing, mean winds and regional currents which is aimed at representing the mean (seasonal scale) background circulation. The observations relate to a specific period in time in which a unique combination of natural forces produced the currents. This means that the character of the model and observations can only be compared for the basic average features.

A-Cape Otway

Model and observed current data from a location offshore from Cape Otway in Victoria, at 19 m water depth are compared in Figure 4.3.2. A significant number of the data have a distribution in a specific range of magnitude (~10-50 cm/s) and direction. The model's tidal current range at this location is approximately similar to the observed signal. The mean current at this location in the model (29.95 cm/s) is marginally weaker than the observed mean current (32.05 cm/s). The difference in mean current direction (Az) is ~ 12^{o}.

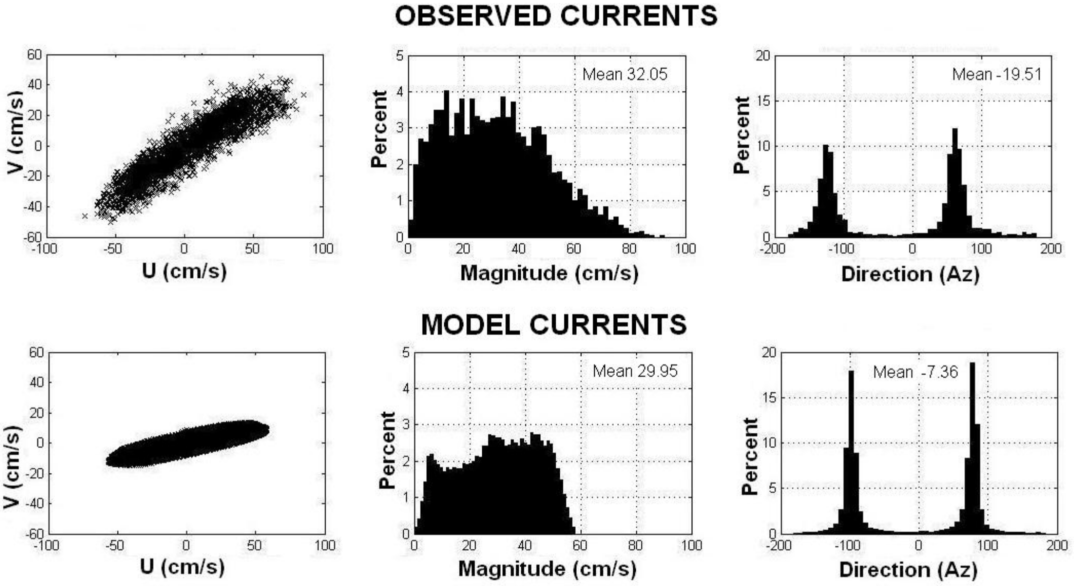

Figure 4.3.2. Comparison of model and mooring data at location A.

B-Stokes Point

The predicted currents southeast from Stokes Point which is located on the southern end of King Island, at 16 m water depth, have mean magnitude which is very close to the observed signal, with just under 1 cm/s difference (Figure 4.2.3). The difference in mean direction is between 14-15^{o}.

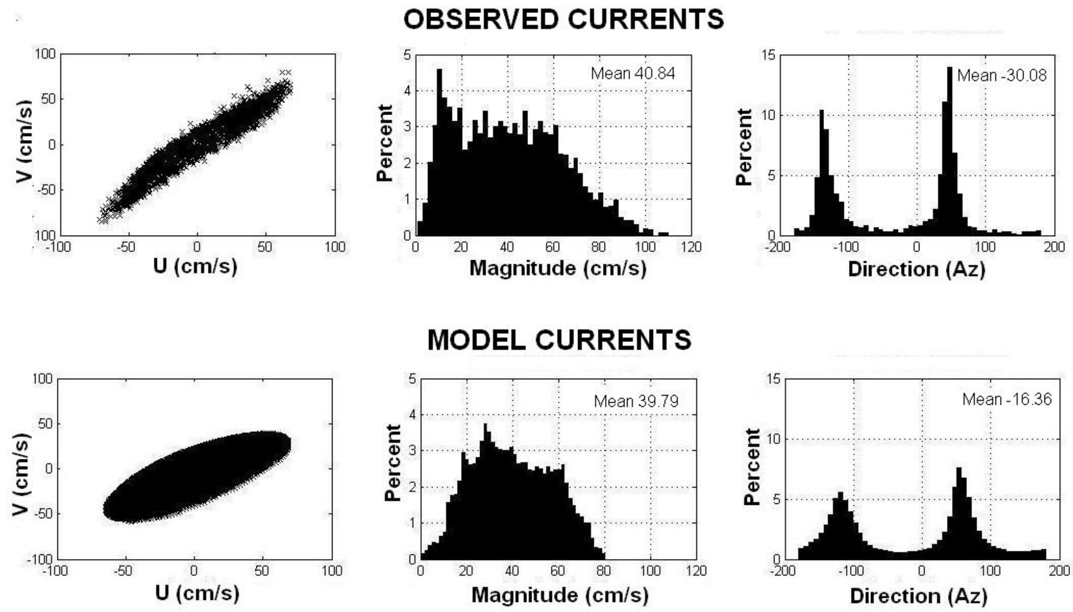

Figure 4.3.3. Comparison of model and mooring data at location B.

C-Banks Strait

Predicted currents in Banks Strait, at 32 m water depth, have mean magnitude which is larger than the observed signal, with a difference of 13-14 cm/s (Figure 4.2.4). The variation in mean direction is within 2°.

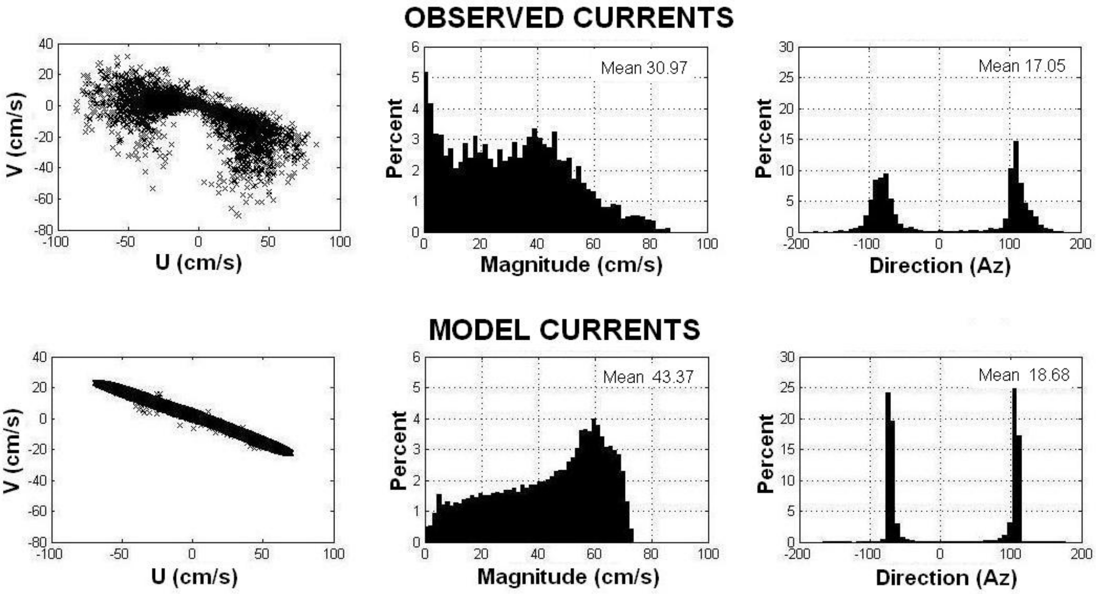

Figure 4.3.4. Comparison of model and mooring data at location C.

D-Lakes Entrance

Predicted currents offshore from Lakes Entrance in Victoria, at 14 m water depth, are in favourable agreement with observed currents (Figure 4.3.5). Although the simulated model tidal range at this location is less than the observed signal by ~ 10 cm, the overall mean magnitudes are within 2 cm/s of each other and the mean directions are within 10^o of each other.

Differences at all locations

The main reasons for the differences at all locations are:

1. The model does not resolve local topographic steering and topographically induced eddies which could be important in defining the local current.
2. Observed data contains natural variability on a wide range of timescales and measurement related errors. The model contains only tidal and low frequency variation with errors mainly coming from uncertainty in forcing data and initial and boundary conditions.
3. The locations in the model suffer from interpolation errors in their geographic locations.
4. The model bathymetry is smoothed, which also reduces local variation.

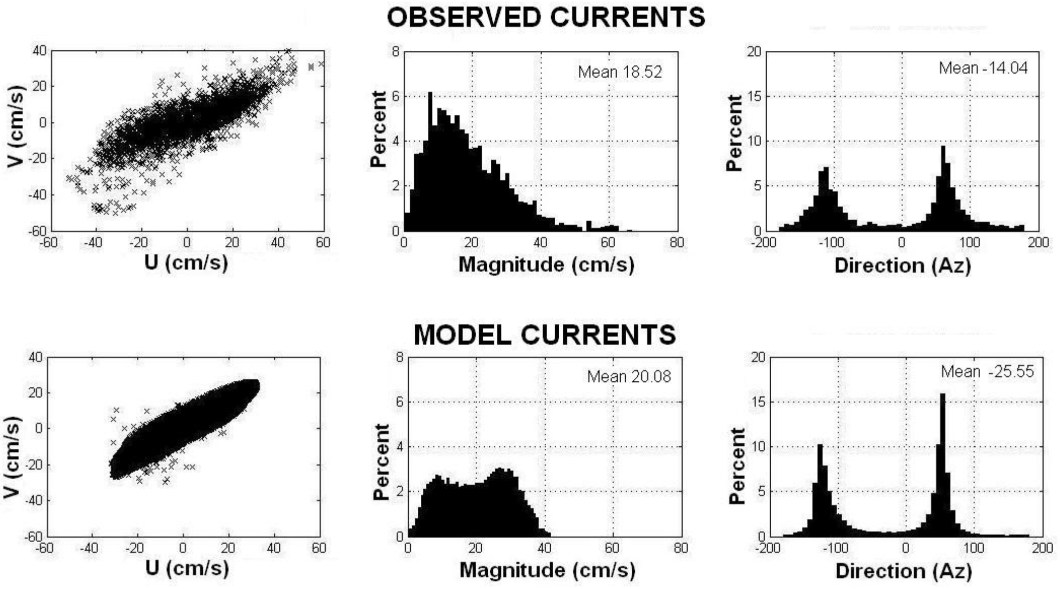

Figure 4.3.5. Comparison of model and mooring data at location D.

4.4 CTD And Underway Observations.

CTD observations described in section 3.7 are presented in this section. The locations of the observations are shown in Figure 4.4.1. They were limited to the northern half of the Strait and to summer and winter only. The data obviously doesn't resolve the entire region well in terms of its climatology. It is useful, however, as a guide to seasonal maxima and minima and the character of water mass properties in the region.

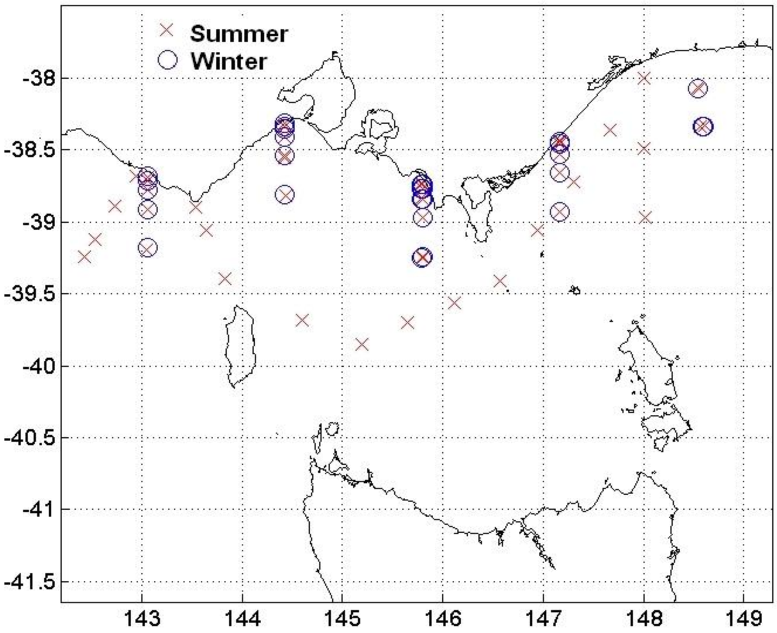

Figure 4.4.1. Locations of CTD casts. (circles-winter, crosses-summer).

The timing of these observations in terms of the seasons is presented in Figure 4.4.2. It shows that time data density is low. The observed ranges are also apparent. Maximum salinities of ~ 35.85 tend to coincide with maximum temperatures of ~ 20^{o}C in late January, however, cooler (~14^{o}C) relatively high salinity (35.78) water has also been observed. A similar maximum temperature was observed in mid-December, but this was not associated with relatively high salinity as in late January. Salinity less than 35.18 and temperature less than 11.8^{o}C is not observed at depths less than 200 m. It is clear from Figure 4.4.2 that there are a majority of months where there is insufficient CTD data to resolve the seasonal cycle adequately for northern Bass Strait.

A TS diagram of all CTD data (4150 TS points), including several deep casts in open ocean areas near Bass Strait, is presented in Figure 4.4.3. The dashed line is a

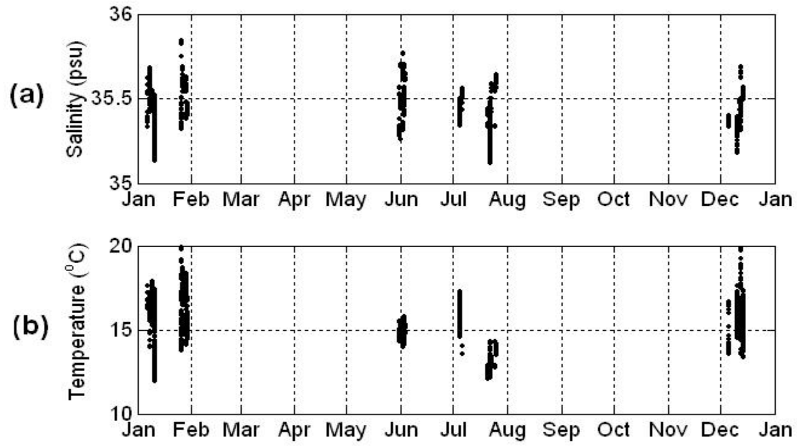

Figure 4.4.2. Timing of CTD observations for (a) salinity and (b) temperature.

mean TS curve for this distribution. The majority of casts, which are in northern Bass Strait, show water with temperatures ranging between ~ 12 and ~20 °C and salinities ranging between ~ 35.2 and ~35.85 .

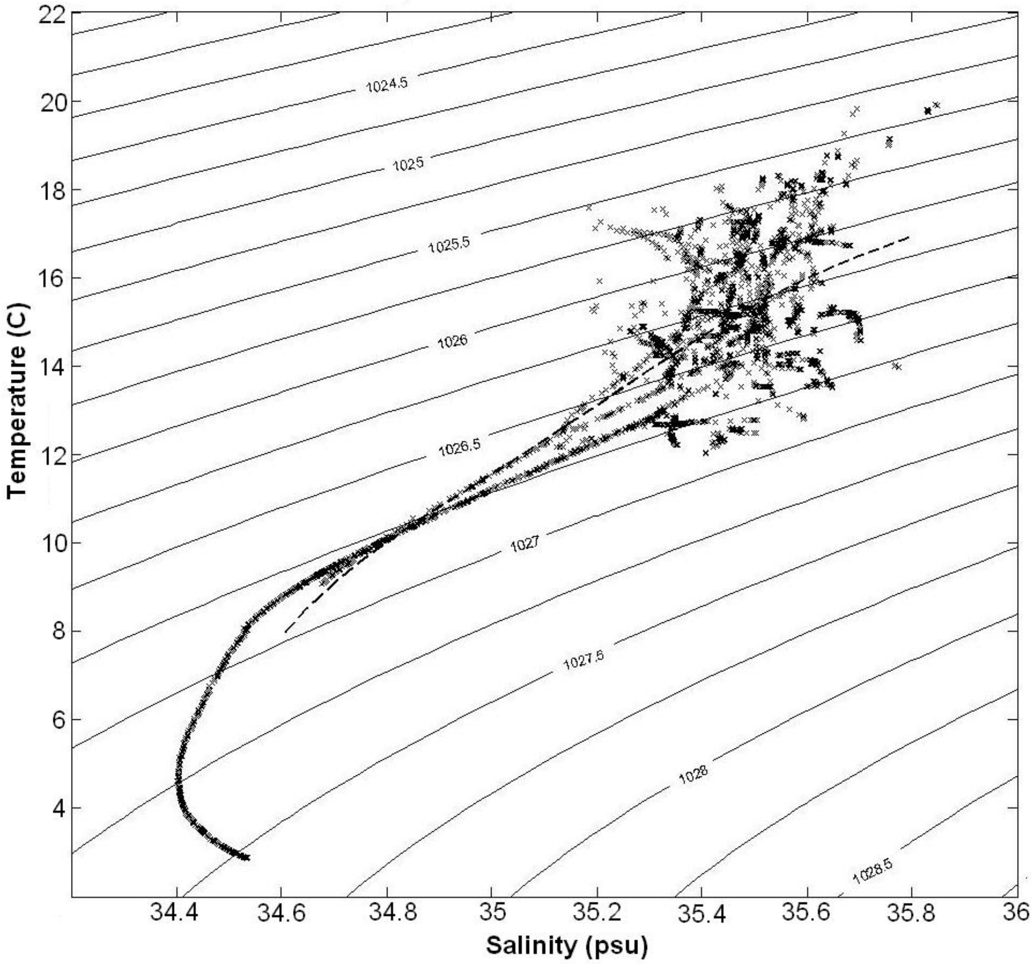

Figure 4.4.3. TS diagram of CTD observations.

The apparent tracks of data in many cases are individual CTD casts.

Several of the casts detect sub-Antarctic Surface Water in waters deeper than 200 m outside the Strait. This is characterised as being fresher and usually cooler than Bass Strait Water. The deepest cast (1350 m) reveals Antarctic Intermediate Water, with its characteristic salinity minimum of around 34.4.

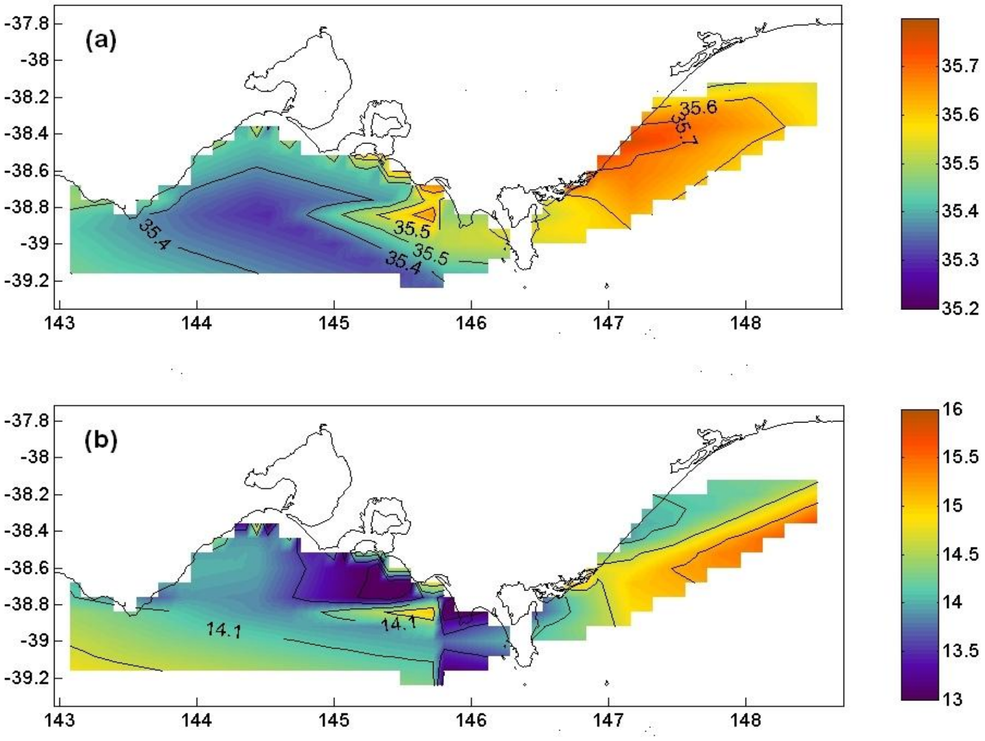

Figure 4.4.4. Winter depth-averaged (a) salinity and (b) temperature (^{o}C) from CTD observations.

The spatial distribution of winter depth-averaged temperature and salinity, from CTD data sampled at less than 200 m depth is shown in Figure 4.4.4. Despite low spatial resolution of this data, and potential biasing in the analysis, it is still clear that salinities observed at the eastern side are up to 0.4 higher than the western side. The temperature distribution shows colder waters (~13.4^{o}C) in shallow coastal areas between Port Phillip Bay and Wilsons Promontory, and warmer water (~15.5^{o}C) to the east.

Figure 4.4.5 illustrates the spatial distribution of summer depth-averaged temperature and salinity from the CTD data. Despite limitations in the data for this type of analysis, there is improved coverage compared to winter. A broad area of salinities >

35.5 can be seen extending from Port Phillip Bay to Lakes Entrance and southwards towards in the south-eastern area of the Strait. Temperatures appear to be up to several degrees higher in the shallower regions (< 50 m) adjacent Victoria. The areas of relatively higher salinity suggest evaporation in summer in the northern parts of the Strait plays a role in increasing the salinity of Strait waters.

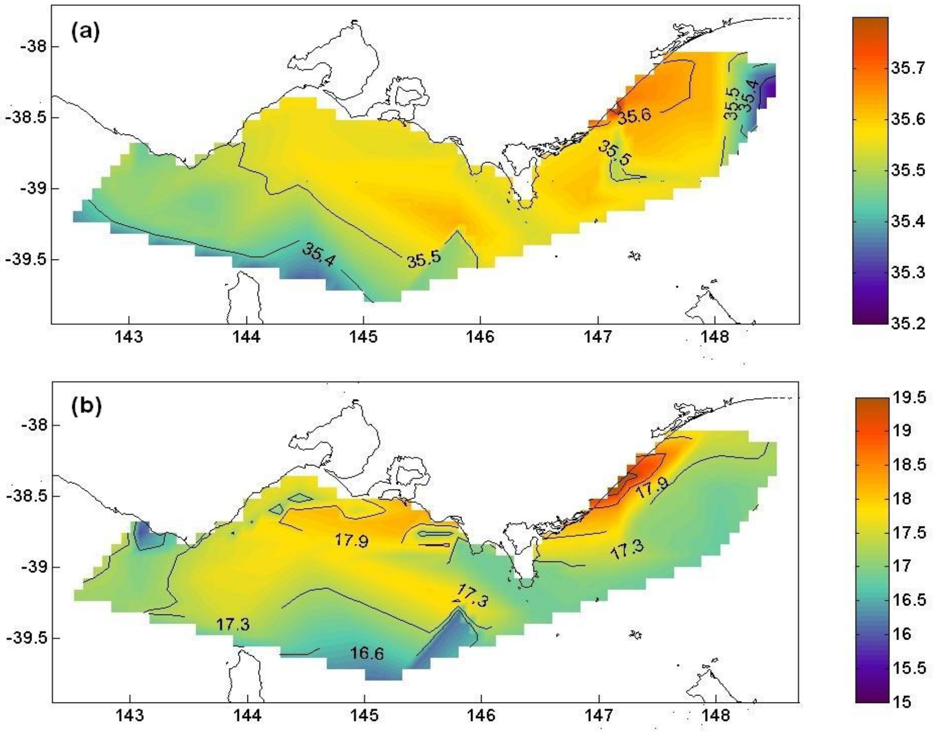

Figure 4.4.5. Summer depth-averaged (a) salinity and (b) temperature (^{o}C) derived from CTD observations.

Underway Salinity Data

The salinity distribution shown in Figure 4.4.6 is derived from salinity data captured by the underway thermosalinograph on RV Franklin voyage FR199104 (May 1991). The distribution is a spatial bi-linear interpolation derived from all quality controlled salinity data along the ship tracks (shown as red dotted lines).

Higher salinity waters are present along the coasts in eastern, southern and northern Bass Strait. Lower salinity water appears to be coming through the south-western passage and spreading into the deeper interior, similar to Tomczak (1985). The result suggests that salinity has strong depth dependence. The areas of high surface salinity correspond to the shallow regions in the Strait. A front is encountered at Banks Strait.

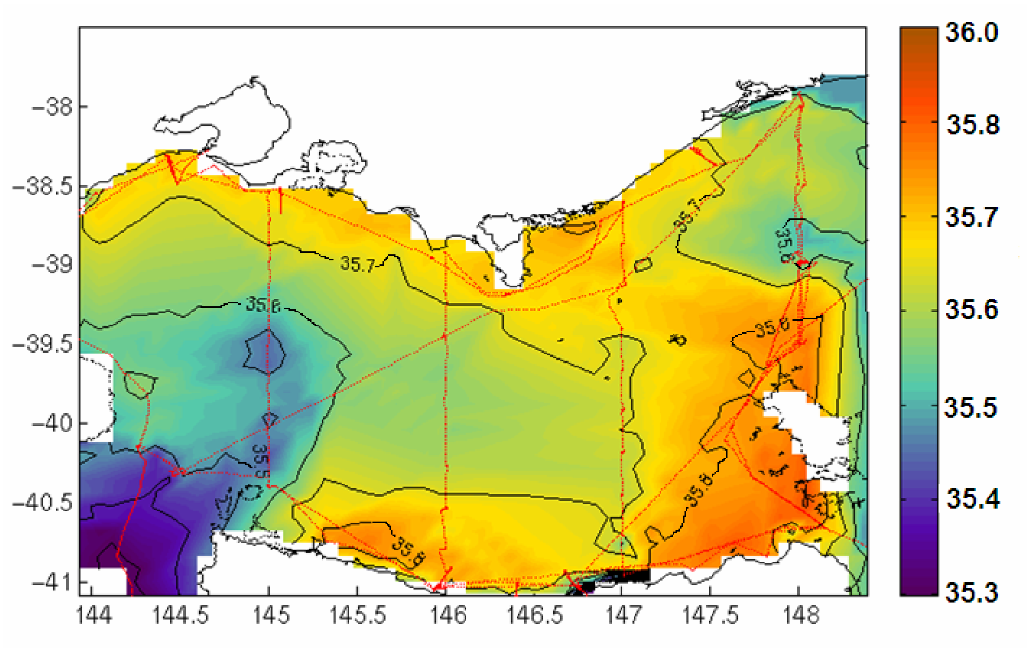

Figure 4.4.6 Surface salinity distribution derived from *RV Franklin* voyage FR199104 underway data. The red dotted line is the ship track.

The distribution of surface salinity appears to be the result of both the erosion of a higher salinity surface-layer in a period of eastward transport, combined with vertical mixing, which, in the interior, mixes surface salt deeper down and entrains deeper lower salinity water to the surface. Further explanation of this result will be given after model results are presented. The next section begins with the results of the reference simulation.

4.5 Annual-Mean Properties

Results from the reference simulation, for the full model domain, are presented in this section with annual-means using the first two years of the simulation. The full domain is shown as this gives the boundary conditions for the Bass Strait region of the model. A TS diagram, using both atlas and model data is presented to summarise annual-mean water masses. Spatial distributions of model and atlas hydrographic/hydrodynamic properties are given on surface and bottom sigma-layers, which are slices through the three-dimensional domain of the terrain-following coordinate system. Annual-mean model and atlas difference fields are also presented. To gain a basic idea of the character of the mean stratification, annual mean distribution of surface and bottom density is shown.

Annual-mean sea-level anomaly from the reference simulation is shown in Figure 4.5.1. At the western entrance to Bass Strait, the annual-mean sea-level gradient rises from 1 cm to 5 cm from the southern to northern ends. This gradient is in agreement with the study by Sandery and Kämpf (2005) (See Figure 2.4.7). The key regional currents (shown in Figure 1.4.1) such as the South Australian Current, Zeehan Current, Flinders Current and East Australian Currents are captured in the result.

The effect of prescribing a seasonal EAC signal is the most obvious feature. This has led to a positive sea-level anomaly of up to 20 cm on the eastern side of the domain. In the north-western corner of the domain, two stationary mesoscale eddies are situated between 39^{o}S, 142^{o}E and 41^{o}S, 142^{o}E which are a dipole pair. The northernmost is a clockwise low pressure eddy and the southernmost is an anticlockwise high pressure eddy. The former is the largest and the result of a convergence in the model on the shelf break and slope between the model SAC and FC. A positive anomaly from the SAC forcing signal of around 5 cm can be seen extending along the southern Victorian coastline to Wilsons Promontory. The annual-mean sea-level anomaly pattern in Bass Strait in the model resembles the circulation driven by positive sea-level anomaly at the north-western open boundary and by westerly winds. The character of residual flow resembles a Strait wide meander. This was first seen, under different circumstances, in Fandry (1981) and is later seen in the studies by Bruce *et al.* (2001), Cirano and Middleton (2004) and Sandery and Kämpf (2005). A negative sea-level anomaly of up to 5 cm exists along the shelf break which is more pronounced on the southern and eastern sides of Tasmania. This feature in the model is related to colder water from south of Tasmania being advected and mixed northwards on the shelf towards the Furneaux Group. On the western side of Tasmania it is related to cold water transporting northwards on the slope in the model FC.

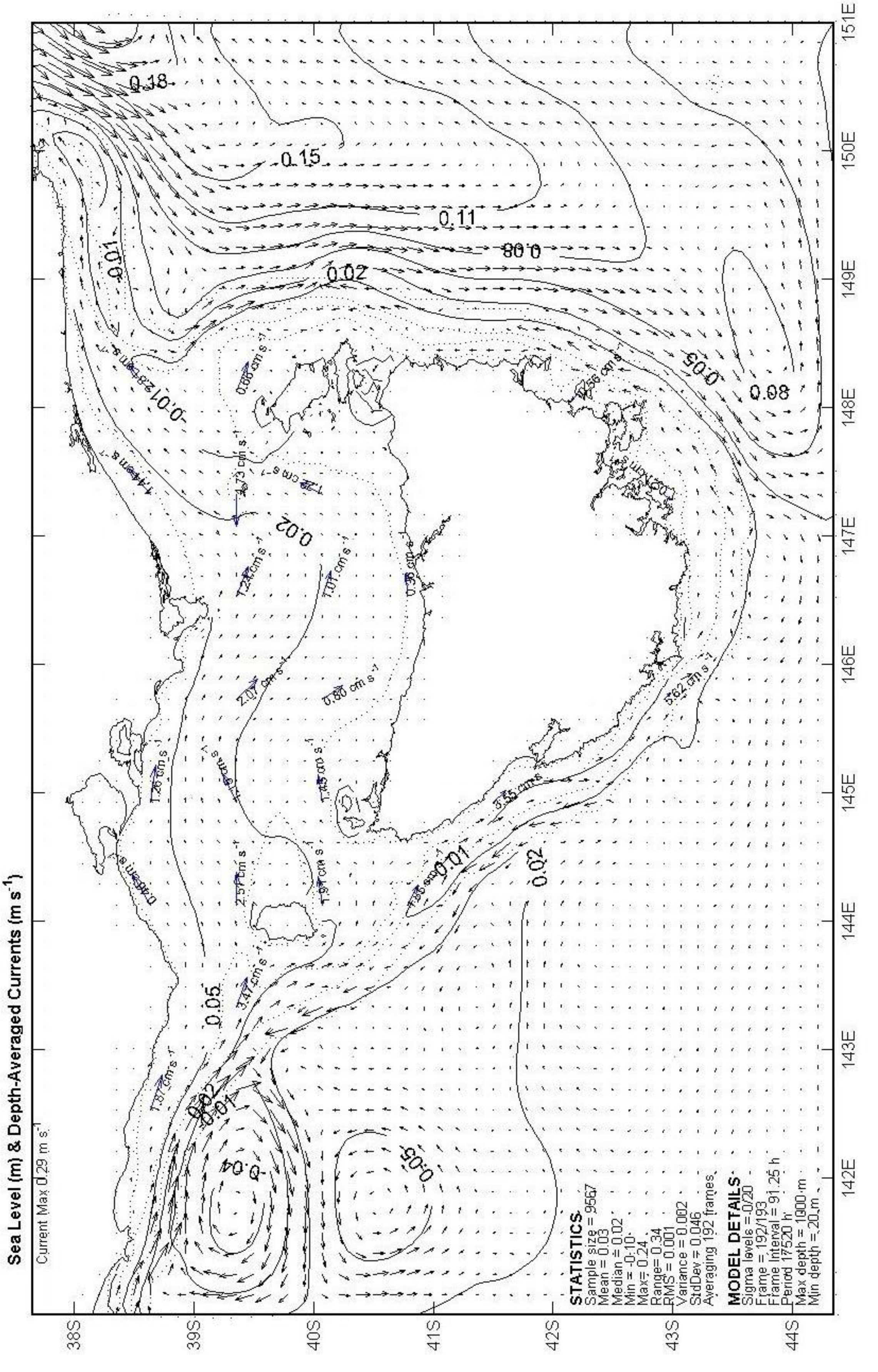

Figure 4.5.1 Annual-mean distribution of sea-level (m) and depth-averaged currents (m/s) in the reference simulation.

Figure 4.5.2 (a-f) shows annual-mean surface-layer and bottom-layer salinity, temperature and σ_T distributions. Annual-mean surface-layer salinity, temperature and density clearly show transport of water mass properties from the north-eastern open boundary to southern Tasmania.

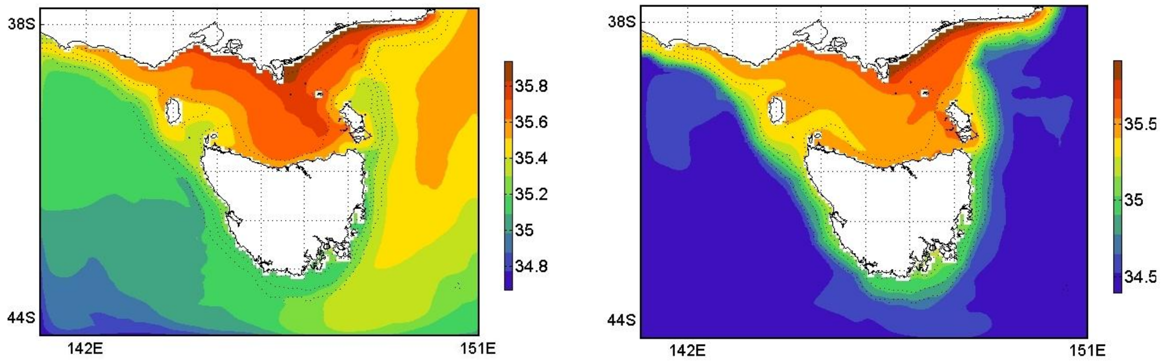

(a) Surface-layer salinity (b) Bottom-layer salinity

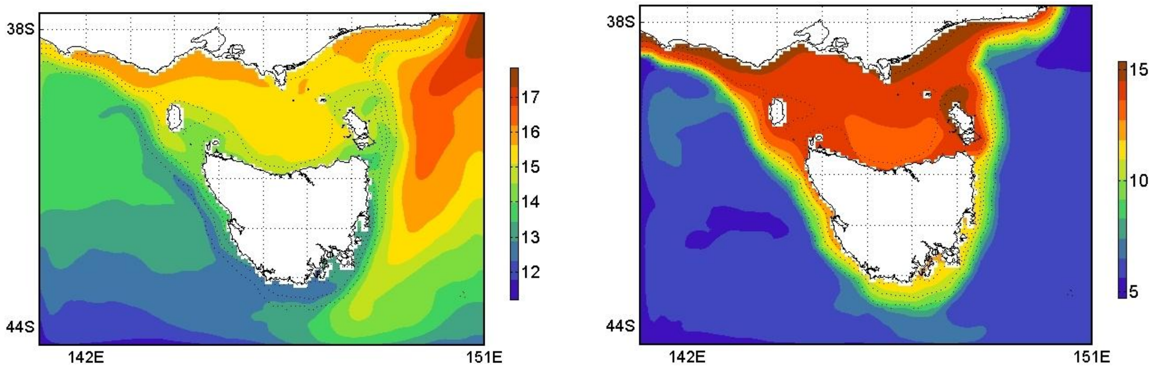

(c) Surface-layer temperature (^oC) (d) Bottom-layer temperature (^oC)

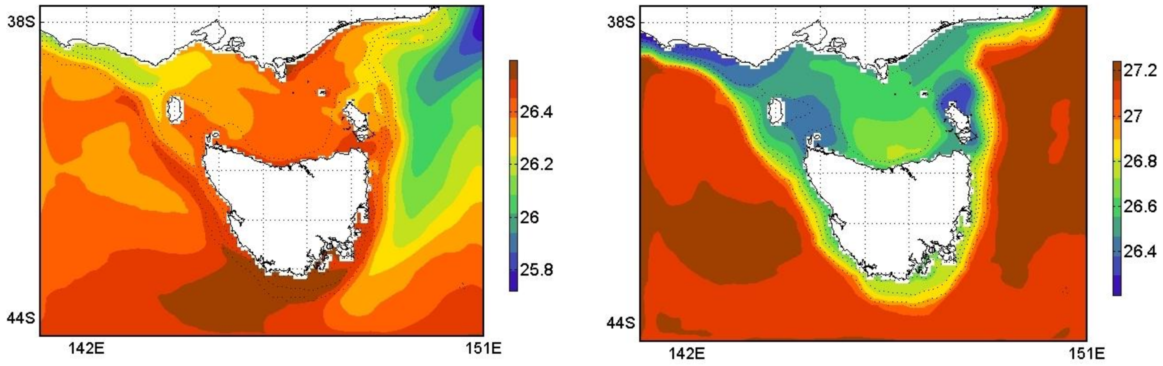

(e) Surface-layer σ_T (kg m^{-3}) (f) Bottom-layer σ_T (kg m^{-3})

Figure 4.5.2 (a-f) Annual-mean surface and bottom-layer salinity, temperature and density distributions in the reference simulation.

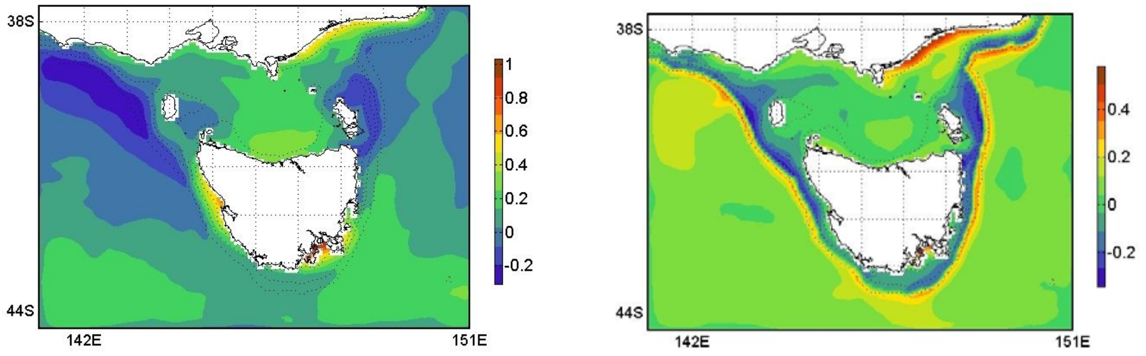

(a) Difference between model and atlas surface-layer salinity

(b) Difference between model and atlas bottom-layer salinity

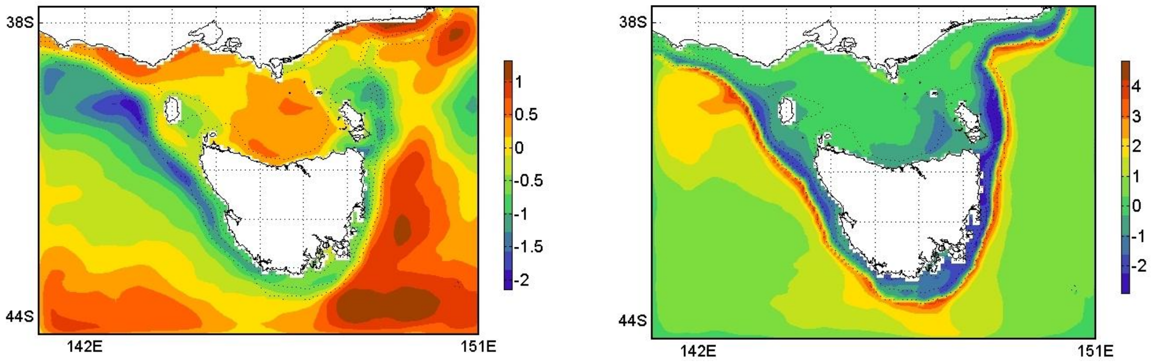

(c) Difference between model and atlas surface-layer temperature (^{o}C)

(d) Difference between model and atlas bottom-layer temperature (^{o}C)

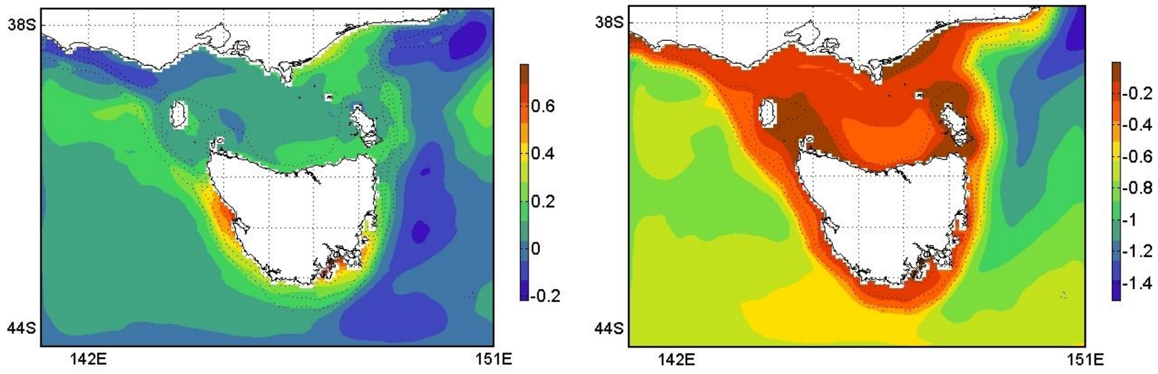

(e) Difference between model and atlas surface-layer σ_T (kg m^{-3})

(f) Model surface–bottom σ_T difference (kg m^{-3})

Figure 4.5.3 (a-e) Differences between the model (reference simulation) and atlas annual-mean surface and bottom-layer salinity, temperature and σ_T distributions. (f) Model surface-bottom-layer density difference.

Annual-mean surface-layer salinity shows that the model produces the saltiest water (35.7-35.8) in the region on the eastern side of the Strait. Annual-mean surface-layer temperature shows that the model produces warm water in northern Bass Strait (~

15-16^{o}C). On an annual basis, the model has cooler water (13-14^{o}C) in the area adjacent the northern Tasmanian coastline, in the southwest passage and in the area surrounding the Furneaux Group. Both temperatures and salinities in the latter two areas are lower than in surrounding areas in the Strait, due to the annual-mean effect of tidal stirring, which is discussed in more detail later.

The annual-mean surface-layer density field shows lighter water at the north-eastern corner of the model domain of ~ 25.9 kg m^{-3} entering the domain with the model EAC forcing. There is a gradual increase in density corresponding to a decrease in temperature towards the south and towards the shelf break. The annual-mean effect of the model SAC current forcing at the north-western part of the domain on density is seen in density contours on the shelf with eastward pro-grade features off Cape Otway, in the western Strait entrances and in the northern Strait interior. Annual-mean surface-layer density excess in the Strait interior is fairly spatially uniform and suggested by the model to be ~ 26.4 kg m^{-3}. Annual-mean surface-layer currents in the Strait are between 1-5 cm s^{-1} and are mostly eastward. The effect of the model Flinders Current is seen in the extension of the 26.4 kg m^{-3} contour in a north-western direction off western Tasmania.

Annual-mean bottom-layer properties in Fig 4.5.2 are fairly uniform in the open-ocean part of the domain. Anomalies in these areas are produced by slope currents in favour of oceanward transport or boundary inflows. Within the Strait, the bottom-layer closely follows bottom topography.

The depth-dependence of properties is evident when their distribution follows bathymetric contours. This is always the case on the continental slope. In the Strait, absence of depth-dependence is related to water properties being either horizontally or vertically well mixed.

The extent of intrusion, in the model, of bottom water into the Strait through the western passages can be seen in annual-mean bottom-layer salinity. The largest is between King Island and Cape Grim. This narrow feature extends approximately 100 km inwards. In the Strait, annual-mean bottom-layer temperature is mainly uniform.

The model suggests, on average, cooler bottom water exists in the southern part of the Strait interior. The predicted annual-mean bottom-layer density distribution in the Strait has signatures of depth-dependence due to a general increase of density with depth.

Annual-mean differences between the model reference simulation and atlas surface-layer and bottom-layer salinity, temperature and σ_T data are shown in Figure 4.5.3(a-e). The general difference between model and atlas surface-layer salinity is around 0.2 in Bass Strait, indicating the model is saltier on average than the atlas. Annual-mean surface-layer salinity difference for the model domain is 0.09. Maximum local differences occur south and west of Tasmania on the shelf. This is where the atlas includes observations of fresher surface waters, presumably of estuarine origin, which are not included in the model. Annual-mean temperature difference for the model domain is 0.01^{o}C. Positive and negative differences between model and atlas annual-mean surface-layer temperature are evident. The model is generally colder by around 1^{o}C along the shelf break and warmer than the atlas by up to 0.5^{o}C in the Strait interior. The model is colder by 0.6^{o}C in Banks Strait and by 0.2^{o}C in the passage between Cape Grim and King Island. The reason for colder anomalies in the passages is inward tidal mixing of the colder waters from outside the passages.

The difference between model and atlas surface-layer density in Bass Strait is relatively small but positive, indicating the model is denser on average than the atlas. This is due to the model being saltier on average. As mentioned earlier, the regions of high difference south and west of Tasmania are due to not including coastal freshwater fluxes, which greatly influence salinity in these areas.

The difference between model and atlas bottom-layer temperature in Bass Strait is relatively small in most areas. In south-eastern Bass Strait the model is up to 2^{o}C colder at the bottom on average than the atlas. The areas of high difference along the shelf break and slope, which are also seen in model and atlas bottom-layer salinity differences, are due to high activity in model vertical transports of water properties. The negative anomalies are the result of upward transport of cooler, fresher water and the positive anomalies are the result of downward transport of warmer, saltier water.

Figure 4.5.3(f) shows the annual-mean difference between model surface-layer and bottom-layer density. This is an indication that, on average in the model, areas in the passages are consistently well mixed vertically and stratification is present in the deeper interior. Open-ocean surface-layer mean flow is also largely traced by this quantity, because density variation of deeper waters is small.

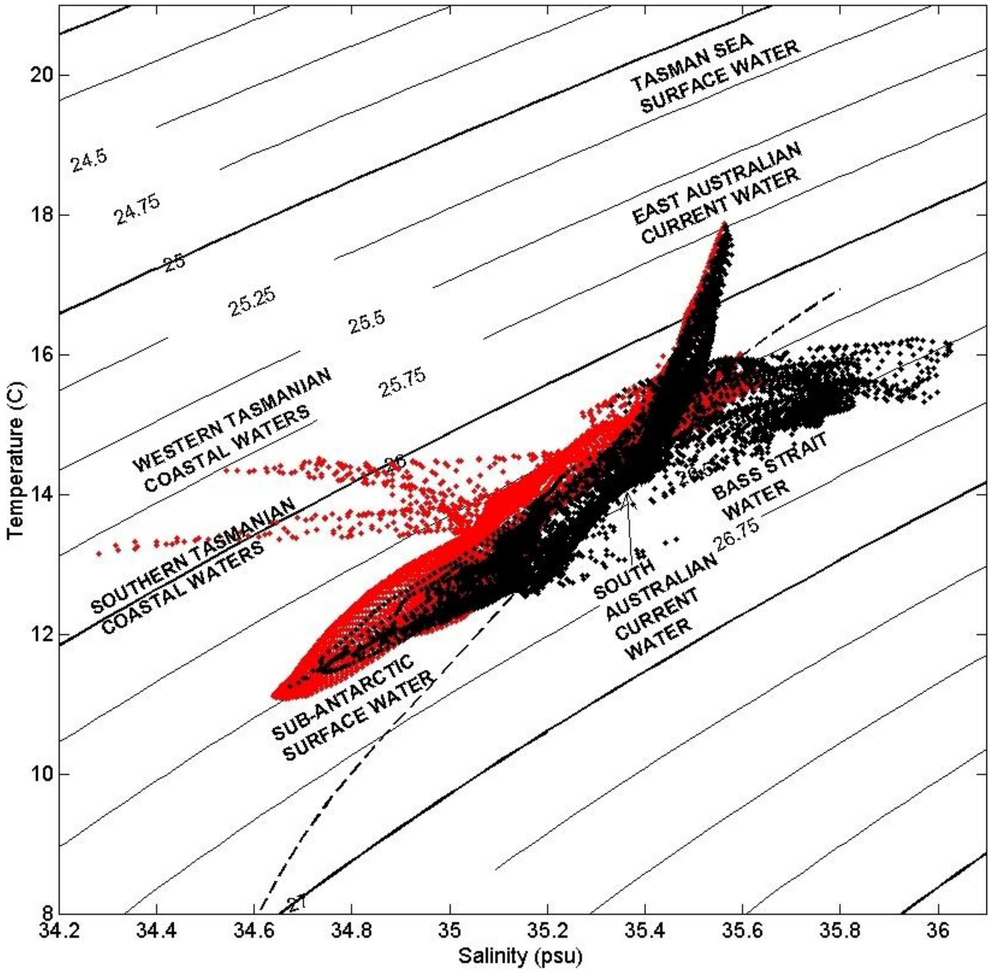

Figure 4.5.4. TS diagram of annual-mean model and atlas data for the region. Black dots are model values and red are atlas values. Dashed line indicates mean TS curve from CTD observations in Bass Strait. The locations of different regional water masses are indicated.

A TS diagram containing annual-mean model and atlas data and a mean TS curve from CTD observations which were described in section 3.7 and are analysed in section 4.7 is shown in Figure 4.5.4. The locations of different regional water masses are indicated based on those identified in section 2.6. The primary water masses which influence are EAC, SACW and SASW. By virtue of its distinctly higher salinity, Bass Strait Water is a positive anomaly from the mean TS curve. This was also the case in previous studies (Gibbs et al., 1986; Tomczak, 1985). In the diagram, the thin extensions to the left of low salinities in atlas data represent surface-layer water of riverine origin from coastal western and southern Tasmania.

4.6 Seasonal-Mean Properties

This section provides results of the reference simulation focusing on the seasonal-means in Bass Strait. Distributions of hydrographic/hydrodynamic properties for both the surface and bottom sigma-layers are presented.

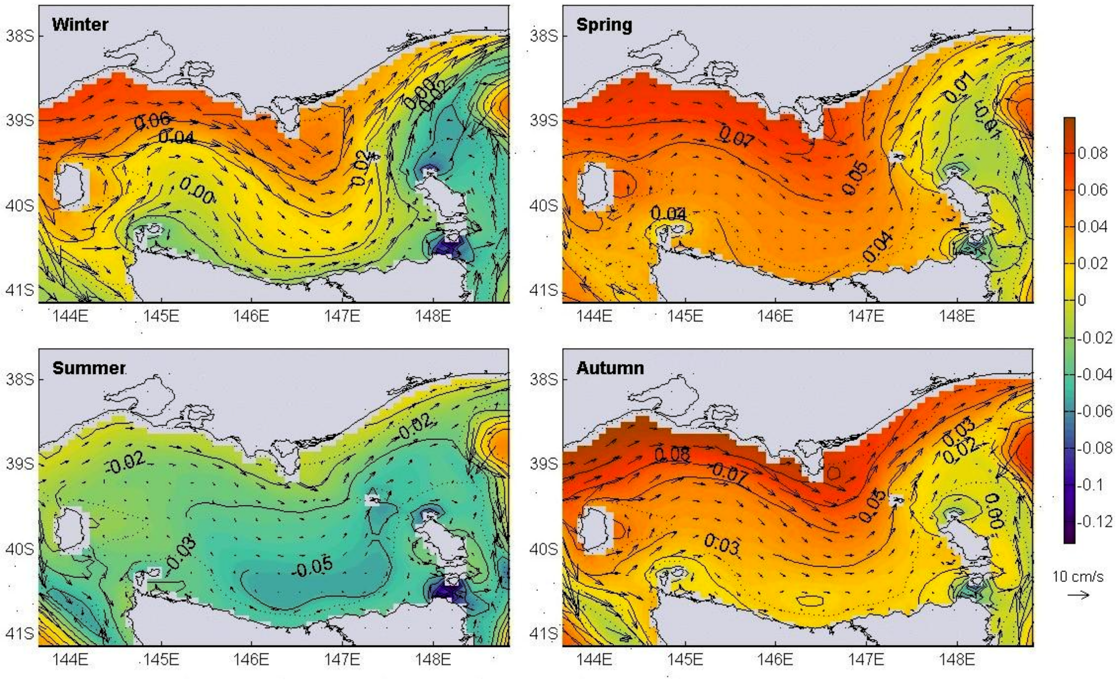

Figure 4.6.1. Seasonal-mean sea-level anomaly (m) and depth-averaged currents (cm/s). (vectors interpolated to every third grid point)

Seasonal-mean sea-level anomaly and depth-averaged currents are shown in Figure 4.6.1. Winter currents in the model are strongest and sea-level gradients are largest compared to other seasons. Sea-level is relatively higher along the Victorian coastline on average in all seasons, driving an eastward current. In the model in summer, a low pressure field develops in southern Bass Strait and drives a cyclonic eddy.

Sea-level is always higher to the east in the Tasman Sea. Seasonal-mean depth-averaged currents and sea-level gradients are mostly parallel indicating that model currents at this scale are mainly in geostrophic balance. Departures from this show where bottom friction is important. The role of topography on the geostrophic balance is seen in the steering affect along coastal boundaries and in Banks Strait, where tides dominate residual sea-level, even at the seasonal mean timescale. The mean sea-level patterns in winter, spring and autumn suggest a general characteristic of the circulation is a topographically steered geostrophic meander as shown in Figure 1.4.1. This has also been a feature of results in several previous studies (Bruce et al., 2001; Cirano, 2004; Middleton and Viera, 1991).

Seasonal-mean surface-layer salinity is illustrated in Figure 4.6.2. Strong vertical mixing over the shelf break off eastern Bass Strait maintains salinity of waters in this area in the model between 35.3 and 35.5. A region to the west of the Furneaux Group has consistently relatively higher salinity (35.5-36.2). The model predicts surface salinity in summer is high in a shallow layer (1-20 m). Bottom salinities never attain these values except in a few locations in shallow water in summer (Figure 4.6.3). The high surface salinities in the model begin appearing in late Spring in shallow waters east of Wilsons Promontory. These anomalies then spread south during the summer.

Surface salinity in the model in summer and autumn is higher than atlas values, except those made recently by Aquenal (2005). The Aquenal survey measured average salinity of 36.33 (the range was 36.26 to 36.41), between 4th-22nd April 2005, in south-eastern Bass Strait, in an area of ~ 25 m water depth, using a Yeo Kal YK-611 water quality analyser with accuracy 0.05 . The high surface salinities suggested by the model and this data will require further work to verify. CARS atlas data and CTD observations may not contain enough observations to resolve this feature (see Figures 3.6.4 and 4.4.1).

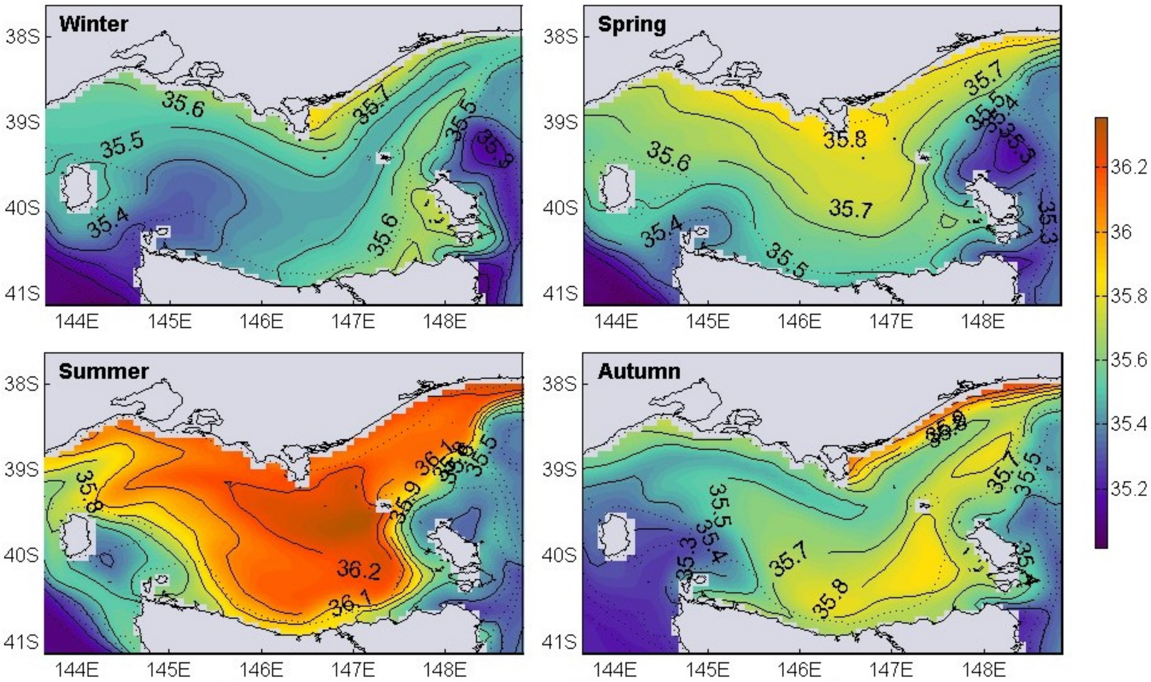

Figure 4.6.2. Seasonal-mean surface-layer salinity.

In the Bass Strait interior of the model, bottom salinity has less variation than surface salinity (Figure 4.6.3). The bottom sigma-level deepens over the continental slope to both the east and west of the Strait, with salinities as low as 34.6 at around 900-1000 m. Seasonal mean bottom salinity is in closer agreement with atlas data than surface values. Values of 36 in the bottom-layer, in shallow ~20 m depth, in the area adjacent the Victorian coastline, east of Wilson’s Promontory, are attained in the model. These anomalously high values could to be due to an over estimate of evaporation or an under estimate of freshwater input in the model.

The winter bottom mean salinity shows a front of 35.4 water advancing through the south-western passage, similar to the results of Tomczak (1985) (Figure 2.6.1). This seems to move south in spring and be closed off in the summer low pressure field. In autumn when winds become more westerly and the SAC starts to gain momentum, the model shows a bottom-layer inflow of 35.2 water from the west. Bottom waters are suggested by the model to always have relatively high salinity in eastern Bass Strait.

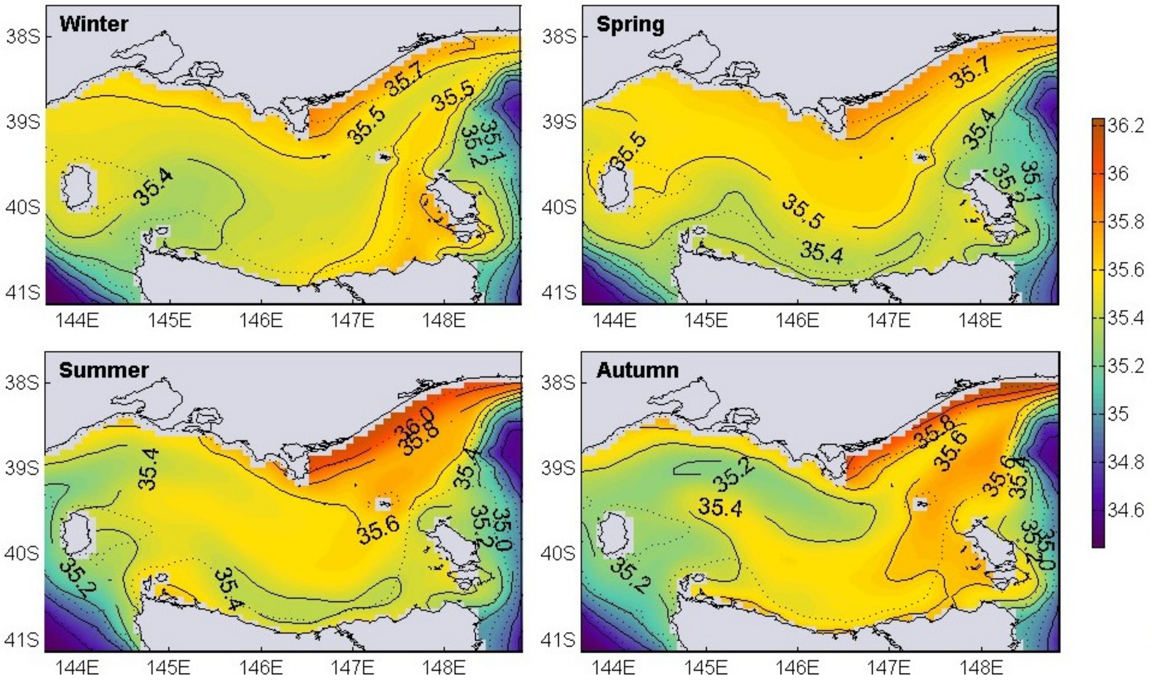

Figure 4.6.3. Seasonal-mean bottom-layer salinity.

Seasonal-mean model-atlas surface-layer salinity difference fields are shown in Figure 4.6.4. The difference fields are the result of a process in the model causing an anomaly between atlas and model data. In summer the high positive salinity anomaly is a sign of evaporation governing surface salinity in the model. Lower salinity anomalies in the western parts of the Strait in winter and autumn indicate eastward advection influencing salinity. In autumn and winter, the high salinity anomaly in the south-eastern part of the interior is the least eroded water mass, i.e. the least affected by lateral eastward advection. This area also corresponds to an area with relatively longer flushing timescales or age. This is shown and described in further detail in section 4.8.

The spring anomaly field indicates air-sea fluxes dominating surface salinities in a widespread area over the shelf. It can also be seen that relatively lower salinities exist around the Furneaux group. The model suggests tidal mixing of ambient ocean waters into this area is important for surface salinity at all times of the year.

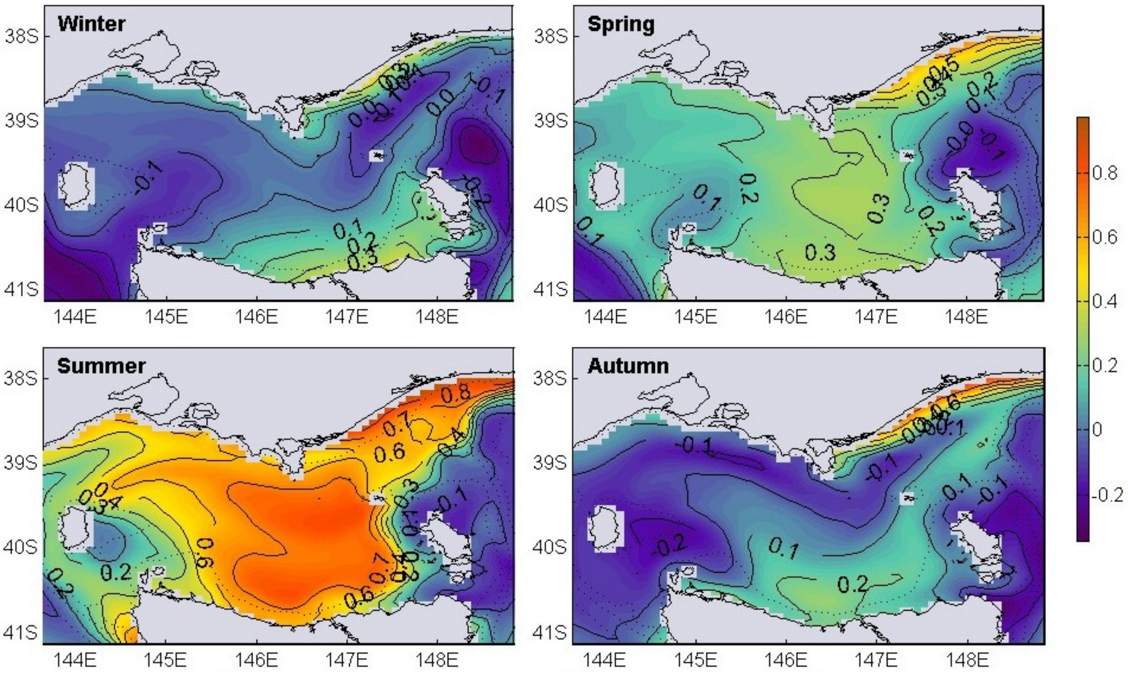

Figure 4.6.4. Seasonal-mean model-atlas surface salinity difference.

Mean seasonal salinity and contours of zonal current speed through section A-A in the model is shown in Figure 4.6.5. Current speed contours are denoted as a heavy line for zero, continuous lines for positive values and dashed lines for negative values. The model suggests that a westward net current flow up to 2 cm/s in a shallow surface-layer exists in the central Strait at this location. A signature of a westward jet (up to 6 cm/s) is found in southern Bass Strait in summer.

In the other seasons in the model, mean seasonal zonal currents have net eastward flow through section A-A with vertical structure in most places. Maximum mean seasonal flow is eastward and found in winter (9 cm/s), near the surface south of 39^{o}S. The shallow saltier surface mixed layer up to 20 m depth in summer is evident. Winter mean salinities in section A-A decrease from north to south, however, are well mixed vertically. The surface mixed layer begins to develop in spring, at the northern end of section A-A, remains through summer and breaks down in autumn. At the location of section A-A, the seasonal-mean mixed layer predicted by the model only extends about two thirds of the way across the Strait.

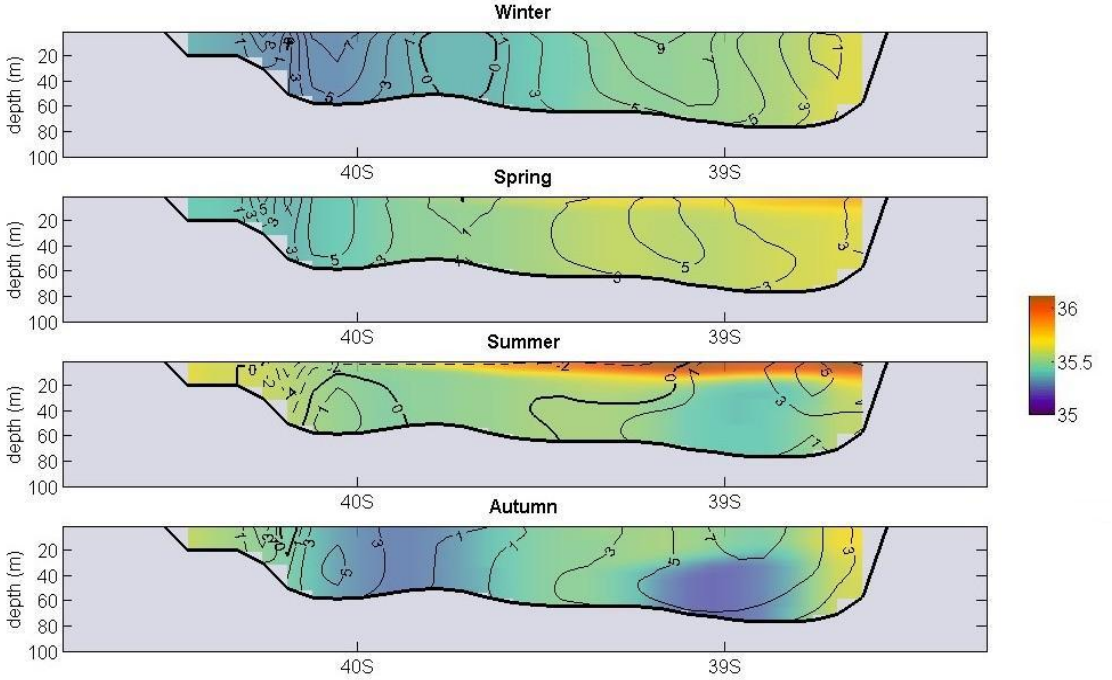

Figure 4.6.5. Section A-A seasonal-mean salinity and zonal current speed (cm s^{-1}). For location of section A-A see Figure 3.4.3.

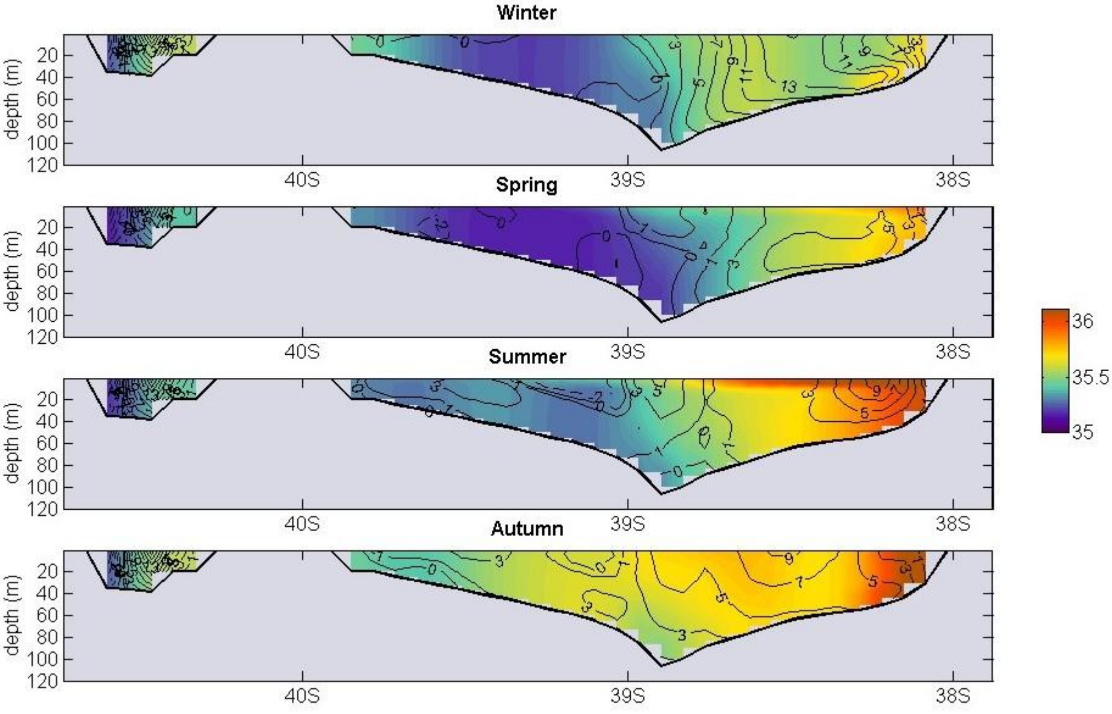

Figure 4.6.6. Section B-B seasonal-mean salinity and zonal current speed (cm s^{-1}). For location of section B-B see Figure 3.4.3.

Seasonal-mean salinities though section B-B and contours of zonal current speed are shown in Figure 4.6.6. Seasonal mean salinity in the eastern part of the Strait is different to the western side. In winter a strong eastward outflow is seen in the northern part of section B-B with currents up to 13 cm/s. Most of the water column in section B-B in winter is vertically well mixed. Salinity is generally highest at the northern end and decreases towards the south until just before Flinders Island. The development of a shallow saltier surface-layer in the model at the northern end of section B-B begins in spring. Some of the salt formed at the surface at this time is mixed over the entire water column in the shallow northernmost end of section B-B. The presence of a shallow (up to 20 m) surface mixed layer extending from the northern end about half way across the passage between Flinders Island and mainland Australia is evident. Waters in the southern half of the Strait at this time are predicted to be relatively lower in salinity until autumn. The model predicts seasonal-mean flow in Banks Strait is westward at all depths in the southern half and eastward in the northern half. The model suggests lower salinity water is brought into Bass Strait though the southern half of Banks Strait.

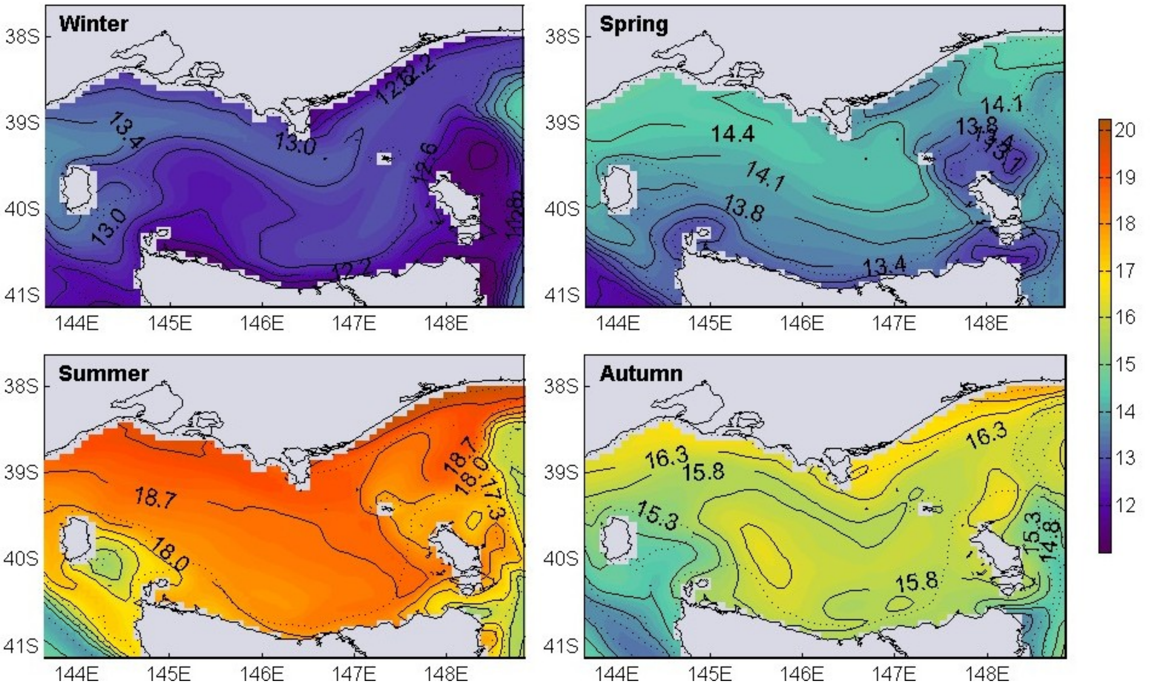

Figure 4.6.7. Seasonal-mean surface-layer temperature (^{o}C).

Seasonal-mean surface-layer temperature is given in Figure 4.6.7. Coolest surface temperatures in the model are in winter ranging from ~13.4^{o}C in the north-western area to about 11.5^{o}C along the Tasmanian coastline and surrounding the

Furneaux Group. Spring mean surface-layer temperatures are predicted by the model to be up to 1-2°C warmer than winter, with colder surface waters in the shallow and tidally influenced parts of eastern and southern Bass Strait. The influence of the model SAC is seen in both winter and spring as an intrusion of relatively warmer water into the north-western area. Summer mean surface-layer temperature reaches maximum values of approximately 20°C in shallow coastal areas in northern Bass Strait. Most of the Strait interior, and the surrounding shelf attains surface-layer temperatures of between 18-19°C. The model predicts relatively lower temperatures in summer and autumn on the southern side of Banks Strait and in the passage between Cape Grim and King Island. This appears to be caused by surface properties being mixed deeper into the water column by tidal stirring, and by entrainment of deeper water from outside the Strait. Autumn mean surface-layer temperatures are several degrees lower than summer. The influence of the model SAC, which induces eastward transport through the north-western entrance to the Strait, is seen in position the 15.8°C contour.

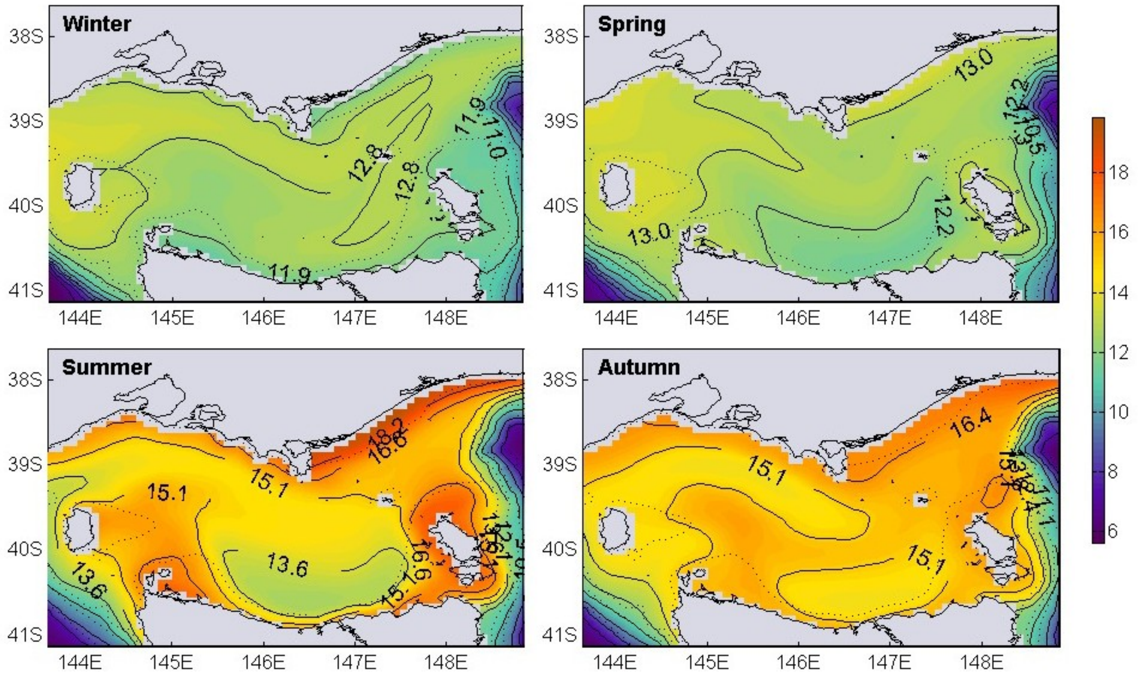

Figure 4.6.8. Seasonal-mean bottom-layer temperature (°C).

Model predictions of seasonal-mean bottom-layer temperatures are presented in Figure 4.6.8. Winter bottom temperatures are up to 0.5°C cooler than those at the surface in the deeper central area. Slight warming of the bottom-layer occurs in spring.

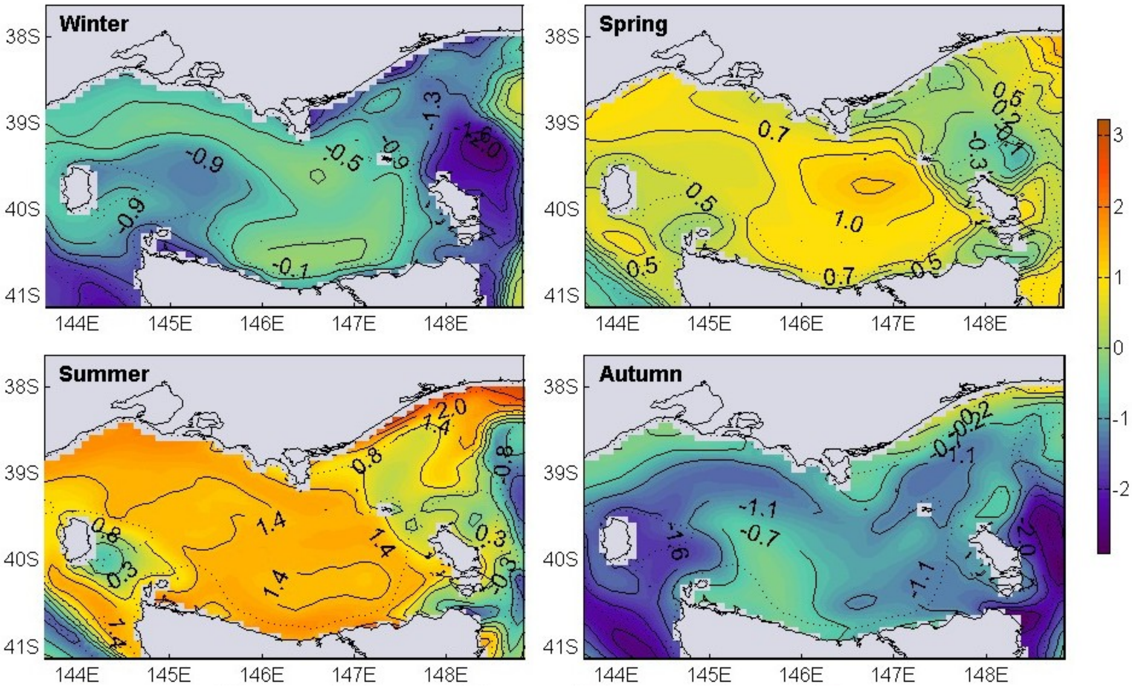

Figure 4.6.9. Seasonal-mean model-atlas surface-layer temperature difference (^{o}C).

Summer bottom temperatures indicate to some extent the character of vertical mixing. Shallower areas in the Strait passages and along coastlines attain bottom temperatures within a few degrees of surface temperatures. The model suggests that a relatively cold pool of water (<13.6^{o}C), remnant from earlier in the year, sits near the deeper bottom in the southern part of the basin in central Bass Strait until autumn. The deeper bottom waters away from the continental shelf in the model, which are at 950 m water depth show little or no mean variation in temperature from around 6^{o}C throughout the year.

Differences between model and atlas surface-layer temperature are shown in Figure 4.6.9. Winter surface-layer temperatures predicted by the model are up to 1^{o}C cooler than values given by the atlas in the shallow parts of the Strait. The differences are smaller (between 0.5 and 0.1^{o}C) in the interior. The reason for this is that the model SAC has brought atlas water-mass values from the boundary through the north-western Strait entrance. The values that have been brought into the model have been modified along the way, however, remain close to those given by the atlas in the Strait interior at this time of year. Warming of the surface-layer in the model in spring is seen in the positive anomalies of up to 1.2^{o}C in central Bass Strait. The surface-layer in summer is predicted to be up to 1.4^{o}C warmer than values given by the atlas. In autumn model surface-layer temperatures are seen to be up to 1.5°C cooler than atlas values depending on location. Possible reasons for the differences, apart from errors in the thermodynamic forcing are

- Atlas values smooth out the processes causing variation and are based on limited observations.
- Model results are a dynamic adjustment to the internal density field and various boundary forcing.
- The model is cast on a significantly finer resolution grid than the atlas.

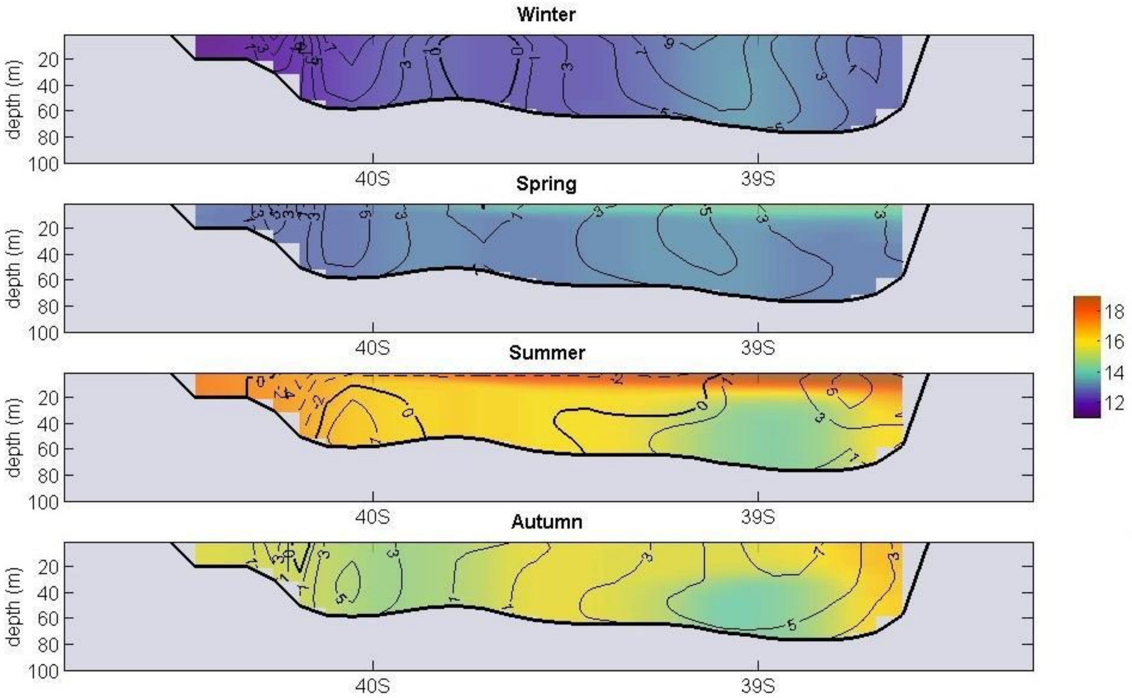

Figure 4.6.10. Section A-A seasonal-mean temperature (°C) and zonal current speed (cm s^{-1}). For location of section A-A see Figure 3.4.3.

As with salinity variation in section A-A, seasonal-mean temperature variation has similar structure (Figure 4.6.10). Contours of the same zonal current speeds are shown. Winter temperatures in the model through section A-A are mostly vertically and horizontally uniform from the effects of wind-driven mixing.

A shallow warmer layer develops near the surface in Spring, extending from the northern end of the section to about two thirds across the Strait. This feature develops further in summer. The model predicts that its depth is up to 20 m. A relatively cooler mass of water (~14^{o}C) lies in the deeper part of section A-A in summer and autumn near 39^{o}S. The model suggests the warm shallow mixed layer in summer breaks down in Autumn. Section B-B temperatures in Figure 4.6.11 have similar features to salinity in Figure 4.6.6. Winter and spring temperatures are relatively uniform, with the development of a shallow warm layer at the northern end of the section in spring. A relatively colder water mass, remnant from the previous season, is found in the model in summer in the deepest part of the section. The shallower ends of the passage between Flinders Island and mainland Australia have vertically well mixed temperatures in summer, however, the deeper interior part has relatively strong temperature variation with depth, and a warmer shallow surface mixed layer up to 20 m depth. The model predicts cooler water enters the Strait via the southern side of Banks Strait and warmer water exits on the northern side in summer and autumn. The results also illustrate how the model resolves a break down of the shallow surface mixed layer in autumn.

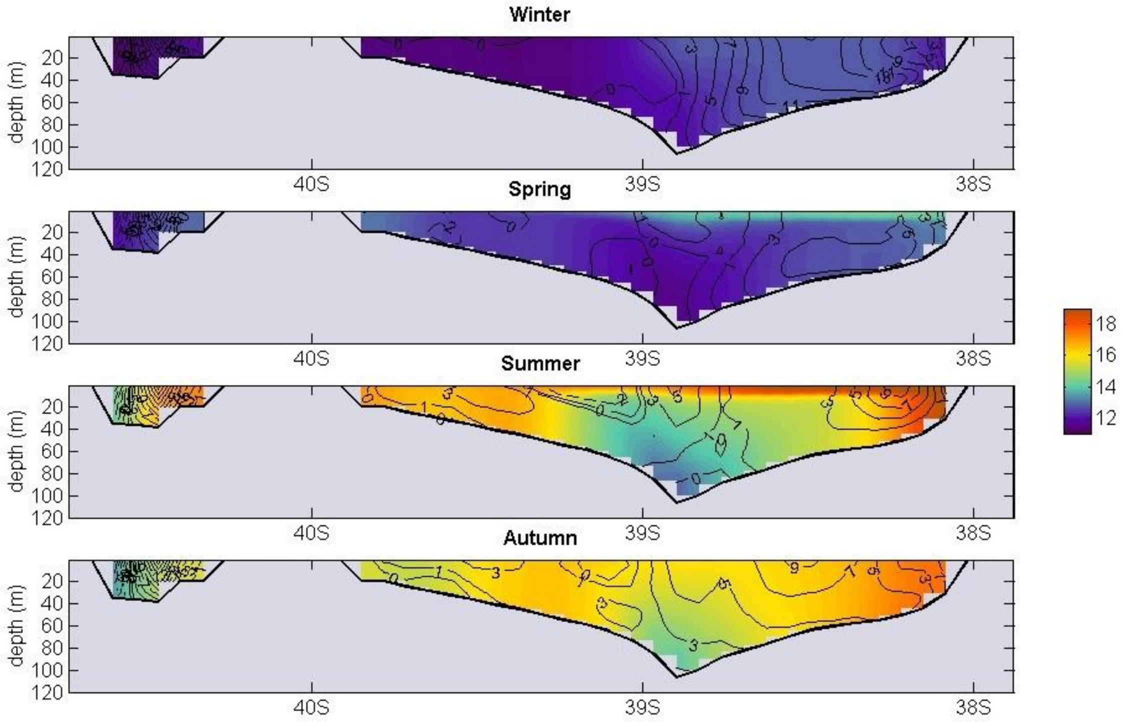

Figure 4.6.11. Section B-B seasonal-mean temperature (^{o}C) and zonal current speed (cm s^{-1}). For location of section B-B see Figure 3.4.3.

Seasonal-mean surface-layer σ_T is shown in Figure 4.6.12. Winter contains the densest water in the year primarily due to cooler temperatures. The model predicts the densest surface water in the Strait in winter exists in shallow waters adjacent northern Tasmania and in eastern Bass Strait. This is due to the presence of both cooler and saltier water. Mean surface densities (σ_T) are lowest in summer in the shallower Strait entrances and in coastal areas. The slightly denser (~0.1 kg m^{-3}) water mass in central Bass Strait is partly an artefact of the sigma-level deepening in this area, but also due to the deeper interior having lower levels of tidal mixing than the entrances. Autumn mean densities reflect the circulation induced by the model SAC and the beginning of cooling by air-sea heat fluxes at this time of year.

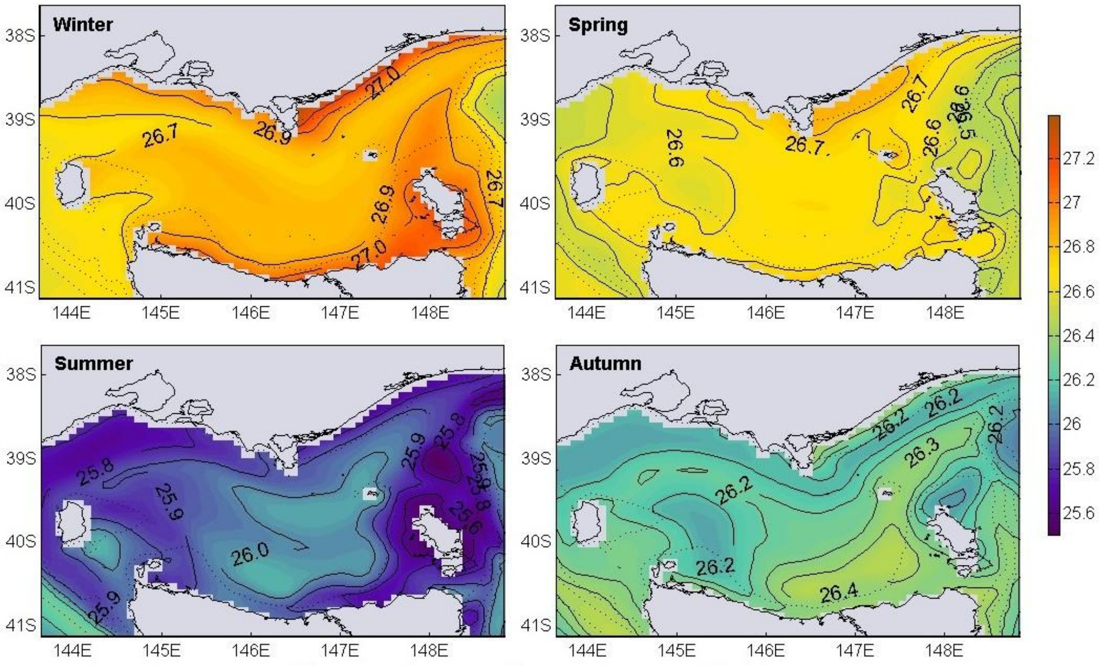

Figure 4.6.12. Seasonal-mean surface-layer σ_T (kg m^{-3}).

Mean winter surface-layer currents are predicted by the model to be generally eastward with features in direction associated with sea-level set-up at this time of year (Figure 4.6.13).

Stronger mean winter currents are predicted between Flinders Island and mainland Australia. In the bottom-left corner of the Figures the influence of the model winter SAC can be seen near the shelf break with south-westward currents. In summer a reversal in model currents occurs at this location.

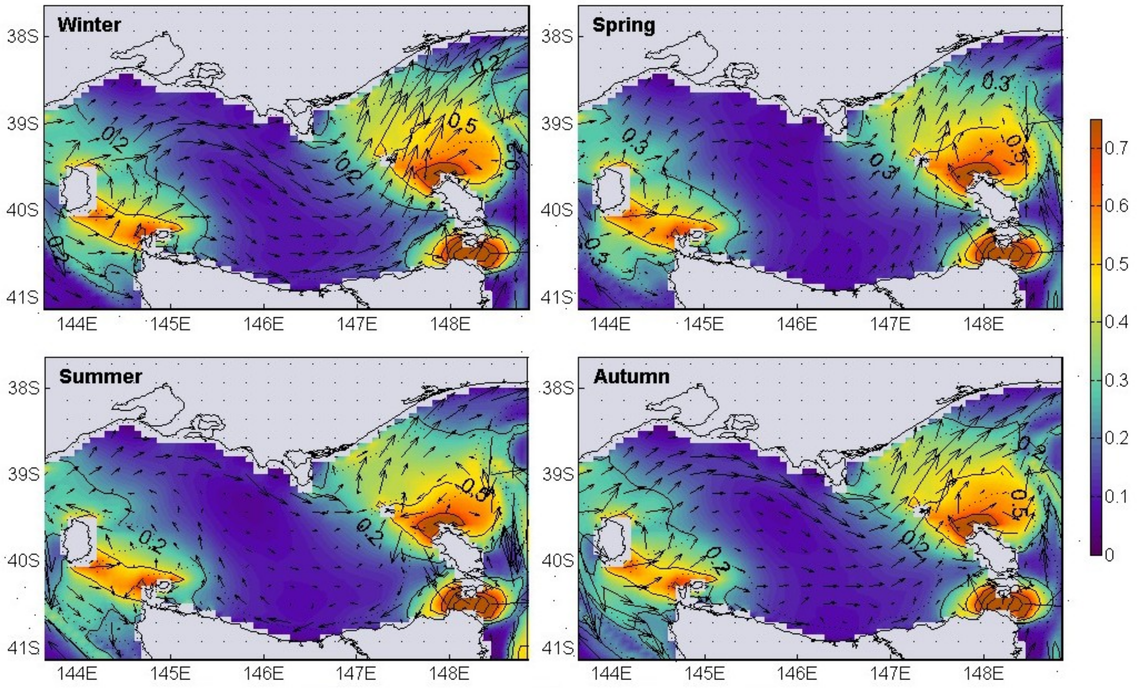

Figure 4.6.13. Seasonal-mean surface-layer currents (m s^{-1}). (vectors interpolated to every third grid point)

Winter currents show strong similarity with autumn currents because of the influence of both westerly winds and the model SAC. Mean summer surface currents in the model develop a clockwise cyclonic circulation, with westward flow along the northern Tasmanian coastline. The distribution of current speeds, indicated by the colorbar, strongly reflects tidal features in the circulation. These are in agreement with McIntosh and Bennett (1984) and Fandry (1985).

Seasonal-mean bottom-layer densities are shown in Figure 4.6.14. In winter and spring, the model predicts mean bottom densities equivalent to those found at deeper levels (200-400 m) off the shelf break. In summer, mean bottom densities in the Strait entrances are the lowest encountered all year, due to strong vertical mixing induced by the tides. No equivalent values are found at depth off the shelf break. The deeper part of the interior has relatively high mean density in summer, associated with remnant colder water from the previous season. The model shows mean bottom density in autumn to be slightly lower in some parts of the Strait than in summer. This is attributed to the gradual mixing down of summer surface water properties at this time of the year.

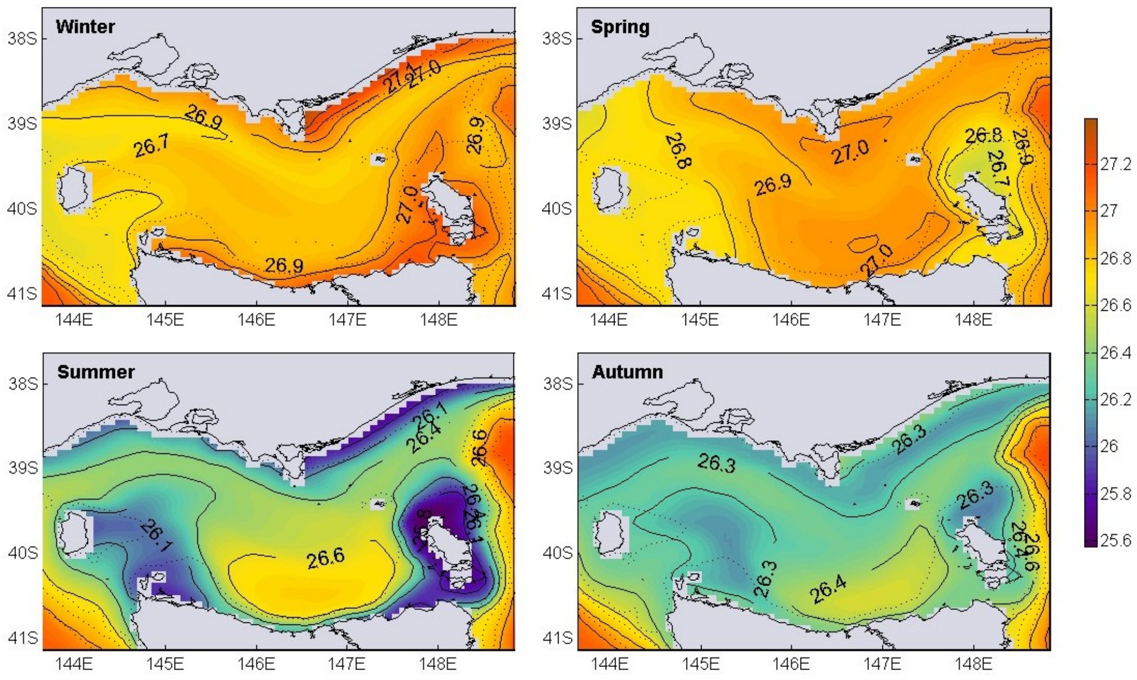

Figure 4.6.14. Seasonal-mean bottom-layer σ_T (kg m^{-3}).

Seasonal-mean bottom-layer currents are shown in Figure 4.6.15. On average, bottom currents are 50% weaker than surface currents due to bottom friction.

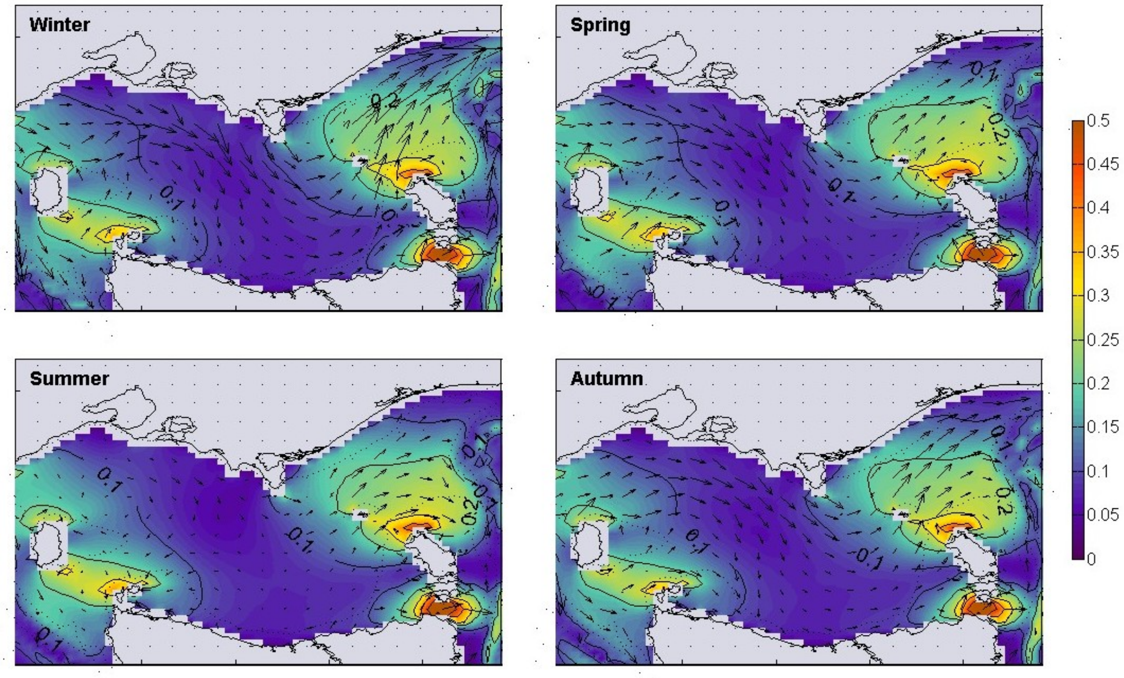

Figure 4.6.15. Seasonal-mean bottom-layer currents (m s^{-1}). (vectors interpolated to every third grid point)

Mean flow in all seasons is mainly eastward, except in summer in southern Bass Strait where the flow is weak and apparently unsystematic. Weakest mean bottom currents are found at the greatest depths in the interior.

Seasonal-mean surface-bottom density differences in the model are given in Figure 4.6.16. The model predicts the entire shelf region shown, on average, will have complete vertical mixing in winter (difference is close to zero), i.e. no stratification. The result for spring shows the interior and shelf break regions developing stratification. Only the entrances remain largely unstratified. In summer, the model predicts strong stratification over most of the Strait interior, except in the shallow parts of the Strait entrances and along the Victorian coastline in the shallow areas adjacent Lakes Entrance. The breakdown of stratification is seen in the model as an almost Strait wide phenomenon in Autumn.

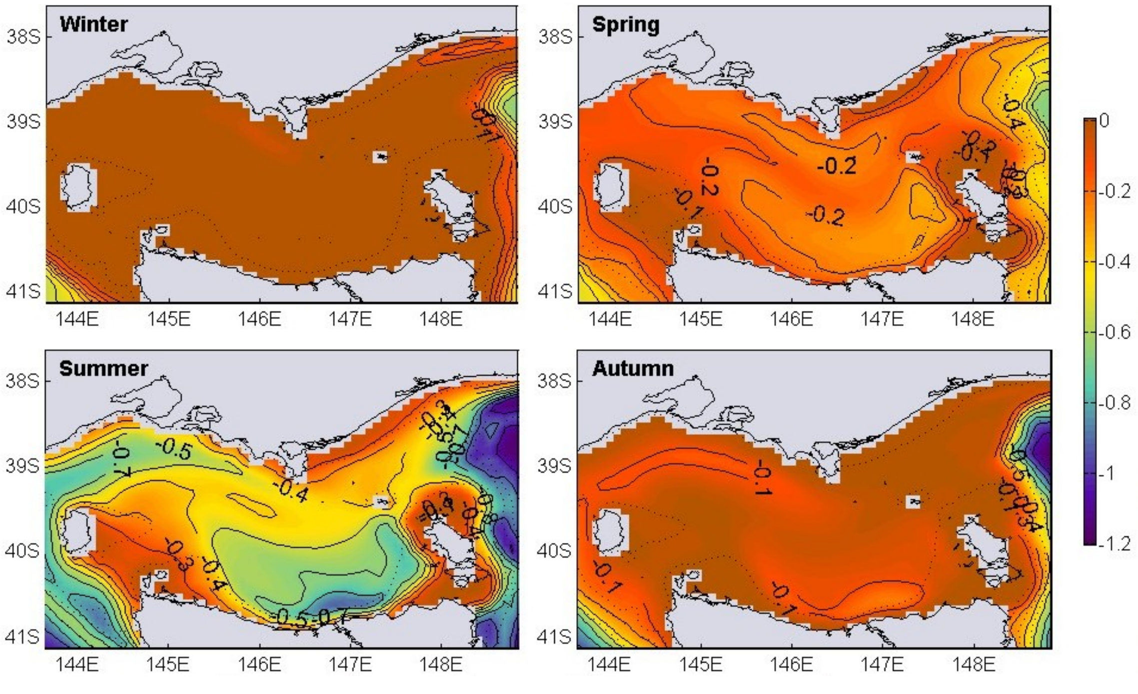

Figure 4.6.16. Seasonal-mean surface and bottom-layer σ_T difference (kg m^{-3}).

The mean seasonal differences between model and atlas depth-averaged density are given in Figure 4.6.17. The largest anomaly occurs along the Victorian coastline near Lakes entrance in winter. This could be due to exclusion of continental runoff in the model, which occurs in winter at this location. The mean anomalies are generally small (<0.1 kg/m^3) in the interior. Where the anomalies occur is a result of a process in the model which is not resolved by the atlas.

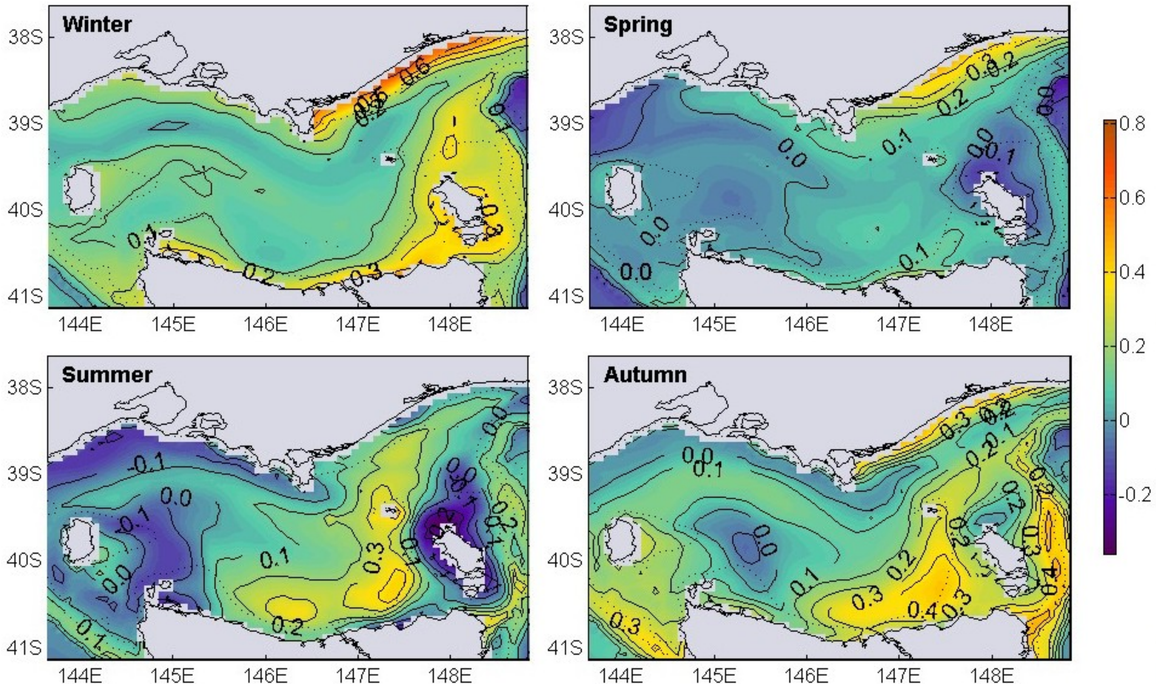

Figure 4.6.17. Difference between seasonal-mean model and atlas depth-averaged σ_T (kg m^{-3}).

Mean seasonal vertical density structure through section A-A is presented in Figure 4.6.18. The model winter and spring densities are close to being vertically and horizontally uniform, with a slight signature of a shallow buoyant surface mixed layer (~10 m depth) beginning to develop in spring. In summer densities are lower than in winter and spring and the shallow (~20 m depth) buoyant surface mixed layer extends from the northern end of the section to about 40^{o}S. A pool of denser ~ 26.5 kg m^{-3} water lies in the deeper part of the section. The breakdown of the shallow surface mixed layer can be seen in the Autumn density in section A-A.

Mean seasonal density through section B-B is illustrated in Figure 4.6.19. Winter mean density in this section is fairly uniform horizontally and vertically. Exception to this is found in shallow waters at the ends of the passage between Flinders Island and mainland Australia, where the density is slightly higher than in the deeper parts. Development of a buoyant shallow surface mixed layer (~10 m depth) at the northern end of the section occurs in spring.

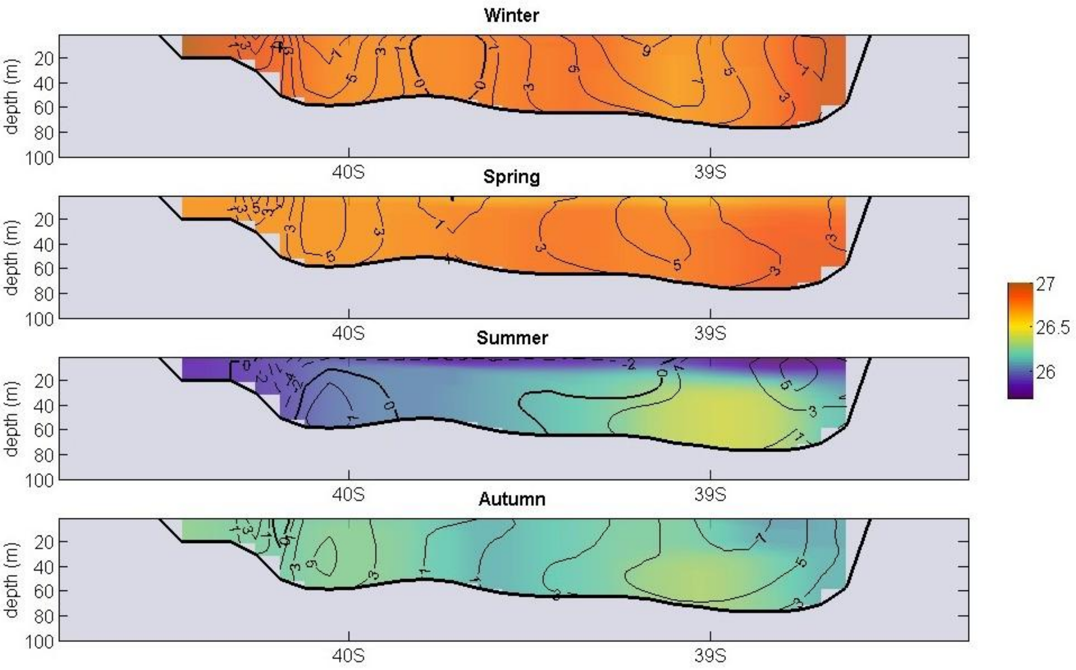

Figure 4.6.18. Section A-A seasonal-mean σ_T (kg m^{-3}) and zonal current speed (cm s^{-1}). For location of section A-A see Figure 3.4.3.

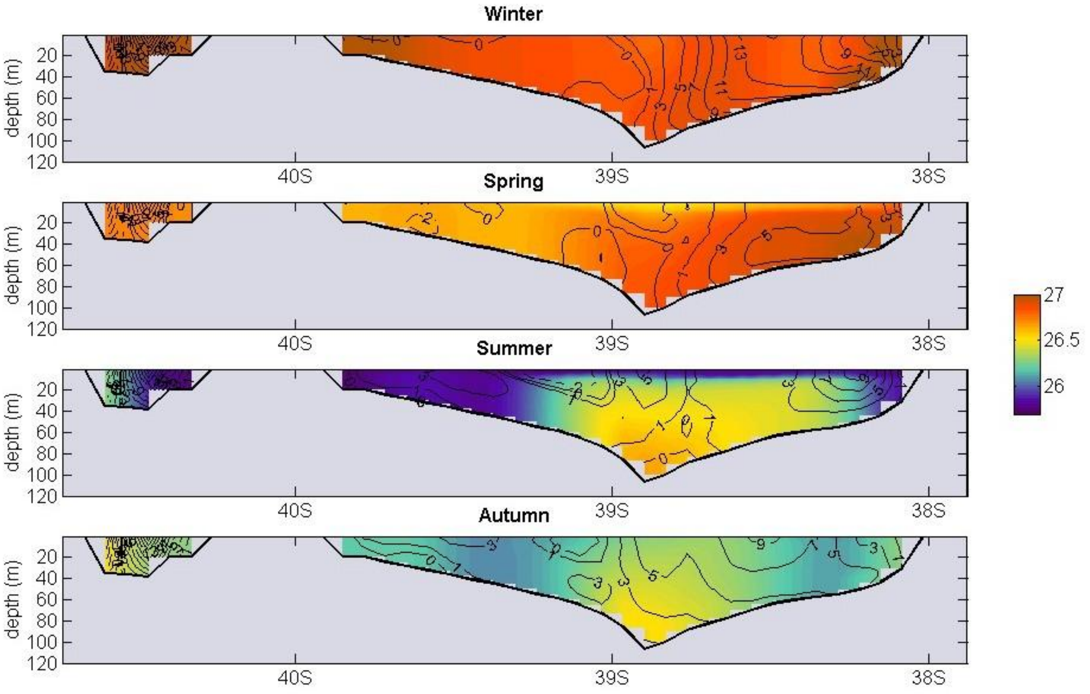

Figure 4.6.19. Section B-B seasonal-mean σ_T (kg m^{-3}) and zonal current speed (cm s^{-1}). For location of section B-B see Figure 3.4.3.

Stratification with a shallow surface mixed layer (~10-15 m depth) is predicted by the model in section B-B in the deeper, middle part of the longer passage, however the shallower ends are vertically well mixed with less dense water. This feature disappears in autumn, with the model predicting the water column becoming vertically well mixed.

4.7 Comparison of Properties in Selected Areas

This section compares seasonal-means from the model and the atlas in both the surface and bottom sigma-layers. A selection of different areas over which the averaging is made, indicated by the diagram at the left of each time series, is presented in the following Figures. The results indicate that there is a general phase lag between model and atlas surface data, of approximately one week, which is more pronounced in shallow water than deep water. Depending on location, model maximum surface temperatures occur up to 2 weeks before the atlas.

Full Model Domain

A time series of seasonal-mean surface and bottom-layer atlas and model temperature and salinity, spatially averaged over the model domain is shown in Figure 4.7.1. The model seasonal temperature cycle in the surface layer is in agreement with atlas data.

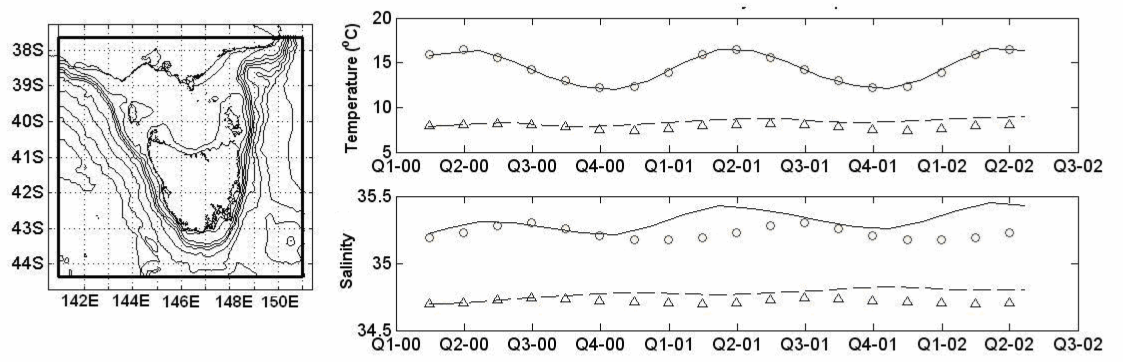

Figure 4.7.1 Time series of seasonal-mean atlas and model surface and bottom-layer temperature and salinity averaged over the entire domain. Atlas surface-layer means are denoted by circles and bottom-layer means by triangles. Model surface-layer means are shown as a continuous line and bottom-layer means as a dashed line.

Both model and atlas data suggest maximum surface-layer temperatures in this region around the middle of February, without significant lag between the two data sets. Model and atlas bottom-layer temperatures show only small seasonal variation when the deep parts (900-1000 m) of the model domain are included. Both atlas and model bottom salinity slightly increases over the 27 month period shown which indicates that the flux budget is not in long-term equilibrium with the overall sources. The least agreement between model and atlas is found in the mean surface-salinity seasonal trend.

Winter values are in agreement, however the model suggests higher mean surface salinities in summer. This is mainly due to high evaporation in the model in the confines of Bass Strait, but also possibly due to higher salinities introduced at the model open boundaries and the lack of coastal freshwater fluxes in certain areas.

Bass Strait Interior

Seasonal-mean surface and bottom-layer atlas and model temperature and salinity, spatially averaged over the Bass Strait interior is given in Figure 4.7.2. This is the same area delimited by crosses in Fig 1.3.1.

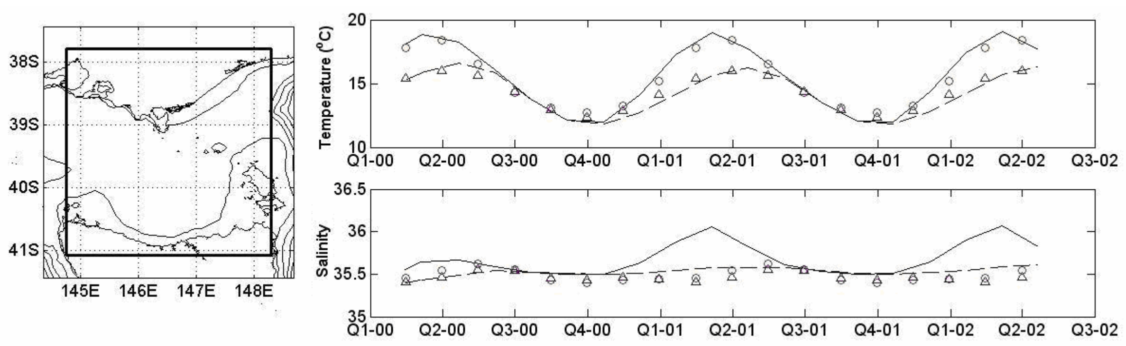

Figure 4.7.2. Same as 4.7.1, but for the area shown.

The seasonal cycle in surface-layer temperature variation in this area shows a phase lag, of about 2 weeks, between model and atlas data. This is probably because no deeper sections are included in the analysis. Model and atlas bottom-layer temperatures are in good agreement in phase and magnitude. The mean seasonal cycle of the development and breakdown of stratification is seen in the divergence and convergence of mean surface and bottom properties, which is in good agreement with the atlas in regards to timing.

Model and atlas surface-layer salinity have the least agreement, with the model predicting mean salinity in the surface-layer significantly higher in summer than suggested by the atlas. Model and atlas winter values of surface and bottom salinity are in agreement for only several months each year. Salinity in Fig, 4.7.2 illustrates the first six months of the simulation are essentially a spin-up period for salinity rather than temperature. A quasi-steady seasonal salinity cycle is established in the second year.

A TS diagram showing seasonal-mean model and atlas data for the interior area is presented in Figure 4.7.3. Model salinities > 36 are in higher proportions in summer, their source being evaporation at the surface. Autumn has maximum salinities similar to summer (~36.2), however, a far smaller proportion of these high salinities exist, suggesting the beginning of erosion of the summer water mass due to vertical mixing and lateral advection.

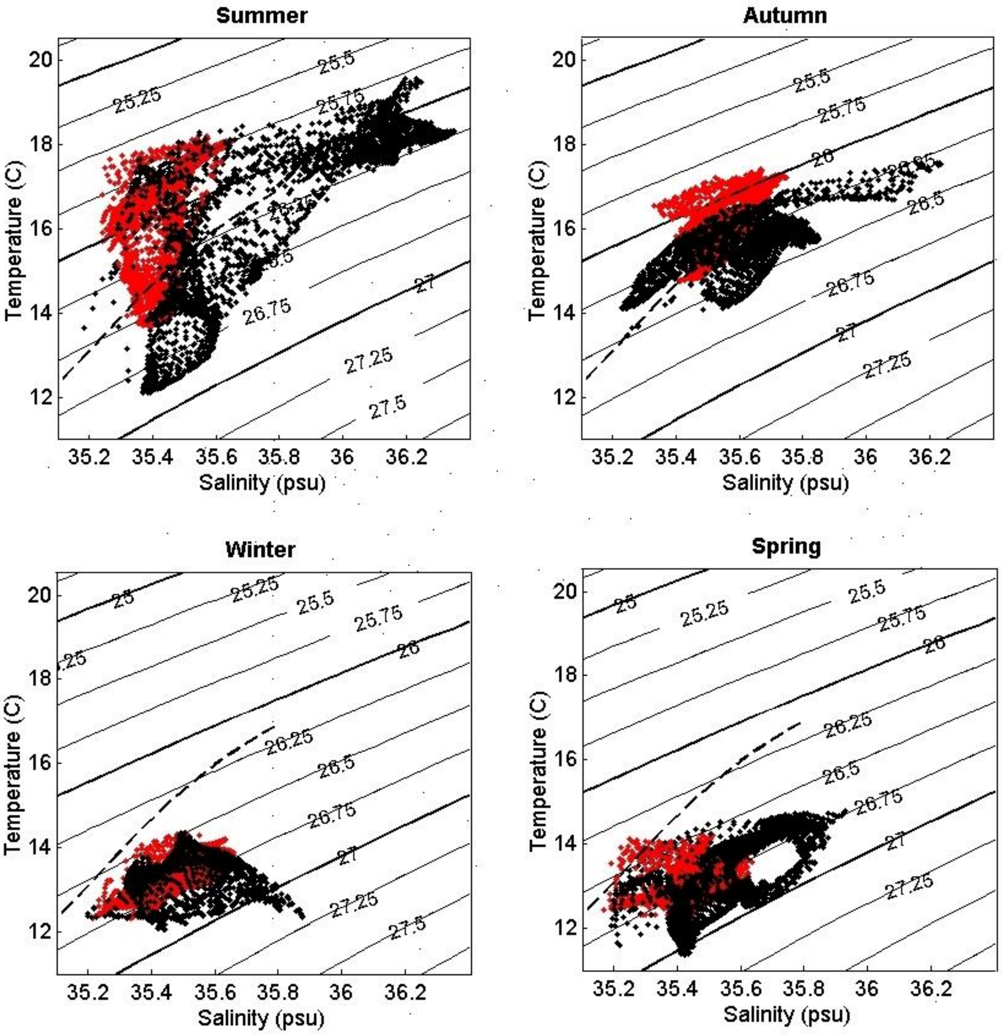

Figure 4.7.3. TS diagram of seasonal-mean model and atlas data for the interior area. Black dots denote model values and red signify atlas values. Dashed line indicates mean TS curve from CTD observations in Bass Strait.

Maximum salinities are lowest in winter and spring (~ 35.8-35.9), yet a proportion are still higher (0.2) than atlas values. In winter, model water properties are in closest agreement with atlas data. Water-mass properties oscillate about the mean TS curve through the seasonal cycle. The model surface salt anomaly formed in summer is mixed out of the interior by the end of each winter. The surface becomes a source of salt through Spring and Summer. The TS diagram for Spring suggests there are two sources of salt in the model which appear to combine to form the same water mass. One source is the surface in the northern Strait interior, the other is the shallow coastal area in south-eastern Victoria extending ~ 150 km east from Wilson's Promontory.

Northwest Passage

Seasonal-mean surface and bottom-layer atlas and model temperatures and salinities, spatially averaged over an area between Cape Otway and King Island, are given in Figure 4.7.4. Here, mean monthly model and atlas surface and bottom temperatures are in good agreement with each other despite the approximate 1-2 week phase lag in surface temperatures. In summer months, model salinities are higher at the surface and lower near the bottom than in the atlas.

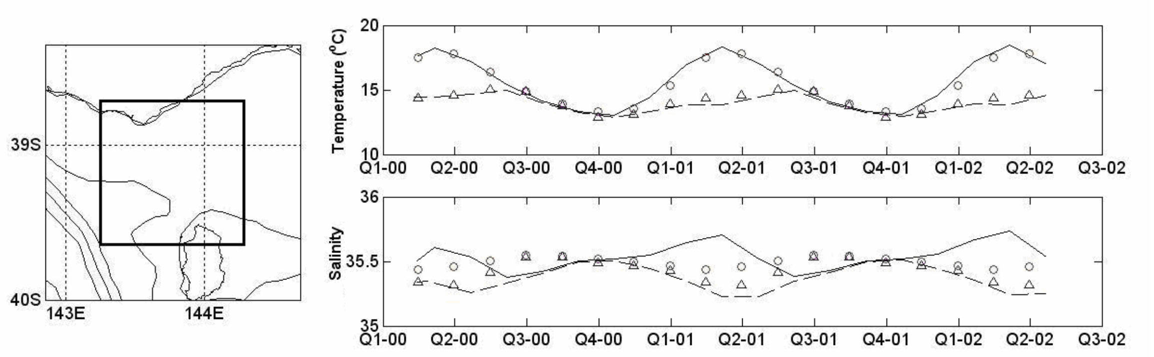

Figure 4.7.4. Same as 4.7.1, but for the area shown.

Closer agreement occurs during winter. The model salinity cycle is, however, strongly out of phase with atlas data. Some of the agreement in salinities at this location is due to the transport of atlas properties into this part of the model domain from the SAC boundary condition.

Southwest Passage

Seasonal-mean surface and bottom-layer atlas and model temperature and salinity spatially averaged over an area between Cape Grim and King Island is shown in Figure 4.7.5. At this location, model and atlas maximum temperatures are in less agreement because the phase lag is most pronounced. This suggests atlas data may be biased by measurements made in the deeper ocean further to the west. If deeper areas away from the shelf are included in the analysis, the model and atlas surface temperature have stronger seasonal correlation. Regardless, model salinities have low seasonal correlation with atlas data exhibiting nearly opposite phase.

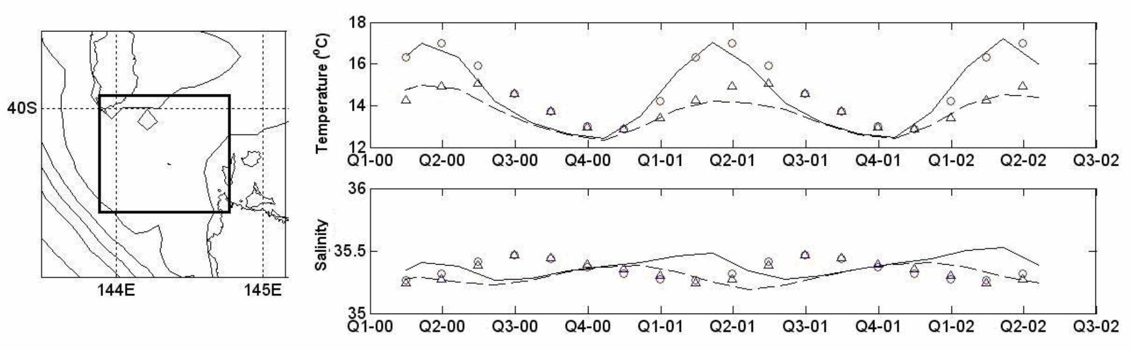

Figure 4.7.5. Same as 4.7.1, but for the area shown.

Banks Strait

Figure 4.7.6 shows seasonal-mean surface and bottom-layer atlas and model temperature and salinity spatially averaged over an area including Banks Strait. Water mass properties at this location are nearly completely vertically well mixed at all times of the year, as seen in both atlas and model surface and bottom temperatures and salinities. Model and atlas salinity are in most favourable agreement at this location. This is because strong tides mix in water-mass properties from the part of the domain containing deeper ocean to the east.

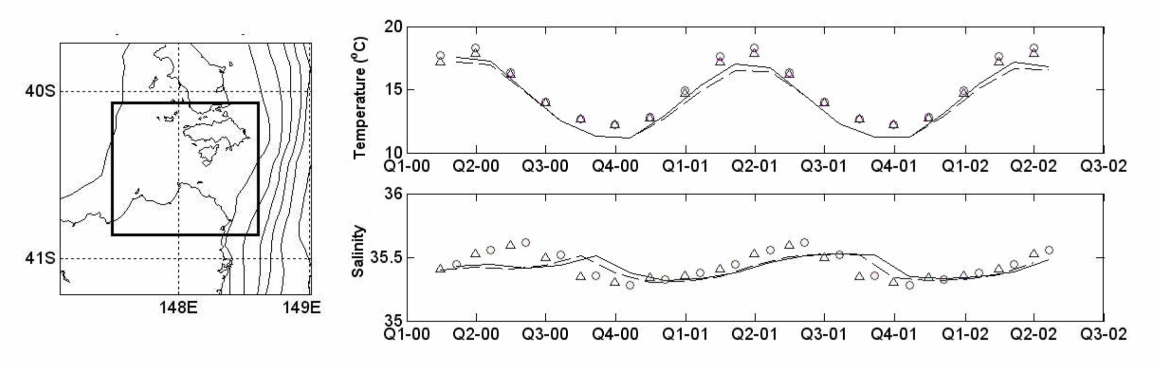

Figure 4.7.6. Same as 4.7.1, but for the area shown.

North-Eastern Area

Figure 4.7.7 shows seasonal-mean surface and bottom-layer atlas and model temperature and salinity spatially averaged over an area southeast of Lakes Entrance in the vicinity of Bass Canyon. This area contains both shallow water (~ 20 m depth) and deeper water (~ 950 m depth). Model and atlas surface and bottom-layer temperatures are in agreement, except for the phase lag of about three weeks. The reasons for this are the same as already suggested. At this location in the model, the surface and bottom salinities experience the largest gradual long-term departure, with bottom salinity gradually increasing over time.

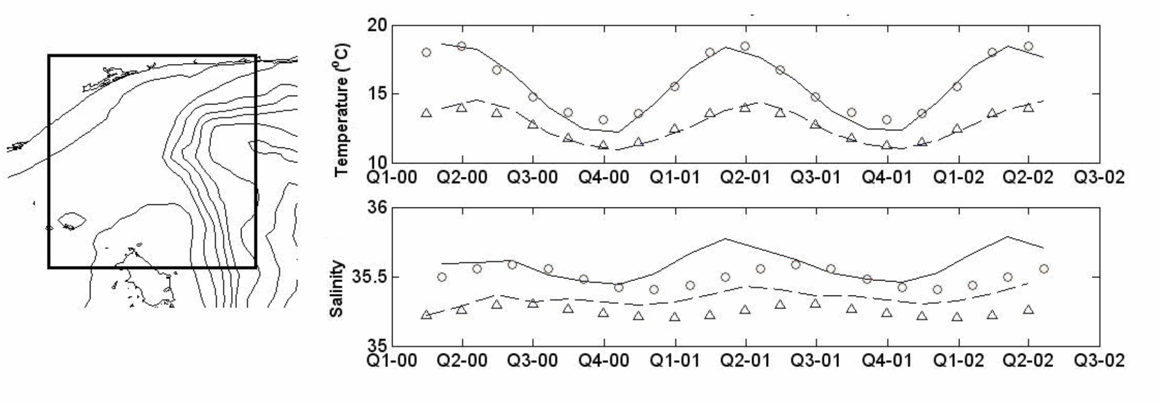

Figure 4.7.7. Same as 4.7.1, but for the area shown.

4.8 Distributions of Transport Timescales

The main seasonal differences in circulation in Bass Strait can be illustrated using mean summer and winter timescale distributions. Figure 4.8.1 shows summer, winter and annual-mean flushing time distributions based on tracer release times. For example, the summer distribution is based on tracer concentration fields released in

December, January and February. The flushing timescale of Bass Strait is of the order of six months. Tracer released in summer months is subject to the circulation in the period ahead of release.

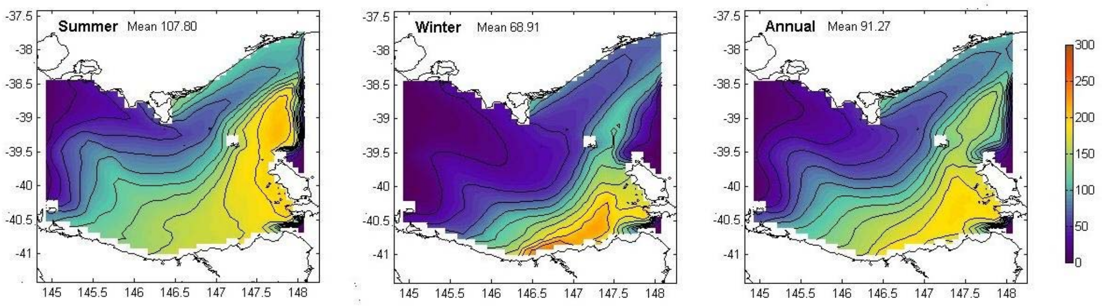

Figure 4.8.1. Lateral distributions of mean flushing times (days).

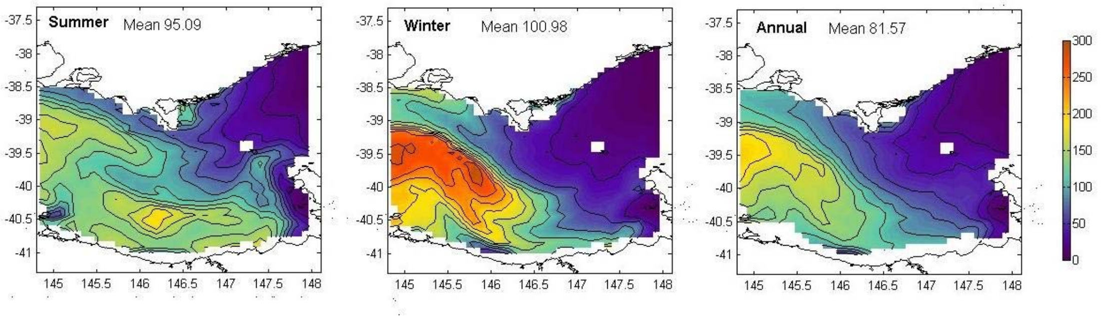

Figure 4.8.2. Lateral distributions of mean residence times (days).

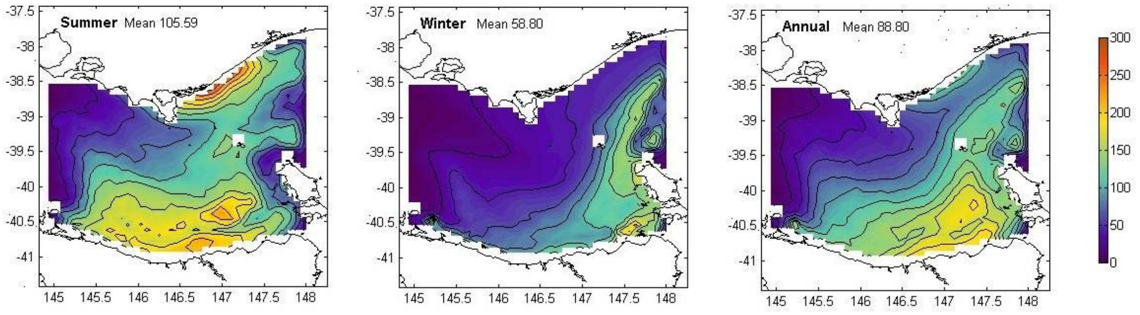

Figure 4.8.3. Lateral distributions of mean water age (days).

Tracer released in summer shows a flushing time pattern influenced by winter circulation and tracer released in winter shows a flushing time pattern influenced by the summer circulation. The annual-mean flushing time distribution is a composite of 12 flushing time patterns based on the release of 12 different tracer concentration fields at the beginning of each month of the first year of the simulation. Results suggest annual-mean flushing times on average are longer in south-eastern Bass Strait and are of the order of 6 months. This reflects the annual residual circulation suggested by the model.

Summer, winter and annual-mean residence time distributions based on particle release times are shown in Figure 4.8.2. The summer distribution is based on particles released in December, January and February. The winter distribution is based on particles released in June, July and August. As with tracer concentration fields and flushing times, particles released in summer are influenced by the winter circulation and particles released in winter are influenced by the summer circulation. The results suggest particles released in southern and south-eastern Bass Strait have mean residence times in the Strait of around 6 months. Particles released in winter east of King Island have mean residence times up to 300 days. Annual-mean residence times show longer values at the western side of the Strait than at the eastern side. This is because the residual throughflow is generally eastward.

Summer, winter and annual-mean age distributions based on the time particles entering the region (in the water column) spend in the region are given in Figure 4.8.3. Unlike mean residence and flushing time distributions, mean age distributions relate to the period in which the mean is calculated. The model suggests mean age of water mass in summer is about 6-7 months in southern Bass Strait. Ages are generally lower in winter in western Bass Strait, however, water in the eastern and south-eastern parts has age around 6 months. Annual-mean age distribution is similar to annual-mean flushing time distribution, highlighting an area in south-eastern Bass Strait with generally older water and longer flushing times.

Summer and winter age distributions in areas A and B (locations given in Figure 1.3.1) are presented in Figure 4.8.4. Areas A and B were chosen because they capture seasonal differences in age distributions. This choice was informed by earlier work and knowledge of the circulation. One could choose other locations or do the same analysis for every grid cell, however, this would not be necessary to illustrate the point. Age data is from the second year of the simulation. In summer, the age distribution in area A suggests an age mixture containing young and old water between 25 and 125 days. A large proportion has age between 50-75 days. Area B in summer generally contains older water than area A, with a peak at around 125 days. No water with age less than 75 days is detected. This distribution represents ageing being induced by the summer circulation in the south-eastern area.

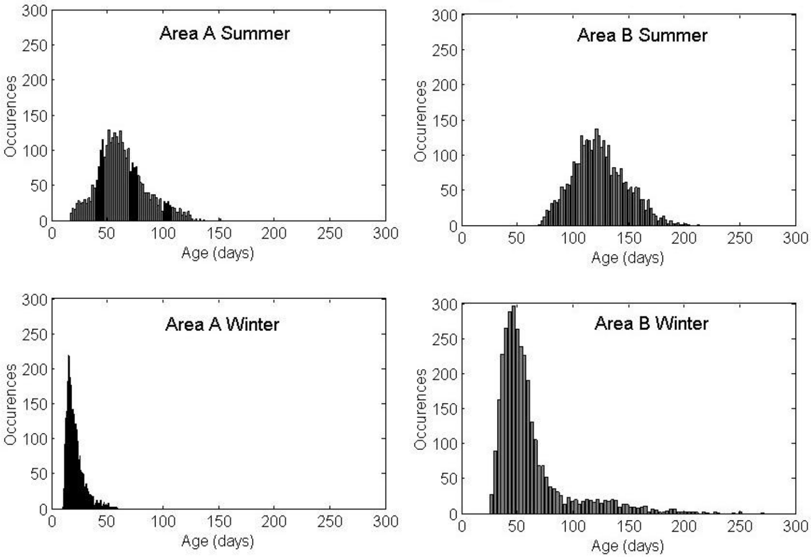

Figure 4.8.4. Summer and winter age distributions in areas A and B. (locations given in Figure 1.3.1)

The age distribution in area A in winter shows the presence of mainly young water with age between 10 and 60 days. In winter, area B has mean age of around 50 days, however, a large fraction of older water with ages between 90 and 200 days is present. These results support the idea that the oldest water resides in the vicinity of area B in winter. In this period a large fraction of new water is brought in from the west near area A. This must be balanced by an export flux from the system, to the north-east, of similar proportion, which must leave in late winter and early spring. It is most likely that this export flux contains a significant proportion of the oldest Strait water because the large portion of oldest water is not detected in areas A or B in summer.

It is not as difficult to interpret water age distributions as it is to interpret flushing time and residence time distributions when investigating seasonal circulation because the former traces the circulation directly. The time varying age distribution of water mass derived from the model suggests summer circulation increases the age of water mass, not flushed in the winter-spring period, by moving remnant older water at the eastern side to the west along the northern Tasmanian coast. The largest fraction of young water is brought in from the west during each winter-spring period. This is accompanied by the largest fraction of old water moving out towards the north-east. The age of water in the Strait has major implications for water mass transformation by air-sea exchanges. Older water is likely to have relatively higher salinity and therefore increased density upon winter cooling. The older water mass forms part of the Bass Strait Cascade.

4.9 Seasonal Cycle of Heat Fluxes

Seasonal variation of heat fluxes and incoming shortwave radiation from the reference simulation (spatially averaged over the region marked with crosses in Fig 1.3.1) is shown in Figure 4.9.1. A positive non-solar heat flux indicates an outgoing flux, whereas a positive solar flux represents an incoming flux. All non-solar heat fluxes, i.e. latent, sensible and longwave are positive at all times of the year, driving cooling of the model ocean, except when sensible heat flux is close to zero for a short period in spring (Figure 4.9.1 (a)). Mean wind speeds used for heat fluxes are shown in Figure 4.1.5 and are largest in winter and weakest in summer.

Latent heat flux is on average the highest of the non-solar heat fluxes and always positive, indicating a large part of the cooling of the model ocean is driven by this heat flux. It also has the largest diurnal variation in summer months, indicated by the thickness of the trace. The second largest non-solar heat flux is the longwave heat flux, which depends only on sea surface temperature. This is fairly constant at around ~ 65 W m^{-2} in agreement with typical values encountered in the ocean in the subtropics (Gill, 1982). The smallest non-solar heat flux is the sensible heat flux which ranges from a monthly mean of ~26 W m^{-2} in June to ~-0.2 W m^{-2} in September.

Sensible and latent heat fluxes are influenced by wind speeds and air-sea temperature differences. The latter via the effect air temperature has on specific humidity. Monthly mean air-sea temperature differences range from ~ 4.5^{o}C in summer to ~ 1.3 ^{o}C in winter. Mean air temperatures are nearly always lower than mean sea surface temperatures, except when mean air temperatures are a fraction higher than sea surface temperatures in September. Since there is no diurnal variation in wind included in the model, the stronger diurnal variation in summer for both latent and sensible heat fluxes is caused by stronger diurnal variation in sea-surface temperature, a response to the model diurnal incoming solar shortwave.

In winter, average sensible and latent heat fluxes over Bass Strait are more influenced by wind speed, however, in summer they are influenced by both wind speed and air-sea temperature differences.

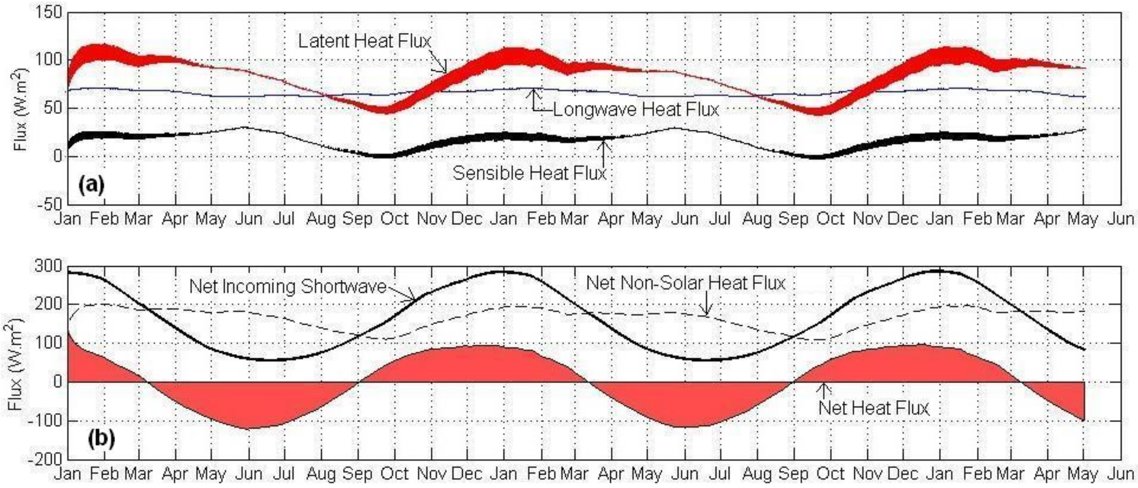

Figure 4.9.1. Simulated (a) non-solar and (b) net heat fluxes.

Figure 4.9.1(b) shows the net heat fluxes from the reference simulation. The net incoming shortwave, which accounts for surface albedo (0.06) and fractional cloud cover (Figure 4.1.7) ranges between about 277 W m^{-2} in summer to 57 W m^{-2} in winter. These maxima and minima correspond to the summer and winter solstices respectively. In Figure 4.9.1(b), the net non-solar heat flux is indicated by the dashed line and the net heat flux by the area filled with red. Net non-solar heat flux is always positive ranging from ~200 W m^{-2} in summer months to ~100 W m^{-2} in spring months, showing mainly an annual cycle of variation. The amplitude for the net heat flux spatially averaged over Bass Strait is suggested by the model to be ~100 W m^{-2}. When the net heat flux is negative, the ocean is losing heat through the surface and when it is positive the ocean is gaining heat. The result for net heat flux is close to having near seasonal equivalence in both heating and cooling periods. The annual-mean net heat flux in the model is close to zero (~ -0.5 W m^{-2}), indicating that a near steady annual cycle of heating and cooling has been achieved by the model. The slightly negative value indicates that from year to year there will be a slight loss of heat in Bass Strait.

4.10 Monthly Mean Fields for the Entire Simulation

The second year of the simulation is closer to steady state in the model than the first. This section presents evidence of this in spatial distributions of monthly mean water mass properties for the first two years and one month of the reference simulation. These results are presented as a guide to the reference simulation, to illustrate in more detail, the differences between the first and second years of the simulation. They are used to show that the model temperature cycle takes less time to spin up than the salinity cycle. Distributions are given for surface-layer temperature, salinity and density. Corresponding monthly mean surface-layer current velocity streamlines are also shown with the density fields. Due to the large amount of data processing required to generate these Figures, the monthly means are based on model output frames with 4 day intervals. Monthly means for water-mass properties are similar to what they would be if a larger amount of frames were averaged, however this is not the case for currents because they have greatest variation at the semidiurnal frequency. Due to this, coupled with the 4 day sampling rate, current streamlines in these results capture the high frequency tidal streams in times of weaker residual (non-tidal) currents. The same would be true if sea-level was averaged in this way.

Figure 4.10.1 shows how monthly mean surface-layer temperature progresses through the heating/cooling seasonal cycle and suggests anomalies in particular months, which on average are repeated each year. The second and third fields for January are in agreement, illustrating that the model largely has a closed seasonal cycle in temperature variation. Figure 4.10.2 illustrates how salinity reaches a closed cycle by the second summer of the simulation. Figure 4.10.3 shows monthly mean surface-layer density. The relationship between density and currents can be seen clearly in winter months where mean density distributions align with mean streamlines. In this situation, water mass properties in the model appear to be dominated by lateral advection of incoming water from the west. The smoothing of frontal structures is the effect of the mixing regime. In the times surrounding the winter season, the major pathway of water through the Strait is along a turning meander rather than a direct eastward flow pattern similar to that suggested by Fandry (1981), Middleton and Black (1994), Bruce *et al.* (2001), Cirano and Middleton (2004) and Sandery and Kämpf (2005) as shown in section 2.4.1. This meander increases transit times across the Strait.

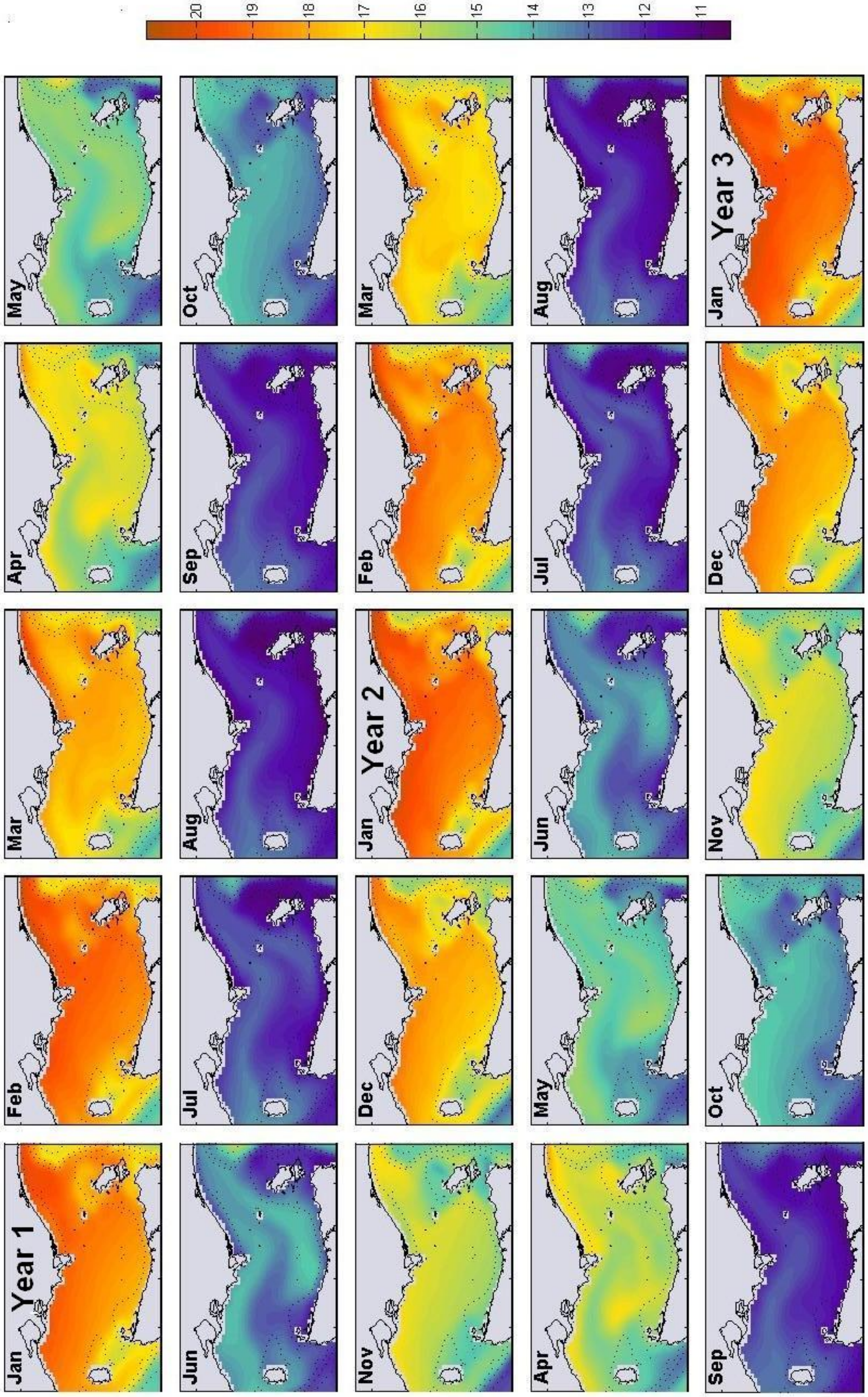

Figure 4.10.1. Monthly mean surface-layer temperature (^oC).

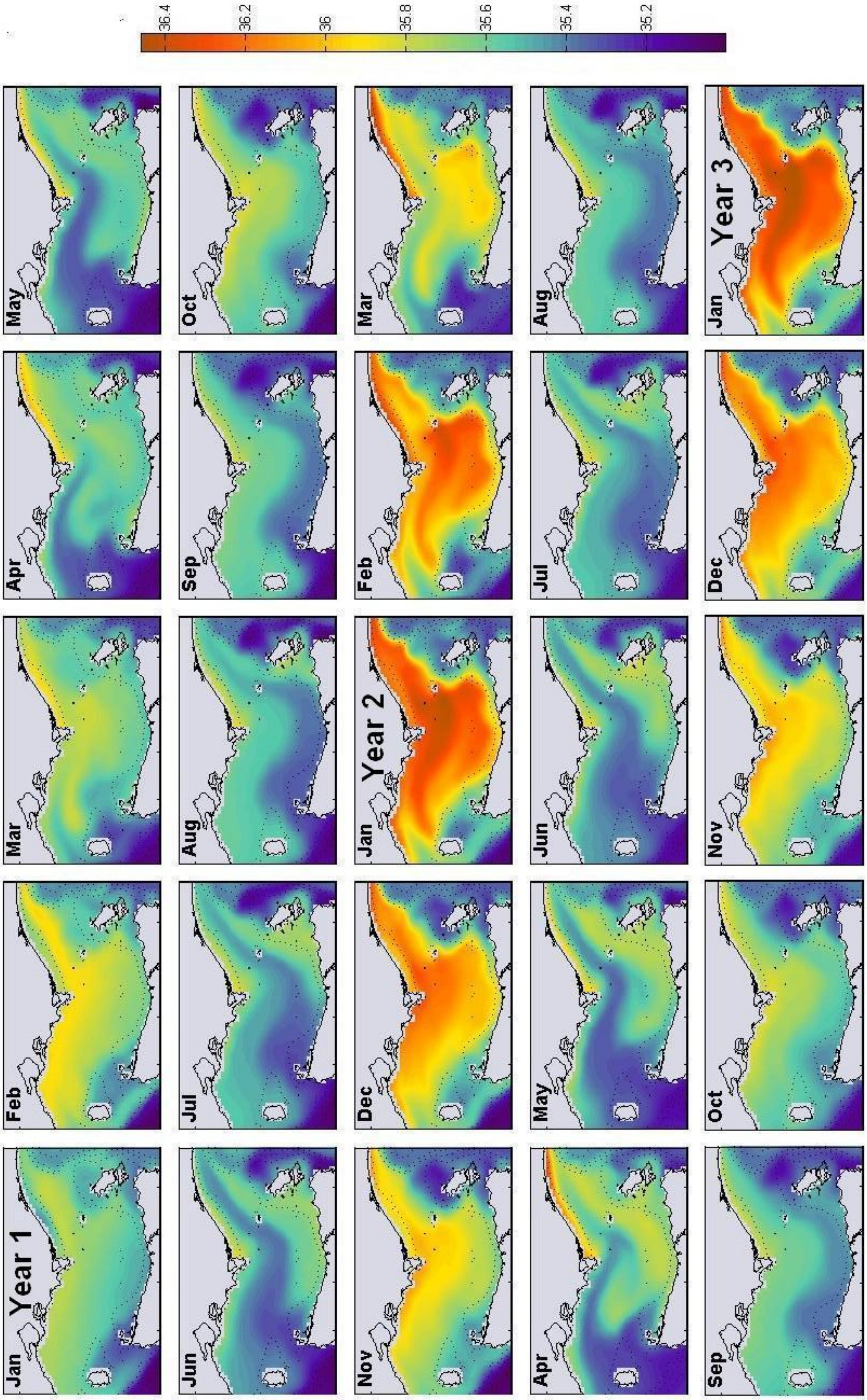

Figure 4.10.2. Monthly mean surface-layer salinity.

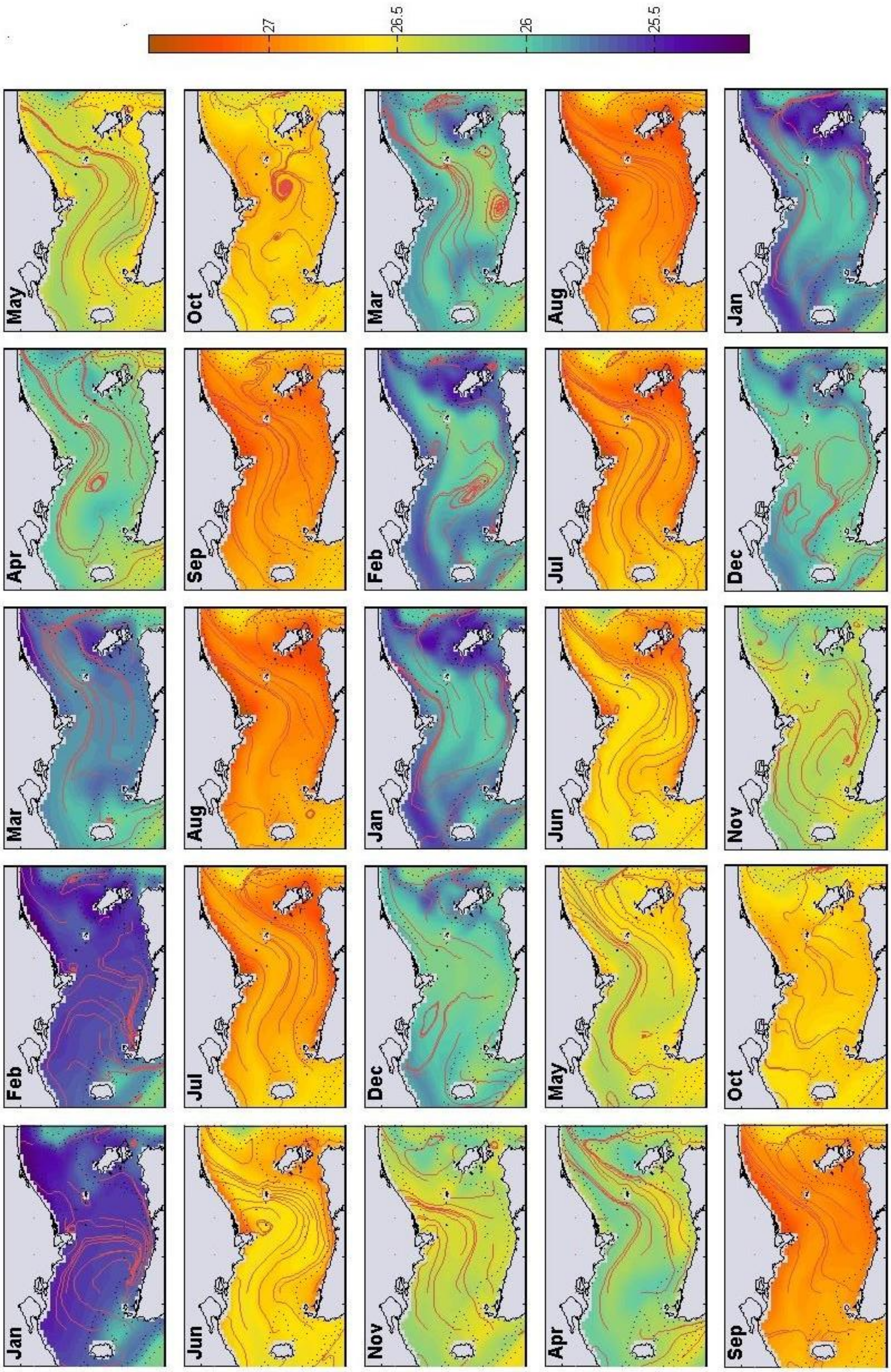

Figure 4.10.3. Monthly mean surface-layer σ_T (kg m^{-3}) and velocity streamlines.

4.11 Evaluation of Results

This section presents a quantitative evaluation and summary of information from the reference simulation, observations and previous studies regarding seasonal variation of physical properties in Bass Strait.

The data used in the study is compiled into monthly means and shown in Appendix A in Table A1, along with annual-means, ranges and summary statistics such as standard deviations, variances and root mean squared (RMS) values. Quantities from the model, and observed quantities, which are based on spatial distributions, are averaged over the control region delimited by crosses in Figure 1.3.1. The first 37 quantities in Table A1 are from the model and based on the second year of the reference simulation. Quantities 38-64 in Table A1 are from observations and previous studies, some of these quantities are means of the spatially varying atmospheric forcing fields presented in section 4.1.1. R^2 correlation coefficients, using the monthly means of selected quantities from the table, are calculated to gain a general assessment of the agreement or otherwise of the climate produced by observations and the climate produced by the model. The same selected quantities are also analysed in terms of the differences in annual-means. Figure A1 in Appendix A graphically illustrates seasonal trends based on the quantities in Table A1 and is presented as a supplement. Both Figure A1 and Table A1 are presented as a summary of the seasonal climate found in both the model and observations. Discussion of all of the trends is not carried out.

Figure 4.11.1 illustrates the seasonal correlations between selected monthly mean data sets given in table 4.11.2. Good seasonal agreement between model and atlas temperature and density, and incoming net shortwave radiation and net heat fluxes exists. In terms of the seasonal trends, low correlation between the wind magnitude data sets, model and atlas surface and bottom salinity and model and NCEP sensible and latent heat flux exists. HR and NCEP wind magnitudes have reasonable seasonal correlation (0.62), however, HR annual-means are ~3 m s^{-1} higher than NCEP. The annual-mean from CGBAPS wind data is ~3.8 m s^{-1} larger than NCEP. This could be explained by the fact that CGBAPS data is not spatially averaged and at a location which experiences stronger winds than further east and north. The low correlation in salinity can be explained in the following way. Salinity in the Bass Strait area in the model is responsive to atmospheric forcing and driven by latent heat fluxes, which are maximum in summer due to the air-sea temperature difference formulation adopted in the model. Salinity in the model decreases during the winter for two reasons. The first is that evaporation minus precipitation becomes slightly negative and the second is that lower salinity water is advected into the Strait from the west. The atlas suggests the reverse, i.e. that salinity in the Strait is maximum in winter and minimum in summer. A possible explanation why atlas salinity has opposite seasonal phase is found in CTD observations. Mean salinity from these observations is higher in winter than in summer, yet maximum salinity is highest in summer and lowest in winter. Due to the fact that the sampling is limited to northern Bass Strait and parts of winter and summer, the atlas may not have included enough salinity measurements to resolve the seasonal cycle in the Strait correctly. This means that the seasonal correlation between Atlas and Model salinity is not valid due to insufficient data.

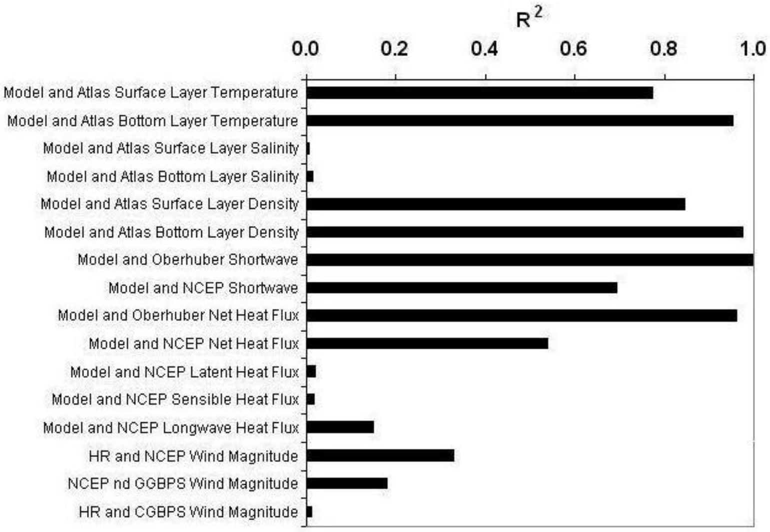

Figure 4.11.1. R^2 correlation coefficients between monthly means of selected quantities.

Differences in annual-means of the same selected quantities, shown in Figure 4.11.1, are shown in table 4.11.1. Despite model salinity having low agreement with the atlas in terms of the seasonal trend, the differences in annual-means are reasonable in both the surface (0.21) and bottom-layers (0.07). Model monthly mean surface salinity data, spatially averaged over the control region, has standard deviation of around 0.2 whilst the equivalent atlas value is 0.08. The similarly defined standard deviation for bottom-layer salinity data is 0.03 for the model whilst the equivalent atlas value is 0.05.

The relatively higher uncertainty in observed and modelled heat fluxes is highlighted in the results. This can be seen in Appendix A in Table A1 (page 166). Annual-mean model and Oberhuber incoming shortwave radiation has a large difference of ~17 W m^{-2}. Annual-mean model and NCEP net heat flux disagree by ~16 W m^{-2}. Model annual-mean net heat flux is close to zero (~-0.5 W m^{-2}). A zero value implies no annual net gain or loss of heat content. NCEP and Oberhuber annual-mean net heat fluxes are large and negative (~ -15 to -16 W m^{-2}) and imply that on an annual basis water mass in Bass Strait loses heat to the atmosphere by air-sea heat fluxes. The seasonal density cycle of water mass in the Strait is suggested to be in near equivalence by Baines and Fandry (1983). If NCEP and Oberhuber values were correct, consistent inflow of warmer water would be necessary, otherwise Strait waters would cool by several degrees each year. The model suggestion that the net heat flux is close to zero is probably more reliable because it is forced by observed quantities and is a dynamic solution involving circulation and water mass properties, which are in good overall agreement with observations. Model annual-mean net heat flux is in closer agreement with the study by Stephens *et al*. (1981).

Model and Atlas Surface-layer Temperature (^{o}C)	0.05
Model and Atlas Bottom-layer Temperature (^{o}C)	-0.26
Model and Atlas Surface-layer Salinity	0.21
Model and Atlas Bottom-layer Salinity	0.07
Model and Atlas Surface-layer Density (kg m^{-3})	0.14
Model and Atlas Bottom-layer Density (kg m^{-3})	0.11
Model and Oberhuber Shortwave (W m^{-2})	17.24
Model and NCEP Shortwave (W m^{-2})	8.51
Model and Oberhuber Net Heat Flux (W m^{-2})	15.19
Model and NCEP Net Heat Flux (W m^{-2})	16.00
Model and NCEP Latent Heat Flux (W m^{-2})	-8.60
Model and NCEP Sensible Heat Flux (W m^{-2})	-3.05
Model and NCEP Longwave Heat Flux (W m^{-2})	4.16
HR and NCEP Wind Magnitude (m s^{-1})	4.07
NCEP and GGBAPS Wind Magnitude (m s^{-1})	-2.10
HR and CGBAPS Wind Magnitude (m s^{-1})	-1.98

Table 4.11.1. Difference in annual-means of selected quantities.

The relatively large differences in annual-mean wind speed magnitude between CGBAPS, Hellerman-Rosenstein and NCEP reanalysis data is also evident. HR winds are ~ 3 times stronger than NCEP winds and CGBAPS winds are ~ 2 times stronger. One would expect that the differences would be larger than scalar quantities on the basis of their non-linear derivation, however, accuracy of wind information is important in the results. This is highlighted in section 5.5 where HR winds, instead of NCEP, are used to force surface momentum fluxes in the model.

4.12 Uncertainty in Model Results and Observations.

Both the model results and observations contain varying degrees of uncertainty. The statistics in Table A1 reflect the varying degrees of uncertainty in all the important variables that govern the physical system. The model result is the response of a physical system to values prescribed at its boundaries. In this study, the values are monthly-mean variables, mainly from a reanalysis data set, which are derived from observations. This type of averaging smooths out variability in the data and to some extent may unrealistically smooth uncertainty. Regardless, the uncertainty in observations propagates in the model domain. Most uncertainty in model results arises from signals prescribed in open-sea boundaries, in surface forcing to generate the momentum, salt and heat fluxes, and in the parameterisation of these fluxes and sub-grid scale mixing. Further uncertainty, but to a lesser degree comes from interpolation errors and approximation of bottom topography and coastal boundaries. The least uncertainty arises from approximations made in the dynamical equations (McIntosh and Bennett, 1984). Model open-boundaries were set some distance from the study region in an attempt to minimize their influence on uncertainty in the results in the area of interest.

Another area, in which compromise was made in the model, was the choice to limit the maximum depth in the open-ocean part of the domain to 1000 m. This choice was made to increase vertical resolution in the upper part of the open ocean. This was an attempt to resolve seasonal water mass variation in the surrounding upper mixed layer which is essentially one of the boundary conditions for the Strait. The effect of doing this was most pronounced on the results for open ocean circulation, which effectively became less geostrophic due to bottom friction. The complexity of modelling water mass properties in Bass Strait is increased because of the extensive shelf break and continental slope surrounding the Strait. These are boundaries between the deep ocean circulation and the shelf seas which are characterised by strong current systems with features such as fronts, meanders, filaments and eddies. The processes of separation, encroachment, upwelling and downwelling also occur along these boundaries. The influence on water mass properties is a complex interactive system which requires further study.

In terms of particular variables, the areas of best agreement between the reference simulation and observations are in the seasonal surface and bottom-layer temperatures and in the incoming shortwave and net heat fluxes. The model also resolves the tides and the seasonal onset and breakdown of stratification in the interior in agreement with observations and previous studies. Model winter salinity distribution is in favourable agreement with the underway derived distributions and Tomczak (1985). The lowest correlation is found between the model and atlas seasonal cycle of salinity and the latent and sensible heat fluxes. Surface salinity values are predicted to be higher in a shallow layer in summer, yet close to atlas values in the other seasons. Bottom salinity values are close to atlas values in all seasons. The low correlation comes from the fact that the phases of seasonal variation are almost opposite, and more pronounced, in shallow water. Model maximum salinities are found in summer, whereas atlas maximum salinities are found in winter. At present there appears to be insufficient data to resolve the salinity cycle. Correlations with model results in terms of salinity are therefore unreliable.

The reference simulation suggests that surface salinity in summer in the central parts of Bass Strait has maximum mean values up to 36.2 in a shallow layer between 2 and 20 m depth. This maximum is ~ 0.4 greater than values given in previous studies, the CARS atlas and historical CTD observations. The present study did not include riverine freshwater fluxes into the region. This is thought to be of minor consequence for salinity in the Strait because a number of inlets in the region exhibit high salinities (Tomczak, 1985). The most prominent Estuary is the Tamar which exhibits salinity of around 34.5 in the entrance channel with low seasonal variation (Lara and Niera, 2003). More recently, mean salinity of 36.33 was observed in south-eastern Bass Strait, between the 4th and 22nd of April 2005, in an area of ~ 25 m water depth. The range of measured values encountered in this survey was 36.26 to 36.41 (Aquenal, 2005).

If errors in the thermodynamic forcing can be assumed to be small, then the model and recent observations suggest a phenomenon which may presently exist. This may have gone undetected due to the timing and locations of sampling or may be reminiscent of a phenomena occurring in years of anomalously high evaporation in summer. The record of salinity in Bass Strait needs more data in order to resolve this.

Maximum values of salinity are could be exaggerated if model evaporation is too high in summer. Even so, in a relative sense, the anomaly and its variation would probably appear with similar features in a model more closely tuned to observations. A decrease in air-sea temperature difference or a decrease in wind speed in summer would lower the latent and sensible heat fluxes, causing less evaporation and warmer water. The temperature cycle in the model would then compare less favourably with observations. The feedback cycles involved in the heat fluxes also depend on the vertical mixing and transport of heat away from the surface.

Another aspect influencing salinity is rainfall over the ocean where large uncertainties exist due to lack of direct measurements. Model salinity in winter was in good agreement with observations and was effectively reduced from high summer surface-layer values by vertical mixing, lateral advection and export of the salt towards the east. Evaporation was limited in winter by small air-sea temperature and humidity differences and precipitation in winter caused a small freshwater flux (negative E-P) into the surface. Rainfall data over the Strait may have been underestimated in summer. It is biased towards land values in coastal areas due to the spatial resolution. The uncertainty in summer surface-layer salinity, as predicted by the model, can be only be verified through improvements in estimates of oceanic precipitation in the region.

CHAPTER 5:
Sensitivity to Variation in Forcing

5.1 Introduction

This chapter presents and analyses selected sensitivity studies which were carried out to test the effects of various changes in forcing. The first three experiments use exactly the same details and parameters as the reference simulation, the only differences are listed in table 5.1. These are designed to illustrate the importance of the processes on the long-term integrations. The assumption made here is that the processes contribute linearly to the system. Non-linear interactions between processes are neglected. The results of these experiments are compared to the reference simulation. In the reference simulation surface-layer fields exhibit larger variation than bottom-layer fields (Table A1). This layer is usually where differences in properties are usually more pronounced and so it is focussed on in this chapter. Depth-averaged flushing times are also presented to summarise the integrated differences between sensitivity studies and model results. The fourth experiment in Section 5.5 differs from the other sensitivity experiments in that it presents the response of the model to coastal-trapped wave forcing only.

Experiment	Description
1	No prescribed seasonal variation in residual sea-level in model open boundaries.
2	No tidal forcing.
3	Surface momentum and heat fluxes forced with Hellerman-Rosenstein wind stresses rather than NCEP reanalysis winds.
4	Coastal-trapped wave forcing.

Table 5.1. Sensitivity experiments.

5.2 Experiment 1

The regional current forcing conditions in the open-sea boundaries were used in the reference simulation to generate hydrographic properties in the open-ocean part of the model domain which were closer to observations. Prescribing an inflow with atlas hydrographic properties leads to propagation of those properties into the model domain. As mentioned earlier, the final maximum amplitudes for the parameters A_{SAC} and A_{EAC}, used in the reference simulation, were 0.12 cm and 0.3 cm respectively. These were largely determined based on adjustments aimed at achieving annual-mean water properties of open-ocean waters in the model domain closer to those given by the CARS2000 atlas, rather than from a complete analysis of historical sea-level data. In this experiment A_{SAC} and A_{EAC} are set to zero.

The results show that if a signal in the north-western model open boundary for the effect of the South Australian Current and the Zeehan Current is not included, salinity becomes lower than observations in south-western Bass Strait. Also, signatures of the East Australian and Zeehan Currents are virtually non existent in these model solutions. The prescribed seasonal sea-level signal in the north-western open-sea boundary gives rise to a model South Australian and Zeehan Current system in winter. The inclusion of this regional current boundary condition is required to maintain a winter front at the western shelf break of Bass Strait. The salinity in the Strait is found to be sensitive to this front.

The effect of prescribing a model EAC was found to have an almost negligible effect on Strait salinity. The EAC was only seen to influence water mass properties in the interior of the Strait if it was prescribed as an unrealistic sustained encroachment on the continental shelf.

Seasonal-mean sea-level anomaly and depth-averaged currents are shown in Figure 5.2.1. The results have the following differences to the reference simulation.

- Winter sea-levels have similar structure but are lower by ~ 5 cm across northern Bass Strait. Sea-level gradients in this season are weaker causing approximately 25% weaker currents.

- Lower sea-levels are found in spring in the south-eastern area.

- Summer circulation has similar features, however low pressure in centre is less pronounced.

- Negative sea-level anomalies are found in autumn.

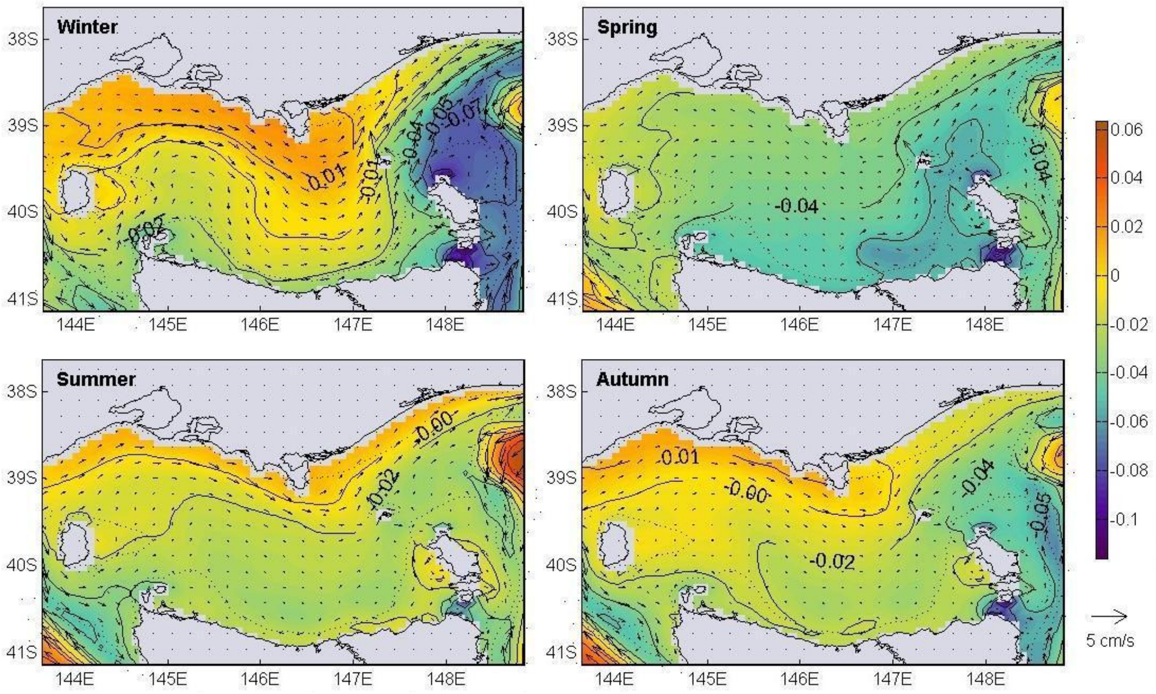

Figure 5.2.1. Seasonal-mean sea-level anomaly (m) and depth-averaged currents (cm s^{-1}) in Experiment 1. (vectors interpolated to every third grid point)

Seasonal-mean surface-layer salinity is given in Figure 5.2.2. The following important differences to the reference simulation are noted.

- Winter surface-layer salinity is lower in western Bass Strait and water of < 35.1 is seen intruding between Cape Grim and King Island in the surface-layer. There is no front in winter along the shelf break west of this passage. A front develops at this location in spring and summer, which acts to maintain higher salinities in Bass Strait. This front disappears in autumn.

- Surface-layer salinities are generally lower (~ 0.1-0.15) than in the reference simulation, but higher than those suggested by the CARS atlas (~ 0.2).

Figure 5.2.3 shows seasonal-mean surface-layer temperature. Important differences to the reference simulation are that

- Surface-layer summer temperatures are approximately similar in southern Bass Strait, however, they are up to 0.5°C warmer in northern parts.

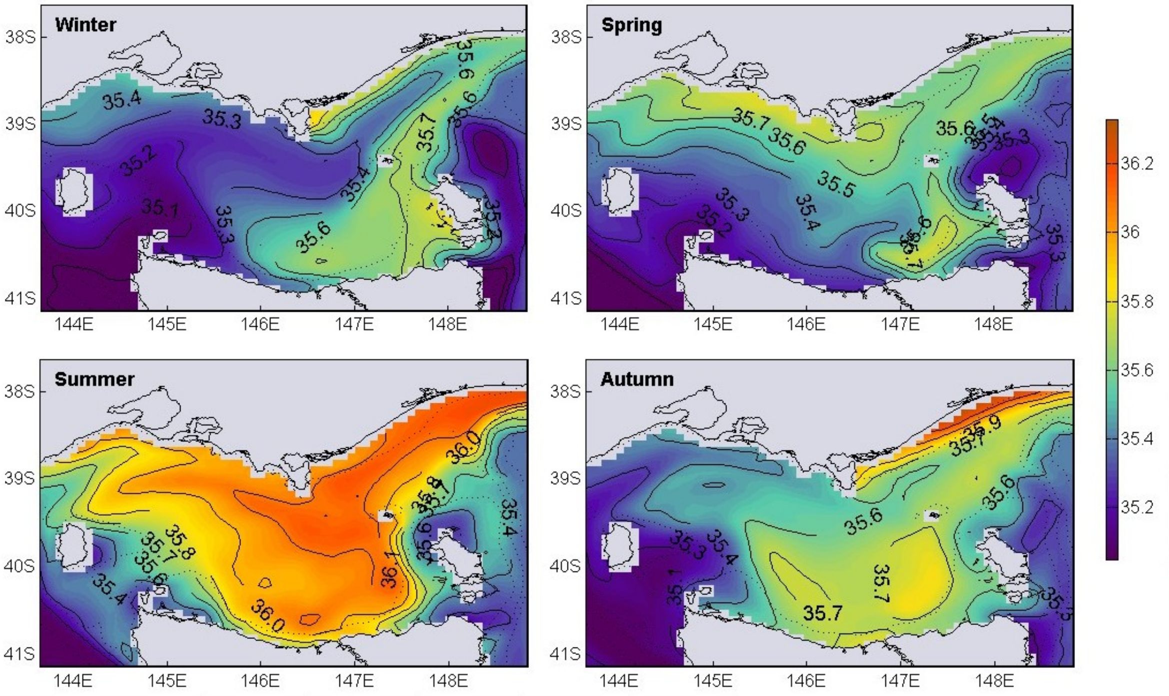

Figure 5.2.2. Seasonal-mean surface-layer salinity in Experiment 1.

- Surface-layer winter temperatures are colder by up to 1.3°C in western parts.

- Surface-layer spring and autumn temperatures are generally up to 0.5°C colder.

Seasonal-mean surface-layer density is shown in Figure 5.2.4. Comparison to the reference simulation reveals that

- Winter surface-layer density is higher by about 1 kg m^{-3}, reflecting the presence of colder water. The densest water is found in similar areas, i.e. the shallow parts of eastern Bass Strait.

- Spring surface-layer density is up to 1.3 kg m^{-3} higher in the interior reflecting the presence warmer water. The densest water is suggested to be in the same areas, i.e. the shallow parts of eastern Bass Strait.

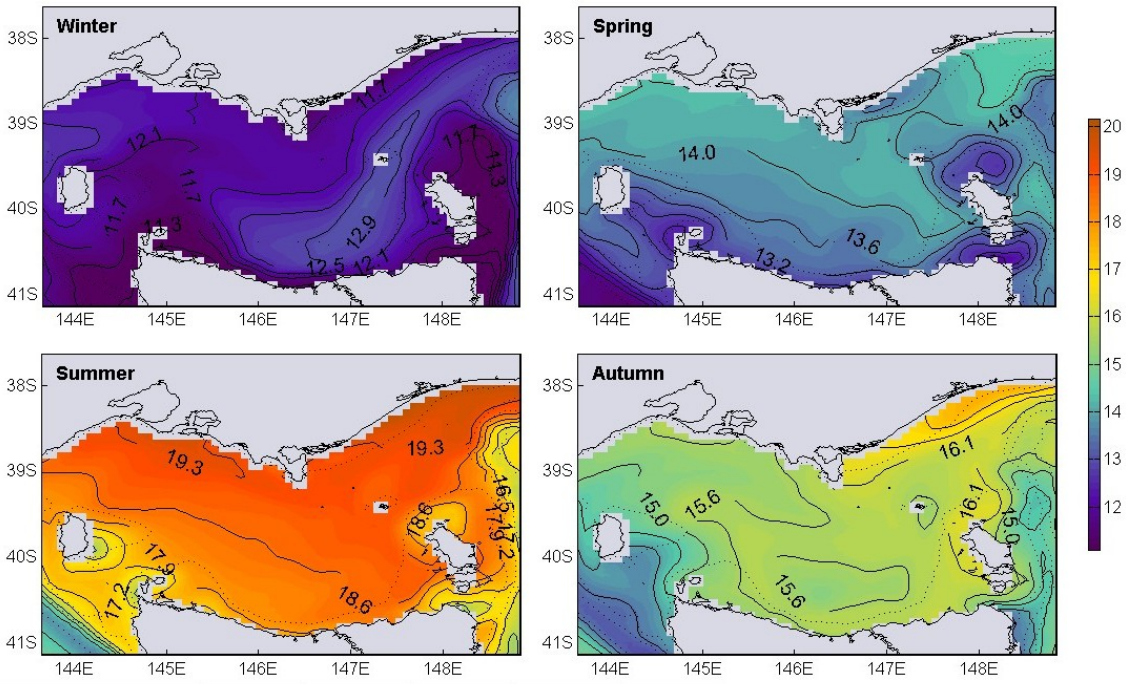

Figure 5.2.3. Seasonal-mean surface-layer temperature (^{o}C) in Experiment 1.

- Summer surface-layer density in the interior is lower, reflecting the presence of lower salinity water than the reference simulation.

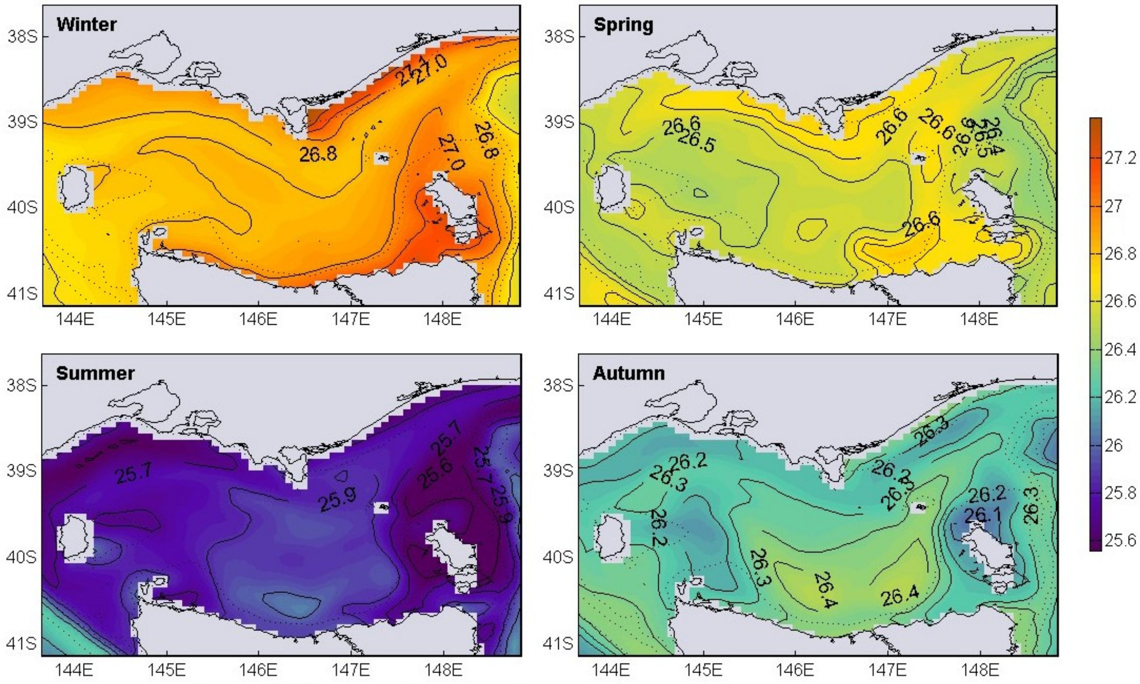

Figure 5.2.4. Seasonal-mean surface-layer σ_T (kg m^{-3}) in Experiment 1.

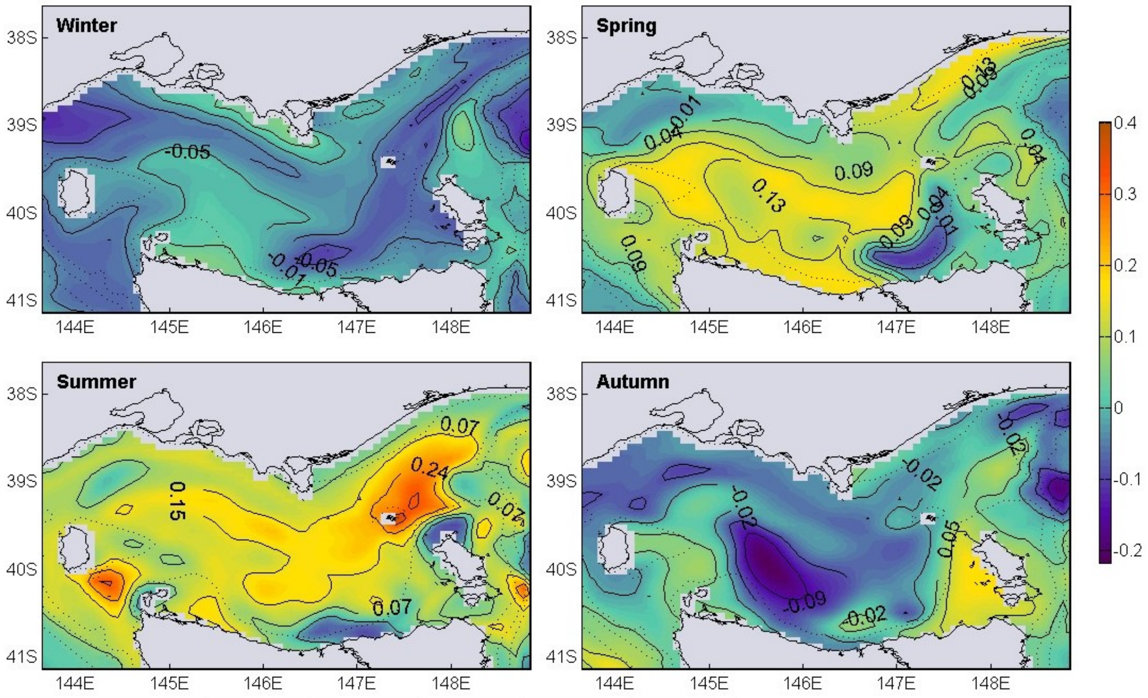

Figure 5.2.5. Difference between reference simulation and Experiment 1 surface-layer σ_T (kg m^{-3}).

- Surface-layer density has comparable values in autumn, however, differences in structure. This result shows the presence of two patches of 26.4 kg m^{-3} in the interior, whereas the reference simulation has only one patch of similar density.

Seasonal-mean surface-layer currents are presented in Figure 5.2.6. With regards to the differences between Experiment 1 and the reference simulation

- Winter, autumn and summer surface-layer currents are lower by about 0.1 m s^{-1} in the interior.

- Spring surface-layer currents are smaller by about 0.2 m s^{-1} in the interior.

A time series of spatial and temporally averaged surface and bottom-layer model and atlas temperatures and salinities is given in Figure 5.2.7. Compared to the reference simulation there is generally warmer surface-layer water and colder bottom-layer water in winter. An explanation for this is weaker vertical mixing leading to greater differentiation of surface and bottom temperatures. Mean salinities are lower in winter than atlas data and the reference simulation. The high surface-layer salinity anomaly in summer is not as pronounced in this experiment as in the reference simulation.

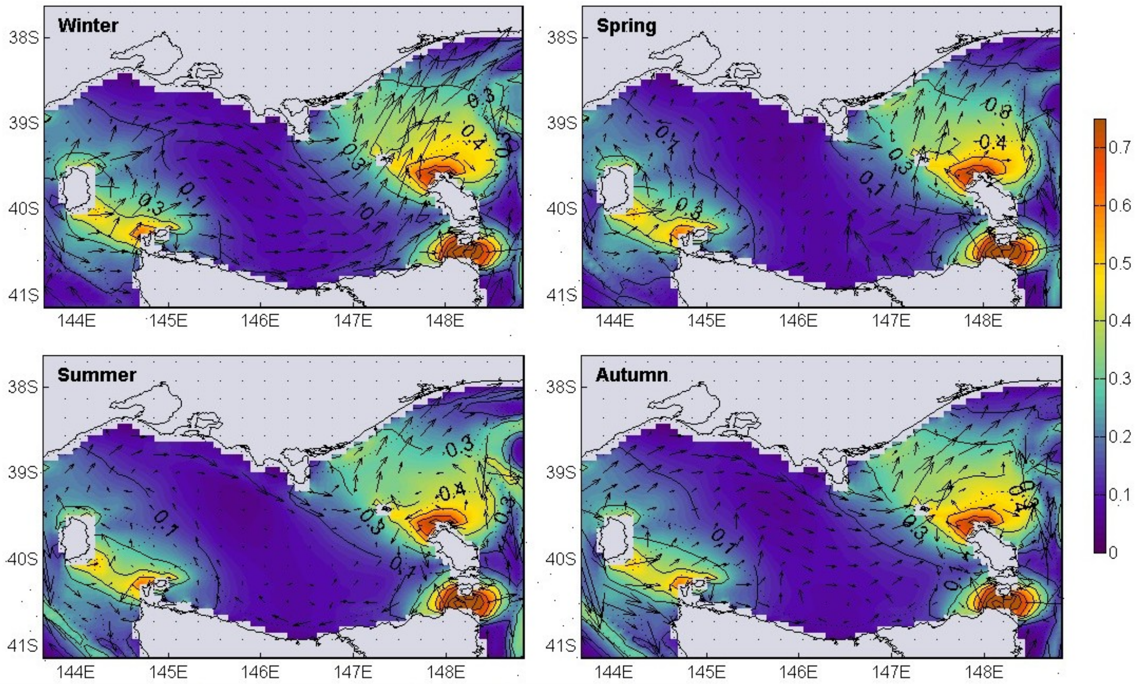

Figure 5.2.6. Seasonal-mean surface-layer currents (m s^{-1}) in Experiment 2. (vectors interpolated to every third grid point)

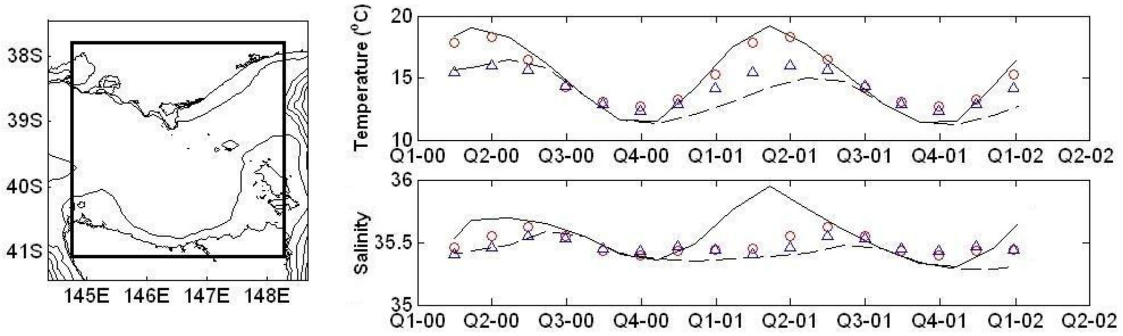

Figure 5.2.7. Time series of seasonal mean surface and bottom-layer model and atlas temperature (°C) and salinity spatially averaged over Bass Strait interior for Experiment 1. Red circles and black triangles represent atlas surface and bottom-layer values respectively. Continuous and dashed lines represent model surface and bottom-layer values respectively.

This is mainly due to this experiment not having a winter front off western Tasmania, caused by the model SAC. In the reference simulation, this front inhibits lower salinity water of more southern origin to enter the Strait via the south-western passage in winter.

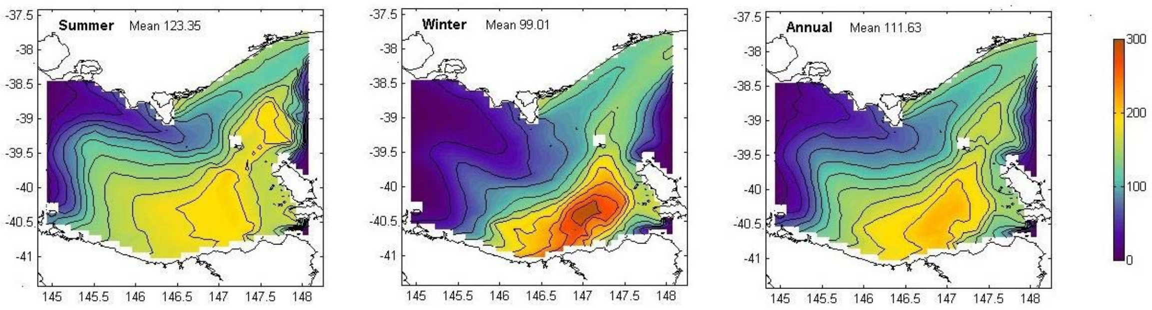

Figure 5.2.8. Annual, winter and summer mean flushing times (days) for Experiment 1.

In this experiment, annual, winter and summer mean flushing times are longer (~ 20 %) than those given in the reference simulation, reflecting weaker currents (Figure 5.2.8). The area with the longest flushing times is about 0.5° further west in this experiment.

5.3 Experiment 2

This experiment illustrates the effect of not including tides in a regional model for Bass Strait. It was shown in section 4.2 that residual tidal flow is minimal in most parts of the Strait. This implies tides play virtually no role in lateral advection of water mass through the Strait interior. On the other hand, the role of tidal mixing in the Strait entrances influences the density field, which in turn affects the currents. This experiment tests the effect of tidal mixing on water mass properties and the residual circulation. The exclusion of tidal forcing in the model is summarised by looking at mean seasonal flushing time distributions.

Seasonal-mean sea-level anomaly and depth-averaged currents are presented in Figure 5.3.1. Comparing these results to the reference simulation shows that

- Sea-level gradients are generally higher leading to stronger currents at all times.
- The summer circulation suggested in the reference simulation is not present.
- The circulation has the similar characteristic meander at all times, with varying strengths in the different seasons which is caused by sea-levels to the north-west being relatively higher.

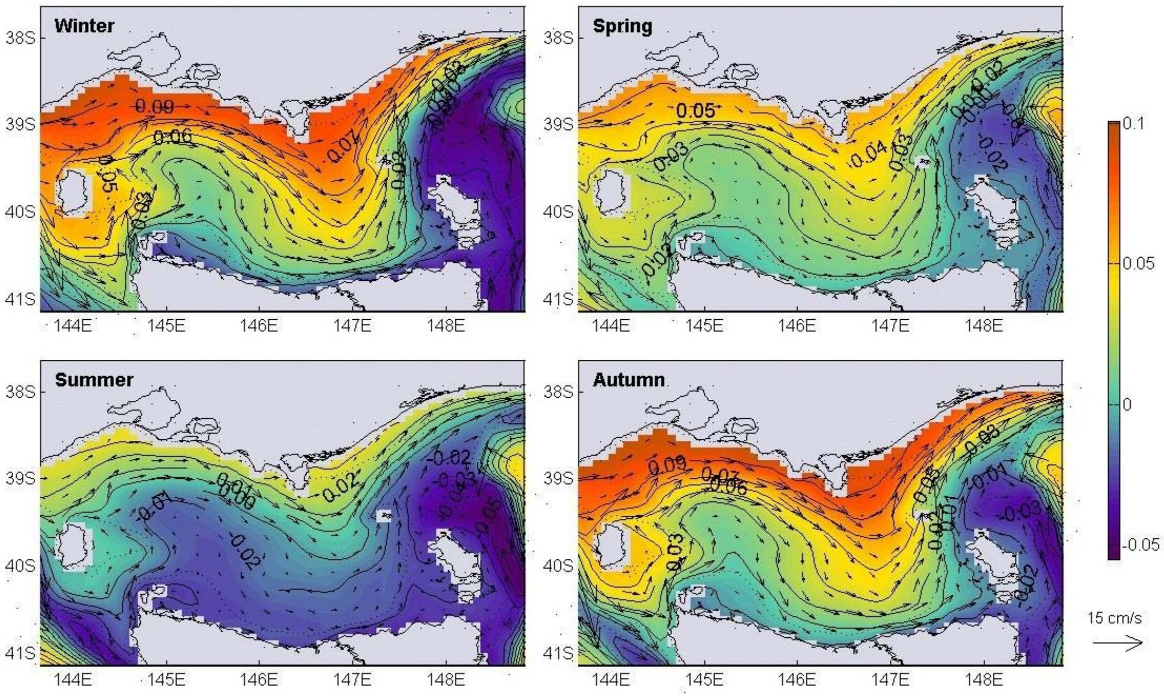

Figure 5.3.1. Seasonal-mean sea-level anomaly (m) and depth-averaged currents (cm s^{-1}) for Experiment 2. (vectors interpolated to every third grid point)

Model predictions of seasonal-mean surface-layer salinity in Experiment 2 are shown in Figure 5.3.2. The results show that with respect to the reference simulation

- Winter salinities are lower by ~0.2 . This seems to be the partially the result of intrusion of water mass through the south-western passage and advection of atlas properties into the northern part of the Strait from the model SAC forcing.

- Salinities in spring are comparable, except for lower salinities (~0.1) along the northern Tasmanian coastline.

- In summer, maximum surface-layer salinity is comparable to the reference simulation in the centre of the Strait, however it is clear that salinities in the Strait entrances are generally higher than the reference simulation (~0.25).

- In general, autumn surface-layer salinities are lower by about 0.2 due to stronger advection of water mass into the Strait from the west.

Seasonal-mean surface-layer temperature in Experiment 2 is given in Figure 5.3.1. Reasons given earlier for the differences here are similar to those given for salinity such as

- Winter surface-layer temperatures are slightly lower by ~0.2°C.

- Surface-layer temperatures are a fraction warmer in spring (~0.1-0.2°C).

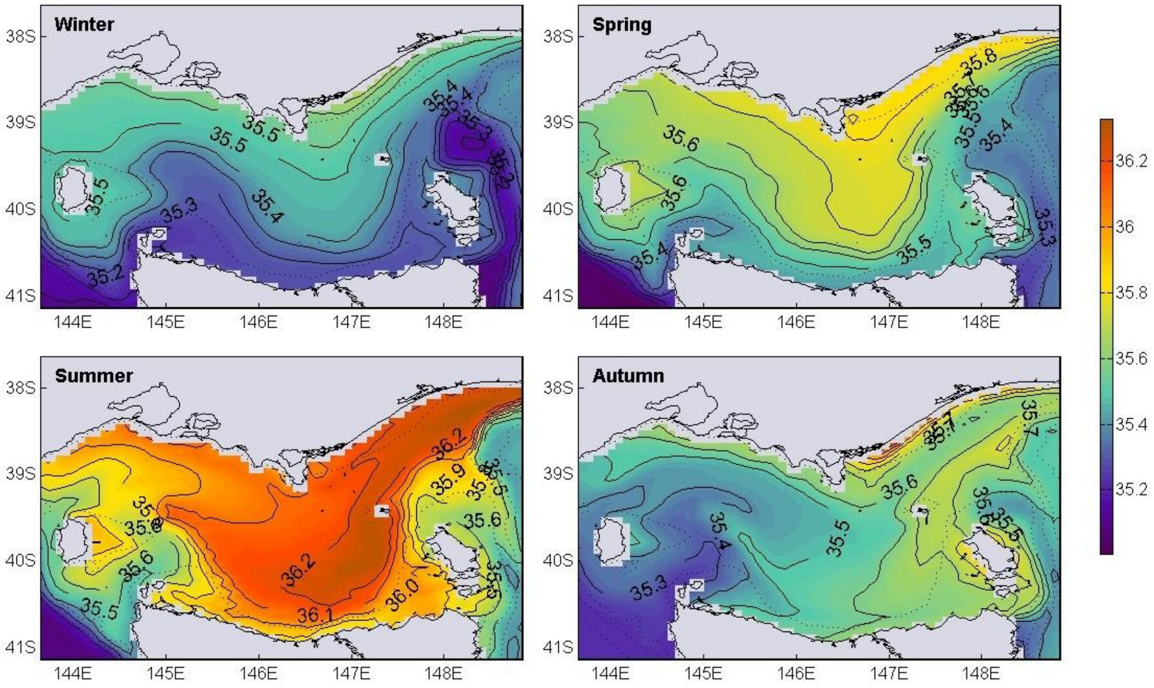

Figure 5.3.2. Seasonal-mean surface-layer salinity in Experiment 2.

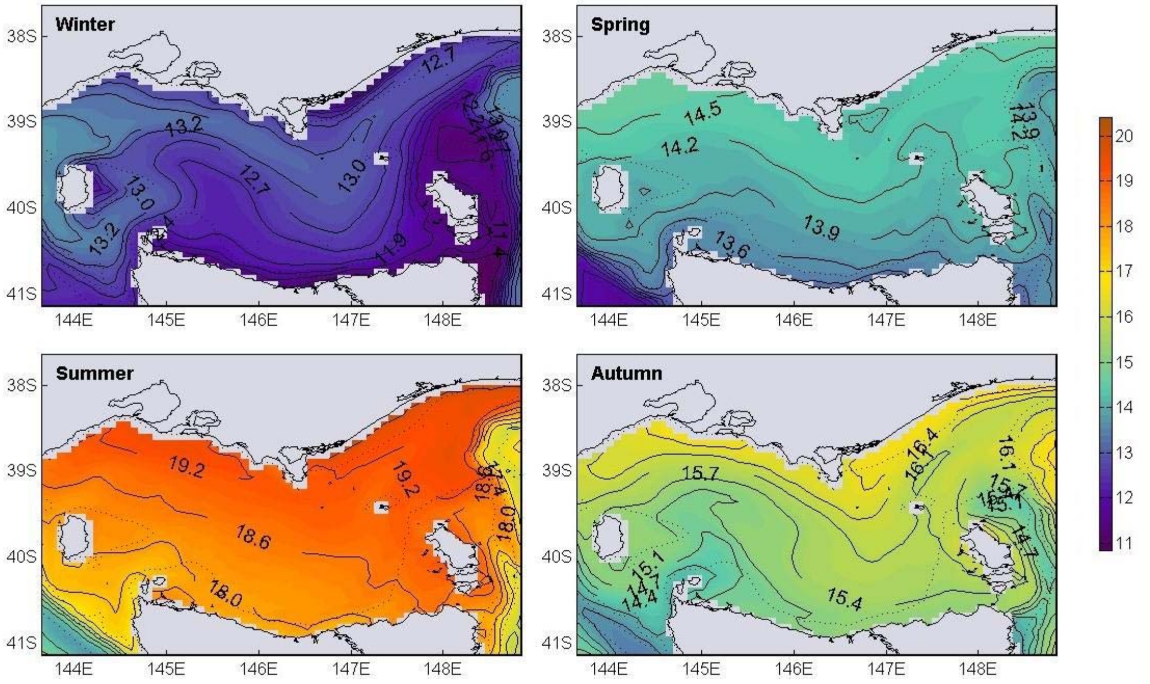

Figure 5.3.3. Seasonal-mean surface-layer temperature (°C) in Experiment 2.

- Summer surface-layer temperatures are generally higher in northern Bass Strait by up to ~0.5°C and significantly higher in Banks Strait by up to 2°C, indicating that the tides mix in cooler water to these areas.

- Autumn surface-layer temperatures are lower by up to ~0.5°C in some parts of the south-western area. They are lower by ~0.2°C in the north-western area and comparable in the north-eastern area.

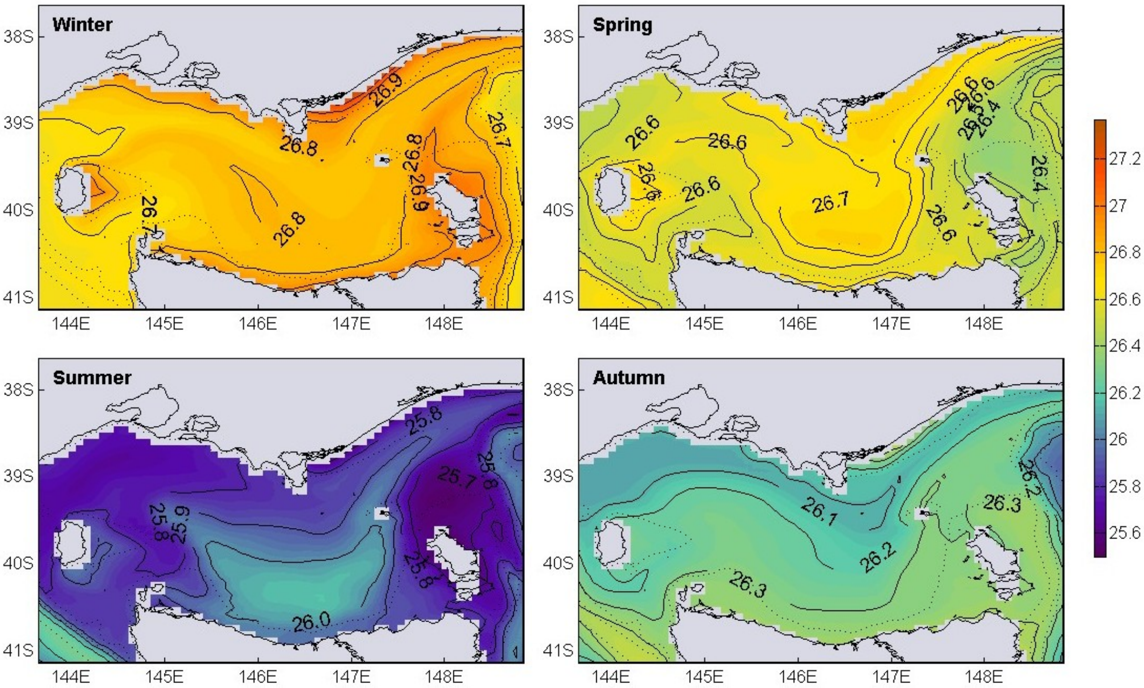

Figure 5.3.4. Seasonal-mean surface-layer σ_T (kg m^{-3}) in Experiment 2.

Figure 5.3.4 shows seasonal-mean surface-layer density in Experiment 2. This result has the following important differences to the reference simulation which are quantified in Figure 5.3.5. The differences include characteristics such as

- Winter surface-layer densities being lower along the northern Tasmanian coastline and in parts of eastern and north-eastern Bass Strait, mainly due to the presence of lower salinity water. Negative areas in Figure 5.3.5 indicate denser water in this experiment caused by colder water.

- Surface-layer densities being lower in spring in eastern Bass Strait which relate to the presence of warmer water in the areas which usually have strong tidal influence. They are also lower along the northern coastal boundary due to warmer water and lower along the southern coastal boundary due to lower salinity water. A pool of denser water in the southern Strait interior is the result of the presence of saltier water.

- Summer surface-layer densities containing a variety of positive and negative anomalies compared to the reference simulation which are caused by a combination of temperature and salinity differences explained earlier.

- Surface-layer density is higher in autumn in an area in the southwest, north of Flinders Island and in the vicinity of Bass Canyon. It is lower in the central south-eastern part of the Strait.

These different characteristics are differences in advection and diffusion which is reflected in the surface-layer current speed distribution shown in Figure 5.3.6.

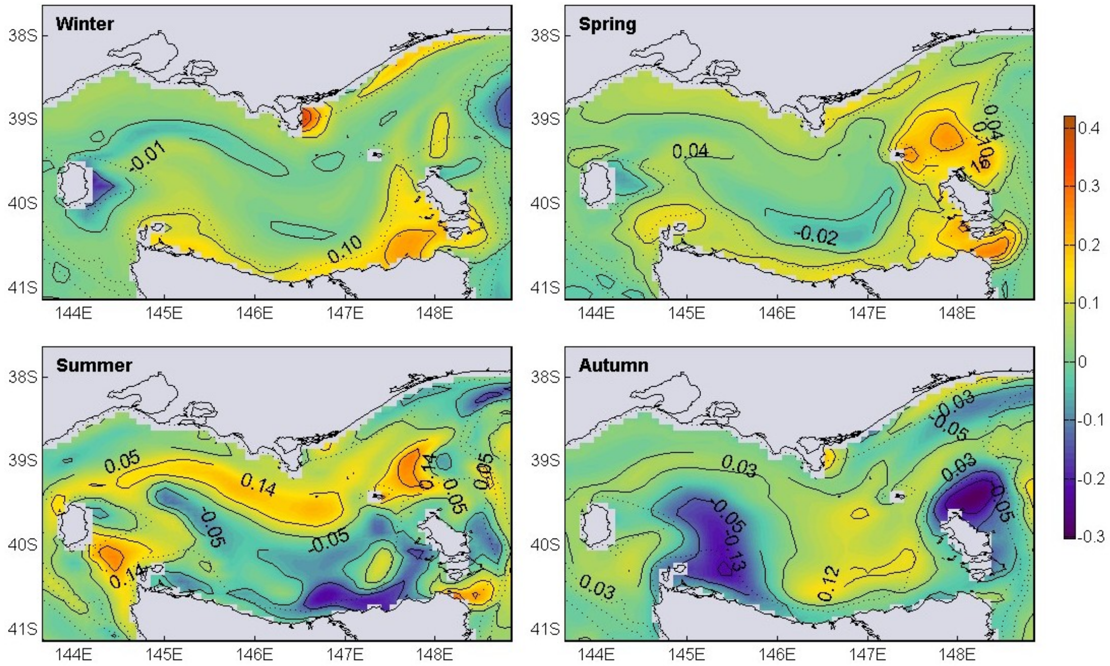

Figure 5.3.5. Difference between Experiment 2 and reference simulation surface-layer σ_T (kg m^{-3}).

A time series of spatial and temporally averaged surface and bottom-layer model and atlas temperatures and salinities is shown in Figure 5.3.7. With no tidal forcing, temperature attains higher surface and lower bottom values in summer. This symbolises weaker vertical mixing, leading to a higher level of apparent stratification.

Wind driven mixing is strong enough, however, to breakdown the stratification in winter. Atmospheric forcing in the model still dominates surface-layer salinities in summer.

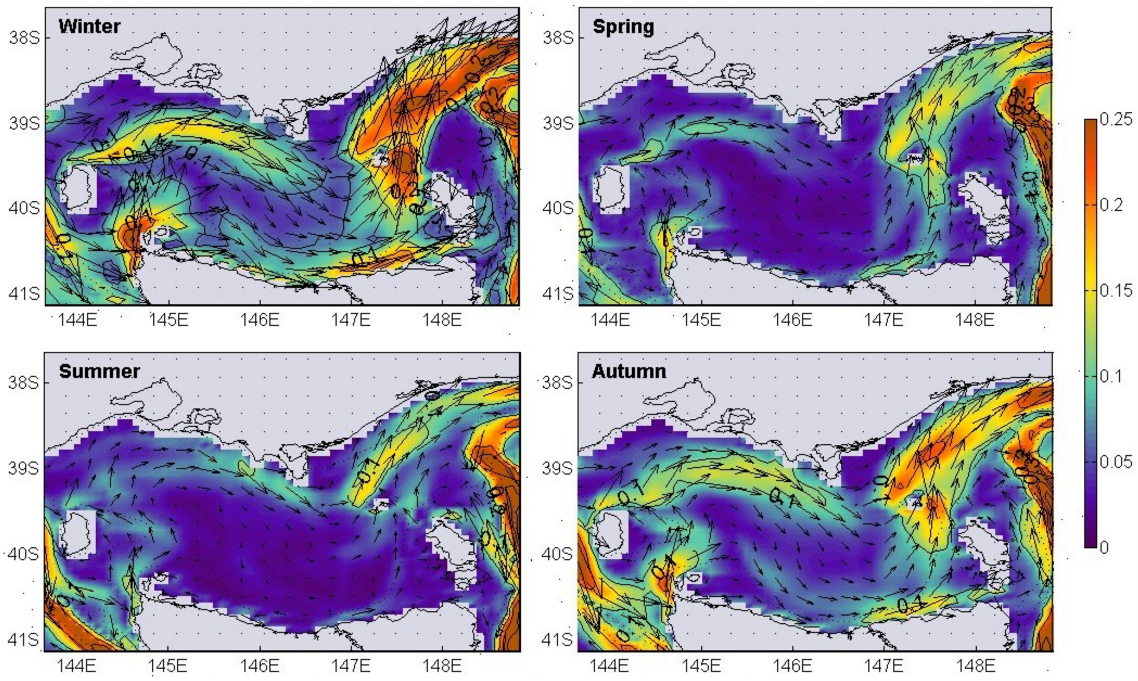

Figure 5.3.6. Seasonal-mean surface-layer currents (m s^{-1}) in Experiment 2. (vectors interpolated to every third grid point)

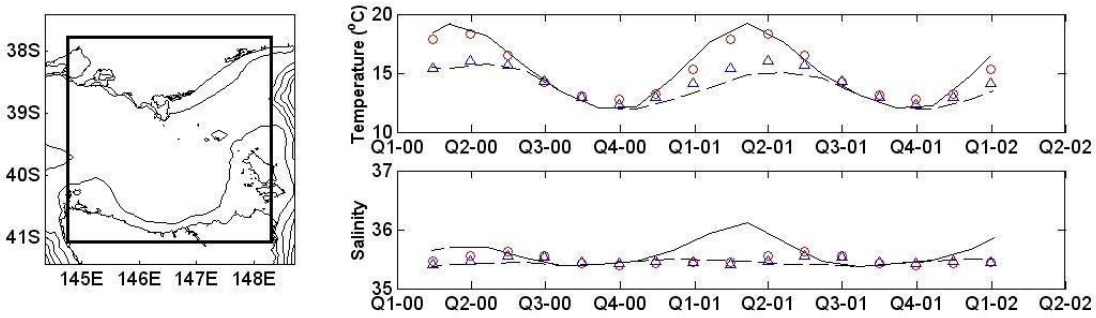

Figure 5.3.7. Same as for 5.2.7 but for Experiment 2.

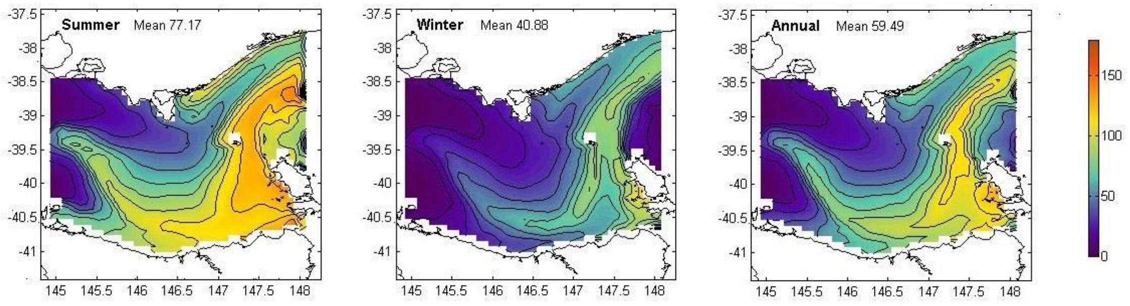

Figure 5.3.8. Annual, winter and summer mean flushing times (days) for Experiment 2.

In Experiment 2, annual, winter and summer mean flushing times are considerably shorter (~35%) than those given in the reference simulation, reflecting overall stronger mean currents (Figure 5.3.8) (note that the colour scale has changed). Less seasonal variation in the circulation is evident in similarities in spatial distribution of the summer and winter flushing times. The large change in strength of the circulation between summer and winter is highlighted in the difference in magnitude of flushing times.

5.4 Experiment 3

The Hellerman-Rosenstein (HR) wind stress climatology is considered to be an over-estimate of wind stresses over the Bass Strait region (M. Tomczak pers. comm., 2005). Comparison with means from a long-term wind data set from Cape Grim Baseline Air Pollution Station (CGBAPS) (shown in Figure 4.1.1 and Table A1) confirms this proposition. Long-term means from NCEP reanalysis data compare much more favourably with CGBAPS data. Forcing the model with HR data therefore provides a guide to an expected (perhaps unreasonable) upper limit for residual circulation in Bass Strait.

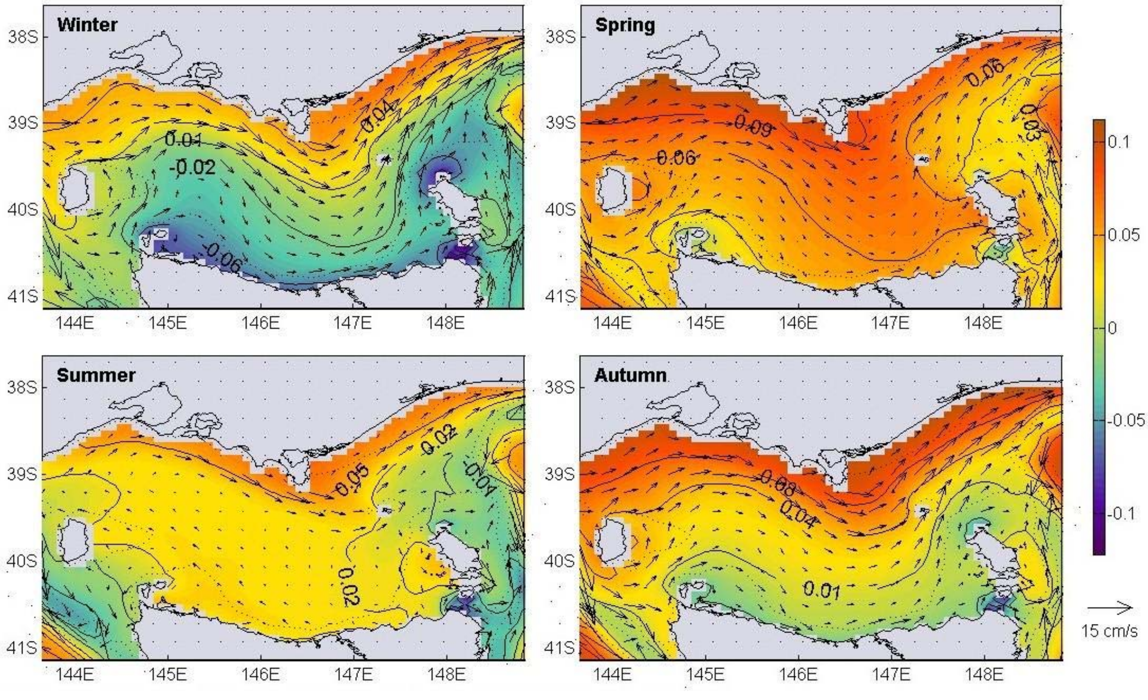

Figure 5.4.1. Seasonal-mean sea-level anomaly (m) and depth-averaged current vectors (cm/s) for Experiment 3 (vectors interpolated to every third grid point)

The main differences in NCEP and HR winds are that HR winds are significantly greater in magnitude, contain less spatial variation and have southerly to westerly mean wind patterns (Figure 4.1.1.3) compared to southerly to north-westerly mean wind patterns in NCEP (Figure 4.1.1.4).

Seasonal-mean sea-level anomaly is shown in Figure 5.4.1. The main differences between this experiment and the reference simulation are as follows:

- Sea-levels are higher in summer, with no negative anomalies occurring, nor does a distinctive low pressure cell develop in the southern interior. Even so, summer depth-averaged currents are westward in southern and western Bass Strait.
- Sea-levels are lower in winter in the southern region by about 4 cm, yet are comparable in the northern and some eastern parts, leading to larger gradients and stronger currents.
- Sea-levels are 1-2 cm higher in spring, yet have similar spatial distribution.
- Sea-levels are comparable in northern Bass Strait in Autumn, however they are up 2-3 cm lower in the southern region, leading to larger gradients and stronger currents.

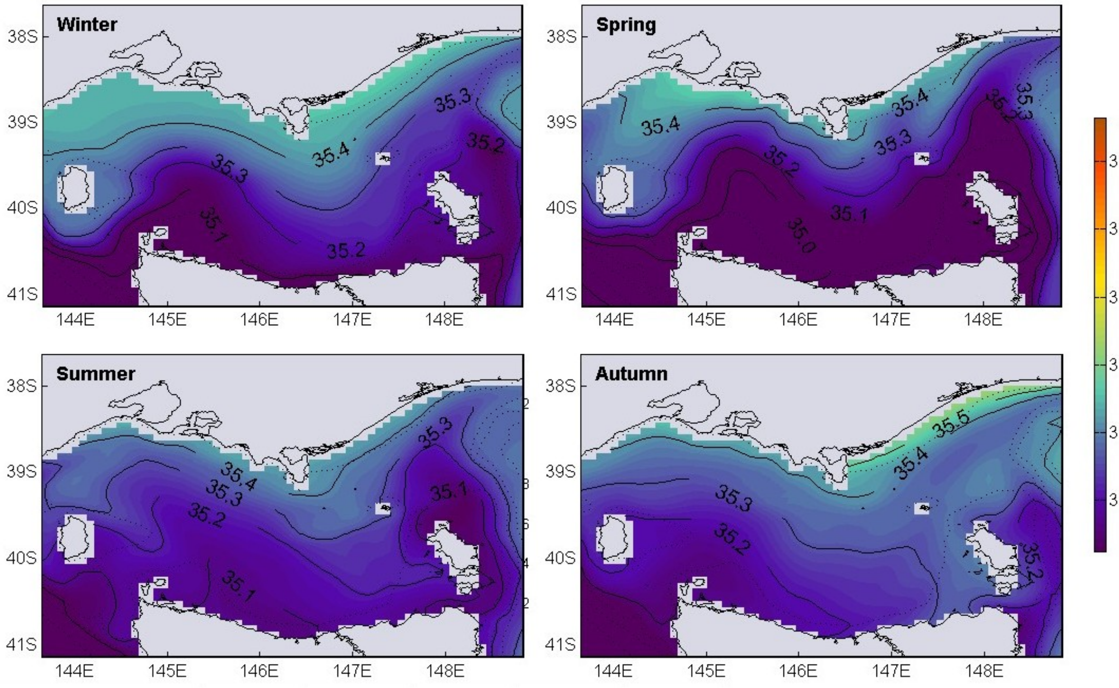

Figure 5.4.2. Seasonal-mean surface-layer salinity in Experiment 3.

Seasonal-mean surface-layer salinity is illustrated in Fig 5.4.2. The main difference between this experiment and the reference simulation is that salinity is lower at all times with less range of variation (~0.5). This is mostly due to lateral inflows as the heat flux forcing is similar to the reference simulation (HR winds used to drive momentum fluxes only, see section 3.6.4, p 66). HR winds are larger in magnitude than NCEP and drive a larger amount of lower salinity water through the south-western entrance in winter. They also enhance open boundary inflow at the north-western corner of the model at times other than summer. Enhanced transport through the south-western entrance is due to the lowering of sea-level in the south-western Strait corner in response to westerly wind forcing.

Seasonal-mean surface-layer temperature distributions for Experiment 3 are illustrated in Figure 5.4.3. Comparing these to the reference simulation reveals that:

- Winter temperatures are comparable in magnitude and distribution.
- Spring temperatures have similar distribution but are ~0.6^{o}C colder along the northern Tasmanian coastline
- Summer temperatures are ~0.25^{o}C warmer with similar distribution.
- Autumn temperatures are up to ~0.5^{o}C warmer in the centre of the Strait, similar along the Victorian coastline, and ~0.5^{o}C colder along the Tasmanian coastline.

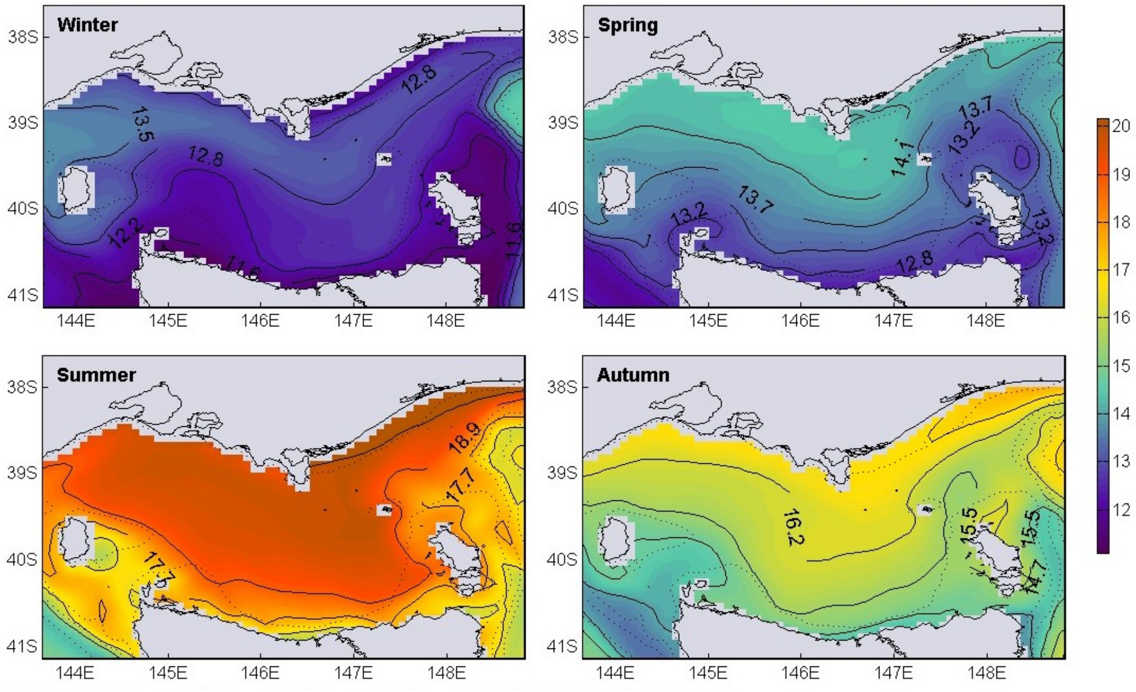

Figure 5.4.3. Seasonal-mean surface-layer temperature (^{o}C) in Experiment 3.

Seasonal-mean surface-layer density is shown in Figure 5.4.4. The main differences between the reference simulation and this experiment are shown in Figure 5.4.5 which gives the seasonal-mean density difference between the experiments as spatial distributions.

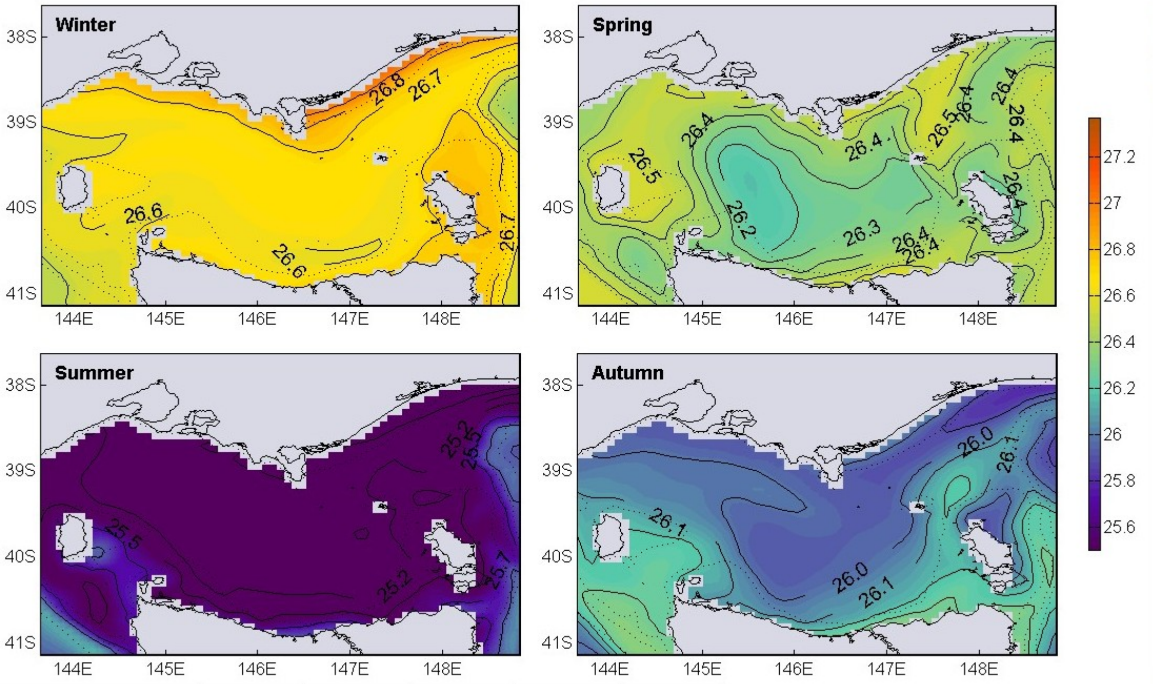

Figure 5.4.4. Seasonal-mean surface-layer σ_T (kg m^{-3}) in Experiment 3.

Surface-layer density difference in winter shows this experiment has higher density (~1 kg m^{-3}) on average due to colder temperatures (Figure 5.4.5). The density difference diminishes in spring yet is still higher (~0.5 kg m^{-3}), again due to the presence of slightly colder water.

Warmer temperatures and lower salinities in summer lead to this experiment having lower density (up to ~1 kg m^{-3}) than the reference simulation. This difference carries into autumn, however, the differences are smaller (~0.25 kg m^{-3}) than summer.

Seasonal-mean surface-layer currents for experiment 3 are shown in Fig 5.4.6. The main difference between the reference simulation and this experiment is that mean currents in the interior of the Strait are approximately 30% larger in this experiment. Currents in the passages are dominated by tides and exhibit smaller differences between experiments.

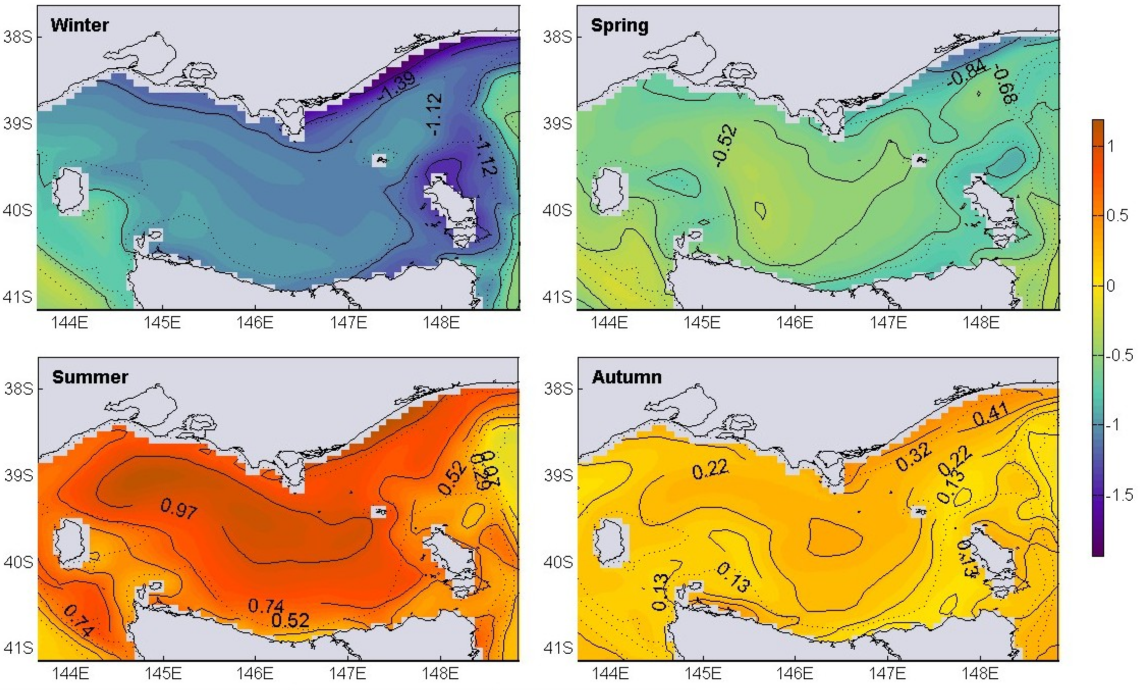

Figure 5.4.5. Difference between reference simulation and Experiment 3 surface-layer σ_T (kg m^{-3}).

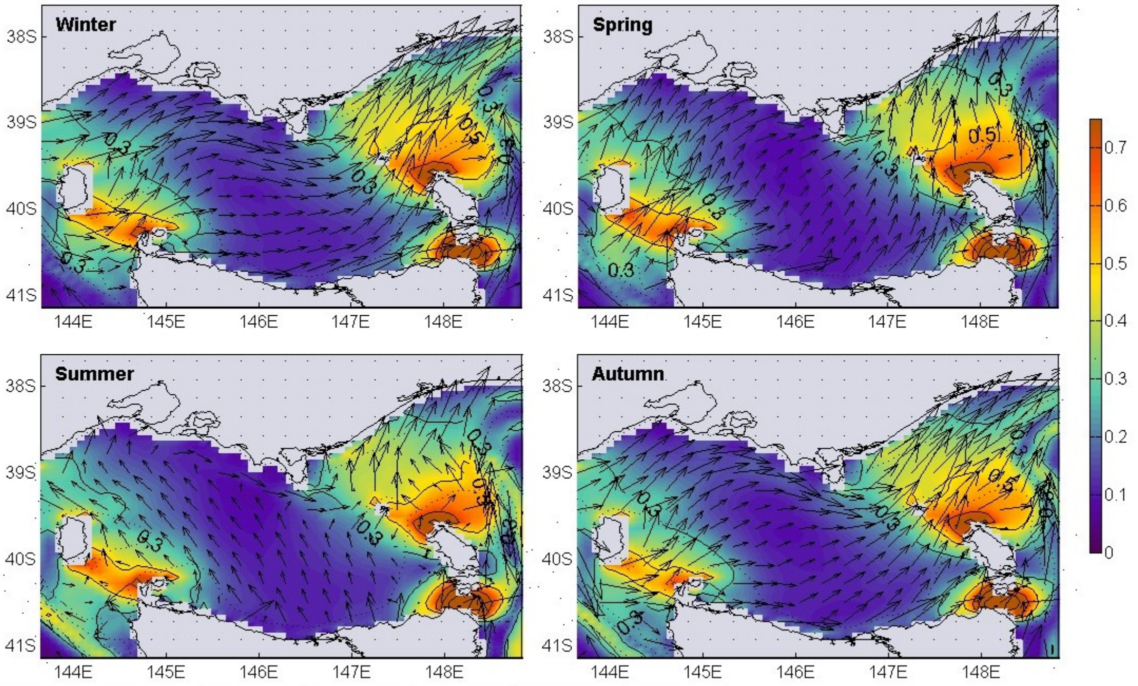

Figure 5.4.6. Seasonal-mean surface-layer currents (m s^{-1}) in Experiment 3. (vectors interpolated to every third grid point)

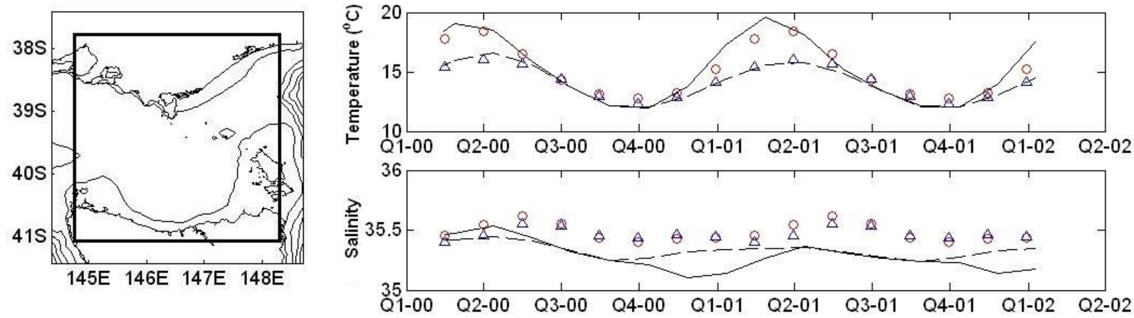

Figure 5.4.7. Same as for 5.2.7 but for Experiment 3.

A time series of spatial and temporally averaged surface and bottom-layer model and atlas temperatures and salinities is shown Figure 5.4.7. With the stronger mean winds, even the prescribed model SAC is not strong enough to maintain a relatively high salinity front off western Bass Strait. Mean salinity in the Strait stabilises in this experiment at a level about 0.2 below atlas values. Figure 5.4.7 shows advection of lower salinity surface-layer water over higher salinity bottom-layer water occurs between September and February.

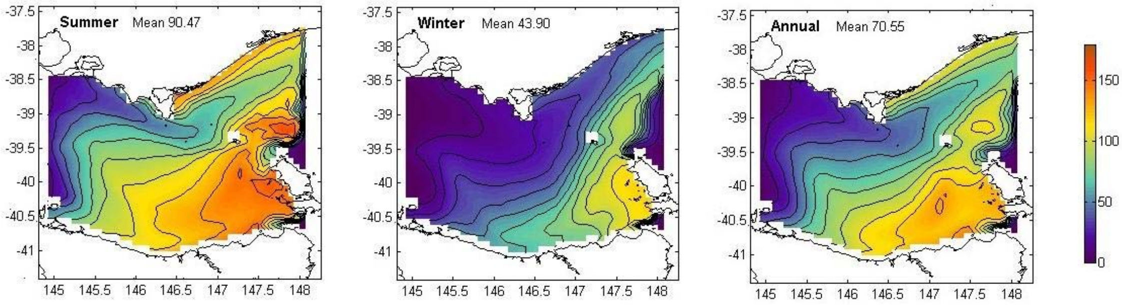

Figure 5.4.8. Annual, winter and summer mean flushing times (days) for Experiment 3.

In Experiment 3, annual, winter and summer mean flushing times are shorter (~20%) than those given in the reference simulation (Figure 5.4.8), reflecting stronger mean currents. Variation in the circulation is evident in differences in the spatial distribution between summer and winter flushing times. A large change in strength of the circulation between summer and winter is highlighted in the difference in magnitude of flushing times between these seasons.

5.5 Residual Effect of Coastal-Trapped Wave Forcing

Results from the first CTW experiment, described in section 3.6.2, are not shown as the results are similar to the second experiment which is shown here. In the first experiment, the forcing signal has zero long-term mean and provides virtually no residual throughflow in Bass Strait. However, the signal supplies a certain amount of energy for mixing and erodes the tracer fronts in similar fashion, yet smaller in magnitude, to results for the second experiment, which are shown in Figure 5.5.1. The second CTW experiment involves forcing the model for one year with the signal labelled ‘Filtered A’ in the north-western open boundary. The original time series and low-pass filtered signals are shown in Figure 5.5.1.

The low-pass 90 day filtered signal illustrates an underlying trend in long-term residual sea-level at Portland in 2004. The first half of the year has mean of around zero whereas the second half of the year it is consistently positive (1.5-3 cm). This is suggested to be related to variation in mean density driven and wind driven processes, both of which change the flux of the South Australian Current (Ridgway and Condie, 2004).

The residual effect predicted by the model on the circulation in Bass Strait is typified in surface-layer tracer concentration fields (Figure 5.5.2). Incident CTWs are predicted by the model not to have a significant effect on residual currents in Bass Strait at seasonal timescales. The main effect is erosion of the tracer fronts, mostly at the western entrance.

The result in Figure 5.5.2 can also be compared with the result for the predicted effect of the tides on residual currents in Figure 4.2.2. The results are similar however the tides produce larger residual currents in the model.

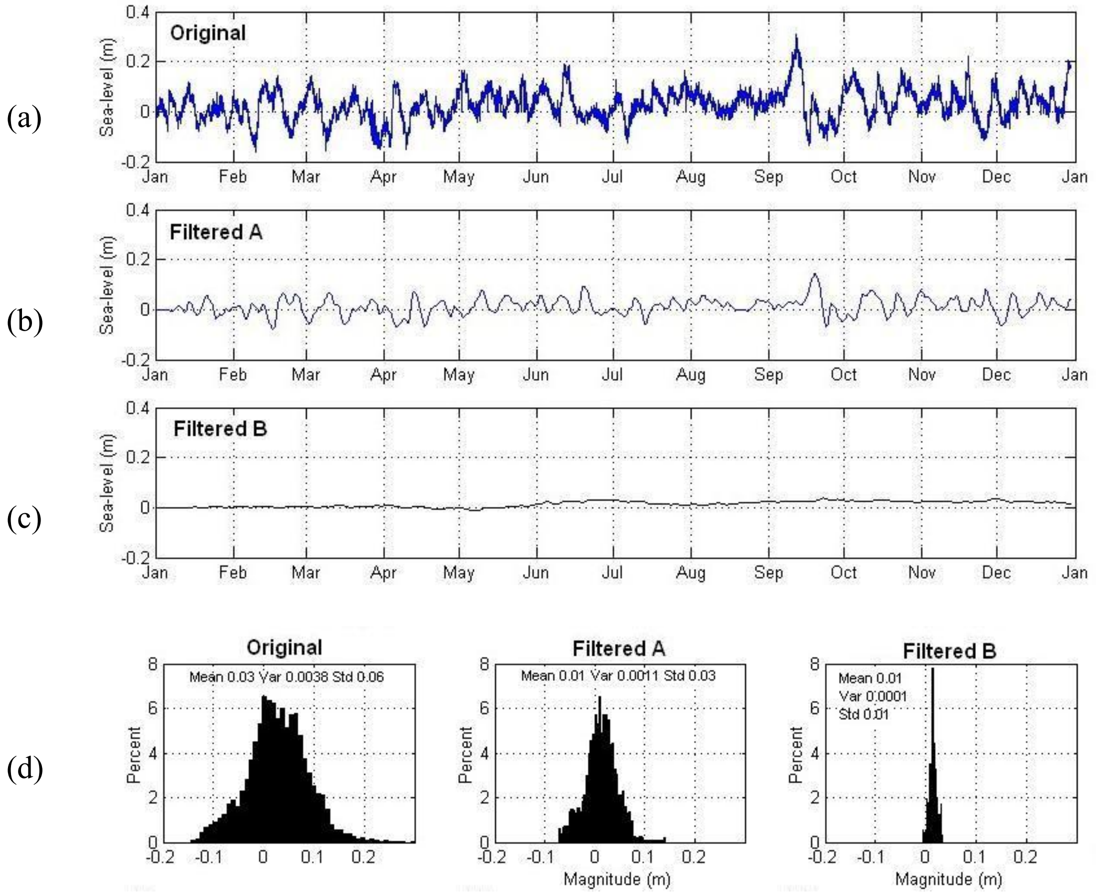

Figure 5.5.1. Time series for 2004 of sea-level measured at the National Tidal Centre Portland station. (a) adjusted residual sea-level, (b) low pass 5 day filtered signal, (c) low pass 90 day filtered signal. (d) histograms of respective distributions.

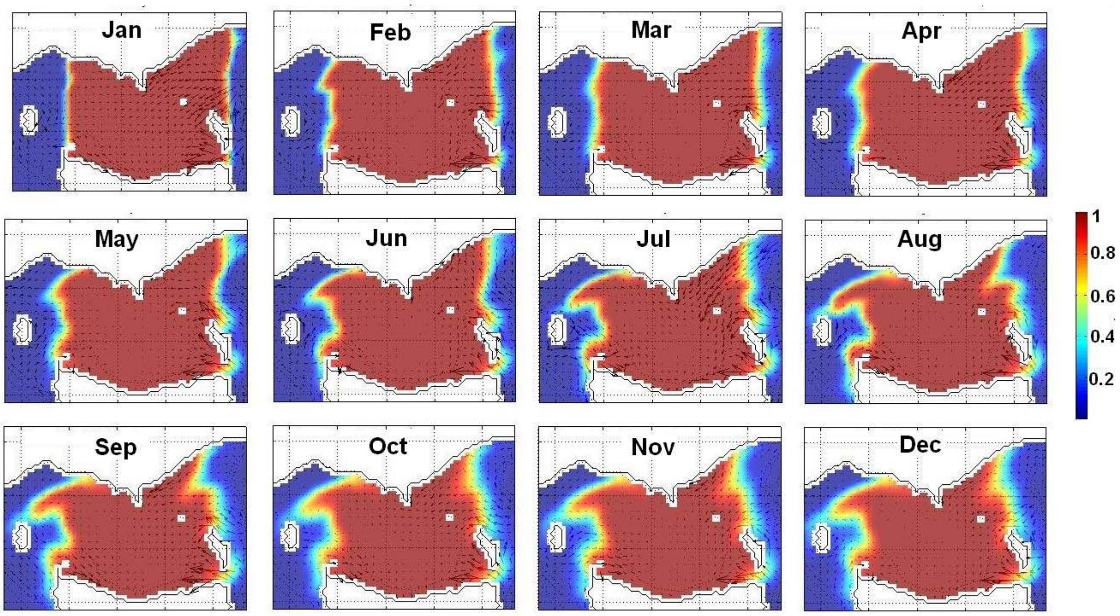

Figure 5.5.2. Monthly mean surface-layer tracer concentration in coastal-trapped wave experiment.

5.6 Overall Sensitivity

Experiment 1 predicted the longest flushing times and weakest mean currents in Bass Strait. Salinity was predicted to be lower in winter and spring than observations suggest. Similar high salinities in the surface-layer in summer were encountered as in the reference simulation. The effect of prescribing a model SAC has an important influence on Strait water mass properties. Although the strength of this forcing was adjusted through many sensitivity studies to an idealized level for the reference simulation, the results show that this is an important aspect to consider in future modelling of Strait water mass property variation. Any attempts to forecast these properties will need to account for residual sea-level along the southern Victorian shelf, west of the Strait. Ideally, temperature, salinity, sea-level and currents will need to be monitored at this location to improve forecasting efforts for Bass Strait waters. The prescription of a somewhat primitive model EAC off the shelf break in the north-eastern corner of the model domain was also tuned in a similar manner to the SAC through many experiments. In experiments with a strong EAC forcing of this type, water mass properties were minimally affected in the eastern side of the Strait. The model EAC was strongly guided by the shelf break and slope. If the EAC was prescribed on the shelf rather than in the open-ocean part of the model domain, the situation was different and water properties did enter the Strait. Therefore it will be important for future forecasting to establish and monitor the degree to which the EAC encroaches onto the shelf in the north-eastern part of Bass Strait.

Experiment 2 did not include tidal forcing and had the shortest flushing times of all the experiments. This coincides with the strongest mean currents and the least seasonal variation in circulation of all the simulations. Here the currents are driven by a combination of sea-level set-up resulting from the SAC boundary forcing, the winds and baroclinic effects. The difference in average Strait water mass properties in the interior was not substantially different from the reference simulation, except in the lower levels of vertical mixing seen in summer. This suggests that atmospheric forcing in the model still dominates seasonal water mass property variation in this scenario involving greater levels of lateral advection. The effect of the tides can be seen in the other experiments to alter water mass properties and residual sea-level in the Strait passages. This is done mainly by strong horizontal and vertical mixing. The model suggests residual sea-level at the Strait entrances influences the overall throughflow and tides modulate this, dampening the mean current system. It therefore is important that the tides be included in models which aim to predict the circulation in Bass Strait. This is also a potential issue for modelling of many other shelf-sea regions.

The sensitivity of water mass properties to mean wind forcing is highlighted in Experiment 3. HR winds represent an upper limit where lateral advection dominates over the role of air-sea fluxes in water mass property variation, in particular salinity. The high levels of lateral eastward advection, seen in the results of this experiment, lead to greater propagation of prescribed water mass properties from the north-western open-sea boundary into the Strait.

CHAPTER 6:
Summary & Conclusions

6.1 Summary

The results show that the seasonal residual circulation in Bass Strait is likely to be characterised by a topographically steered geostrophic current meander in winter and spring with residual eastward advection and a large clockwise eddy circulation in summer and possibly autumn. The modelling suggests that both features are driven by local mean winds and pressure gradients surrounding the Strait entrances. These two main different characters of the seasonal circulation, along with topographically induced eddies act to increase the mean age of water parcels in the Strait.

The reference simulation was studied using various transport timescale methods. Issues relating to the differences and similarities between age, residence and flushing time distributions in the case of an oceanic Strait were pointed out. The results provided first order impressions, in a high-resolution three-dimensional model, of water age, flushing time and residence time distributions and their seasonal variation for Bass Strait. Water age was found to be the most useful and easiest timescale to interpret time-varying circulation because of the way it traces the circulation directly. This was used to show how ‘new’ water is transported into the Strait from the west, how it encounters the Bass Strait meander and leads to ‘older’ water in south-eastern Bass Strait in winter. The older water was seen to be flushed out of the interior towards the end of winter and beginning of spring. Remnant portions of ‘older’ water not flushed in this period became caught in the summer circulation which induced further ‘ageing’.

Seasonal mean flushing time distributions were used to characterise the integrated differences, or advection-diffusion climates, of the reference simulation and the sensitivity studies. Shortest flushing times were found when tides were not included in the model in Experiment 2. These were of the order of 100-125 days in south-eastern Bass Strait. Using HR winds for surface momentum fluxes in Experiment 3 produced relatively short flushing times which were around 125-150 days in the south-eastern part of the Strait. The longest flushing times were found in the Experiment 1 involving no regional current forcing. These were of the order of 200-300 days in the south-eastern area. The reference simulation had flushing times which were of the order of 180-200 days in south-eastern Bass Strait, which was in closer agreement to Sandery and Kämpf (2005). Most seasonal variation in the circulation occurred in the reference simulation and was highlighted by greater differences between summer and winter flushing time distributions.

The importance of the SAC was highlighted in this study. Its true variation is not well understood or as prescribed in the model. The reference simulation is an attempt to study the long-term background seasonal variation in water mass properties and circulation in Bass Strait. The differences in results between this experiment, which included a parameterized SAC open-sea boundary forcing, and Experiment 1 (which did not include this forcing) highlight the importance of sea-level at the north-western corner of the Strait. This demonstrates how the circulation in Bass Strait is coupled to far field effects occurring further west in the ocean, particularly on the shelf. Sea-level and associated currents along southern Australia have both seasonal and interannual variation. Future forecasting efforts will need to closely focus on this issue.

The results suggest that the prescription of a strong EAC in the open-ocean part of the model domain had minimal influence on water mass properties in Bass Strait. The case is different when the EAC was prescribed as a sustained encroachment on the shelf. The EAC is strongly influenced by the topography in this region and appears to have a preference to propagate southwards off eastern Bass Strait rather than cross the shelf break. Water mass properties in Bass Strait in the model are least sensitive to varying strengths in EAC forcing when it was prescribed in the open-ocean. Inspection of SST imagery (not shown) suggests the degree of encroachment of the EAC onto the shelf in north-eastern Bass Strait is a minor process occurring maybe once or twice a year. This will, however, need to be considered in future studies. Further evidence for this being a minor process is the persistence of the well known thermohaline front between eastern Bass Strait and the Tasman Sea.

6.2 Key Findings

This study is the first modelling study which attempts to resolve the seasonal circulation in Bass Strait. Previous modelling studies have either been process oriented or focused mainly on the winter circulation. The findings of this study support early suggestions in the literature (Gibbs et al., 1986) that a westward surface transport is present in the Strait in summer. This study suggests that this transport is confined mainly to the surface-layer in southern and western Bass Strait and that a surface to bottom westward jet is present adjacent northern Tasmania. This periodic reversal of the typical winter flow pattern occurring in summer in the southern region of Bass Strait (see summer currents in Figure 1.4.1 and compare summer and winter currents in Figures 4.6.1 and 4.6.13) influences water mass properties, flushing times, residence times and age distribution. Mean sea-level at the north-western corner of the Strait was shown to be a more important factor controlling the Strait's residual seasonal circulation than mean-sea-levels in the open-ocean off eastern Bass Strait.

The results suggest a shallow surface-layer where salinities in summer in central and northern Bass Strait are higher than most, but not all, observations to date. Recent observations support model predictions. Significant gaps still exist in salinity data required to resolve the seasonal cycle of variation in the Strait.

The present study provides the first example of climate-averaged three-dimensional flushing times, residence times and age distributions, and their associated seasonal variation. It suggests that long flushing times (of the order of 180-200 days) are associated with 'older water' and are found in south-eastern Bass Strait. The summer circulation induces aging by moving older water not flushed out in the winter-spring period back to the southern central part of the Strait.

The results show that tidal mixing plays an important role in the entrances to Bass Strait. Although tidal residual currents were predicted to have virtually no influence on driving throughflow, the mixing induced by them in the Strait entrances alters water mass properties and the overall dynamics. It is suggested that by altering water mass properties, the tides modulate residual sea-level gradients, which would otherwise create stronger mean currents. Being a broad expanse of relatively shallow shelf-sea, Bass Strait is unique in terms of its circulation characteristics. The overall nature of the tides could also be unique to the region. Nonetheless, modelling studies of other shelf-seas may also need to investigate the importance of either including or excluding the effects of tides on the residual circulation.

The last key finding of this study, which is supported by previous studies, is a common topographically steered geostrophic meander in times of residual eastward transport, as shown in Figure 1.4.1.

6.3 Conclusions

A regional oceanographic model for Bass Strait was developed in order to study physical processes, such as tidal, wind and density driven advection and mixing at seasonal time scales. The character of tidal flow was well represented in the model. Mean currents at selected locations compared favourably with current-meter data. Water mass property distributions predicted by the model were in favourable agreement, particularly in winter, with the distributions derived from limited *in situ* observations. Collectively, the data is evidence for the existence of a mean winter current system involving a characteristic geostrophic meander. The summer circulation was predicted by the model to be characterised by a low pressure clockwise circulation in the interior. There is not enough observational data at present to verify this. In the model, both winter and summer processes were reflected in mean sea-level, transport timescale and water mass property distributions.

The relatively higher salinities in the model are derived from high evaporation in summer. Eastward advection along the meander in winter, spring and autumn was reflected in surface salinity distributions. Positive salinity anomalies in winter, for example, occurred in areas subject to the least erosion by lateral advection. Seasonal temperature variation in model data was more depth dependent and not as good a tracer of lateral transports. Water properties in the passages in the model were seen to be affected by tidal mixing. Tidal residual currents were shown to be relatively small, however the effect of tides on the flushing times of Bass Strait was shown to be very important. It is thought that the tides modulate seasonal mean sea-level gradients in critical locations, i.e. the Strait entrances, creating an environment of denser water mass properties than would otherwise exist. Sensitivity to mean winds was shown to be high and to have a significant effect on water mass properties and flushing times. HR winds were shown to be the least suitable wind climatology for the region in terms of resolving the seasonal ocean climate of the region.

Transport timescale methods using Eulerian and Lagrangian tracers were used as diagnostic tools for sensitivity studies. The study illustrated the useful nature of these methods for summarising the advective-diffusive flow climates of regional models. Flushing time, residence time and age distributions were shown to be able to identify seasonal variation in the circulation. The age distribution was able to be used to trace the source and sinks of water mass in the system. Age was seen to correlate with a positive salinity/density anomaly in south-eastern Bass Strait in winter in times when lateral advection dominated water-mass properties over air-sea fluxes. This was because age was defined to trace only lateral advection and diffusion. The ‘older’ water was shown to leave the south-eastern region in winter and spring via the continental shelf north of the Furneaux Group. The ‘older’ water in winter is hypothesised to be the source water for the Bass Strait Cascade.

6.4 Further Research

The process of dense shelf water cascading into the deeper ocean may be significant to climate when integrated over the world’s oceans. Further research focussing on the Bass Strait Cascade would therefore be an important requirement for understanding this process. Detailed modelling studies and observations would refine knowledge of these processes. In terms of regional modelling, including all the relevant processes in the simulations is the challenge. This also requires that the processes can first be identified. Simulations can be made more realistic by including the effects of regional coastal freshwater fluxes, surface waves, and by using high frequency forcing data derived from observations. Results are always dependent on the quality of surface forcing data and the resolution of observations. These are important factors influencing prediction skill and capability. A coupled ocean-atmosphere regional model for Bass Strait and evaluation of its performance in the study of the region’s climate would be a challenging and interesting area of further development and investigation.

NCEP reanalysis forcing data, used in the model, are long-term monthly means based mostly on daily records made in between 1948 and 1996. Model results should therefore provide a reasonably up to date image of the background mean climatological variation. Further research is required to understand the impact of climate change on circulation and water mass properties in Bass Strait. The issue is complex and requires attention because of the many changes likely to occur. Climate change may modify the wind fields and variability of both the EAC and SAC. The role of winds was shown to be a significant factor influencing model results implying a change in wind climatology will cause a direct change in the circulation and its properties. The EAC may increase in strength as a result of climate change. Model sensitivity to EAC forcing was low implying that this may be of minor significance for Bass Strait. The sensitivity of Bass Strait water properties to the SAC system was shown to be significant. Until climate variation in this system is better understood, it will not be clear as to how flushing times of Bass Strait change as a result of climate change.

Appendix A

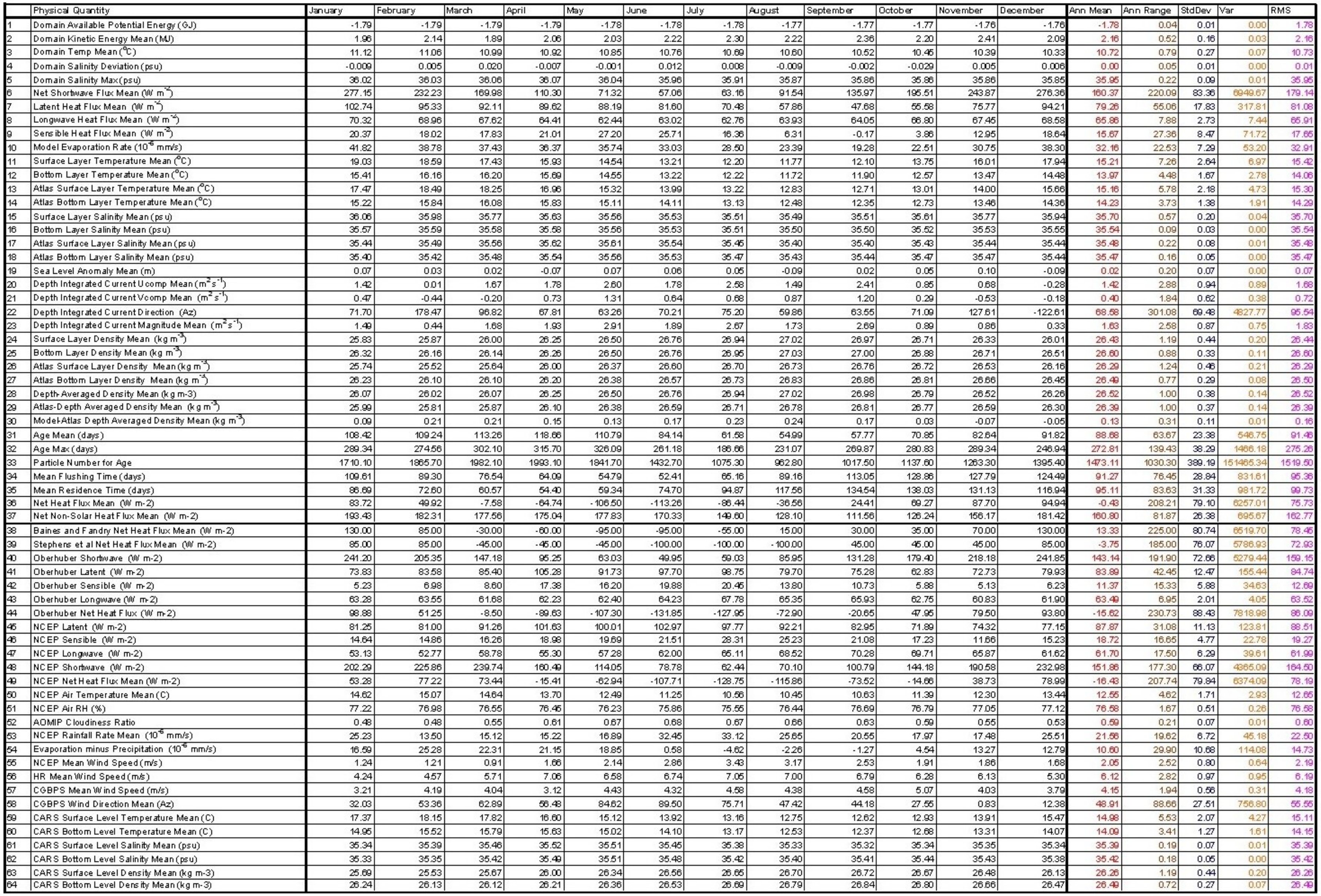

	Physical Quantity	January	February	March	April	May	June	July	August	September	October	November	December	Ann Mean	Ann Range	StdDev	Var	RMS
1	Domain Available Potential Energy (GJ)	-1.79	-1.79	-1.79	-1.79	-1.78	-1.78	-1.78	-1.77	-1.77	-1.77	-1.76	-1.76	-1.78	0.04	0.01	0.00	1.78
2	Domain Kinetic Energy Mean (MJ)	1.96	2.14	1.89	2.06	2.03	2.22	2.30	2.22	2.36	2.20	2.41	2.09	2.16	0.52	0.16	0.03	2.16
3	Domain Temp Mean ($^{\circ}$C)	11.12	11.06	10.99	10.92	10.85	10.76	10.69	10.60	10.52	10.46	10.39	10.33	10.72	0.79	0.27	0.07	10.73
4	Domain Salinity Deviation (psu)	-0.009	0.005	0.020	-0.007	-0.001	0.012	0.008	-0.009	-0.002	-0.029	0.005	0.006	0.00	0.05	0.01	0.00	0.01
5	Domain Salinity Max (psu)	36.02	36.03	36.06	36.07	36.04	35.96	35.91	35.87	35.86	35.86	35.86	35.85	35.95	0.22	0.09	0.01	35.95
6	Net Shortwave Flux Mean (W m^{-2})	277.15	232.23	169.98	110.30	71.32	57.06	63.16	91.54	135.97	195.51	243.87	276.36	160.37	220.09	83.36	6949.67	179.14
7	Latent Heat Flux Mean (W m^{-2})	102.74	95.33	92.11	89.62	88.19	81.60	70.48	57.86	47.68	55.58	75.77	94.21	79.26	55.06	17.83	317.81	81.08
8	Longwave Heat Flux Mean (W m^{-2})	70.32	68.96	67.62	64.41	62.44	63.02	62.76	63.93	64.05	66.80	67.45	68.58	65.86	7.88	2.73	7.44	65.91
9	Sensible Heat Flux Mean (W m^{-2})	20.37	18.02	17.83	21.01	27.20	25.71	16.36	6.31	-0.17	3.86	12.95	18.64	15.67	27.36	8.47	71.72	17.66
10	Model Evaporation Rate (10^{-6} mm/s)	41.82	38.78	37.43	36.37	35.74	33.03	28.50	23.39	19.28	22.51	30.75	38.30	32.16	22.53	7.29	53.20	32.91
11	Surface Layer Temperature Mean ($^{\circ}$C)	19.03	18.59	17.43	15.93	14.54	13.21	12.20	11.77	12.10	13.75	16.01	17.94	15.21	7.26	2.64	6.97	15.42
12	Bottom Layer Temperature Mean ($^{\circ}$C)	15.41	16.16	16.20	15.69	14.55	13.22	12.22	11.72	11.90	12.57	13.47	14.48	13.97	4.48	1.67	2.78	14.06
13	Atlas Surface Layer Temperature Mean ($^{\circ}$C)	17.47	18.49	18.25	16.96	15.32	13.99	13.22	12.83	12.71	13.01	14.00	15.66	15.16	5.78	2.18	4.73	15.30
14	Atlas Bottom Layer Temperature Mean ($^{\circ}$C)	15.22	15.84	16.08	15.83	15.11	14.11	13.13	12.48	12.35	12.73	13.46	14.36	14.23	3.73	1.38	1.91	14.29
15	Surface Layer Salinity Mean (psu)	36.06	35.98	35.77	35.63	35.56	35.53	35.51	35.49	35.51	35.61	35.77	35.94	35.70	0.57	0.20	0.04	35.70
16	Bottom Layer Salinity Mean (psu)	35.57	35.59	35.58	35.58	35.56	35.53	35.51	35.50	35.50	35.52	35.53	35.55	35.54	0.09	0.03	0.00	35.54
17	Atlas Surface Layer Salinity Mean (psu)	35.44	35.49	35.56	35.62	35.61	35.54	35.46	35.40	35.40	35.43	35.44	35.44	35.48	0.22	0.08	0.01	35.48
18	Atlas Bottom Layer Salinity Mean (psu)	35.40	35.42	35.48	35.54	35.56	35.53	35.47	35.43	35.44	35.47	35.47	35.44	35.47	0.16	0.05	0.00	35.47
19	Sea Level Anomaly Mean (m)	0.07	0.03	0.02	-0.07	0.07	0.06	0.05	-0.09	0.02	0.05	0.10	-0.09	0.02	0.20	0.07	0.00	0.07
20	Depth Integrated Current Ucomp Mean (m^{2} s^{-1})	1.42	0.01	1.67	1.78	2.60	1.78	2.58	1.49	2.41	0.85	0.68	-0.28	1.42	2.88	0.94	0.89	1.68
21	Depth Integrated Current Vcomp Mean (m^{2} s^{-1})	0.47	-0.44	-0.20	0.73	1.31	0.64	0.68	0.87	1.20	0.29	-0.53	-0.18	0.40	1.84	0.62	0.38	0.72
22	Depth Integrated Current Direction (Az)	71.70	178.47	96.82	67.81	63.26	70.21	75.20	59.86	63.55	71.09	127.61	-122.61	68.58	301.08	69.48	4827.77	95.54
23	Depth Integrated Current Magnitude Mean (m^{2} s^{-1})	1.49	0.44	1.68	1.93	2.91	1.89	2.67	1.73	2.69	0.89	0.86	0.33	1.63	2.58	0.87	0.75	1.83
24	Surface Layer Density Mean (kg m^{-3})	25.83	25.87	26.00	26.25	26.50	26.76	26.94	27.02	26.97	26.71	26.33	26.01	26.43	1.19	0.44	0.20	26.44
25	Bottom Layer Density Mean (kg m^{-3})	26.32	26.16	26.14	26.26	26.50	26.76	26.95	27.03	27.00	26.88	26.71	26.51	26.60	0.88	0.33	0.11	26.60
26	Atlas Surface Layer Density Mean (kg m^{-3})	25.74	25.52	25.64	26.00	26.37	26.60	26.70	26.73	26.76	26.72	26.53	26.16	26.29	1.24	0.46	0.21	26.29
27	Atlas Bottom Layer Density Mean (kg m^{-3})	26.23	26.10	26.10	26.20	26.38	26.57	26.73	26.83	26.86	26.81	26.66	26.45	26.49	0.77	0.29	0.08	26.50
28	Depth-Averaged Density Mean (kg m-3)	26.07	26.02	26.07	26.25	26.50	26.76	26.94	27.02	26.98	26.79	26.52	26.26	26.52	1.00	0.38	0.14	26.52
29	Atlas-Depth Averaged Density Mean (kg m^{-3})	25.99	25.81	25.87	26.10	26.38	26.59	26.71	26.78	26.81	26.77	26.59	26.30	26.39	1.00	0.37	0.14	26.39
30	Model-Atlas Depth Averaged Density Mean (kg m^{-3})	0.09	0.21	0.21	0.15	0.13	0.17	0.23	0.24	0.17	0.03	-0.07	-0.05	0.13	0.31	0.11	0.01	0.16
31	Age Mean (days)	108.42	109.24	113.26	118.66	110.79	84.14	61.58	54.99	57.77	70.85	82.64	91.82	88.68	63.67	23.38	546.75	91.46
32	Age Max (days)	289.34	274.56	302.10	315.70	326.09	261.18	186.66	231.07	269.87	280.83	289.34	246.94	272.81	139.43	38.29	1466.18	275.26
33	Particle Number for Age	1710.10	1865.70	1982.10	1993.10	1841.70	1432.70	1075.30	962.80	1017.50	1137.60	1263.30	1395.40	1473.11	1030.30	389.19	151465.34	1519.50
34	Mean Flushing Time (days)	109.61	89.30	76.54	64.09	54.79	52.41	65.16	89.16	113.05	128.86	127.79	124.49	91.27	76.45	28.84	831.61	95.36
35	Mean Residence Time (days)	86.69	72.60	60.57	54.40	59.34	74.70	94.87	117.56	134.54	138.03	131.13	116.94	95.11	83.63	31.33	981.72	99.73
36	Net Heat Flux Mean (W m-2)	83.72	49.92	-7.58	-64.74	-106.50	-113.26	-86.44	-36.56	24.41	69.27	87.70	94.94	-0.43	208.21	79.10	6257.01	75.73
37	Net Non-Solar Heat Flux Mean (W m-2)	193.43	182.31	177.56	175.04	177.83	170.33	149.60	128.10	111.56	126.24	156.17	181.42	160.80	81.87	26.38	695.67	162.77
38	Baines and Fandry Net Heat Flux Mean (W m-2)	130.00	85.00	-30.00	-60.00	-95.00	-95.00	-55.00	15.00	30.00	35.00	70.00	130.00	13.33	225.00	80.74	6519.70	78.46
39	Stephens et al Net Heat Flux Mean (W m-2)	85.00	85.00	-45.00	-45.00	-45.00	-100.00	-100.00	-100.00	45.00	46.00	45.00	85.00	-3.75	185.00	76.07	5786.93	72.93
40	Oberhuber Shortwave (W m-2)	241.20	205.35	147.18	95.25	63.03	49.95	59.03	85.95	131.28	179.40	218.18	241.85	143.14	191.90	72.66	5279.44	159.15
41	Oberhuber Latent (W m-2)	73.83	83.58	85.40	105.28	91.73	97.70	98.75	79.70	75.28	62.83	72.73	79.93	83.89	42.45	12.47	155.44	84.74
42	Oberhuber Sensible (W m-2)	5.23	6.98	8.60	17.38	16.20	19.88	20.46	13.80	10.73	5.88	5.13	6.23	11.37	15.33	5.88	34.63	12.69
43	Oberhuber Longwave (W m-2)	63.28	63.55	61.68	62.23	62.40	64.23	67.78	65.35	65.93	62.75	60.83	61.90	63.49	6.95	2.01	4.05	63.52
44	Oberhuber Net Heat Flux (W m-2)	98.88	51.25	-8.50	-89.63	-107.30	-131.85	-127.95	-72.90	-20.65	47.95	79.50	93.80	-15.62	230.73	88.43	7818.98	86.09
45	NCEP Latent (W m-2)	81.25	81.00	91.26	101.63	100.01	102.97	97.77	92.21	82.95	71.89	74.32	77.15	87.87	31.08	11.13	123.81	88.51
46	NCEP Sensible (W m-2)	14.64	14.86	16.26	18.98	19.69	21.51	28.31	25.23	21.08	17.23	11.66	15.23	18.72	16.65	4.77	22.78	19.27
47	NCEP Longwave (W m-2)	53.13	52.77	58.78	55.30	57.28	62.00	65.11	68.52	70.28	69.71	65.87	61.62	61.70	17.50	6.29	39.61	61.99
48	NCEP Shortwave (W m-2)	202.29	225.86	239.74	160.49	114.05	78.78	62.44	70.10	100.79	144.18	190.58	232.98	151.86	177.30	66.07	4365.09	164.50
49	NCEP Net Heat Flux Mean (W m-2)	53.28	77.22	73.44	-15.41	-62.94	-107.71	-128.75	-115.86	-73.52	-14.66	38.73	78.99	-16.43	207.74	79.84	6374.09	78.19
50	NCEP Air Temperature Mean (C)	14.62	15.07	14.64	13.70	12.49	11.25	10.56	10.45	10.63	11.39	12.30	13.44	12.55	4.62	1.71	2.93	12.66
51	NCEP Air RH (%)	77.22	76.98	76.55	76.46	76.23	75.86	75.55	76.44	76.69	76.79	77.05	77.12	76.58	1.67	0.51	0.26	76.58
52	AOMIP Cloudiness Ratio	0.48	0.48	0.55	0.61	0.67	0.68	0.67	0.66	0.63	0.59	0.55	0.53	0.59	0.21	0.07	0.01	0.60
53	NCEP Rainfall Rate Mean (10^{-6} mm/s)	25.23	13.50	15.12	15.22	16.89	32.45	33.12	25.65	20.55	17.97	17.48	25.51	21.56	19.62	6.72	45.18	22.50
54	Evaporation minus Precipitation (10^{-6} mm/s)	16.59	25.28	22.31	21.15	18.85	0.58	-4.62	-2.26	-1.27	4.54	13.27	12.79	10.60	29.90	10.68	114.08	14.73
55	NCEP Mean Wind Speed (m/s)	1.24	1.21	0.91	1.66	2.14	2.86	3.43	3.17	2.53	1.91	1.86	1.68	2.05	2.52	0.80	0.64	2.19
56	HR Mean Wind Speed (m/s)	4.24	4.57	5.71	7.06	6.58	6.74	7.05	7.00	6.79	6.28	6.13	5.30	6.12	2.82	0.97	0.95	6.19
57	CGBPS Mean Wind Speed (m/s)	3.21	4.19	4.04	3.12	4.43	4.32	4.58	4.38	4.58	5.07	4.03	3.79	4.15	1.94	0.56	0.31	4.18
58	CGBPS Wind Direction Mean (Az)	32.03	53.36	62.89	56.48	84.62	89.50	75.71	47.42	44.18	27.55	0.83	12.38	48.91	88.66	27.51	756.80	55.56
59	CARS Surface Level Temperature Mean (C)	17.37	18.15	17.82	16.60	15.12	13.92	13.16	12.75	12.62	12.93	13.91	15.47	14.98	5.53	2.07	4.27	15.11
60	CARS Bottom Level Temperature Mean (C)	14.95	15.52	15.79	15.63	15.02	14.10	13.17	12.53	12.37	12.68	13.31	14.07	14.09	3.41	1.27	1.61	14.15
61	CARS Surface Level Salinity Mean (psu)	35.34	35.39	35.46	35.52	35.51	35.45	35.38	35.33	35.32	35.34	35.35	35.34	35.39	0.19	0.07	0.01	35.39
62	CARS Bottom Level Salinity Mean (psu)	35.33	35.35	35.42	35.49	35.51	35.48	35.42	35.40	35.41	35.44	35.43	35.38	35.42	0.18	0.05	0.00	35.42
63	CARS Surface Level Density Mean (kg m-3)	25.69	25.53	25.67	26.00	26.34	26.56	26.65	26.70	26.72	26.67	26.48	26.13	26.26	1.19	0.44	0.20	26.26
64	CARS Bottom Level Density Mean (kg m-3)	26.24	26.13	26.12	26.21	26.36	26.53	26.69	26.79	26.84	26.80	26.66	26.47	26.49	0.72	0.27	0.07	26.49

Table A1. Monthly-mean data and statistics from model and observations.

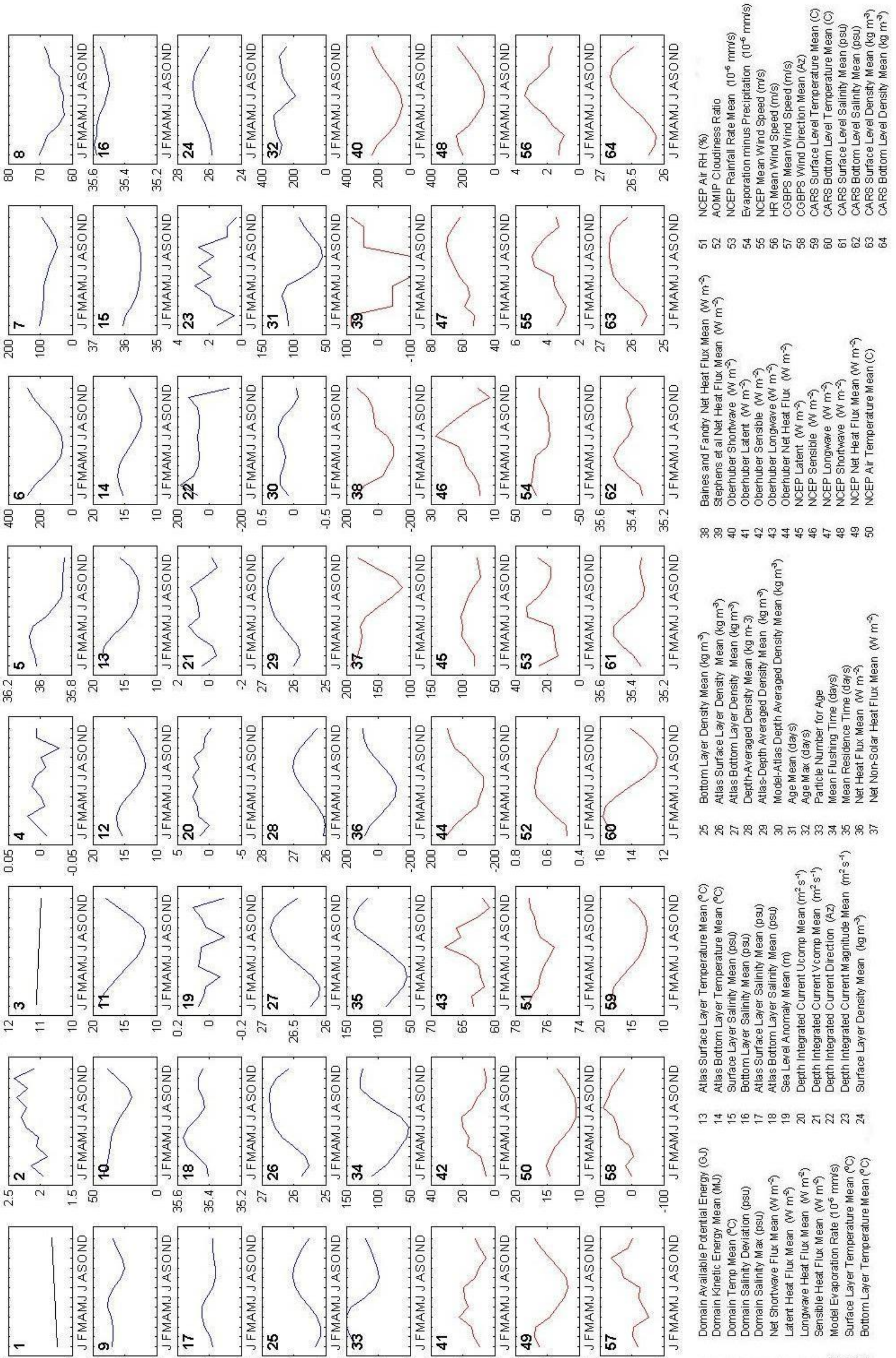

Figure A1. Monthly-mean seasonal trends from model results, previous studies and observations

References

2002. Geoscience Australia. Australian Bathymetry and Topography Grid, ANZCW0703004301.

Anon, 2005. Ocean Currents around Tasmania. CSIRO Marine and Atmospheric Research.

Antonia, R.A., Chambers, A.J., Rajagopalan, S. and Sreenivasan, K.R., 1977. Measurements of Turbulent Fluxes in Bass Strait. Journal of Physical Oceanography, 8: 28-37.

Aquenal, 2005. Gunns Ltd Pulp Mill Marine Biological and Pollutant Survey at the Proposed Outfall Site, Hobart.

Baines, P.G., Edwards, R.J. and Fandry, C.B., 1983. Observations of a New Baroclinic Current along the Western Continental Slope of Bass Strait. Australian Journal of Marine and Freshwater Research, 34: 155-157.

Baines, P.G. and Fandry, C.B., 1983. Annual Cycle of the Density Field in Bass Strait. Australian Journal of Marine and Freshwater Research, 34: 143-153.

Baines, P.G., G. Hubbert, and S. Power, 1991. Fluid transport through Bass Strait. Continental Shelf Research, 11: 269-293.

Blackman, D.R., Hinwood, J.B. and Lleonart, G.T., 1987. Temperature anomaly in Western Bass Strait. Australian Journal of Marine and Freshwater Research, 38(191-195).

Boland, F.M., 1971. Temperature-Salinity Anomalies at Depths between 200 m and 800 m in the Tasman Sea. Australian Journal of Marine and Freshwater Research, 22: 55-62.

Brodie, R. and Radok, R., 1970. Tides, weather and surface drift in Bass Strait. Horace Lamb Centre for Oceanographic Research, Flinders University of South Australia, 35.

Bruce, B.D., Condie, S.A. and Sutton, C.A., 2001. Larval distribution blue grenadier (*Macruronus novazelandiae Hector*) in south-eastern Australia: further evidence for a second spawning area. Australian Journal of Marine and Freshwater Research, 52: 603-610.

Bye, J.T., 1983. The general circulation in a dissipative basin with longshore wind stresses. Journal of Physical Oceanography, 13: 1553-1563.

Church, J., Freeland, H. and Smith, R.L., 1986. Coastal-Trapped Waves on the East Australian Continental Shelf Part 1: Propagation of Modes. Journal of Physical Oceanography, 16: 1929-1943.

Cirano, M., 2000. Wintertime Circulation within the Southeast Indian Ocean: A Numerical Study,. PhD Thesis, University of NSW.

Cirano, M., and Middleton, J. F., 2004. Aspects of the Mean Wintertime Circulation along Australia's Southern Shelves: Numerical Studies. Journal of Physical Oceanography, 34: 668-684.

Condie, S.A., 1995. Interactions between western boundary currents and shelf waters: A mechanism for coastal upwelling. Journal of Geophysical Research, 100(C12): 24,811-24,818.

Cushman-Roisin, B., 1994. Introduction to Geophysical Fluid Dynamics, New Jersey.

da Silva, A., Young, C.C. and Levitus, S., 1994. Algorithms and Procedures, Vol. 1 of Atlas of Surface Marine Data 1994. NOAA Atlas NESDIS 6. U. S. Department of Commerce, Washington, D. C. : 84 pp.

Deleersnijder, E., Campin, J.M. and Delhez, E.J.M., 2001. The concept of age in marine modelling I. Theory and preliminary modelling results. Journal of Marine Systems, 28: 229-267.

Deleersnijder, E. and Delhez, E.J.M., 2004. Symmetry and asymmetry of water ages in a one-dimensional flow. Journal of Marine Systems, 48: 61-66.

Deleersnijder, E., Mouchet, A., Delhez, E.J.M. and Beckers, J.M., 2002. Transient Behaviour of Water Ages in the World Ocean. Mathematical and Computer Modelling, 36: 121-127.

Delhez, E.J.M., 2006. Transient residence and exposure times. Ocean Science, 2: 1-9.

Delhez, E.J.M., Campin, J.M., Hirst, A.C. and Deleersnijder, E., 1999. Toward a general theory of the age in ocean modelling. Ocean Modelling, 1: 17-27.

Delhez, E.J.M. and Deleersnijder, E., 2002. The concept of age in marine modelling II. Concentration distribution function in the English Channel and the North Sea. Journal of Marine Systems, 31: 279-297.

Delhez, E.J.M., Heemink, A.W. and Deleersnijder, E., 2004. Residence time in a semi-enclosed domain from the solution of an adjoint problem. Estuarine, Coastal and Shelf Science, 61: 691-702.

Dunn, J.R. and Ridgway, K.R., 2002. Mapping ocean properties in regions of complex topography. Deep Sea Research Part I : Oceanographic Research, 49(3): 591-604.

England, M.H., 1995. The age of water and ventilation timescales in a global ocean model. Journal of Physical Oceanography, 25: 2756-2777.

Evans, S.R. and Middleton, J.F., 1998. Regional Model of Shelf Circulation near Bass Strait: A New Upwelling Mechanism. Journal of Physical Oceanography, 28: 1439-1457.

Fandry, C.B., 1981. Development of a Numerical Model of Tidal and Wind Driven Circulation in Bass Strait. Australian Journal of Marine and Freshwater Research, 32: 9-21.

Fandry, C.B., 1982. A Numerical Model of the Wind-Driven Transient Motion in Bass Strait. Journal of Geophysical Research, 87(C1): 499-517.

Fandry, C.B., 1983. Model for the Three-dimensional structure of Wind-driven and Tidal Circulation in Bass Strait. Australian Journal of Marine and Freshwater Research, 34: 121-141.

Fandry, C.B., Hubbert, G.D. and McIntosh, P.C., 1985. Comparison of predictions of a numerical model and observations of tides in Bass Strait. Australian Journal of Marine and Freshwater Research, 36(6): 727-752.

Flinders, M., 1798. Narrative of the expedition of the Colonial Sloop Norfolk 1798-1799

Flinders, M., 1814. A Voyage to Terra Australis, 1 & 2. G. & W. Nichol: London.

Geernaert, G.L., Katsaros, K.B. and Richter, K., 1986. Variation of the drag coefficient and its dependence on sea state. Journal of Geophysical Research, 91: 7667–7679.

Gibbs, C.F., Arnott, G.H., Longmore, A.R. and Marchant, J.W., 1991. Nutrient and Plankton Distribution near a Shelf Break Front in the Region of the Bass Strait Cascade. Australian Journal of Marine and Freshwater Research, 42: 201-217.

Gibbs, C.F., Tomczak, M.J. and Longmore, A.R., 1986. The Nutrient Regime of Bass Strait. Australian Journal of Marine and Freshwater Research, 37: 451-466.

Gill, A.E., 1982. Atmosphere-Ocean Dynamics. International Geophysics Series. Harcourt Brace and Company.

Godfrey, S.J., Jones, I.S.F., Garrey, J., Maxwell, H. and Scott, B.D., 1980. On the winter cascade from Bass Strait into the Tasman Sea. Australian Journal of Marine and Freshwater Research, 31: 275-286.

Hall, T. and Haine, T.W.N., 2004. Tracer age symmetry in advective-diffusive flows. Journal of Marine Systems, 48: 51-59.

Haney, R.L., 1990. On the Pressure Gradient Force over Steep Topography in Sigma Coordinate Ocean Models. Journal of Physical Oceanography, 21: 610-619.

Hannah, C.G., 1992. Geostrophic Control with Wind Forcing: Application to Bass Strait. Journal of Physical Oceanography, 22: 1596-1599.

Hellerman, S. and Rosenstein, M., 1983. Normal monthly wind stress over the world ocean with error estimates. Journal of Physical Oceanography, 13
1093-1104. .

Herzfeld, M., 1997. The annual cycle of sea surface temperature in the Great Australian Bight. Progress in Oceanography, 39: 1-27.

Herzfeld, M. and Tomczak, M., 1997. Numerical modelling of sea surface temperature and circulation in the Great Australian Bight. Progress in Oceanography, 39: 29-78.

Hirst, A.C., 1999. Determination of water component age in ocean models: application to the fate of North Atlantic Deep Water. Ocean Modelling, 1: 81-94.

Jones, I.S.F., 1980. Tidal and Wind-driven Currents in Bass Strait. Australian Journal of Marine and Freshwater Research, 31: 109-117.

Jones, I.S.F. and Padman, L., 1983. Semidiurnal internal tides in Eastern Bass Strait. Australian Journal of Marine and Freshwater Research, 34: 159-171.

Jones, J.E., 2002. Coastal and Shelf Sea modelling in the European Context. Oceanography and Marine Biology: an annual review, 40: 37-141.

Kaempf, J., 2005. Cascading-driven upwelling in submarine canyons at high latitudes. Journal of Geophysical Research, 110(C02007): 1-10.

Kalnay, E. et al., 1996. The NCEP/NCAR 40-Year Reanalysis Project. Bulletin of the American Meteorological Society, 77: 437-471.

Kämpf, J., Doubell, M., Griffin, D., Matthews, R.L. and Ward, T.M., 2004. Evidence of large seasonal coastal upwelling system along the southern shelf of Australia. Geophysical Research Letters, 31: 1-4.

Karstensen, J. and Tomczak, M., 1998. Age determination of mixed water masses using CFC and oxygen data. Journal of Geophysical Research, 103(C9): 18599-18609.

Kottek, M., Grieser, J., Beck, C., Rudolf, B. and Rubel, F., 2006. World Map of Köppen-Geiger Climate Classification updated. Meteorol. Z. , 15: 259-263.

Lara, A.L. and Neira, F.J., 2003. Studies on the early life history of fishes in the Tamar Estuary, Tasmania. Unpublished Final Project Report to Natural Heritage Trust: 70.

Luick, J.L., Kase, R. and Tomczak, M., 1994. On the formation and spreading of the Bass Strait cascade. Continental Shelf Research, 14: 385-399.

Luyten, P.J. et al., 1999. COHERENS —A Coupled Hydrodynamical-Ecological Model for Regional and Shelf Seas: User Documentation., Management Unit of the Mathematical Models of the North Sea.

.

Maier-Reimer, E. and Sündermann, J., 1982. On Tracer Methods in Computational Hydrodynamics. Engineering Application of Computational Hydraulics, 1(Pitman Advanced Publ. Program, Boston).

Marinov, D., Norro, A. and Zaldivar, J.-M., 2006. Application of COHERENS model for hydrodynamic investigation of Sacca di Goro coastal lagoon (Italian Adriatic Sea shore). Ecological Modelling, 193: 52-68.

McIntosh, P.C. and Bennett, A.F., 1984. Open ocean modelling as an inverse problem: M2 tides in Bass Strait. Journal of Physical Oceanography, 14: 601-614.

Mesinger, F. and Janic, Z.I., 1985. Problems and numerical methods of the incorporation of mountains in atmospheric models. Lectures in Applied Mathematics, 22: 81-121.

Middleton, J.F., 1994. The Baroclinic Response of Straits and Bays to Coastal-Trapped Wave Scattering. Journal of Physical Oceanography, 24: 521-539.

Middleton, J.F. and Black, K.P., 1994. The low frequency circulation in and around Bass Strait: a numerical study. Continental Shelf Research, 14: 1495-1521.

Middleton, J.F. and Cirano, M., 2002. A northern boundary current along Australia's southern shelves: The Flinders Current. Journal of Geophysical Research, 107.

Middleton, J.F. and Viera, F., 1991. The Forcing of Low Frequency Motions within Bass Strait. Journal of Physical Oceanography, 21: 695-708.

Mirshak, R. and Allen, S.E., 2005. Spin-up and the effects of a submarine canyon: Applications to upwelling in Astoria Canyon. Journal of Geophysical Research, 110(C02013): 1-14.

Monin, A. and Obukhov, A., 1954. Basic turbulent mixing laws in the atmospheric nearsurface layer. Trans. Geophys . Inst. Akad. Nauk USSR, 151: 163–187.

Monsen, N.E., Cloem, J.E., Lucas, L.V. and Monismith, S.G., 2002. A comment on the use of flushing time, residence time, and age as transport time scales. Limnology and Oceanography, 47(5): 1545-1553.

Newell, B.S., 1960. Hydrology of south-eastern Australian waters: Bass Strait and New South Wales tuna fishing area, CSIRO Aust. Div. Fish. Oceanogr.

Nihoul, J.C.J., Deleersnijder, E. and Djenidi, S., 1989. Modelling the General Circulation of Shelf Seas by 3D k-e Models. Earth Science Reviews, 26(1989): 163-189.

Oberhuber, J.M., 1988. Oberhuber's Climatological Atlas of Heat Fluxes and Radiation Budget Over the Global Ocean. NCAR, Boulder, CO, http://dss/ucar/edu/datasets/ds541.0/.

Oliviera, A. and Baptista, A.M., 1997. Diagnostic modeling of residence times in estuaries. Water Resources Research, 33: 1935-1946.

Paulson, C.A. and Simpson, J.J., 1977. Irradiance Measurements in the Upper Ocean. Journal of Physical Oceanography, 7: 952-956.

Ridgway, K.R. and Condie, S.A., 2004. The 5500-km-long boundary flow off western and southern Australia. Journal of Geophysical Research, 109.

Ridgway, K.R. and Godfrey, J.S., 1997. Seasonal cycle of the East Australian Current. Journal of Geophysical Research, 102(C10): 22,921-22,936.

Ridgway, K.R., J.R., Dunn, and J.L., Wilkin, 2001. Ocean interpolation by 4-dimensional weighted least squares - application to the waters around Australasia. Journal of Atmospheric and Oceanic Technology.

Roughan, M. and Middleton, J.H., 2002. A comparison of observed upwelling mechanisms off the east coast of Australia. Continental Shelf Research, 22: 2551-2572.

Ruddick, K.G., 1995. Modelling of coastal processes influenced by freshwater discharge of the Rhine, University of Liege, Belgium, 247 pp.

Sadrinasab, M. and Kämpf, J., 2004. Three-dimensional flushing times in the Persian Gulf. Geophysical Research Letters, 31(L24301): 10.1029/2004GL020425.

Sandery, P.A. and Kämpf, J., 2007. Transport timescales for identifying seasonal variation in Bass Strait, south-eastern Australia. Estuarine, Coastal and Shelf Science, 74(4): 684-696.

Sandery, P.A. and Kämpf, J., 2005. Winter-Spring Flushing of Bass Strait, South-Eastern Australia, A Numerical Modelling Study. Estuarine, Coastal and Shelf Science, 63: 23-31.

Siefredt, L. and Barnier, B., 1993. Banque de Donness AVISO Vent/flux Climatologie des Analysis de Surface du CepMMT Tech rep. 91 1430 025: 99 pp.

Smith, D.J. and Longmore, A.R., 1980. Phosphate Distribution in Bass Strait and South-eastern Australian Coastal Waters. Australian Journal of Marine and Freshwater Research, 31: 119-128.

Steinhorn, I., 1991. Salt flux and evaporation. Journal of Physical Oceanography, 21: 1681-1683.

Stephens, G.L., Campbell, G.G. and Vonder Haar, T.H., 1981. Earth Radiation Budgets. Journal of Geophysical Research, 86(C10): 9739-9760.

Takeoka, H., 1984. Fundamental concepts of exchange and transport time scales in a coastal sea. Continental Shelf Research, 3: 311-326.

Tomczak, M.J., 1985. The Bass Strait water cascade during winter 1981. Continental Shelf Research, 4: 255-278.

Tomczak, M.J., 1987. The Bass Strait water cascade during summer 1981-1982. Continental Shelf Research, 7: 561-572.

Trenberth, K.E., C., O.J. and G., L.W., 1989. A Global Ocean Wind Stress Climatology Based on ECMWF Analyses. Tech. rep. NCAR/TN-338+STR, National Centre for Atmospheric Research, Boulder, Colorado 98 pp.

Walker, S.J., 1999. Coupled hydrodynamic and transport models of Port Phillip Bay, a semi-enclosed bay in south-eastern Australia. Australian Journal of Marine and Freshwater Research, 50: 469-481.

Zimmerman, J.T.F., 1988. Estuarine Residence Times in Hydrodynamics of Estuaries, CRC Press. Inc., Florida US, 1: 75-84.